Direct Computation of Instability Points with Inequality Constraints Using the Finite Element Method

H. Tschöpe
E. Oñate
P. Wriggers

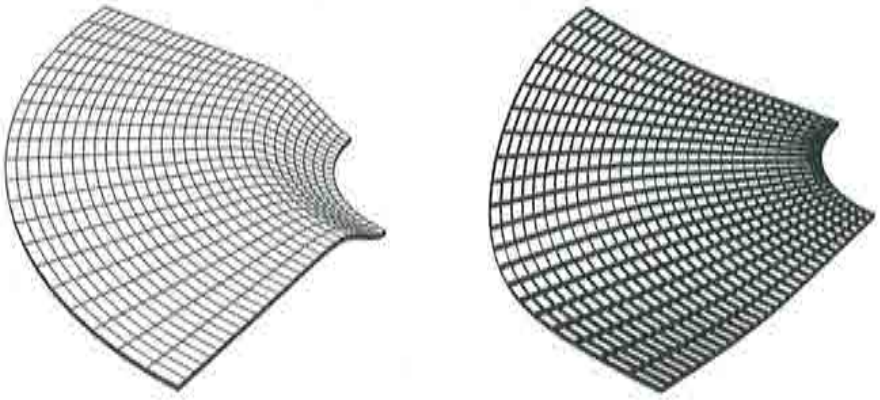

Monograph CIMNE Nº-61, July 2001

Direct Computation of Instability Points with Inequality Constraints Using the Finite Element Method

H. Tschöpe
E. Oñate
P. Wriggers

Monograph CIMNE Nº-61, July 2001

International Center for Numerical Methods in Engineering
Gran Capitán s/n, 08034 Barcelona, Spain

INTERNATIONAL CENTER FOR NUMERICAL METHODS IN ENGINEERING
Edificio C1, Campus Norte UPC
Gran Capitán s/n
08034 Barcelona, Spain

Primera edición Julio 2001

DIRECT COMPUTATION OF INSTABILITY POINTS WITH INEQUALITY CONSTRAINTS USING THE FINITE ELEMENT METHOD

Monografía CIMNE M61

ISBN: 84-89925-81-X

Depósito legal: B-34516-2001

Contents

Chapter 1

Introduction

1.1 Motivation

In structural mechanics buckling phenomena often have serious consequences as they mean a loss of stability or a shape change of the whole structure. Typical examples for these phenomena are the buckling of rods, plates, beams, arches and shell structures. Further examples for phenomena that are connected with a stability loss are diffuse necking bifurcation problems or the formation of shear bands in elastic-plastic solids. With the weight optimization of mechanical components, an important issue in e.g. aeronautics, structures become thinner and thus more susceptible to buckling.

Since the buckling of a structure is a dynamic process, a proper description of such phenomena has to account for dynamic effects. Nevertheless as long as the load on a structure is lesser than the critical load, i.e. the load where buckling takes place, the load–deformation relation in most cases can be sufficiently described quasi-staticly. To safely dimension a structure in a static mechanical problem for example, dynamic effects can be neglected, since the objective here is a mere detection of the critical loads.

Critical points can be grouped in limit load points and bifurcation points. At bifurcation points the mechanical structure does not necessarily buckle in contrary to limit load points. A bifurcation of the load–deflection path simply indicates that two or more different solutions for the problem exist. The behavior of a structure at those points is determined by material or geometrical imperfections.

The history of stability theory for mechanical problems dates back to the 18th century and the early works of [Euler, 1774], who studied the buckling of beams. A lot of experimental and theoretical investigation has been dedicated to the buckling of plates and shells at the beginning of the 20th century, see [Lorenz, 1908], [Timoshenko, 1910], [Zoelly, 1915]. An important step was the concept proposed by [Koiter, 1945], which allows the calculation of the post–buckling behavior of elastic structures by performing a series expansion of the displacement state in the vicinity of a bifurcation point.

When numerical methods such as the Finite Element Method (FEM) were developed more complex mechanical problems could be solved. With the introduction of arclength methods, by [Wemper, 1971], [Riks, 1972] in engineering and [Keller, 1977], [Rheinboldt, 1981] in mathematics, even the computation of complex non-linear load–deflection paths became feasible. The load parameter was considered as an additional degree of freedom and a control equation was added and solved simultaneously with the governing equa-

tions. Further contributions and enhancements to these arclength methods were made by e.g. [Crisfield, 1981] and [Ramm, 1981] who introduced improvements on the control equations of the method. The use of a quadratic predictor for the arclength method was demonstrated in [Wagner, 1991a]. Detection of critical points however was made with indicator functions that had to be computed accompanyingly to incremental–iterative path computation methods. The value of those functions indicates whether a critical point has been passed during path computation. Examples of these are the determinant of the tangent stiffness matrix or the number of negative diagonal elements.

The next step was to compute critical points instead of only localizing them. This can be accomplished by interpolating or extrapolating an indicator function to get estimates of the critical values. A different approach is made in the limit load analysis that bases on the idea of a tangent stiffness matrix split and the formulation of an eigenvalue problem for the critical load.

With the extension of the set of equations by a condition for critical points the direct computation of a critical point becomes faesible. In the mathematical literature these methods can be found in [Abbott, 1978], [Seydel, 1979], [Moore and Spence, 1980], [Werner and Spence, 1984] to name only a few. The extended system was applied to engineering problems for the first time in [Wriggers et al., 1988]. Enhancements on the algorithm were proposed in [Wriggers and Simo, 1990]. [Reitinger, 1994] implemented the method in the optimization process of structures. Another method of interest is the critical displacement method (CDM) which was developed in recent years by [Oñate and Matias, 1996]. Here, the secant stiffness matrix is used to make a prediction of the critical displacements first. Then, in a second step the critical load is computed.

For the post–buckling behavior at bifurcation points it is characteristic that a second or more different paths can be traced. For this purpose [Decker and Keller, 1980] solves the bifurcation equation directly, so that with the access of the consistent tangents in the bifurcation point a branch switching is possible. [Wagner and Wriggers, 1988] proposed a path switching by perturbating the solution in the equilibrium state and provoke a transition to secondary paths, that can be traced with arclength methods.

Although generally the computation of critical point is feasible, some problems remain to be solved. The critical displacement method and the extended system proved to give good results, however both are not perfect and have certain disadvantages. The CDM as an indirect method only predicts the critical values, but gives good results even at greater distances from the critical point.The extended system as direct method computes the critical points directly but does not converge in all cases and is dependent on the initial values. Moreover all techniques have mainly been tested for model type problems.

The objective of this thesis is to apply the computation methods for critical points to more complex mechanical problems involving inequality constraints. Prior to this extension to a new class of problems appropriate methods among the existing ones for the critical point detection are chosen. Therefore the CDM and the extended system as the most promising techniques will be compared and evaluated. A one step prediction of the critical load based on the extended system will be developed that enables a better evaluation. The possibilities of a combination of both methods will be examined. A conceivable combination is to use the prediction of a CDM computation as starting value for the extended system and enhance the convergence of the latter.

In a second step critical point detection methods are extended to problems that involve

inequality constraints. In this context constitutive damage models and contact problems are studied. Damage models account for the loss of stiffness caused by the growth of cracks and micro-cavities in a material. The list of publication on this subject starts with [Kachanov, 1958] and contains important works of [Lemaitre, 1971], [Chaboche, 1974] and [Gurson, 1977]. Inequality constraints are used in damage models to account for the damage progression of a material. A violation of the constraints results in damage progression. Among the existing damage models a rather simple damage model will be chosen for the tests with the critical point computation techniques.

Numerical contact mechanics, as the other topic, is a field of research that came up in the past 20 years. The restriction that bodies in contact problems are not allowed to penetrate the adjacent surface leads to inequality constraints, that have to be incorporated in the global set of equations. Important works are the publications of [Hallquist, 1979], [Curnier, 1984], [Laursen and Simo, 1993], [Wriggers and Miehe, 1992] and [Wriggers and Miehe, 1994]. The CDM and the extended system will be applied to a selection of mechanical damage and contact problems to demonstrate the critical point computation for inequality constraint problems.

1.2 Structure of the thesis

In chapter 2 the continuum mechanical bases are summarized. Starting with the kinematics of a deformation process, strain measures are defined. A description of stress measures follows. Large deformations are taken into account. The chapter ends with the mechanical conservation laws.

Chapter 3 discusses constitutive relations. The St.Venant constitutive law is derived as a hyperelastic material. This model is extended in the following by a simple damage model, which involves inequality constraints.

In chapter 4 the bases of the previous chapters, conservation laws , constitutive laws and boundary conditions are combined to a mechanical boundary problem. Starting with the weak form of the conservation law of linear momentum the problem is formulated and the Finite Element Method with the Newton–Raphson method as solution technique is introduced. Load–deflection path computation with arclength methods concludes this chapter.

Chapter 5 is dedicated to contact. The master–slave concept for contact detection is adopted. The non–penetration rule for adjacent bodies leads to inequality constraints. The integration of which in the FEM formulation of the previous chapter gives a constrained optimization problem, for which solution methods are presented. The contact terms that have to be added to the global set of equations are presented.

With chapters 2 to 5 the type of mechanical problems to be studied in this thesis is described mathematically. The chapters 6 and 7 focus on the topic of critical points.

In chapter 6 the issue of stable and unstable equilibrium is discussed, which leads to the definition of critical points. Criteria and methods for detection and computation of these points are presented.

The extensions of critical point detection methods are the subject of chapter 7. Damage and contact as inequality constraints are discussed. Besides this a simple method for the introduction of displacement boundary conditions is given. The one step prediction of

the critical load is presented basing on ideas of both the CDM and the extended system

Numerical examples in chapter 8 are used to examine the direct computation of critical points with the extensions to inequality constraints. The CDM and the extended system are evaluated for this type of problems. The first part of this chapter is a comparison of both methods with the objective of a possible combination. Here damage is also considered. In the second part of the chapter some examples with contact are shown.

Chapter 9 contains a short summary of the thesis. Conclusions from the examples are drawn and a perspective for further developments is given. In appendix A the mathematical terms of constrained optimization problems are given. The inverse iteration method which is needed in the CDM can be found in appendix B.

Chapter 2

Continuum mechanics

In this chapter the basics of continuum mechanics are summarized, that are necessary for a derivation of the Finite Element Method and the following topics. More detailed introductions into continuum mechanics can be found in almost all books covering this subject, as e.g. [Truesdell and Noll, 1965], [Becker and Bürger, 1975], [Marsden and Hughes, 1983] and [Ogden, 1984]. The underlying mathematical theory of tensor and vector calculus is explained in e.g. in [de Boer, 1982] or [Klingbeil, 1989].

The mathematical framework for the deformation process is given in the first part of this chapter. Due to the nature of the instability problems considered in this thesis, large deformations of the bodies will be taken into account. Then strain and stress measures are defined, which will be combined in constitutive models in chapter 3. For a complete description of a continuum mechanical problem material independent conservation laws as well as boundary conditions are necessary.

2.1 Kinematics

2.1.1 Bodies and Motion

As a reference frame the Euclidean vector space $\mathbb{E}^3$ is chosen with the Cartesian coordinate system spanned by the base vectors $\mathbf{e}_1, \mathbf{e}_2, \mathbf{e}_3$. With the origin O every point in this space has a unique vector representation and can be written as

$$\mathbf{x} = \sum_{i=1}^{3} x^i \, \mathbf{e}_i = x^i \, \mathbf{e}_i \qquad \text{with} \qquad \mathbf{x} \in \mathbb{E}^3, \quad x^i \in \mathbb{R}.$$

In the last notation for $\mathbf{x}$ the Einstein summation convention, with a summation over a double occuring index, has been applied, which will be used in this thesis.
A material body or continuum, is now defined as a continuous compact set of points $\mathcal{M}$, which is mapped into the Euclidean vector space. The region in $\mathbb{E}^3$ occupied by the continuum is denoted by $\mathcal{B}$, its boundary or surface $\partial\mathcal{B}$.

$$\mathbf{x} = x^i \, \mathbf{e}_i = \varphi(\mathcal{M}, t) \tag{2.1}$$

The topologic mapping $\varphi(\mathcal{M}, t)$ is bijective and continuous at all times t and for all points of $\mathcal{M}$.

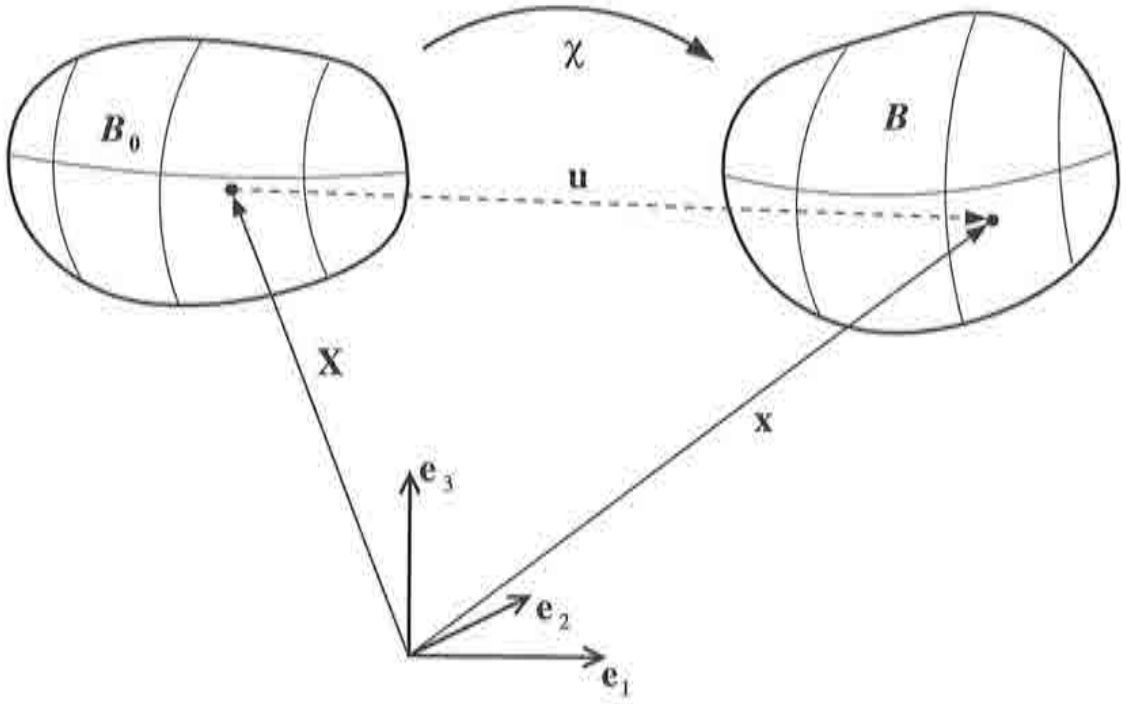

Figure 2.1: Kinematic relations

A reference configuration $\varphi_0 = \varphi(\mathcal{M}, t_0)$ at a certain time t_0 is chosen as a point of departure. Conveniently t_0 is a time, where the body is in an undeformed, unloaded and stress-free state named *initial configuration* $\mathcal{B}_0$ in which the coordinates of all points of $\mathcal{B}_0$ are given by:

$$\mathbf{X} = X^i \, \mathbf{e}_i = \varphi(\mathcal{M}, t_0) \qquad \text{with} \qquad \mathbf{X} \in \mathbb{E}^3 \tag{2.2}$$

The situation is illustrated in figure 2.1. The *current configuration* $\mathcal{B}$ represents the state of the body at a time $t > t_0$ with the coordinates $\mathbf{x}$. Now the following mapping $\boldsymbol{\chi}$ can be defined as

$$\mathbf{x} = \boldsymbol{\chi}(\mathcal{M}, t) = \varphi(\mathcal{M}, t) \circ \varphi^{-1}(\mathcal{M}, t_0). \tag{2.3}$$

Replacing the points $\mathcal{M}$ by their representation in the initial configuration equation (2.3) can be rewritten as

$$\mathbf{x}(\mathbf{X}, t) = \boldsymbol{\chi}(\mathbf{X}, t).$$

The displacement vector $\mathbf{u}$ can be introduced as the difference of the initial and the current coordinates:

$$\mathbf{u} = \mathbf{x} - \mathbf{X} \tag{2.4}$$

In this thesis the *Lagrangian* or material description will be used, where the reference configuration is assumed to be the undeformed initial one.

2.1.2 Convective coordinates

Considering a body given by a parameterization with the variables ξ_i, its *convective coordinates* can be expressed by

$$\mathbf{x} = \mathbf{x}(\xi_i, t) = x^j(\xi_i, t)\, \mathbf{e}_j \qquad \text{with} \quad i, j = 1, 2, 3.$$

A natural base is constructed differentiating $\mathbf{x}$ with respect to the parameters ξ_i.

$$\mathbf{g}_i = \frac{\partial \mathbf{x}(\xi_i, t)}{\partial \xi_i} = \frac{\partial x^j(\xi_i, t)}{\partial \xi_i} \mathbf{e}_j$$

The resulting *covariant base vectors* $\mathbf{g}_i$ of the parameterization are denoted by a subscript index. The dual base, a second set of base vectors consisting of the *contravariant base vectors* (denoted by a superscript index), are related with the covariant ones by

$$\mathbf{g}_i \cdot \mathbf{g}^j = \delta_i^j\,, \qquad \text{with} \quad \delta_i^j = \begin{cases} 1 & \text{for } i = j \\ 0 & \text{for } i \neq j \end{cases}$$

being the *Kronecker* delta. The scalar product of two base vector leads to the useful co- and contravariant metric coefficients g_{ij} and g^{ij} respectively.

$$g_{ij} = \mathbf{g}_i \cdot \mathbf{g}_j \quad , \quad g^{ij} = \mathbf{g}^i \cdot \mathbf{g}^j$$

For the reference configuration with the representation $\mathbf{X}$ the co- and contravariant base vectors $\mathbf{G}_i, \mathbf{G}^j$ and the metric coefficients G_{ij}, G^{ij} can be calculated in a similar manner.

In coordinates systems with orthonormal base vectors the difference between co- and contravariant vanishes, so that for Cartesian coordinates $\mathbf{e}_i = \mathbf{e}^i$ and $\mathbf{e}_i \cdot \mathbf{e}_k = \delta_{ik}$.

2.1.3 Analysis of strain

Basing on the terms of the previous sections, several strain measures can be introduced. Using the mapping $\boldsymbol{\chi}$ of the initial into the current configuration the *deformation gradient* $\mathbf{F}$ is defined as the partial derivative of the mapping $\boldsymbol{\chi}$ with respect to the initial coordinates $\mathbf{X}$:

$$\mathbf{F} = \frac{\partial \boldsymbol{\chi}}{\partial \mathbf{X}} = \frac{\partial \mathbf{x}}{\partial \mathbf{X}} = \mathbf{1} + \frac{\partial \mathbf{u}}{\partial \mathbf{X}} = \begin{pmatrix} \frac{\partial x_1}{\partial X_1} & \frac{\partial x_1}{\partial X_2} & \frac{\partial x_1}{\partial X_3} \\ \frac{\partial x_2}{\partial X_1} & \frac{\partial x_2}{\partial X_2} & \frac{\partial x_2}{\partial X_3} \\ \frac{\partial x_3}{\partial X_1} & \frac{\partial x_3}{\partial X_2} & \frac{\partial x_3}{\partial X_3} \end{pmatrix} \tag{2.5}$$

This deformation gradient $\mathbf{F}$ can be thought of as a mapping of an infinitesimal line element $d\mathbf{X}$ in the initial configuration into its corresponding line element $d\mathbf{x}$ of the current configuration.

$$d\mathbf{x} = \mathbf{F}\, d\mathbf{X} \tag{2.6}$$

The deformation gradient is not symmetric in general ($\mathbf{F} \neq \mathbf{F}^T$) . If the inverse $\mathbf{F}^{-1}$ exists, it is

$$\mathbf{F}^{-1} = \frac{\partial \mathbf{X}}{\partial \mathbf{x}}. \tag{2.7}$$

A necessary and sufficient condition for the existence of $\mathbf{F}^{-1}$ is, that the *Jacobi determinant* is not equal to zero $J = \det \mathbf{F} \neq 0$. This requirement is fulfilled by the bijectivity of $\boldsymbol{\chi}$. The continuity of $\boldsymbol{\chi}$ even assures the stronger restriction that $J > 0$.

The deformation gradient $\mathbf{F}$ is a two field tensor of second order. Rewriting it in base vector notation with Cartesian coordinates yields:

$$\mathbf{F} = \frac{\partial x^i}{\partial X^j}\, \mathbf{e}_i \otimes \mathbf{E}_j \tag{2.8}$$

The measure of the square of a line element in the current configuration $ds = d\mathbf{x}\, d\mathbf{x} = d\mathbf{X}\, \mathbf{C}\, d\mathbf{X}$ leads to the definition of the *right Cauchy–Green* strain tensor

$$\mathbf{C} = \mathbf{F}^T\mathbf{F} \tag{2.9}$$

Doing the same for a line element in the initial configuration $dS = d\mathbf{X}\, d\mathbf{X} = d\mathbf{x}\, \mathbf{b}^{-1} d\mathbf{x}$ defines the *left Cauchy–Green* strain tensor:

$$\mathbf{b} = \mathbf{F}\mathbf{F}^T \tag{2.10}$$

The definition of the *Green–Lagrange* strain tensor $\mathbf{E}$ originates from the concept of the difference of the squares of line elements in initial and current state $ds - dS = d\mathbf{X}\, 2\mathbf{E}\, d\mathbf{X}$:

$$\mathbf{E} = \frac{1}{2}\left(\mathbf{F}^T\mathbf{F} - \mathbf{I}\right) \tag{2.11}$$

$\mathbf{E}$ is symmetric ($\mathbf{E} = \mathbf{E}^T$) and refers to the current configuration. Its equivalent for the initial configuration is the *Euler–Almansi* strain tensor $\mathbf{e}^A$:

$$\mathbf{e}^A = \frac{1}{2}\left(\mathbf{I} - \mathbf{F}^{-T}\mathbf{F}^{-1}\right) \tag{2.12}$$

For the Finite Element formulation used in this thesis, the form (2.13) of the Green–Lagrange strain tensor $\mathbf{E}$ in terms of the displacements $\mathbf{u}$ is more convenient. Linear and nonlinear contributions can be identified easily. The notation $\mathbf{F} = (\mathbf{I} - Grad\ \mathbf{u})$ for (2.5) yields the following form:

$$\mathbf{E} = \frac{1}{2}(\underbrace{Grad\ \mathbf{u} + Grad^T\mathbf{u}}_{\text{linear}} + \underbrace{Grad^T\mathbf{u}\ Grad\ \mathbf{u}}_{\text{nonlinear}}) \tag{2.13}$$

A differential operator "$Grad$" with capital letter depicts the gradient with respect to the initial configuration, i.e. $Grad(\cdot) = \frac{\partial(\cdot)}{\partial \mathbf{X}}$, whereas "$grad$" depicts the gradient with respect to the current configuration, i.e. $grad(\cdot) = \frac{\partial(\cdot)}{\partial \mathbf{x}}$. Neglecting the nonlinear part of equation (2.13) leads to the deformation tensor $\boldsymbol{\epsilon}$ of the geometrically linear theory, which accounts only for small deformations.

2.1.4 Transformation relations

Since vector and tensor valued variables can refer to several configurations, e.g. the initial or current configuration, transformation relations have to be specified. Transport theorems provide the functional relation between line, surface and volume elements in both configurations.

For line elements equation (2.6) with $d\mathbf{x} = \mathbf{F}d\mathbf{X}$ holds. The relation between a vector area element in the current configuration $d\mathbf{a}$ and the area vector in the initial configuration $d\mathbf{A}$ is stated in *Nanson's formula*:

$$d\mathbf{a} = J\mathbf{F}^{-T}d\mathbf{A} \tag{2.14}$$

Therein $d\mathbf{a}$ is the product of the outward normal vector $\mathbf{n}$ of the surface with $|\mathbf{n}| = 1$ and the absolute area $d\mathbf{a} = \mathbf{n}da$. Applying this the absolute values of the areas are connected via the relation

$$da = j\,dA \qquad \text{with} \quad j = \|J\mathbf{F}^{-T}\mathbf{N}\|. \tag{2.15}$$

The transformation of volume elements is simply a multiplication with the Jacobi determinant:

$$dv = J\,dV \tag{2.16}$$

The importance of the requirement that $J > 0$ is fulfilled becomes obvious here, since otherwise negative volume elements would occur.

More about transformation relations can be found in [Marsden and Hughes, 1983] and [Wriggers, 1988].

2.2 Stress tensors

To determine the inner forces of a mechanically loaded continuum, stress as a local measure will be given. Assuming a body $\mathcal{B}$ and a surface in the interior of $\mathcal{B}$ created by cutting the body in two parts, on both surfaces the stress vector $\mathbf{t}$ can be constructed. It is defined in each point as the limit of the quotient of force vector $_{\Delta}\mathbf{f}$ and area $_{\Delta}a$, representing the force per unit area acting on the surface:

$$\mathbf{t} = \lim_{\Delta a \to 0} \frac{{}_{\Delta}\mathbf{f}}{{}_{\Delta}a} = \frac{d\mathbf{f}}{da}$$

According to the Cauchy-theorem $\mathbf{t}$ can be written as the product of the *Cauchy stress tensor* $\boldsymbol{\sigma}$ with the outward normal vector $\mathbf{n}$:

$$\mathbf{t}(\mathbf{x}, t, \mathbf{n}) = \boldsymbol{\sigma}(\mathbf{x}, t)\ \mathbf{n}(\mathbf{x}, t) \tag{2.17}$$

In an orthonormal coordinate system the first index in $\boldsymbol{\sigma}$ indicates the direction of the stress component and the second the direction of the surface normal. As a consequence of the conservation of angular momentum it can be shown, that $\boldsymbol{\sigma}$ is symmetric ($\boldsymbol{\sigma} = \boldsymbol{\sigma}^T$).

Inserting the definition of the stress vector $\mathbf{t}$ into equation (2.17), Nanson's formula (2.14) can be used to derive the *1. Piola–Kirchhoff stress tensor* $\mathbf{P}$.

$$d\mathbf{f} = \boldsymbol{\sigma}\,\mathbf{n}\,da = \boldsymbol{\sigma}\,d\mathbf{a} = \boldsymbol{\sigma}\,J\mathbf{F}^{-T}\,d\mathbf{A} = \mathbf{P}\,d\mathbf{A}$$

$$\mathbf{P} = J\,\boldsymbol{\sigma}\,\mathbf{F}^{-T} \tag{2.18}$$

$\mathbf{P}$ is a two field tensor and it is non–symmetric ($\mathbf{P} \neq \mathbf{P}^T$). To overcome this disadvantage the symmetric *2. Piola–Kirchhoff stress tensor* $\mathbf{S}$ is defined:

$$\mathbf{S} = \mathbf{F}^{-1}\mathbf{P} = J\,\mathbf{F}^{-1}\boldsymbol{\sigma}\,\mathbf{F}^{-T} \tag{2.19}$$

2.3 Conservation laws

In this paragraph the fundamental physical conservation laws will be summarized . These have to be fulfilled by every material body and have axiomatic character. Those laws are applicable to every part of the body and are valid locally and globally.

2.3.1 Conservation of mass

The mass density $\rho = \rho(\mathbf{x})$ is defined as the mass per volume $\rho = \frac{dm}{dV}$. The mass conservation law states, that the mass remains constant through time. Rewriting the mass m of a material body $\mathcal{B}$ in integral form

$$m = \int_{\mathcal{B}} \rho\,dv, \tag{2.20}$$

for the mass in initial and current configuration this means, that

$$m_0(\mathcal{B}_0, t) = \int_{\mathcal{B}_0} \rho_0\,dV = \int_{\mathcal{B}} \rho\,dv = \int_{\mathcal{B}_0} \rho\,J\,dV = m(\mathcal{B}, t) \tag{2.21}$$

The requirement $m = const.$ implies the time derivative $\frac{d}{dt}m = 0$ to be equal to zero:

$$\frac{d}{dt}m = \frac{d}{dt}\int_{\mathcal{B}} \rho\,dv = \int_{\mathcal{B}} (\dot{\rho} + \rho\,div\,\dot{\mathbf{x}})\,dv = 0 \tag{2.22}$$

Since the volume of integration $\mathcal{B}$ can be chosen arbitrarily, the integrand has to be equal to zero. Then the local form of the mass conservation law is:

$$\dot{\rho} + \rho\,div\,\dot{\mathbf{x}} = 0 \quad , \qquad \rho_0 - \rho \det \mathbf{F} = 0 \tag{2.23}$$

Due to the mapping χ in section 2.1, which is bijective and continuous, the conservation of mass is fulfilled automatically.

2.3.2 Conservation of momentum

Writing $\mathbf{p}$ for the linear momentum of a body $\mathcal{B}$ and $\mathbf{f}$ for the sum of the forces the conservation of linear momentum means:

$$\dot{\mathbf{p}}(\mathcal{B},t) = \mathbf{f}(\mathcal{B},t)$$

Applying the physical definition of the linear momentum of a rigid body $\mathbf{p} = m\dot{\mathbf{x}}$ to a deformable one, the mass has to be split into the integrals of the previous section and the conservation law obtains the form of the right side of equation (2.24). For the forces on the left side it can distinguished between body or volume forces $\hat{\mathbf{b}}$ and surface loads $\hat{\mathbf{t}}$.

$$\frac{d}{dt}\int_{\mathcal{B}} \rho\dot{\mathbf{x}}\, dv = \int_{\mathcal{B}} \rho\hat{\mathbf{b}}\, dv + \int_{\partial\mathcal{B}} \hat{\mathbf{t}}\, da \tag{2.24}$$

The formulation of the surface loads $\hat{\mathbf{t}}$ as in equation (2.17) permits the application of the Gauss theorem for the transformation of a surface integral into a volume integral. The last integral in equation (2.24) then transforms to

$$\int_{\partial\mathcal{B}} \boldsymbol{\sigma}\mathbf{n}\, da = \int_{\mathcal{B}} div\, \boldsymbol{\sigma}\, \mathbf{n}\, dv.$$

Then the local form of equation (2.24) has the following form:

$$\rho\ddot{\mathbf{x}} = div\, \boldsymbol{\sigma} + \rho\hat{\mathbf{b}} \tag{2.25}$$

For the body $\mathcal{B}_0$ in the initial configuration the Cauchy stress tensor $\boldsymbol{\sigma}$ transforms into the 1.Piola–Kirchhoff tensor $\mathbf{P}$. The capital letter for the divergence denotes the differentiation with respect to the initial coordinates $\mathbf{X}$.

$$\rho_0\ddot{\mathbf{x}} = Div\mathbf{P} + \rho_0\hat{\mathbf{b}}_0 \tag{2.26}$$

Similar to the definition of the linear momentum the angular momentum $\mathbf{L}$ and the torques $\mathbf{M}$ combine to the axiom of the conservation of angular momentum:,

$$\dot{\mathbf{L}}(\mathcal{B},t) = \mathbf{M}(\mathcal{B},t) \tag{2.27}$$

The angular momentum in physics for a rigid body being equal to the outer product of the radius vector and the linear momentum ($\mathbf{L} = (\mathbf{x} - \mathbf{x}_0) \times \mathbf{p}$) has in continuum mechanics an integral form. On the right hand side of equation (2.28) again the split into torques due to volume and surface forces is done.

$$\frac{d}{dt}\int_{\mathcal{B}} (\mathbf{x} - \mathbf{x}_0) \times \rho\dot{\mathbf{x}}\, dv = \int_{\mathcal{B}} (\mathbf{x} - \mathbf{x}_0) \times \rho\hat{\mathbf{b}}\, dv + \int_{\partial\mathcal{B}} (\mathbf{x} - \mathbf{x}_0) \times \mathbf{t}\, da \tag{2.28}$$

Together with the Boltzmann–theorem, that excludes distributed surface or volume torques, the symmetry of the Cauchy stress tensor $\boldsymbol{\sigma}$ can be obtained from the conservation of angular momentum after some mathematical operations.

2.3.3 Conservation of energy

The total energy of a body is the sum of kinetic energy K and internal energy U.

$$E(\mathcal{B},t) = U(\mathcal{B},t) + K(\mathcal{B},t) = \int_{\mathcal{B}} \rho\epsilon \, dv + \frac{1}{2}\int_{\mathcal{B}} \rho\dot{\mathbf{x}}\dot{\mathbf{x}} \, dv \tag{2.29}$$

ϵ is the internal energy per unit mass (specific energy), consisting of mechanical, potential and specific thermal energy. The rate at which work is done on the body by the surface loads $\hat{\mathbf{t}}$ on $\partial\mathcal{B}$ and the volume forces $\hat{\mathbf{b}}$ is the mechanical power $\dot{W}$.

$$\dot{W} = \int_{\partial\mathcal{B}} \hat{\mathbf{t}} \cdot \dot{\mathbf{x}} \, da + \int_{\mathcal{B}} \rho\hat{\mathbf{b}} \cdot \dot{\mathbf{x}} \, dv \tag{2.30}$$

The two contributions for the thermal power $\dot{Q}$ are the heat flux per time $\mathbf{q}$ through the boundary and the specific heat conduction r by radiation.

$$\dot{Q} = -\int_{\partial\mathcal{B}} \mathbf{q} \cdot \mathbf{n} \, da + \int_{\mathcal{B}} \rho r \, dv \tag{2.31}$$

Inserting those integrals in the first law of thermodynamics and applying the Gauss theorem leads to

$$\frac{d}{dt}\int_{\mathcal{B}} \rho\epsilon \, dv = \int_{\partial\mathcal{B}} \boldsymbol{\sigma} : \mathbf{I} - div\,\mathbf{q} + \rho r \, dv,$$

which yields for the local form of the conservation law of energy

$$\rho\dot{\epsilon} = \boldsymbol{\sigma} : \mathbf{d} - div\,\mathbf{q} + \rho r. \tag{2.32}$$

For the initial configuration the following form can be obtained after a transformation.

$$\rho_0\dot{e} = \mathbf{S} : \dot{\mathbf{E}} - Div\,\mathbf{Q} + \rho_0 r \tag{2.33}$$

The heat flux per time through the boundary in the initial configuration is $\mathbf{Q} = J\mathbf{F}^T\mathbf{q}$ according to the transformation rules.

2.3.4 Entropy law

Denoting the entropy change of body $\mathcal{B}$ by $\dot{S}$ and the inner and outer entropy production by S_i and S_o respectively, the mathematical form of the entropy law is

$$\dot{S}(\mathcal{B},t) = S_o(\mathcal{B},t) + S_i(\mathcal{B},t) \tag{2.34}$$

Introducing the entropy per unit mass or specific entropy $\eta = \eta(\mathbf{x},t)$ and the specific internal entropy production $\hat{\eta}$, yields for the entropy terms

$$S(\mathcal{B},t) = \int_{\mathcal{B}} \rho\eta \, dv \quad , \qquad S_i(\mathcal{B},t) = \int_{\mathcal{B}} \rho\hat{\eta} \, dv \geq 0. \tag{2.35}$$

The outer entropy production is caused by absorption of heat and is proportional to the thermal energy $\dot{Q}$. It is equal to the quotient of the rate of thermal energy $\dot{Q}$ and the absolute temperature $\Theta > 0$. With $\dot{Q}$ from equation (2.31), the outer entropy production S_o is

$$S_o(\mathcal{B},t) = \int_{\mathcal{B}} \frac{\rho r}{\Theta}\, dv - \int_{\partial\mathcal{B}} \frac{1}{\Theta}\mathbf{q}\cdot\mathbf{n}\, dv. \tag{2.36}$$

According to the second law of thermodynamics $S_i \geq 0$, with the equality sign holding only for reversible processes. For irreversible processes S_i is greater than zero. With this relation the *Clausius–Duhem* inequality can be obtained from equations (2.36) and (2.35):

$$\frac{d}{dt}\int_{\mathcal{B}} \rho\eta\, dv \geq \int_{\mathcal{B}} \frac{\rho r}{\Theta}\, dv - \int_{\partial\mathcal{B}} \frac{1}{\Theta}\mathbf{q}\cdot\mathbf{n}\, dv \tag{2.37}$$

With partial integration and the conservation law of energy (2.32) the local form of the Clausius Duhem inequality is then

$$\rho(\Theta\dot{\eta} - \dot{\epsilon}) + \boldsymbol{\sigma} : \mathbf{d} - \frac{1}{\Theta}\mathbf{q}\cdot grad\,\Theta \geq 0. \tag{2.38}$$

For the initial configuration the local form of (2.37) can be deduced by transformation of (2.38).

$$\rho_0(\Theta\dot{\eta} - \dot{\epsilon}) + \mathbf{S} : \dot{\mathbf{E}} - \frac{1}{\Theta}\mathbf{Q}\cdot Grad\,\Theta \geq 0 \tag{2.39}$$

The *Helmholtz* free energy Ψ, which is equal to the mechanical power $\dot{W}$ in an reversible, isothermal ($\Theta = const.$) process, is defined as

$$\Psi = \epsilon - \eta\Theta \tag{2.40}$$

Using this definition the local forms of the Clausius Duhem inequality can be rewritten as

$$\begin{aligned} -\rho(\dot{\Psi} + \eta\dot{\Theta}) + \boldsymbol{\sigma} : \mathbf{d} - \frac{1}{\Theta}\mathbf{q}\cdot grad\,\Theta &\geq 0 \\ \rho_0(\dot{\Psi} + \eta\dot{\Theta}) + \mathbf{S} : \dot{\mathbf{E}} - \frac{1}{\Theta}\mathbf{Q}\cdot Grad\,\Theta &\geq 0 \end{aligned}$$

2.4 Boundary conditions

For a complete definition of a mechanical problem initial and boundary conditions are necessary. Since in the following chapters the type of problems considered in this thesis will be restricted to isothermal, static or quasi-static problems, only boundary conditions are treated in more detail here.
Two kind of boundary conditions are known as the "classical" boundary conditions, displacement and stress boundary conditions. A third type, the contact boundary conditions

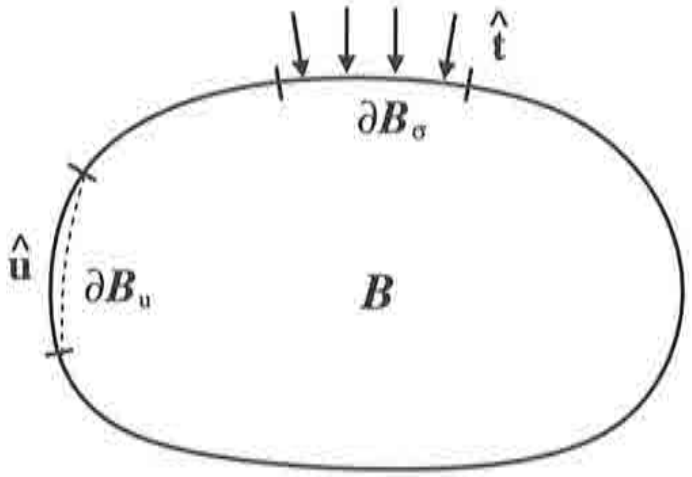

Figure 2.2: Boundary conditions

will be presented in chapter 5. On the surface of a body ∂B, that is subjected to boundary conditions, different zones are identified, where either displacement or stress boundary conditions are imposed, see figure 2.2.

On the *Neumann*-boundary $\partial\mathcal{B}_{0\sigma} \subset \partial\mathcal{B}_0$ the stress vector $\hat{\mathbf{T}}$ is prescribed. Neumann boundary conditions are mostly specified with respect to the initial configuration and have the form

$$\mathbf{PN} = \hat{\mathbf{T}} \quad \text{on} \quad \partial\mathcal{B}_{0\sigma} \tag{2.41}$$

$\mathbf{N}$ is the outward directed unit vector normal to the surface and $\mathbf{P}$ the 1. Piola–Kirchhoff stress tensor. For the current configuration the Neumann–boundary conditions reads:

$$\boldsymbol{\sigma}\mathbf{n} = \hat{\mathbf{t}} \quad \text{on} \quad \partial\mathcal{B}_\sigma \tag{2.42}$$

According to section 2.1.4 the stress vectors in both configurations are related by

$$\hat{\mathbf{T}} = j\hat{\mathbf{t}}. \tag{2.43}$$

On the *Dirichlet* boundary $\partial\mathcal{B}_{0u} \subset \partial\mathcal{B}_0$, $\partial\mathcal{B}_u \subset \partial\mathcal{B}$ displacement values $\hat{\mathbf{u}}$ are prescribed.

$$\mathbf{u} = \hat{\mathbf{u}} \tag{2.44}$$

Here no distinction between the configurations is necessary for Dirichlet boundary conditions.

Chapter 3

Constitutive relations

Besides kinematic relations and stress tensors, individual material properties are needed to connect the strain and stress measures. Constitutive relations provide a functional connection between the independent variables of a continuum $\chi(\mathcal{B}, t)$ and $\Theta(\mathcal{B}, t)$ and dependent ones as e.g. stresses $\boldsymbol{\sigma}$ and heat flux $\mathbf{q}$. With the following general principles of material theory the stress–strain relations can be restricted:

- The *principle of determinism* distinguishes between the dependant and independent variables. For a simple material the local history of $\mathbf{F}$, Θ and $\nabla\Theta$ suffices to determine the history of the thermo–kinetic process.
- The *principle of equipresence* only permits the same set of variables for all constitutive relations, as long as no further restrictions are imposed.
- The axiom of the *material objectivity* states, that the material response is independent of the observer.
- The *principle of material symmetry* postulates that the material response of bodies in the reference configuration with an inner symmetry remains unaffected by symmetry transformations.
- Through the *principle of local impact* the material functions are depending pointwise on the independent variables .
- The *principle of consistency* means, that constitutive relations have to be compliant with the conservation laws.

Applying those principles individually to a material its characteristic set of independent variables can be determined.

In the first section of this chapter the thermodynamical bases of the material theory are given. The difference between elastic deformation and deformation with internal dissipation is shown and the thermodynamic equations are specialized for each type individually in the next sections. As a general simplification only isothermal deformation processes are considered.

In the elastic section the hyperelastic St. Venant material law is derived. The focus of the dissipative deformation section is set on damage as dissipative effect. After a short

description of damage, a simple damage model is presented, which is based on the St. Venant material law. This model was chosen because of its simplicity. It was considered as sufficient for the aim of this thesis to test the use of critical point computation methods for problems with inequality constraints.

3.1 Thermodynamics of deformation

According to the fundamental hypothesis of thermodynamics at any instant of a thermodynamic process the thermodynamic state is completely defined by a set of state variables. A convenient assumption for the deformation process of a continuum is that this set of state variables consists of the deformation gradient $\mathbf{F}$, the temperature Θ, the temperature gradient $\nabla\Theta$ and a set of k internal variables $\boldsymbol{\alpha}$ associated with dissipative mechanisms.

As a consequence the free energy is a function of the state variables $\Psi = \Psi(\mathbf{F}, \Theta, \nabla\Theta, \boldsymbol{\alpha})$, so that its rate of change is given by

$$\dot{\Psi} = \frac{\partial \Psi}{\partial \mathbf{F}} : \mathbf{F}^T + \frac{\partial \Psi}{\partial \Theta}\,\dot{\Theta} + \frac{\partial \Psi}{\partial (\nabla\Theta)} \cdot (\dot{\nabla\Theta}) + \frac{\partial \Psi}{\partial \boldsymbol{\alpha}} \cdot \dot{\boldsymbol{\alpha}} \tag{3.1}$$

$$\text{with} \qquad \frac{\partial \Psi}{\partial \boldsymbol{\alpha}} \cdot \dot{\boldsymbol{\alpha}} = \sum_{i=1}^{k} \frac{\partial \Psi}{\partial \alpha_i}\,\dot{\alpha}_i$$

due to the evolution of the internal variables. With equation (3.1) the Clausius–Duhem inequality (2.41) can be rewritten as follows:

$$\left(\boldsymbol{\sigma}\mathbf{F}^{-T} - \rho\frac{\partial \Psi}{\partial \mathbf{F}}\right) : \dot{\mathbf{F}} - \rho\left(\eta + \frac{\partial \Psi}{\partial \Theta}\right)\dot{\Theta} - \rho\frac{\partial \Psi}{\partial (\nabla\Theta)} \cdot (\dot{\nabla\Theta}) - \rho\frac{\partial \Psi}{\partial \boldsymbol{\alpha}} \cdot \dot{\boldsymbol{\alpha}} - \frac{1}{\Theta}\mathbf{q} \cdot \nabla\Theta \geq 0 \tag{3.2}$$

Since this inequality must hold for any thermo–kinetical process without restrictions the state variables can assume any values. This leads to the well known requirements for the free energy Ψ:

$$\boldsymbol{\sigma} = \rho\,\frac{\partial \Psi}{\partial \mathbf{F}}\,\mathbf{F}^T \quad , \quad \eta = -\frac{\partial \Psi}{\partial \Theta} \quad , \quad \frac{\partial \Psi}{\partial (\nabla\Theta)} = 0 \tag{3.3}$$

In (3.3) the second equation implies, that the free energy Ψ works as a thermodynamic potential for the entropy η. The third equation states, that the free energy is independent of the temperature gradient $\nabla\Theta$. The remaining terms of the Clausius–Duhem inequality form the scalar valued dissipation function $D_{diss} = D_{diss}(\boldsymbol{\alpha}, \nabla\Theta)$. It consist of internal and thermal dissipation terms.

$$D_{diss} = \underbrace{\rho\,\frac{\partial \Psi}{\partial \boldsymbol{\alpha}} \cdot \dot{\boldsymbol{\alpha}}}_{internal} - \underbrace{\frac{1}{\Theta}\,\mathbf{q} \cdot \nabla\Theta}_{thermal} \geq 0 \tag{3.4}$$

Concerning the constitutive behavior of materials this permits to distinguish between elastic constitutive relations and constitutive relations with internal dissipation.

3.2 Elastic deformation

The ideal elastic deformation of a continuum is a reversible process without internal dissipation. This implies that a body $\mathcal{B}$ consisting of a material obeying an elastic material law returns to its initial form $\mathcal{B}_0$ when the loads are released completely. Moreover its material properties remain unchanged. For modest deformations this idealization holds for most of the materials.

Since no internal dissipation occurs, no internal variables are needed in the elastic deformation model. Equation (3.2) then simplifies to a form with the independent variables $\mathbf{F}$, Θ and $\nabla\Theta$ only.

$$\left(\boldsymbol{\sigma}\mathbf{F}^{-T} - \rho\frac{\partial\Psi}{\partial\mathbf{F}}\right) : \dot{\mathbf{F}} - \rho\left(\eta + \frac{\partial\Psi}{\partial\Theta}\right)\dot{\Theta} - \rho\frac{\partial\Psi}{\partial(\nabla\Theta)}(\dot{\nabla\Theta}) - \frac{1}{\Theta}\mathbf{q}\cdot\nabla\Theta \geq 0 \tag{3.5}$$

In the dissipation function (3.4) only the thermal term remains. It expresses the dissipation due to heat conduction.

$$D_{diss} = -\frac{1}{\Theta}\mathbf{q}\cdot\nabla\Theta \geq 0 \tag{3.6}$$

In this thesis a restriction to isothermal processes will be made ($\dot{\Theta} = 0$), thus only the first equation of (3.3) is left.

$$\boldsymbol{\sigma} = \rho\frac{\partial\Psi}{\partial\mathbf{F}}\mathbf{F}^T \tag{3.7}$$

Temperature does no longer belong to the set of independent variables, so that $\Psi = \Psi(\boldsymbol{\sigma})$ only. This step leads from *thermoelasticity* to *hyperelasticity*. Equation (3.7) is the fundamental potential relation for hyperelasticity or *Green elasticity*. It states, that all hyperelastic material laws can be deduced from a potential Ψ, the Helmholtz free energy. Introducing the deformation energy $W(\mathbf{F}) = \rho_0\Psi(\mathbf{F})$ as a measure of the specific potential energy of a reference volume element yields

$$\boldsymbol{\sigma} = \frac{1}{J}\frac{\partial W(\mathbf{F})}{\partial\mathbf{F}}\mathbf{F}^T. \tag{3.8}$$

Since the deformation energy is a potential, the stress field is conservative and the deformation energy does not depend on the deformation path.

Specializing those material laws further for isotropic materials, the principles of material objectivity and symmetry impose further restrictions, see [Ogden, 1984]. The stress tensor $\boldsymbol{\sigma}$ is then written as a function of the left Cauchy–Green strain tensor $\mathbf{b}$.

$$\boldsymbol{\sigma} = \frac{2}{J}\frac{\partial W(\mathbf{b})}{\partial\mathbf{b}}\mathbf{b} \tag{3.9}$$

Transforming this back to the initial configuration a similar equation for the second Piola–Kirchhoff stress tensor $\mathbf{P}$ is obtained with W depending on the right Cauchy–Green strain tensor $\mathbf{C}$ or the Green–Lagrange strain tensor $\mathbf{E}$.

$$\mathbf{S} = 2\frac{\partial W(\mathbf{C})}{\partial\mathbf{C}} = \frac{\partial W(\mathbf{E})}{\partial\mathbf{E}} \tag{3.10}$$

Further limitations for the deformation energy can be derived regarding the limit cases:

- For the initial undeformed configuration the deformation energy has to be zero. ($W(\mathbf{E} = \mathbf{0}) = 0$)
- W has to be positive if deformation takes pace ($W > 0$ for $\mathbf{F} \neq \mathbf{0}$)
- W goes to infinity, if the body is compressed to a point or stretched to infinity ($\lim_{J \to +\infty} W = +\infty, \lim_{J \to 0} W = +\infty$)

3.2.1 St.Venant material

The *St. Venant material* model is a rather simple hyperelastic material law for compressible solids. For a St.Venant material the linear relation (3.11) between the second Piola–Kirchhoff stress tensor $\mathbf{S}$ and the Green–Lagrange strain tensor $\mathbf{E}$ is assumed.

$$\mathbf{S}(\mathbf{E}) = \lambda(tr\ \mathbf{E})\mathbf{I} + 2\mu\mathbf{E} \tag{3.11}$$

The parameters λ and μ are material specific elastic constants, named the Lamé constants. They are related to the Young's modulus E and Poisson's ratio ν by the equations

$$E = \frac{\mu(2\lambda + 2\mu)}{\lambda + \mu} \quad , \quad \nu = \frac{\lambda}{2(\lambda + \mu)} \tag{3.12}$$

For the first Piola–Kirchhoff and the Cauchy stress tensor $\mathbf{P}$ and $\boldsymbol{\sigma}$ respectively the corresponding relations are obtained by transformation.

$$\mathbf{P}(\mathbf{E}) = \lambda\ (tr\ \mathbf{E})\ \mathbf{F} + 2\mu\mathbf{F}\ \mathbf{E} \tag{3.13}$$

$$\boldsymbol{\sigma}(\mathbf{E}) = \frac{1}{J}\left[\lambda\ (tr\ \mathbf{E})\ \mathbf{F}\mathbf{F}^{\mathbf{T}} + 2\mu\ \mathbf{F}\mathbf{E}\mathbf{F}^{\mathbf{T}}\right] \tag{3.14}$$

Although the relation between $\mathbf{S}$ and $\mathbf{E}$ is linear, $\mathbf{S}$ depends nonlinearly on the displacements $\mathbf{u}$ which can be seen by replacing $\mathbf{E}$ with its definition (2.13). The deformation energy of a St.Venant material is given by

$$W_{SV} = W_{SV}(\mathbf{E}) = \frac{\lambda}{2}\ (tr\mathbf{E})^2 + \mu\ tr\mathbf{E}^2, \tag{3.15}$$

or

$$W_{SV} = W_{SV}(\mathbf{E}) = \frac{1}{2}\ \mathbf{E} : (\mathbf{D}_{SV}\mathbf{E}). \tag{3.16}$$

$\mathbf{D}_{SV}$ is the fourth order elasticity tensor according to the definition

$$\mathbf{D}_{SV} = \lambda\ \mathbf{I} \otimes \mathbf{I} + 2\mu\ \mathbf{I}. \tag{3.17}$$

The St.Venant material model is generally described as a model for large displacements and large rotations but small strains. It can be shown, that the components of the second Piola–Kirchhoff stress and the Green–Lagrange strain tensor do not change under rigid body rotations or displacements, see e.g. [Bathe, 1996]. Thus only straining of a material will yield an increase in the components of the stress tensor. The major disadvantage the St.Venant material suffers from becomes obvious, when the limit cases mentioned in

the previous section are considered. Supposing a compression to a point the St.Venant material yields for the Cauchy stresses $\boldsymbol{\sigma} = \mathbf{0}$. With this restriction the material law is not suited for the description of finite strains.

Hooke's law of linear elasticity

For the limit case of small displacements the St.Venant material model can be reduced to *Hooke's law* for linear elasticity. For small displacements the derivatives with respect to the initial and the current coordinate system are set to be equal $\frac{\partial}{\partial \mathbf{X}}(\cdot) \approx \frac{\partial}{\partial \mathbf{x}}(\cdot)$. As a consequence this yields $\mathbf{S} \approx \mathbf{P} \approx \boldsymbol{\sigma}$. Neglecting further the nonlinear terms of the Green–Lagrange strain tensor $\mathbf{E}$ in (2.13) leads to the infinitesimal strain tensor $\boldsymbol{\epsilon} = \frac{1}{2}(Grad\ \mathbf{u} + Grad^T \mathbf{u})$. Hooke's law (3.18) can then be deduced from equation (3.11).

$$\boldsymbol{\sigma} = \lambda\ (tr\ \boldsymbol{\epsilon})\ \mathbf{I} + 2\mu\boldsymbol{\epsilon} \tag{3.18}$$

Conveniently the constitutive relation $\boldsymbol{\sigma} = \mathbf{D}\boldsymbol{\epsilon}$ is written using the vector notations

$$\begin{pmatrix} \sigma_{11} \\ \sigma_{22} \\ \sigma_{33} \\ \sigma_{12} \\ \sigma_{23} \\ \sigma_{13} \end{pmatrix} \quad \text{and} \quad \begin{pmatrix} \epsilon_{11} \\ \epsilon_{22} \\ \epsilon_{33} \\ 2\epsilon_{12} \\ 2\epsilon_{23} \\ 2\epsilon_{13} \end{pmatrix}$$

for the stress and strain tensors, where the symmetry characteristics of both tensors have been used to shorten the vectors. The constitutive tensor $\mathbf{D}_{SV}$ can then be written as a symmetric second order tensor:

$$\mathbf{D}_{SV} = \frac{E}{(1+\nu)(1-2\nu)} \begin{pmatrix} 1-\nu & \nu & \nu & 0 & 0 & 0 \\ \nu & 1-\nu & \nu & 0 & 0 & 0 \\ \nu & \nu & 1-\nu & 0 & 0 & 0 \\ 0 & 0 & 0 & \frac{1-2\nu}{2} & 0 & 0 \\ 0 & 0 & 0 & 0 & \frac{1-2\nu}{2} & 0 \\ 0 & 0 & 0 & 0 & 0 & \frac{1-2\nu}{2} \end{pmatrix} \tag{3.19}$$

For two dimensional problems the special cases of *plain stress* and *plain strain* can be defined.

Plain stress

The plain stress state is characterized by the fact, that the stresses in the third (out of plane) direction vanish ($\sigma_{13} = \sigma_{23} = \sigma_{33} = 0$). This approximation is valid for solids with a small extension in the out of plane direction, as e.g. model membranes or the in–plane action of beams and plates. The constitutive tensor $\mathbf{D}_{ps}$ for this type of problem is

$$\mathbf{D}_{ps} = \frac{E}{(1-\nu)^2} \begin{pmatrix} 1 & \nu & 0 \\ \nu & 1 & 0 \\ 0 & 0 & \frac{1-\nu}{2} \end{pmatrix}. \tag{3.20}$$

The missing strains in the out of plane direction can be calculated with the following equations.

$$\epsilon_{13} = \epsilon_{23} = 0 \qquad \epsilon_{33} = -\frac{\nu}{1-\nu}(\epsilon_{11}+\epsilon_{22}) \tag{3.21}$$

Plain strain

For slices (of unit thickness) of solids that are treated as 2D problems, the plane strain state is used. Here the strains in the out of plane direction are zero ($\epsilon_{13} = \epsilon_{23} = \epsilon_{33} = 0$). The constitutive tensor $\mathbf{D}_{pn}$ is then

$$\mathbf{D}_{pn} = \frac{E}{(1+\nu)(1-2\nu)} \begin{pmatrix} 1-\nu & \nu & 0 \\ \nu & 1-\nu & 0 \\ 0 & 0 & \frac{1-2\nu}{2} \end{pmatrix}. \tag{3.22}$$

The stresses in the out of plane direction can be obtained with the formulas

$$\sigma_{13} = \sigma_{23} = 0 \quad , \qquad \sigma_{33} = \nu\,(\sigma_{11}+\sigma_{22}). \tag{3.23}$$

3.3 Deformation with internal dissipation

Deformation with internal dissipation is connected with a set of internal variables which account for the irreversible changes taking place in the interior of a body during the deformation process. The fundamental equations of thermodynamics are assumed to be valid for irreversible processes too, so that the equations of section 3.1 hold. As in the case of elastic deformations in this thesis the deformation processes are supposed to be isothermal ($\dot{\Theta} = 0$), consequently equation (3.7) remains as the only one of (3.3). With the restriction of a constant temperature the dissipation function (3.4) reduces to

$$D_{diss} = \rho \frac{\partial \Psi}{\partial \boldsymbol{\alpha}} \cdot \dot{\boldsymbol{\alpha}} \geq 0, \tag{3.24}$$

with the conjugated thermodynamic forces $\rho\frac{\partial \Psi}{\partial \boldsymbol{\alpha}}$. To distinguish between dissipative and the non–dissipative range of a material, a function f is defined with

$$f_i(\boldsymbol{\sigma}, \boldsymbol{\alpha}) \leq 0. \tag{3.25}$$

For $f < 0$ the material response is non–dissipative or elastic. The term "elastic" is used here in the sense of "reversible elastic", meaning not only that a continuum returns to its initial undeformed state, when the loads are removed, but also that no internal degradation took place. If the equality sign holds in equation (3.25) ($f = 0$), f describes a hyperplane in stress space indicating the limit of the elastic region. If (3.25) is violated the material law becomes dissipative and degradation occurs. The internal variables $\boldsymbol{\alpha}$ evolve according to the evolution laws that indicate the rate of change $\dot{\boldsymbol{\alpha}}$ until restriction (3.25) is valid again. Because of its properties f can be seen as an inequality constraint, which always has to be fulfilled in a deformation process.

For the dissipative case that corresponds to a violation of constraint (3.25) the rate of change of the internal variables $\dot{\alpha}$ are given by equations of evolution or flux equations.

More information about dissipative deformation in general can be found in the books of [Lemaitre and Chaboche, 1990] and [Lubliner, 1990].

3.3.1 Damage

The physical effects that are known as internal damage are the presence and evolution of cracks and cavities at the microscopic level. This might lead to a complete loss of load carrying capability of a material. From the continuum–mechanical point of view damage can be seen as a loss of stiffness of a material. The characterization of internal damage depends crucially on the specific type of material considered. Generally the degradation of materials can be divided into three classes, *brittle*, *ductile* and *fatigue* damage. The difference between the first two types is that for brittle damage plastic deformations are negligible, whereas for ductile damage large plastic deformations occur. Fatigue damage is the degradation in time of materials that are repeatedly submitted to loading–unloading processes on cyclic loading conditions for example fatigue failures can be observed. In this thesis only so called elastic damage models will be treated. After removing the loads a body is assumed to return to its initial state without lasting plastic deformations. The effect of damage will only be noticeable in a different response to a subsequent loading of the material.

To represent damage mathematically, several approaches have been proposed, see e.g. the overview article of [de Souza Neto et al., 1998] or the textbooks of [Lemaitre, 1984] and [Lemaitre, 1996]. For the most general case of anisotropic damage [Chaboche, 1984] proposed a fourth order damage tensor, [Murakami and Ohno, 1981] a tensor of second order. Here only isotropic damage will be considered, so that damage is represented by a single scalar damage variable d:

$$d \in [0;1] \quad , \qquad d = \begin{cases} 0 & \text{undamaged} \\ 1 & \text{completely damaged} \end{cases}$$

The damage parameter d is introduced as a measure of stiffness loss of a material. It ranges from 0 to 1, $d = 0$ for an undamaged virgin material and $d = 1$ for a completely damaged material. For the physical definition of the damage parameter a situation according to figure 3.1 is considered.
Assuming an arbitrary plane (defined by the normal vector $\mathbf{n}$) in the interior of body $\mathcal{B}$, created by cutting the body in two halves, a representative volume element (RVE) on the micro–meso scale as shown by the magnified cube on the right side in figure 3.1 is taken. δA_0 is the overall intersection area of the plane and the RVE, δA_D the are covered by the surface intersections of microcracks and microcavities in δA_0. Then the damage parameter d is defined as the quotient of those two variables:

$$d = \frac{\delta A_D}{\delta A_0}$$

Considering now a simple one–dimensional homogenous stress state, the definition of damage as the effective surface density of microdefects results:

$$d = \frac{S_D}{S_0} = \frac{E_0 - E_D}{E_0} \tag{3.26}$$

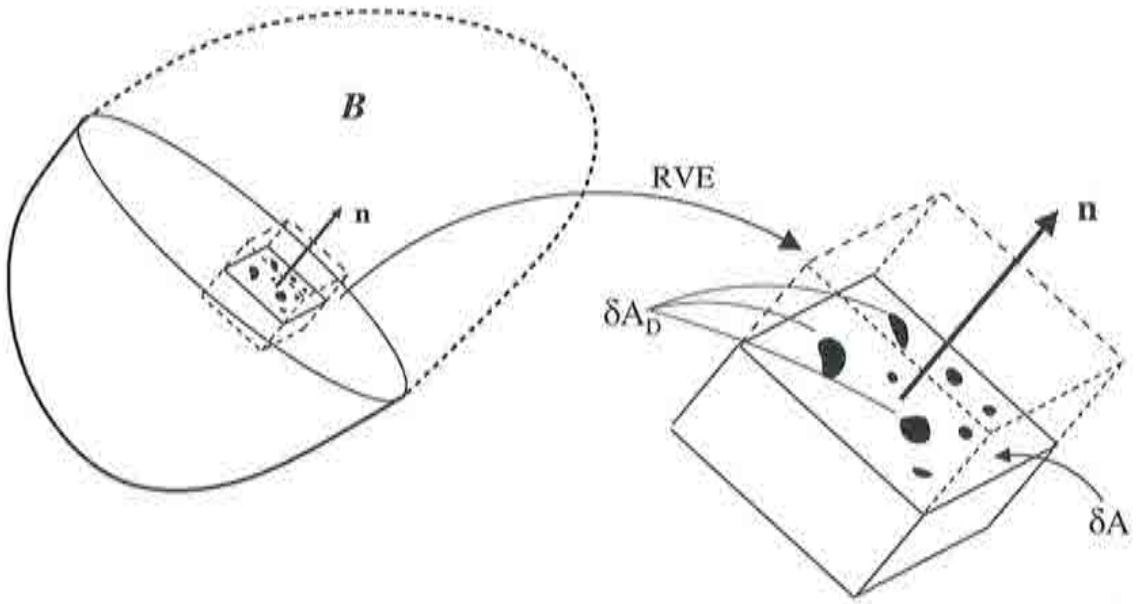

Figure 3.1: Micro–meso definition of damage

In terms of Young's modulus for the virgin material E_0 and the damaged material E_D d can be defined as the right hand side of equation (3.26). In the case of isotropic damage the scalar d is inserted in the constitutive equations assuming, that it holds for all directions in space.

Since the defects are open in such a way, that no microforces are acting on the surfaces of the microcracks and microcavities, it is convenient to introduce an effective Cauchy stress tensor related to the usual Cauchy stress tensor by

$$\boldsymbol{\sigma}^* = \frac{\boldsymbol{\sigma}}{1-d}. \tag{3.27}$$

This definition corresponds to the observation that the defects do not contribute to the load carrying area of a body. To avoid a micromechanical analysis for each type of defect the *hypothesis of strain equivalence* is postulated. It states that:

"The deformation behavior of the damaged material is represented by the constitutive laws of the virgin material with the true stress replaced by the effective stress."

This means that generally a material is assumed to behave elastically as described by laws of section 3.2 and damage effects are imposed on these laws.

To distinguish between elastic behavior and damage effects, a damage criterion f is considered:

$$f(\boldsymbol{\sigma}, d) \leq 0 \tag{3.28}$$

If the criterion is violated, the damage parameter d increases. Its rate of change $\dot{d}$ is given by an evolution law.

3.3.2 A simple damage model

In this thesis a rather simple damage model will be used, which originally was developed for concrete, see [Oliver et al., 1990] and [Oñate, 1994]. In the articles [Oliver, 1995] and [Oliver and Pulido, 1999] it was used to model strong discontinuities in materials. The model is based on a simple isotropic elastic St.Venant material law of section 3.2.1. Plastic deformations are excluded.

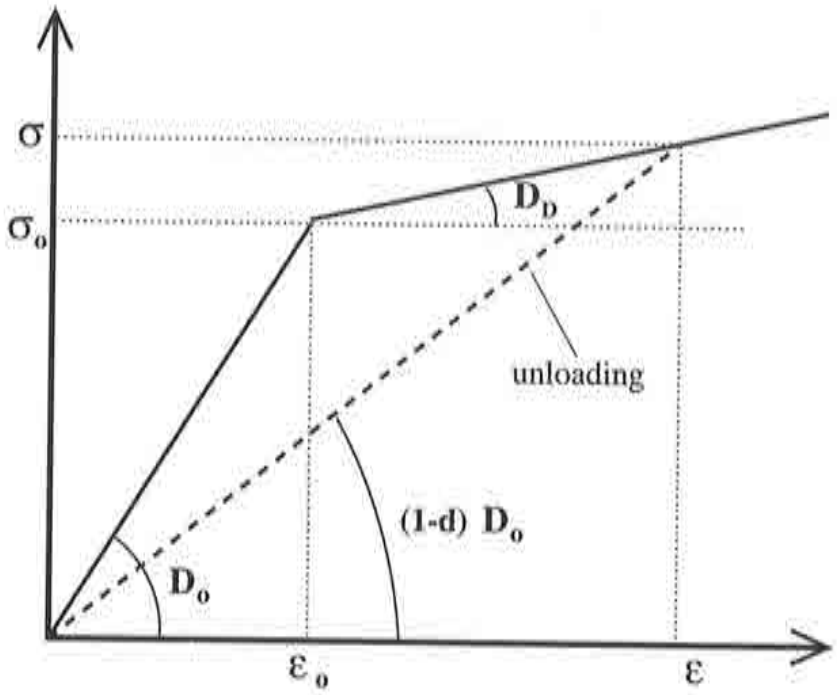

Figure 3.2: Constitutive plot for the simple damage model in 1D

For the one dimensional case the constitutive plot of the simple damage model is depicted in figure 3.2. It is basically a bilinear model. Until the stresses reach the threshold value σ_0, the material elasticity is characterized by $\mathbf{D}_0$. For stresses greater than σ_0 internal damage influences the material stiffness now defined by $\mathbf{D}_D$. The dashed line shows the unloading path, which is the secant to the point on the loading path obtained just before the load is decreased. On reloading the dashed path is followed, damage progresses if the intersection with the original path (solid line) is reached.

To derive the simple damage law the damage or degradation parameter d is inserted in the deformation energy for the St.Venant material.

$$W_D = (1-d)\, W_{SV} = (1-d)\, \frac{1}{2}\, \mathbf{E} : (\mathbf{D}_{SV}\mathbf{E}) \qquad (0 \le d \le 1) \tag{3.29}$$

With equation (3.10) the following form yields the relation of the second Piola–Kirchhof stress tensor and the Green–Lagrange strain tensor:

$$\mathbf{S} = (1-d)\, \mathbf{D}_{SV}\, \mathbf{E} = (1-d)\, \mathbf{S}^* \tag{3.30}$$

Besides the constitutive relation a suitable stress norm is needed:

$$\overline{\sigma}_S = \sqrt{\mathbf{S} : (\mathbf{D}_{SV}^{-1}\, \mathbf{S})} \tag{3.31}$$

Equation (3.31) can as well be transformed to a strain based law. In strain space this norm is expressed in terms of $\mathbf{E}$.

$$\overline{\sigma}(\mathbf{E}) = \sqrt{\mathbf{E} : (\mathbf{D}_{SV}\, \mathbf{E})} = \sqrt{2W_{SV}(\mathbf{E})} \quad \Longrightarrow \quad \overline{\sigma}_S = (1-d)\,\overline{\sigma} \tag{3.32}$$

With the norm (3.32) the damage criterion is defined as

$$f(\overline{\sigma}_S, q) = \overline{\sigma}_S - q \leq 0. \tag{3.33}$$

q here is the hardening variable. Using the relation $q(\tau^t) = (1-d)\tau^t$ and (3.32) this criterion can be reformulated:

$$\begin{aligned} f(\overline{\sigma}_S, q) &= (1-d)\,\overline{\sigma} - (1-d)\,\tau_t \\ \Longrightarrow \quad f(\mathbf{E}, \tau^t) &= \overline{\sigma} - \tau^t \leq 0 \qquad \text{with} \quad \tau^t = \max_{s\in(-\infty,t)} \{\overline{\sigma}^0, \overline{\sigma}^s\} \end{aligned}$$

τ^t is either the norm (3.31) of the initial threshold value for undamaged material ($\tau^0 = \overline{\sigma}^0$) or the maximum stress value in terms of the norm (3.32), that has been reached in the previous damage history of the material. Condition (3.33) states that damage in the material is initiated when the norm $\overline{\sigma}$ (3.32) exceeds the initial damage threshold τ^0. For pre-damaged material a damage progression takes place when the constraint (3.33) is violated.

The evolution law for the threshold value $\dot{\tau}^t = \lambda$ with $\tau^t \geq \tau^0$ leads to the *Kuhn–Tucker* conditions for the damage model:

$$\lambda \geq 0 \quad , \quad f \leq 0 \quad , \quad \lambda f = 0 \tag{3.34}$$

The consistency condition $\lambda \dot{f} = 0$ follows from (3.34) . The evolution law for q is then

$$\dot{q} = \frac{\partial q}{\partial \tau^t}\, \dot{\tau}^t. \tag{3.35}$$

The damage parameter d depends on the degradation state of the material and has the following properties:

$$d = G(\tau^t) = \frac{1}{1+H}\left(1 - \frac{\tau^0}{\tau^t}\right) \tag{3.36}$$

H is the hardening–softening parameter, a material constant. For the undamaged material $\tau^t = \tau^0$ the damage parameter is zero ($d = 0$) in agreement with the definition.

For the further numerical computations the tangent damage moduli $\mathbf{D}_{tan}$ are of importance. Therefore basing on equation (3.30) the rates of change or incremental form of the constitutive damage relation are deduced.

$$\dot{\mathbf{S}} = (1-d)\,\mathbf{D}_{SV}\dot{\mathbf{E}} - \dot{d}\,\mathbf{D}_{SV}\mathbf{E} = \mathbf{D}_{tan}\dot{\mathbf{E}} \tag{3.37}$$

The evolution laws for d and $\overline{\sigma}$ are

Stress norm: $\quad \overline{\sigma}^t = \sqrt{\mathbf{E} : (\mathbf{D}_{SV}\mathbf{E})}$

IF $\quad f(\overline{\sigma}^t, \tau^t) \leq 0$

$$\begin{aligned} \tau^t &= \tau^s \\ d^t &= d^t(\tau^t) = \frac{1}{1+H}\left(1 - \frac{\tau^0}{\tau^t}\right) \\ \mathbf{S} &= (1-d^t)\mathbf{D}_{SV}\mathbf{E} \\ \mathbf{D}_{tan} &= (1-d^t)\mathbf{D}_{SV} \end{aligned}$$

ELSE

$$\begin{aligned} \tau^t &= \overline{\sigma}^t \\ d^t &= d^t(\tau^t) = \frac{1}{1+H}\left(1 - \frac{\tau^0}{\tau^t}\right) \\ \mathbf{S} &= (1-d^t)\mathbf{D}_{SV}\mathbf{E} \\ \mathbf{D}_{tan} &= (1-d^t)\mathbf{D}_{SV} - \frac{\tau^0}{(1+H)}\,\frac{1}{\overline{\sigma}^{t\,3}}(\mathbf{D}_{SV}\mathbf{E}) \otimes (\mathbf{D}_{SV}\mathbf{E}) \end{aligned}$$

Table 3.1: Algorithm for the simple damage model

$$\dot{d} = \frac{\tau_0}{1+H}\,\frac{1}{\overline{\sigma}^2}\,\dot{\overline{\sigma}} \quad , \quad \dot{\overline{\sigma}} = \frac{1}{\overline{\sigma}}\,(\mathbf{D}_{SV}\mathbf{E})\,\dot{\mathbf{E}}.$$

For the tangent constitutive damage tensor $\mathbf{D}_{tan}$ which is equal to the consistent tangent damage tensor, it has to be distinguished between the two cases of elastic behavior ($f \leq 0$) and damage progression.

$$\mathbf{D}_{tan} = \begin{cases} (1-d)\,\mathbf{D}_{SV} & \text{for} \quad f \leq 0 \\ (1-d)\mathbf{D}_{SV} - \frac{\tau^0}{(1+H)}\,\frac{1}{\overline{\sigma}^3}(\mathbf{D}_{SV}\mathbf{E}) \otimes (\mathbf{D}_{SV}\mathbf{E}) & \text{else} \end{cases} \tag{3.38}$$

In table 3.1 the simple damage model is summarized in an algorithmic form. A superscript t for the stress norm $\overline{\sigma}^t$ and the damage parameter d^t is introduced to underline, that both are dependent on the current load state. $\tau^t = \tau^s$ in the first part of the algorithm means, that no update of the threshold value τ^t is necessary and its former value is adopted.

Chapter 4

The Finite Element Method

This chapter is concerned with the numerical solution of mechanical boundary value problems. The *Finite Element Method* (FEM) is used as a numerical tool to solve these boundary value problems.

In this thesis only isothermal, quasi–static mechanical problems are considered. The parameter t originally meant as the time now takes the role of a parameter describing different steps of the loading history in a quasi–static analysis.

For the application of the FEM the weak form of the governing equations is a prerequisite. Generally, two different approaches can be distinguished. If a potential exists, variational principles are applied to derive the weak form. For the second approach the weak form is obtained from the conservation laws, namely the conservation law of linear momentum for the problem type in this thesis. In the first part of this chapter both approaches are derived and equivalence is demonstrated. By applying the FEM a nonlinear equation system is obtained, which is solved with a *Newton–Raphson* algorithm.

The last part of this chapter is dedicated to the computation of equilibrium paths. By determining the response of a mechanical structure for different load levels a path in load–deflection space can be constructed. To overcome the difficulties that arise, when nonlinear paths have to be traced this way, path following or arclength procedures are used. Several types of the latter are given here.

For in depth coverage of the subject of this chapter the reader should refer to standard text books, such as [Crisfield, 1991a], [Zienkiewicz and Taylor, 1989], [Bathe, 1996] or other.

4.1 Weak form of the balance of momentum

In this thesis only isothermal problems will be studied ($\Theta = const; \dot{\Theta} = 0$), so that no coupling between mechanical and thermal variables exists and a purely mechanical description of the problem is sufficient. Therefore the following derivation will be restricted to the weak form of the balance of linear momentum (2.26).

Using the restriction to static problems, which implies that $\dot{\mathbf{x}} = \ddot{\mathbf{x}} = 0$, equation (2.26) can be further specialized to the static form of the balance of momentum:

$$Div\,\mathbf{P} + \rho_0 \hat{\mathbf{b}}_0 = 0 \tag{4.1}$$

Applying the *Galerkin method*, equation (4.1) is scalar multiplied by a vector valued test function $\delta\mathbf{u}$ and integrated over the volume $\mathcal{B}_0$.

$$\int_{\mathcal{B}_0} (Div\,\mathbf{P} + \rho_0\hat{\mathbf{b}}) \cdot \delta\mathbf{u}\; dV \;=\; 0 \qquad \text{with} \quad \delta\mathbf{u} \;=\; 0 \text{ on } \partial\mathcal{B}_0 \tag{4.2}$$

The test functions $\delta\mathbf{u}$ can be chosen arbitrarily but are required to be equal to zero on the boundary. Partial integration of (4.2) under consideration of the Neumann boundary conditions (2.41) the weak form of the balance of momentum G_S is obtained:

$$G_S(\mathbf{u}, \delta\mathbf{u}) \;=\; \int_{\mathcal{B}_0} \mathbf{P} : Grad\,\delta\mathbf{u}\; dV \;-\; \int_{\mathcal{B}_0} \rho_0\hat{\mathbf{b}} \cdot \delta\mathbf{u}\; dV \;-\; \int_{\partial\mathcal{B}_{0\sigma}} \hat{\mathbf{T}} \cdot \delta\mathbf{u}\; dA \;=\; 0 \tag{4.3}$$

The subscript s is introduced here, to denote the terms originating from the solid. In chapter 5 additional terms emanating from contact contributions will be added. With the following equivalence

$$\mathbf{P} : Grad\,\delta\mathbf{u} \;=\; \mathbf{S}\mathbf{F}^T : Grad\,\delta\mathbf{u} \;=\; \mathbf{S} : \frac{1}{2}\left(\mathbf{F}^{\mathbf{T}}\, Grad\,\delta\mathbf{u} \;+\; Grad^T\delta\mathbf{u}\;\mathbf{F}\right) \;=\; \mathbf{S} : \delta\mathbf{E} \tag{4.4}$$

the first integral can be transformed and the tensors in the product replaced by the 2.Piola–Krichhoff stress tensor $\mathbf{S}$ and the Green–Lagrange strain tensor $\mathbf{E}$. Equation (4.3) then turns into

$$G_S(\mathbf{u}, \delta\mathbf{u}) \;=\; \int_{\mathcal{B}_0} \mathbf{S} : \delta\mathbf{E}\; dV \;-\; \int_{\mathcal{B}_0} \rho_0\hat{\mathbf{b}} \cdot \delta\mathbf{u}\; dV \;-\; \int_{\partial\mathcal{B}_{0\sigma}} \hat{\mathbf{T}} \cdot \delta\mathbf{u}\; dA \;=\; 0. \tag{4.5}$$

$\delta\mathbf{E}$ here is the variation of the Green–Lagrange strain tensor, see (4.4) for a definition. By applying the same procedure to the current configuration, a reduction of (2.25) to the static form and integration leads to

$$\int_{\mathcal{B}} (Div\,\boldsymbol{\sigma} + \rho\hat{\mathbf{b}}) \cdot \delta\mathbf{u}\; dv \;=\; 0. \tag{4.6}$$

After partial integration and the transformation of the first integral this finally yields

$$G_S(\mathbf{u}, \delta\mathbf{u}) \;=\; \int_{\mathcal{B}} \boldsymbol{\sigma} : \delta\mathbf{e}\; dv \;-\; \int_{\mathcal{B}} \rho\,\hat{\mathbf{b}} \cdot \delta\mathbf{u}\; dv \;-\; \int_{\partial\mathcal{B}\sigma} \hat{\mathbf{t}} \cdot \delta\mathbf{u}\; da \;=\; 0, \tag{4.7}$$

with $\delta\mathbf{e}$ being the variation of the Euler–Almansi strain tensor given by

$$\delta\mathbf{e} \;=\; \frac{1}{2}\left(grad\,\delta\mathbf{u} \;+\; grad^T\delta\mathbf{u}\right). \tag{4.8}$$

Although this equation is formally equal to the virtual work in the linear theory, it has to be taken into account, that the stress and virtual strain tensors have to be evaluated in the current configuration.

4.2 Variational formulation

The second way of deriving the weak form is viable if a potential exist. It is of importance for chapter 6 when critical points will be defined. The deformation energy W for hyperelastic material is by definition a potential for the stored elastic energy of a continuum. Besides the term for the elastic energy, terms considering the energy of applied body and surface loads have to be added. The potential for an isothermal, static problem is then:

$$\Pi_S = \int_{\mathcal{B}_0} W \, dV - \int_{\mathcal{B}_0} \rho_0 \hat{\mathbf{b}} \cdot \mathbf{u} \, dV - \int_{\partial\mathcal{B}_{0\sigma}} \hat{\mathbf{T}} \cdot \mathbf{u} \, dA \longrightarrow Min. \tag{4.9}$$

Applying the *principle of the minimum of the elastic potential* the unknown displacement function $\mathbf{u}$ is required to minimize the potential Π_S. The minimum of equation (4.9) can be computed from the variation of the potential Π_S.

$$\delta\Pi_S = \int_{\mathcal{B}_0} \delta W \, dV - \int_{\mathcal{B}_0} \rho_0 \hat{\mathbf{b}} \cdot \delta\mathbf{u} \, dV - \int_{\partial\mathcal{B}_{0\sigma}} \hat{\mathbf{T}} \cdot \delta\mathbf{u} \, dA = 0 \tag{4.10}$$

For the St.Venant material, the potential and its variation yield

$$\Pi_S = \int_{\mathcal{B}_0} \frac{1}{2} \left(\mathbf{E} : (\mathbf{D}_{SV}\mathbf{E})\right) \, dV - \int_{\mathcal{B}_0} \rho_0 \hat{\mathbf{b}} \cdot \mathbf{u} \, dV - \int_{\partial\mathcal{B}_{0\sigma}} \hat{\mathbf{T}} \cdot \mathbf{u} \, dA \tag{4.11}$$

$$\delta\Pi_S = \int_{\mathcal{B}_0} \mathbf{E} : \mathbf{D}_{SV}\delta\mathbf{E} \, dV - \int_{\mathcal{B}_0} \rho_0 \hat{\mathbf{b}} \cdot \delta\mathbf{u} \, dV - \int_{\partial\mathcal{B}_{0\sigma}} \hat{\mathbf{T}} \cdot \delta\mathbf{u} \, dA = 0 \tag{4.12}$$

At this point the equivalence of the weak form (4.12) derived from a potential and the weak form of the balance of momentum (4.5) is obvious.

4.3 Finite Element Method

The Finite Element method is a numerical technique for the solution of partial differential equations. As a convention from now on the St.Venant material model will be assumed as the constitutive model. The introduction of damage in the governing equations later is straightforward, since only the scalar $(1 - d)$ term has to be inserted.

The area of integration $\mathcal{B}_0$ in (4.5) is divided into smaller finite elements Ω^e. Mathematically this reads as:

$$\mathcal{B}^h = \bigcup_{e=1}^{n_e} \Omega^e \tag{4.13}$$

n_e is the total number of elements. It is required that the partition with finite elements is non–overlapping and without interior gaps. The superscript h here and in the following denotes the discretization and approximation of quantities by the FEM.

The weak form (4.5) can now be applied on the elemental level. The individual elemental contribution are then assembled to the global form.

$$G_S^h(\mathbf{u}^h, \delta\mathbf{u}^h) = \bigcup_{e=1}^{n_e} \int_{\Omega^e} \mathbf{S} : \delta\mathbf{E}^h \, dV - \int_{\Omega^e} \rho \, \hat{\mathbf{b}} \cdot \delta\mathbf{u}^h \, dV - \int_{\partial\Omega^e \sigma} \hat{\mathbf{t}} \cdot \delta\mathbf{u}^h \, dA = 0 \quad (4.14)$$

The unknown quantities $\mathbf{u}$ as well as its derivatives $\nabla\mathbf{u}$, the test functions $\delta\mathbf{u}$ and its derivatives $\nabla\delta\mathbf{u}$ are interpolated in each element by a sum of nodal shape functions N_j and nodal values $\mathbf{v}_j$.

$$\begin{aligned} \mathbf{u}^h &= \sum_{i=j}^{n_n} N_j \, \mathbf{v}_j & \nabla \mathbf{u}^h &= \sum_{j=1}^{n_n} \mathbf{v}_j \otimes \nabla N_j \\ \delta\mathbf{u}^h &= \sum_{j=1}^{n_n} N_j \, \delta\mathbf{v}_j & \nabla \delta\mathbf{u}^h &= \sum_{j=1}^{n_n} \delta\mathbf{v}_j \otimes \nabla N_j \end{aligned} \quad (4.15)$$

For the examples in this thesis linear and quadratic polynomes are used. The variable n_n in the summations is the number of nodes per element. Since *isoparametric* elements are implemented a similar interpolation is made for the coordinates $\mathbf{X}$.

$$\mathbf{X}^h = \sum_{j=1}^{n_n} N_j \, \mathbf{X}_j \quad (4.16)$$

A shorter matrix formulation for the Green–Lagrange strain tensor $\mathbf{E}$ and its variation $\delta\mathbf{E}$, which are functions of $\mathbf{u}$ and $\delta\mathbf{u}$, is given by

$$\mathbf{E}^h = \mathbf{B}(\mathbf{v}) \, \mathbf{v} \quad (4.17)$$

$$\delta\mathbf{E}^h = \hat{\mathbf{B}}(\mathbf{v}) \, \delta\mathbf{v}. \quad (4.18)$$

The matrices $\mathbf{B}$ and $\hat{\mathbf{B}}$ contain the derivatives of the shape functions ∇N in an order that has to be specified according to the element theory applied.

After extracting the virtual nodal displacements the weak form (4.14) can be rewritten as a product of the global vector of the nodal virtual displacements $\delta\mathbf{v}$ and a vector quantity $\mathbf{G}_S^h$.

$$G_S^h(\mathbf{v}, \delta\mathbf{v}) = \delta\mathbf{v}^T \cdot \mathbf{G}_S^h(\mathbf{v}) = \bigcup_{e=1}^{n_e} \delta\mathbf{v}_e^T \cdot \mathbf{G}_e^h = \bigcup_{e=1}^{n_e} G_e^h \qquad \forall \, \delta\mathbf{v} \in \mathbb{R}^N \quad (4.19)$$

Equation (4.19) has to hold for arbitrary $\delta\mathbf{v}$, with the exception of $x \in \partial\mathcal{B}$ where $\delta\mathbf{v} = \mathbf{0}$ has to be fulfilled. This leads to a system of nonlinear equations

$$\mathbf{G}_S^h = \mathbf{R}(\mathbf{v}) - \mathbf{P} = 0. \quad (4.20)$$

$\mathbf{G}_s^h$ is split into two terms: $\mathbf{R}$ contains the contributions originating from the inner energy and the term $\mathbf{P}$ depicts the contributions of the external load with

$$\mathbf{R}(\mathbf{v}) = \bigcup_{e=1}^{n_e} \int_{\Omega^e} \hat{\mathbf{B}}^T(\mathbf{v}_e) : \mathbf{S}(\mathbf{v}_e)\, dV \tag{4.21}$$

$$\mathbf{P}(\mathbf{v}) = \bigcup_{e=1}^{n_e} \left[\int_{\Omega^e} \rho\, \hat{\mathbf{b}}\, dV = \int_{\partial\Omega^e \sigma} \hat{\mathbf{t}}\, dA \right]. \tag{4.22}$$

The equations system (4.20) has to be solved for the unknown nodal displacement vector $\mathbf{v}$. Equation system (4.20) is nonlinear and can not be solved analytically. The Newton–Raphson method, which will be presented in the following section, is used to solve (4.20) iteratively. Therefore the derivative of $\mathbf{G}$ with respect to the nodal displacements, the tangent stiffness matrix $\mathbf{K}_T$ is needed:

$$\mathbf{K}_T = \frac{\partial \mathbf{G}_S^h}{\partial \mathbf{v}} \tag{4.23}$$

Since $\mathbf{G}_S^h$ can be assembled from the elemental contributions, also the tangent stiffness matrix $\mathbf{K}_T$ consists of an assemblation of its elemental parts $\mathbf{K}_T^e$. For problems, where the loads are displacement independent, the stiffness matrix can be computed by:

$$\frac{\partial \mathbf{G}_S^h}{\partial \mathbf{v}} = \bigcup_{e=1}^{n_e} \int_{\Omega^e} \left[\mathbf{B}^T(\mathbf{v}_e) \mathbf{D}_{SV} \mathbf{B}(\mathbf{v}_e) + \overline{\mathbf{G}}^T \hat{\mathbf{S}}(\mathbf{v}_e) \overline{\mathbf{G}} \right] dV = \bigcup_{e=1}^{n_e} \mathbf{K}_T^e. \tag{4.24}$$

The matrices $\overline{\mathbf{G}}$ are not dependent on the displacements and contain only derivatives of the shape functions. $\hat{\mathbf{S}}$ is formed by stresses. It is furthermore convenient to split $\mathbf{K}_T$ into the sum of the three matrices $\mathbf{K}_L$, $\mathbf{K}_U$ and $\mathbf{K}_\sigma$.

$$\mathbf{K}_T = \mathbf{K}_L + \mathbf{K}_U + \mathbf{K}_\sigma \tag{4.25}$$

The $\mathbf{B}$–matrices are split into linear $\mathbf{B}_l$ and nonlinear parts $\mathbf{B}_{nl}$.

$$\mathbf{B} = \mathbf{B}_l + \mathbf{B}_{nl}(\mathbf{v}) \tag{4.26}$$

The linear stiffness matrix $\mathbf{K}_L$ contains the parts of the integral that are not dependent on the nodal displacements $\mathbf{v}$.

$$\mathbf{K}_L = \bigcup_{e=1}^{n_e} \int_{\Omega^e} \mathbf{B}_l^T \mathbf{D}_{SV} \mathbf{B}_l\, dV \tag{4.27}$$

In the initial displacement matrix $\mathbf{K}_U$ the nonlinear terms of the integral (4.24) are assembled.

$$\mathbf{K}_U(\mathbf{v}_e) = \bigcup_{e=1}^{n_e} \int_{\Omega^e} \left[\mathbf{B}_l^T \mathbf{D}_{SV} \mathbf{B}_{nl}(\mathbf{v}_e) + \mathbf{B}_{nl}^T(\mathbf{v}_e) \mathbf{D}_{SV} \mathbf{B}_l + \mathbf{B}_{nl}^T(\mathbf{v}_e) \mathbf{D}_{SV} \mathbf{B}_{nl}(\mathbf{v}_e) \right] dV \tag{4.28}$$

The initial stress matrix $\mathbf{K}_\sigma$ is the second term of the sum in equation (4.24).

$$\mathbf{K}_\sigma(\mathbf{v}_e) = \bigcup_{e=1}^{n_e} \int_{\Omega^e} \overline{\mathbf{G}}^T \hat{\mathbf{S}}(\mathbf{v}_e) \overline{\mathbf{G}} \, dV \tag{4.29}$$

To simplify the notation in the following chapters the superscript h for the FE-formulation of the weak form will be omitted ($\mathbf{G}_S^h \doteq \mathbf{G}_S$).

4.4 Newton–Raphson Method

The *Newton–Raphson Method* can be obtained by performing a *Taylor series expansion* of $\mathbf{G}_s$:

$$\mathbf{G}_S(\mathbf{v}) = \mathbf{G}_S(\mathbf{v}_0) + \frac{\partial \mathbf{G}_S}{\partial \mathbf{v}} {}_\Delta\mathbf{v} + O({}_\Delta\mathbf{v}^2) \tag{4.30}$$

The terms of quadratic and higher order in ${}_\Delta\mathbf{v}$ are summarized in the rest term $O({}_\Delta\mathbf{v}^2)$. After linearization of (4.30) by neglecting the nonlinear terms, equation (4.30) together with (4.20) yields the incremental iterative algorithm:

$$\mathbf{K}_T(\mathbf{v}^i) \, {}_\Delta\mathbf{v}^{i+1} = -\mathbf{G}_S(\mathbf{v}^i) \tag{4.31}$$

$\mathbf{K}_T$ is the tangent stiffness matrix defined by equation (4.23). Index i in (4.31) is the iteration counter.

The complete algorithm is given in table 4.1. Common initial solution vectors $\mathbf{v}_0$ often are either the solution vector of the previous load step $\mathbf{v}_t$ or the zero vector $\mathbf{v}_0 = \mathbf{0}$ if this is the first load step. The Newton–Raphson algorithm converges quadratically in the vicinity of the solution.

Starting value:	$\mathbf{v}^0 = \mathbf{v}^t$
Iteration loop:	$i = 0, 1, \ldots$ until convergence
Solve for ${}_\Delta\mathbf{v}$:	$\mathbf{K}_T(\mathbf{v}^i) \, {}_\Delta\mathbf{v}^{i+1} = -\mathbf{G}_S(\mathbf{v}^i)$
Update:	$\mathbf{v}^{i+1} = \mathbf{v}^i + {}_\Delta\mathbf{v}^{i+1}$
Check convergence:	$\|\mathbf{G}_S(\mathbf{v}^{i+1})\| \leq TOL$

Table 4.1: The Newton–Raphson algorithm

4.5 Computation of the equilibrium path

In order to determine the response of a mechanical structure for different load levels, a scaling parameter λ for the load terms $\mathbf{P}$ is introduced in the non–linear equation system (4.20):

$$\mathbf{G}_S(\mathbf{v}) = \mathbf{R}(\mathbf{v}) - \lambda \mathbf{P} = \mathbf{0} \tag{4.32}$$

Since $\mathbf{P}$ reflects the manner external loads are applied and remains unaltered by λ, only the size of all loads varies. The relative size of the individual loads with respect to each other does not change.

To illustrate the structural response graphically, it is convenient to plot λ against an assorted displacement degree of freedom. This degree of freedom is chosen such that it reflects the behavior of the entire structure. Figure 4.1 shows an example of such a load–displacement or equilibrium path.

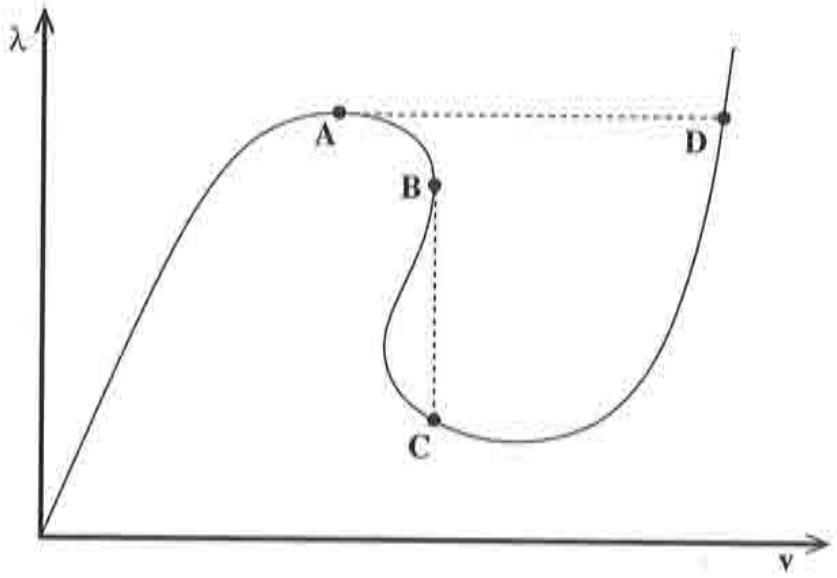

Figure 4.1: Example for a non–linear load–displacement path

In figure 4.1 other possible characteristics of non–linear load–displacement paths are shown. If the load factor λ is increased beyond the point A, the displacement will suddenly jump to point D and the path lying in between both points cannot be followed. A is a limit load point of the equilibrium path, the structure behaves dynamically. Since this thesis is restricted to quasi–static analysis the real dynamic behavior cannot be reflected. Instead, the computation might not converge or jump to point D as indicated by the dashed path in figure 4.1.

A conceivable remedy for this problem is to compute the problem displacement controlled by prescribing a displacement degree of freedom that is augmented instead of the load factor λ. The limitations of this control type will be observed at point B in figure 4.1, where the path then jumps to point C.

Hence a combined load displacement control is needed to determine the load–displacement between A, D and B, C. Therefore, path following or *arclength* methods have been developed. Essential publications on this topic are [Wemper, 1971], [Riks, 1972] and [Ricks, 1979]. The idea of the arclength methods is to consider the load parameter λ as an additional degree of freedom in the system of equations (4.32). To solve for the now $N+1$ unknowns, i.e. displacements $\mathbf{v}$ and load parameter λ, a control equation $f(\mathbf{v}, \lambda) = 0$ is added as an additional constraint to problem (4.32):

$$\begin{pmatrix} \mathbf{G}_S(\mathbf{v},\lambda) \\ f(\mathbf{v},\lambda) \end{pmatrix} = \mathbf{0} \tag{4.33}$$

To solve the non–linear system of equations (4.33) with the Newton–Raphson method, the linearization of $\mathbf{G}_S$ and f, i.e. the derivatives $\mathbf{G}_{,\mathbf{v}} = \mathbf{K}_T$, $\mathbf{G}_{,\lambda} = \mathbf{P}$, $\mathbf{f}_{,v}$ and $f_{,\lambda}$ are needed:

$$\begin{bmatrix} \mathbf{K}_T^i & -\mathbf{P} \\ \mathbf{f}_{,\mathbf{v}}^{i\,T} & f_{,\lambda}^i \end{bmatrix} \begin{pmatrix} {}_{\Delta}\mathbf{v}^{i+1} \\ {}_{\Delta}\lambda^{i+1} \end{pmatrix} = - \begin{pmatrix} \mathbf{G}_S(\mathbf{v}^i,\lambda^i) \\ f^i(\mathbf{v}^i,\lambda^i) \end{pmatrix} \tag{4.34}$$

A comma in the subscript is an abbreviation of a derivative with respect to the parameter following the comma.

The additional terms in the matrix on the left hand side of (4.34) have the disadvantage that the tangent stiffness matrix $\mathbf{K}_T$ no longer has a band structure. With existing solution algorithms a direct solution of (4.34) takes a considerably higher computational effort than the original problem (4.31). This disadvantage can be circumvented by a partitioning algorithm, which exploits the specific nature of (4.34) more efficiently. A split of the displacement increment ${}_{\Delta}\mathbf{v} = {}_{\Delta}\mathbf{v}_G + {}_{\Delta}\lambda_{\Delta}\mathbf{v}_P$ allows a separation of (4.34) in two coupled problems. Equation (4.34) then reads:

$$\mathbf{K}_T^i\ {}_{\Delta}\mathbf{v}_G^{i+1} + {}_{\Delta}\lambda^{i+1}\mathbf{K}_T^i\ {}_{\Delta}\mathbf{v}_P^{i+1} - {}_{\Delta}\lambda^{i+1}\mathbf{P} = -\mathbf{R} + \lambda\mathbf{P} \tag{4.35}$$

$$\mathbf{f}_{,\mathbf{v}}^{i\,T}\ {}_{\Delta}\mathbf{v}_G^{i+1} + {}_{\Delta}\lambda^{i+1}\ \mathbf{f}_{,\mathbf{v}}^{i\,T}\ {}_{\Delta}\mathbf{v}_P^{i+1} + {}_{\Delta}\lambda^{i+1} f_{,\lambda}^i = f^i(\mathbf{v}^i,\lambda^i) \tag{4.36}$$

Sorting the terms in (4.35) according to the dependency on λ, two separate equation systems yield. Solving (4.36) for ${}_{\Delta}\lambda$ the algorithm of table 4.2 can be constructed.
The arclength method is based on a two–step solution strategy. At the beginning of a new load step the load factor increment ${}_{\Delta}\lambda$ is predicted as shown in table 4.2. The parameter ${}_{\Delta}s$ is the constant arclength increment, that has to be supplied by the user and depends on the problem to be computed. At different positions on the load–displacement path different signs of the load increment ${}_{\Delta}\lambda^0$ have to be chosen. When $\mathbf{K}_T$ is positive definite at the beginning of a load step, the positive value is used. When a limit point is passed a sign change has to be applied. [Bergan et al., 1978] developed the *current stiffness parameter* as an indicator for the choice of the sign.

$$c_{csp} = \frac{k^0}{k^t} \quad \text{with} \quad k^t = \frac{\mathbf{P}^T\,{}_{\Delta}\mathbf{v}_P^t}{{}_{\Delta}\mathbf{v}_P^{t\,T}\,{}_{\Delta}\mathbf{v}_P^t} \tag{4.37}$$

The current stiffness parameter c_{csp} is the quotient of k^t at the current load step and the first one $k^0 = k^t|_{t=0}$. The superscript t for the displacements ${}_{\Delta}\mathbf{v}_p^t$ is added to emphasize that it is referred to the displacements of the current load step. At limit points the product in the nominator of k^t changes the sign since displacement increment and load vector no longer have the same direction.

For the control equation $f(\mathbf{v},\lambda)$ of the corrector step a variety of expressions have been proposed in literature. In this thesis the control types of an iteration on a normal

Predictor:	$\mathbf{K}_T(\mathbf{v}^0)\ {}_\Delta\mathbf{v}_P^0$	$=$	$\mathbf{P}$
	${}_\Delta\lambda^0$	$=$	$\pm \dfrac{\Delta s}{\sqrt{({}_\Delta\mathbf{v}_P^0)^T\ {}_\Delta\mathbf{v}_P^0}}$
Iteration loop:	$i = 0, 1, \ldots$	until convergence	
Solve for ${}_\Delta\mathbf{v}$:	$\mathbf{K}_T(\mathbf{v}^i)\ {}_\Delta\mathbf{v}_G^{i+1}$	$=$	$-\ \mathbf{G}(\mathbf{v}^i, \lambda^i)$
	$\mathbf{K}_T(\mathbf{v}^i)\ {}_\Delta\mathbf{v}_P^{i+1}$	$=$	$\mathbf{P}$
Compute increments:	${}_\Delta\lambda^{i+1}$	$=$	$-\dfrac{f^i + \mathbf{f}_{,\mathbf{v}}^{i\,T}\ {}_\Delta\mathbf{v}_G^{i+1}}{f_{,\lambda}^i + \mathbf{f}_{,\mathbf{v}}^{i\,T}\ {}_\Delta\mathbf{v}_P^{i+1}}$
	${}_\Delta\mathbf{v}^{i+1}$	$=$	${}_\Delta\mathbf{v}_G^{i+1} + {}_\Delta\lambda^{i+1}\ {}_\Delta\mathbf{v}_P^{i+1}$
Update:	$\mathbf{v}^{i+1} = \mathbf{v}^i + {}_\Delta\mathbf{v}^{i+1}$		$\lambda^{i+1} = \lambda^i + {}_\Delta\lambda^{i+1}$
Check convergence:	$\|\mathbf{G}_S(\mathbf{v}^{i+1}, \lambda^{i+1})\| \leq TOL$		

Table 4.2: Algorithm for arclength procedure

plane, on a tangent plane and on spherical hyperplanes will be given. The two previously mentioned types of load and displacement control can be derived as well from a constraint equation f. Therefore, they can also be viewed as a special type of arclength method. A good overview on the subject of the arclength method can be found in [Wagner, 1991b] or [Crisfield, 1991a].

Load controlled arclength method

For the simple case of a load controlled problem the control equation $f(\mathbf{v}, \lambda)$ reads

$$f(\lambda) = \lambda - c. \tag{4.38}$$

The derivatives of f are trivial to calculate:

$$\mathbf{f}_{,\mathbf{v}}^T = 0, \quad f_{,\lambda} = 1 \tag{4.39}$$

The increment of the load parameter ${}_\Delta\lambda$ in the algorithm 4.2 then simplifies to

$${}_\Delta\lambda^{i+1} = -f^i. \tag{4.40}$$

Displacement controlled arclength method

In the displacement controlled arclength method the displacements of a selected degree of freedom v_a are prescribed by the control equation

$$f(\mathbf{v}) = v_a - c. \tag{4.41}$$

The derivatives of f are constant:

$$f_{,\lambda} = 0, \quad \mathbf{f}_{,\mathbf{v}}^T = \mathbf{e}_a^T \qquad \text{with} \quad \mathbf{e}_a^T = \{0, 0, 0, \ldots, 1, \ldots, 0, 0, 0\} \tag{4.42}$$

$\mathbf{e}_a$ is vector with only the component corresponding to the degree of freedom a equal to one, whereas all others are zero. The increment of the load parameter $_{\Delta}\lambda$ in table 4.2 is then

$$_{\Delta}\lambda^{i+1} = -\frac{f^i + {}_{\Delta}v_{Ga}^{i+1}}{{}_{\Delta}v_{Pa}^{i+1}}. \tag{4.43}$$

Iteration on a normal plane

The control equation for the iteration on a normal plane has the form

$$f(\mathbf{v}, \lambda) = (\mathbf{v}^m - \mathbf{v}^t)^T(\mathbf{v} - \mathbf{v}^m) + (\lambda^m - \lambda^t)(\lambda - \lambda^m) = 0. \tag{4.44}$$

The underlying idea is illustrated in figure 4.2. Starting from the point $(\mathbf{v}^t, \lambda^t)$ of the last converged load step, a predictor step to $(\mathbf{v}^m, \lambda^m)$ is made. It is now required that the subsequent corrector step is orthogonal to the predictor step as shown in figure 4.2.

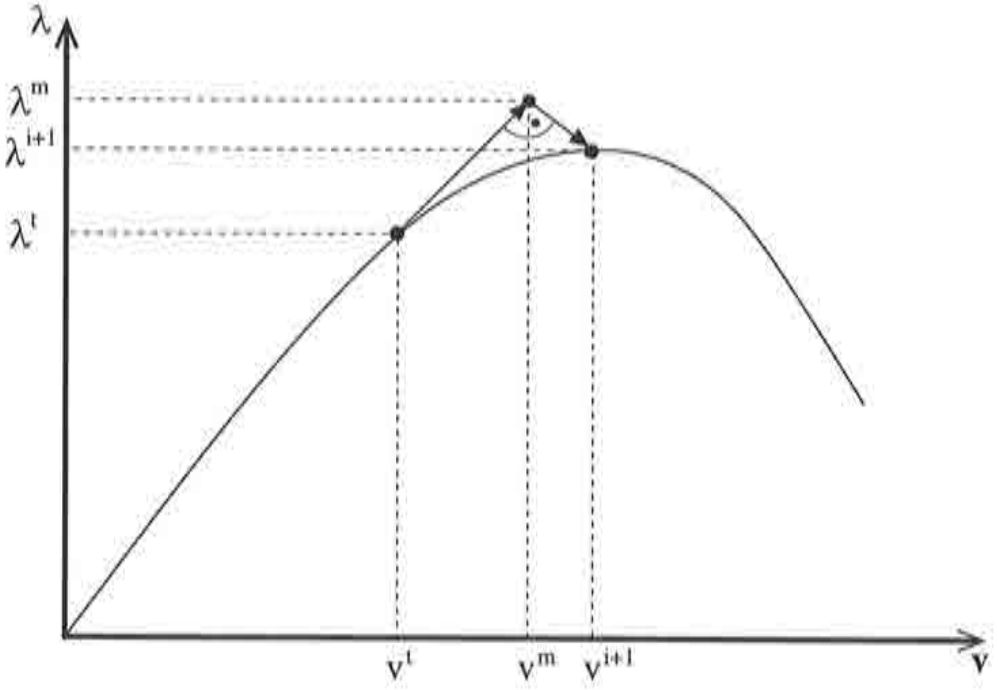

Figure 4.2: Arclength with iteration on a normal plane

The index m here denotes an intermediate state in the iteration process. Generally, two possibilities exist for the choice of m. Setting $m = 1$ all the following iteration steps are orthogonal to the first predictor step, the normal plane remains constant throughout the iteration process. If $m = i$ a continuous update of the normal plane is made and each iteration step is orthogonal to the precedent one, see [Menzel and Schwetlick, 1978], [Ramm, 1981]. With $\mathbf{v}^t$, λ^t, $\mathbf{v}^m$ and λ^m as constants, the derivatives of the control equation for the iteration on a normal plane are:

$$\mathbf{f}_{,\mathbf{v}}^{i\,T} = (\mathbf{v}^m - \mathbf{v}^i)^T, \qquad f_{,\lambda}^i = \lambda^m - \lambda^i \tag{4.45}$$

The equation for the load parameter increment is now somewhat more complicated:

$$\Delta\lambda^{i+1} = -\frac{f^i + (\mathbf{v}^m - \mathbf{v}^i)^T \Delta\mathbf{v}_G^{i+1}}{(\lambda^m - \lambda^i) + (\mathbf{v}^m - \mathbf{v}^i)^T \Delta\mathbf{v}_P^{i+1}} \tag{4.46}$$

Iteration on a tangent plane

The iteration on a tangent plane is rather similar to the iteration on a normal plane. Here orthogonality between the tangent vector to the equilibrium path $(\Delta\mathbf{v}_P, 1)$ is required, leading to the control equation and its derivatives

$$f(\mathbf{v}, \lambda) = \Delta\mathbf{v}_P^T(\mathbf{v} - \mathbf{v}^m) + (\lambda - \lambda^m) = 0. \tag{4.47}$$

$$\mathbf{f}_{,\mathbf{v}}^{i\,T} = \Delta\mathbf{v}_P^{i+1\,T}, \quad f_{,\lambda}^i = 1 \tag{4.48}$$

With these derivatives the load parameter increment is obtained as follows:

$$\Delta\lambda^{i+1} = -\frac{f^i + \Delta\mathbf{v}_P^{i+1\,T} \Delta\mathbf{v}_G^{i+1}}{1 + \|\Delta\mathbf{v}_P^{i+1}\|^2} \tag{4.49}$$

Iteration on spherical hyperplanes

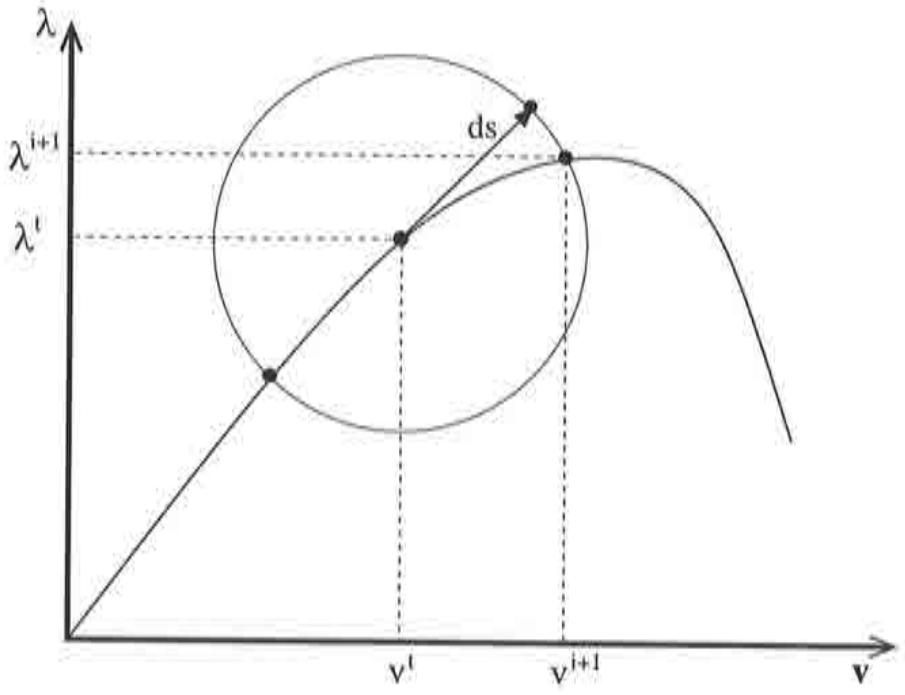

Figure 4.3: Arclength with iteration on spherical hyperplanes

The basic idea of an iteration on spherical hyperplanes was introduced by Crisfield and is described in [Crisfield, 1991a]. The length of the vector $({}_{\Delta}\mathbf{v}, {}_{\Delta}\lambda)$ is set equal to a constant value ${}_{\Delta}s$ in the control equation.

$$f(\mathbf{v},\lambda) = \sqrt{(\mathbf{v}-\mathbf{v}^t)^T(\mathbf{v}-\mathbf{v}^t)+(\lambda-\lambda^t)^2} - {}_{\Delta}s = c - {}_{\Delta}s = 0 \tag{4.50}$$

Figure 4.3 shows the iteration on spherical hyperplanes in a load–displacement diagram. Whereas [Crisfield, 1981] solves this quadratic equation directly, [Schweizerhof and P.Wriggers, 1986] linearized this control equation consistently:

$$\mathbf{f}_{,\mathbf{v}}^{i\,T} = \frac{1}{c}(\mathbf{v}-\mathbf{v}^t)^T \quad , \quad f_{,\lambda}^{i} = \frac{1}{c}(\lambda-\lambda^t)$$

The increment of the load parameter λ is then:

$${}_{\Delta}\lambda^{i+1} = -\frac{f^i(f^i+ds)+(\mathbf{v}-\mathbf{v}^t)^T{}_{\Delta}\mathbf{v}_G^{i+1}}{(\lambda-\lambda^t)+(\mathbf{v}-\mathbf{v}^t)^T{}_{\Delta}\mathbf{v}_P^{i+1}} \tag{4.51}$$

The disadvantage of a slightly lower robustness compared to Crisfield's algorithm is compensated by an easier implementation. In Crisfield's method the satisfaction of the constraint is required in every iteration step, see [Schweizerhof and P.Wriggers, 1986] for a comparison of both methods and the normal plane iteration type.

Remark: A whole class of cylindrical control equations can be constructed, when scaling factors are inserted in the scalar products of the displacement and load factor increments in (4.50). In [Crisfield, 1991a] this method can be found under the name cylindrical arclength method.

Chapter 5

Contact

In this chapter the formulation of a frictionless, non-thermal contact will be presented. Large deformations are taken into account, due to the nature of the instability problems considered in this thesis. The description of contact presented here follows closely the one in [Wriggers, 1995] and [Scherf, 1997].

The outline of the chapter is as follows: In the first section the kinematical formulation of the normal contact with the master–slave concept is given. The requirement of a non–penetration of the bodies leads to a geometrical constraint. The interpretation of which as contact pressure is the subject of the following section. With the incorporation of the constraint in the variational equation the question of solution methods for constrained optimization problems arises. Here the common methods are presented and discussed briefly. The linearization of the contact terms suitable for a solution of the equation system with the Newton–Raphson method then concludes the general part of the contact representation. The specific discretization of the contact surface with the node–to–segment element for a two dimensional contact and the combination with the penalty method are contained in the last section of this chapter.

5.1 Normal contact

For the modeling of contact the master-slave concept of [Hallquist, 1979] will be used. It proved to be suitable for this purpose in recent years, as several papers show, see e.g. [Curnier, 1984], [Wriggers and Miehe, 1992] or [Laursen and Simo, 1993].
Multi-body contact problems can be treated as a combination of several two-body pair problems. Figure 5.1 shows an arbitrary contact pair. One of the bodies is chosen as the master $\mathcal{B}^M$, the other as the slave $\mathcal{B}^S$. This choice can be done arbitrarily, but commonly the body with a finer surface discretization is assumed to be the master. To reduce the computational effort a part of both surfaces is marked as a possible contact zone. In most of the mechanical problems this can be done in advance as the general behavior of the problem can be predicted by means of engineering experience. Denoting the surfaces as $\partial\mathcal{B}^M, \partial\mathcal{B}^S$ and the contact parts by a subscript c the mathematical relation is $\partial\mathcal{B}_c^M \subset \partial\mathcal{B}^M, \partial\mathcal{B}_c^S \subset \partial\mathcal{B}_c^M$. The orientation of the contact surfaces are given by the outward directed normal vectors $\mathbf{n}^{\mathbf{M}}$ and $\mathbf{n}^{\mathbf{S}}$, which will be used in the following to distinguish between the interior and the exterior of a body. Penetration then occurs, if a part of the slave contact surface $\partial\mathcal{B}_c^S$ is located in the interior of $\mathcal{B}^M$. This part of both

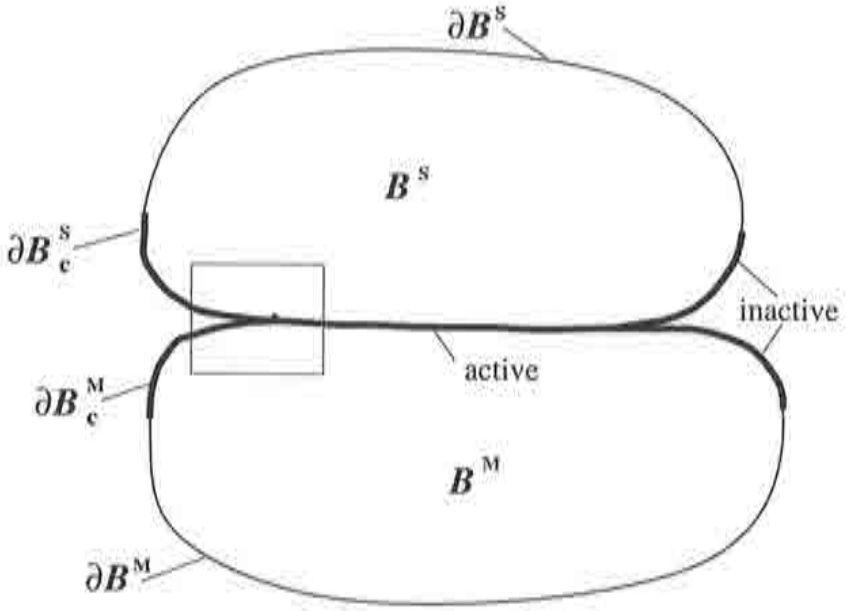

Figure 5.1: Master-Slave contact

boundaries that penetrates or touches the other body is referred to as the active part of the contact surfaces $\partial\mathcal{B}_c^{M^*}, \partial\mathcal{B}_c^{M^*}$.
For completion it shall be mentioned, that the following relations hold:

$$\mathcal{B} = \mathcal{B}^M \cup \mathcal{B}^S \qquad \partial\mathcal{B} = \partial\mathcal{B}^M \cup \partial\mathcal{B}^S$$
$$\partial\mathcal{B}_c = \partial\mathcal{B}_c^M \cup \partial\mathcal{B}_c^S \qquad \partial\mathcal{B}_c^* = \partial\mathcal{B}_c^{M^*} \cup \partial\mathcal{B}_c^{S^*}$$

Zooming into the contact as indicated by the rectangular in figure 5.1 shows the penetration of a slave node into the master body, see figure 5.2.
Both contact surfaces $\partial\mathcal{B}_c^M$ and $\partial\mathcal{B}_c^S$ are discretized with nodes and interpolation functions. For a given slave node $\mathbf{x}^S$ on $\partial\mathcal{B}_c^S$ the distance function to the parameterized master surface $\mathbf{x}^M(\xi_\alpha, t)$ is defined as

$$d(\xi_\alpha, t) = \|\mathbf{x}^S - \mathbf{x}^M(\xi_\alpha, t)\| \quad \text{with} \quad \alpha = 1, 2. \tag{5.1}$$

The adjacent master point $\mathbf{x}^M(\overline{\xi}_\alpha, t)$ for the slave point $\mathbf{x}^S$ can be found minimizing the distance function

$$d(\xi_\alpha, t) = \|\mathbf{x}^S - \mathbf{x}^M(\xi_\alpha, t)\| \longrightarrow MIN, \tag{5.2}$$

where $\overline{\xi}_\alpha$ denote the values of the parameterization for the minimal distance. In the following all variables with an over-line refer to the adjacent master point for a given slave node $\mathbf{x}^S$, so that $\overline{\mathbf{n}}$ and $\overline{\mathbf{a}}_\alpha$ are the normal and tangent vector in $\overline{\mathbf{x}}^M = \mathbf{x}^M(\overline{\xi}_\alpha, t)$. Equation (5.2) then yields the necessary condition

$$\frac{d}{d\xi_\alpha} d(\xi_\alpha, t) = \frac{\mathbf{x}^S - \mathbf{x}^M(\xi_\alpha, t)}{\|\mathbf{x}^S - \mathbf{x}^M(\xi_\alpha, t)\|} \mathbf{x}^M_{,\alpha}(\xi_\alpha) = 0. \tag{5.3}$$

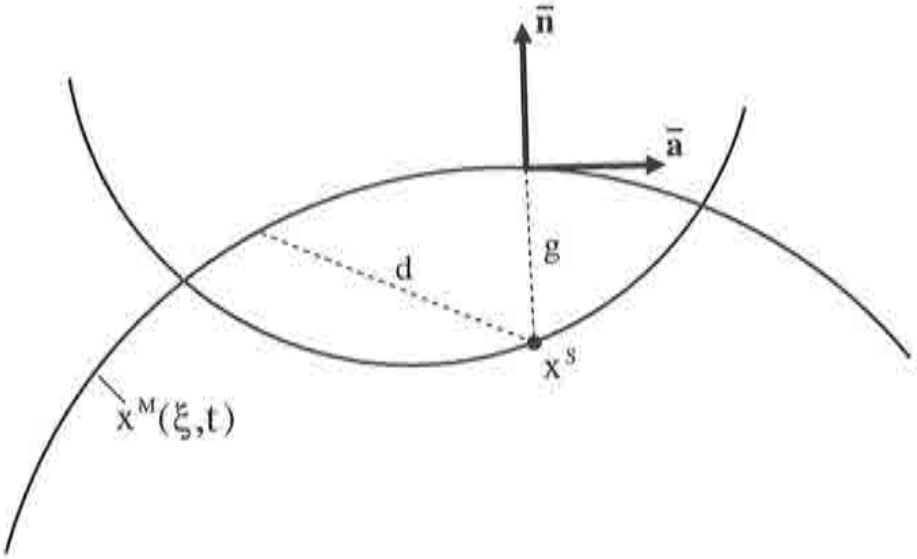

Figure 5.2: Contact kinematics

In order to be equal to 0 the first and the second term in (5.3) have to be orthogonal. Since $\mathbf{x}^M_{,\alpha}(\xi_\alpha)$, the derivatives of the master surface with respect to the parameterization variables ξ_α, are the tangent vectors $\mathbf{a}^M_\alpha$, the first term must be the normal vector $\mathbf{n}^M$, which reads as $\mathbf{n}^M \cdot \mathbf{a}^M_\alpha = 0$. This means that the adjacent master point $\mathbf{x}^M$ is the orthogonal projection of $\mathbf{x}^S$ onto the master surface $\partial\mathcal{B}^M_c$. The convective coordinate system in $\overline{x}^M$ can be calculated through

$$\bar{\mathbf{a}}_\alpha = \mathbf{x}_{,\alpha}(\bar{\xi}_\alpha, t) \quad , \quad \bar{\mathbf{n}} = \frac{\bar{\mathbf{a}}_1 \times \bar{\mathbf{a}}_2}{\|\bar{\mathbf{a}}_1 \times \bar{\mathbf{a}}_2\|}. \tag{5.4}$$

Now the local gap function g_N can be introduced, which permits to distinguish between the different contact states:

$$g_N = \left[\mathbf{x}^S - \bar{\mathbf{x}}^M\right] \cdot \bar{\mathbf{n}} \tag{5.5}$$

If g_N is positive the bodies are separated, no contact occurs in this point. Equality to 0 means that the surfaces are in touch, and a negative value is obtained if penetration takes place.

$$g_N \begin{cases} > 0 & \text{Separation} \\ = 0 & \text{Contact} \\ < 0 & \text{Penetration} \end{cases} \tag{5.6}$$

In the geometrical contact formulation it is required that no penetration occurs, which results in the kinematical constraint

$$g_N \geq 0. \tag{5.7}$$

A penetration function g_N^+, suitable for the incorporation of constraint (5.7) in the global system of equation with the penalty method is then

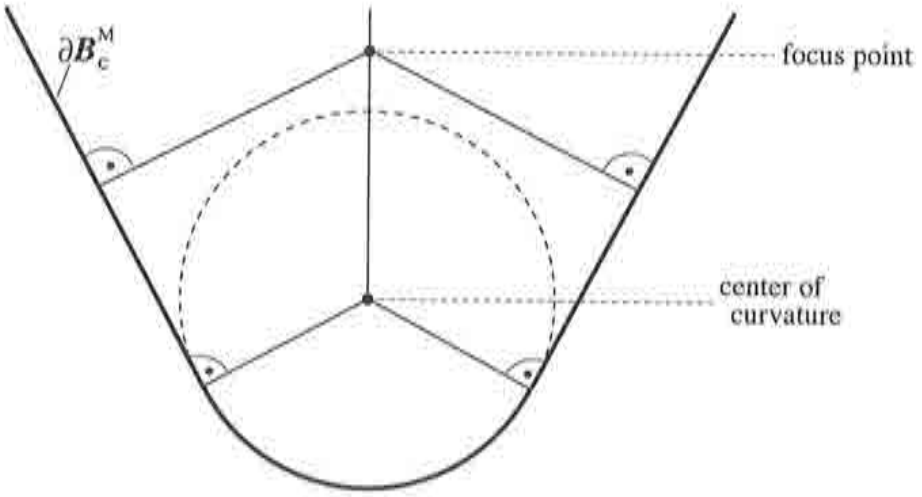

Figure 5.3: Uniqueness of the projection

$$g_N^+ = \begin{cases} |g_N| & \text{for} \quad g_N < 0 \\ 0 & \text{else} \end{cases} \tag{5.8}$$

Complications of the master–slave concept are to be expected, when the projection of the slave node into the master surface is not unique. In [Curnier et al., 1994] some criteria are developed regarding the transformation of the slave surface into line elements on the master surface. The results are illustrated in figure 5.3. The projection is not unique, if the slave node is a center of curvature of the master surface or a focus point, which means an intersection point of equally long normal vectors.

Remark: The formulation given above leads to a purely geometrical constraint. The requirement of non-penetration has to be seen as an idealization, because even experiments prove, that in a microscopic scale tiny penetrations occur. In the numerical simulation tiny penetrations are inevitable, if e.g. a penalty formulation is used to add the contact constraints.

5.2 Contact pressure

According to the basic axiom of Newton where actio equals reactio, for the infinitesimal force vectors in the contact zone equation (5.9) holds.

$$\mathbf{t}^S da^S = -\bar{\mathbf{t}}^M d\bar{a}^M \tag{5.9}$$

In the active areas $\partial\mathcal{B}_c^{M*}$ and $\partial\mathcal{B}_c^{S*}$ the contact surfaces are equal $da^S = d\bar{a}^M$, so that equation (5.9) can be rewritten as

$$\mathbf{t}^S = -\bar{\mathbf{t}}^M. \tag{5.10}$$

In the non-active regions $\partial\mathcal{B}_c^M \backslash \partial\mathcal{B}_c^{M*}$ and $\partial\mathcal{B}_c^S \backslash \partial\mathcal{B}_c^{S*}$ the surface stresses are equal to zero $\mathbf{t}^S = \bar{\mathbf{t}}^M = 0$. With the master body defining the reference system the contact stress vector $\bar{\mathbf{t}} = \mathbf{t}^M$ can now be split in a normal and a tangent part:

$$\mathbf{t} = \underbrace{t_N \, \overline{\mathbf{n}}}_{\text{normal}} + \underbrace{t_\alpha \, \overline{\mathbf{a}}_\alpha}_{\text{tangent}} \tag{5.11}$$

The assumption of a frictionless contact leads to the simplification that the tangent stresses are zero $\mathbf{t}_\alpha = \mathbf{0}$. Furthermore the condition that no adhesive stresses are allowed in this contact model results in $t_N \leq 0$. The normal contact stress is equal to the contact pressure $t_N = p_N$. Equation (5.11) then reduces to

$$\mathbf{t} = p_N \overline{\mathbf{n}}. \tag{5.12}$$

The well known Kuhn-Tucker conditions for frictionless contact problems (5.13) provide the basis for the mathematical treatment of the constraint optimization problem.

$$-g_N^+ \leq 0 \quad , \quad p_N \leq 0 \quad , \quad p_N g_N^+ = 0 \tag{5.13}$$

Constitutive equations

During the whole contact formulation a smooth contact surface was assumed. Real surfaces however are rough. In a microscopic scale they contain asperities, which form a smooth surface in the macroscopic scale, where a statistical averaging process over the asperities is made. The macroscopic contact surface may differ substantially from the microscopic one. If contact occurs, those microasperities deform, a smoothing and a tiny penetration takes place. A constitutive law for this zone relates the average contact pressure to a geometrical variable. An overview of those laws can be found in [Song and Yovanovich, 1987]. Typically potential laws are postulated as in equation (5.14), which is taken from [Kragelski et al., 1982].

$$\mathbf{t}_N = -c_N |g_N^+|^m \tag{5.14}$$

The material parameters c_N and m have to be determined experimentally. According to [Oden and Martins, 1985] m ranges between $2 \leq m \leq 3.33$.

Remark: In coupled thermo-mechanical problems the contact pressure is of crucial importance, because the heat conduction depends on it. [Zavarise et al., 1992] used an exponential law for the modeling. For the primary goal of the non-penetration enforcement a simple contact law as in equation (5.14) with $m = 1$ is sufficient. Section 5.4.2 will show that such a law equals the constraint to be used in the penalty formulation.

5.3 Incorporation of the contact constraints

The incorporation of the inequality contact constraints into the variational formulation is a constrained optimization problem, the mathematics of which is described in detail in [Bertsekas, 1982] and [Luenberger, 1992]. Formally the variational equation (4.5) with the solid terms G_S is extended by the addition of contact terms G_C.

$$G = G_S + G_C \tag{5.15}$$

For the precedential potential Π, from which G is derived, this means that

$$\Pi = \Pi_S + \Pi_C \qquad \text{with} \quad \delta\Pi = G. \tag{5.16}$$

In the case of a permanent contact with a priori knowledge of contact surfaces those terms adopt a form similar to boundary conditions, e.g. (5.17).

$$G = G_S + \underbrace{\int_{\partial B_C} p_N \, \delta g_N \, dA}_{\text{contact terms } G_C} \tag{5.17}$$

Generally the contact zone is unknown and has to be determined during the iteration process, which means that it is subjected to constant changes.

5.4 Solution methods for constrained optimization problems

Equation (4.5) in combination with (5.7) is a nonlinear constrained optimization problem of the general mathematical form (A.1), see appendix A for the mathematical framework.

Among the solution methods for this problem type it can be distinguished between different groups. There are first of all the primal methods. They depart from a feasible starting point in a direction, where the objective function decreases until an optimal solution is obtained. Thereby it must be assured at each step, that the path remains in the feasible region. The *feasible direction method*, the *gradient projection method* and the *reduced gradient method* are examples of primal methods.

The *penalty* and *barrier* methods, the second type, will be treated here in more detail due to their importance in numerical contact mechanics. They aim at regularizing the problem by adding the constraints to the potential and approximating so the constrained optimization problem by an unconstrained optimization problem.

The third group are the dual methods named like this, because they try to solve the dual problem of equation (A.2) with the Lagrange multipliers. *Cutting plane methods* and the *Augmented Lagrange method* are examples for those.

The last type are the *Lagrange methods* that aim at solving the first–order necessary condition directly. Mostly this is done by extending the conjugated gradient method or the Newton method.

The last section dealing with solution methods is dedicated to some minor important approaches. They consist partially of a combination of two methods, with the objective to overcome the restrictions and disadvantages of each one individually.

Comparing the notation of the mathematical definitions in the appendix A with the notation of this chapter it should be paid attention to the fact, that although inequality constraints are denoted with a g in both cases they are formulated as $\mathbf{g} \leq \mathbf{0}$ in the mathematical section and as $\mathbf{g_N} \geq 0$ otherwise.

5.4.1 The Lagrange multiplier method

In the Lagrange multiplier method the constraints are added with a multiplier λ_N to the potential as shown for one constraint in equation (5.18). This means basically, that the first order necessary condition (A.2) is solved directly:

$$\Pi = \Pi_S - \int_{\partial B_C} \lambda_N g_N^+ \, dA \longrightarrow MIN \tag{5.18}$$

For the variational equation (5.15) this term is calculated in a straightforward manner (5.19). The necessary Kuhn-Tucker conditions for this case are given in (5.13).

$$G_C = - \int_{\partial B_C} \lambda_N \delta g_N^+ \, dA \tag{5.19}$$

Special care has to be taken, because the inequality constraint is represented as equality constraint in (5.19). Doing this generally would mean to force even the inactive contact surfaces to come into contact. To prevent this the active set strategy is introduced. At each iteration step the active contact surface is determined. All the constraints involved therein are set to be equality constraints and are added to (5.15). The inactive constraints are neglected. Now the Lagrange multiplier method is compliant with the first order necessary conditions, since for a multipliers λ_N and the inequalities g_N it can be stated:

Constraint active:	$\lambda_N \geq 0,$	$g_N^+ = 0$
Constraint inactive:	$\lambda_N = 0,$	$- g_N^+ < 0$

Comparing (5.19) to (5.17) the Lagrange multipliers λ_N can be identified as the negative contact pressure.

$$p_N = - \lambda_N \tag{5.20}$$

The major disadvantage of the Lagrange multiplier method is, that the multipliers are additional degrees of freedom. This increases the computational effort, especially since the stiffness matrix of the FEM typically has a band structure, that will be destroyed by the multiplier degrees of freedom. The second disadvantage are zero valued terms on the diagonal of the stiffness matrix when the constraints are fulfilled exactly.

5.4.2 Penalty and Barrier methods

In the penalty method a penalty function $f(g_N^+)$ is added to the potential, when the constraint is violated. Figure 5.4 shows an example. The penalty function is zero as long as the value of u is lesser than u_0. Once this threshold is passed the function grows rapidly. Here too a constant verification of the current contact surface is necessary.
A common choice for the penalty function is a simple quadratic equation as is done in equation (5.21). For the contact terms G_c this means, that the rather simple form of equation (5.22) is obtained.

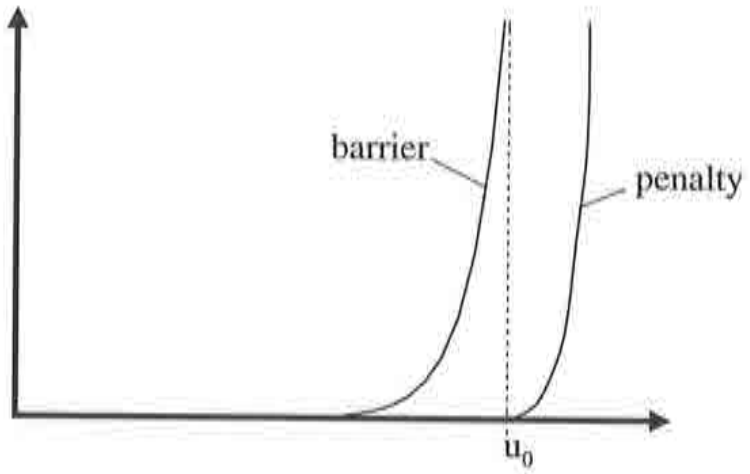

Figure 5.4: Comparison of barrier and penalty method

$$\Pi = \Pi_S + \int_{\partial B_C} \frac{1}{2} \epsilon_N g_N^{+2} \, dA \longrightarrow MIN \tag{5.21}$$

$$G_C = \int_{\partial B_C} \epsilon_N g_N^{+} \delta g_N^{+} \, dA \qquad \text{with} \qquad \epsilon_N > 0 \tag{5.22}$$

A proper choice of the penalty parameter ϵ_N is important for the solution. It can be proved, that for the limit case $\epsilon_N \to \infty$ the solution of (5.21) converges against the exact solution of the constrained variational problem. For infinite values the regularized formulation yields the correct solution. On the other hand a reasonable sized value for ϵ_N is desirable, since otherwise the matrix $\mathbf{K_T}$ becomes ill conditioned. Too big values result in a bad convergence rate or even divergence. Smaller values always are connected with a stronger violation of the constraints. This means, that by applying the penalty method a tiny rest penetration has to be accepted. An ideal value for ϵ_N has about the same size as the tangent stiffness matrix contributions of the elements connected to the contact nodes.

The contact pressure corresponds in this formulation to the product of penalty parameter and penetration function

$$p_N = \epsilon_N \, g_N^{+}. \tag{5.23}$$

The contact regularized this way can be interpreted as a linear constitutive law. Note the equivalence to equation (5.14) with $m = 1$ and $c_N = \epsilon_N$.

The usual strategy when using the penalty method is that in each iteration the active set is verified and changed if necessary. A second method, that will be dealt with in chapter 7 is the converged active set strategy. Here the active set is chosen, when the first constraint is violated and remains fixed until the solution procedure converges. Then the active set is reevaluated and newly iterated until convergence. The final solution is reached, when no changes in the active set have to be made, after an iteration process has converged.

A second form of regularized contact is the formulation of the constraints with barrier functions. A look at figure 5.4 explains the difference. Whereas penalty functions become active only, when the constraint is violated, barrier methods already intervene in the vicinity of the constraint value. The idea is to establish a barrier that grows to infinity the closer the value of u approaches to the limit u_0 and to prevent a passing or a penetration. A problem arises if u passes u_0 in one large step, so that the barrier function cannot activate. Once in the infeasible region on the righthand side of u_0 in diagram 5.4, it is difficult to shift it back into the feasible region.

Both methods do not solve the problem exactly, they only regularize it. On the other side they do not suffer from the disadvantages of the Lagrange multiplier method. The number of unknowns does not increase and no special solvers have to be applied. Especially these facts are the reason, why most of all the penalty method is very popular in contact mechanics. The ease of implementation in FEM codes is a further advantage connected with this.

5.4.3 Augmented Lagrange

The Augmented Lagrange method is basically a combination of the penalty method with the Lagrange multiplier method. Both terms are added to the potential (5.24), the multiplier term and the quadratic penalty function term. The variation gives the necessary condition for the minimum point (5.25).

$$\Pi = \Pi_S - \int_{\partial B_C} \lambda_N g_N^+ \, dA + \int_{\partial B_C} \frac{1}{2} \epsilon_N g_N^{+2} \, dA \longrightarrow MIN \tag{5.24}$$

$$G_C = \int_{\partial B_C} \left[\overline{\lambda}_N + \epsilon_N g_N^+ \right] \delta g_N^+ \, dA \tag{5.25}$$

The multipliers λ_N are no longer additional degrees of freedom, but are treated as constant. They are held constant during an iteration phase until a preliminary convergence is obtained. Then the multipliers are updated and a further iteration loop is computed. This procedure lasts until final convergence is reached. The problem can be regarded as solved, if the update values of the multipliers stay below a certain predefined threshold.

$$\overline{\lambda}_{N_{new}} = \overline{\lambda}_{N_{old}} - \epsilon_N g_{N_{new}}^+ \tag{5.26}$$

Equation (5.26) shows a typical first order update. The penalty terms of the current step are shifted into the multipliers. The multipliers can be interpreted as additional load terms. The advantage of this method compared to a simple penalty method is, that the penalty parameter ϵ_N can be chosen much smaller and ill-conditioning is less likely to occur. In comparison to the Lagrange multiplier method the advantage is a non-augmentation of the equation system. The disadvantage of the Augmented Lagrange method is a higher computational effort created by the second iteration loop.

This method was also applied to mechanical contact problems, but mainly for cases, where the penalty method failed, see e.g. [Wriggers et al., 1985]. If the pure penalty method already gives a satisfactory result, the supplementary computational effort is not justified.

5.4.4 Other methods

A variety of other methods exist besides the ones presented here. Only two more, that have been used for contact problems shall be mentioned briefly. For a more general overview on the subject of constrained optimization it is referred to [Luenberger, 1992].

Cross constraint method

In [Zavarise et al., 1998] the cross constraint method is proposed for contact problems. The idea thereby is to regularize the constraints by a general exponential function:

$$\Pi = \Pi_S + \int_{\partial B_C} (\alpha e^{a g_N} + \beta e^{b g_N}) \, dA \tag{5.27}$$

Visualizing this class of functions in diagram 5.4 they range in between the barrier and the penalty function. The idea is to combine penalty and barrier methods in such a way, that already in the feasible region on the lefthand side vicinity of u_0 a barrier term is established and on the other side a penalty term exists in case the constraint is violated. This way it is achieved, that the minimal point of the unconstrained potential can be exactly shifted to the constraint limit. Moreover the functional remains smooth and the admissible range of the solution is not restricted. To avoid ill-conditioning it can be combined with an augmentation scheme similar to the penalty term in Augmented Lagrange.

Interior point methods

Interior point methods came up in the recent years, delivering astonishingly good results for linear problems. In a second step it was intended to extend those to nonlinear problems, too. In [Christensen et al., 1998] a comparison of a potential reduction interior point method with the standard Newton method was performed. Christensen proved in this paper, that at the present stage of development Newton methods are superior both in robustness and speed.

5.5 Linearization of the contact contributions

The contact term in the global set of equations are given by equation (5.17). The generic variable t_N for the contact stress has to be chosen according to the selected constraint representation of the previous section.

$$G_c = \bigcup_{e=1}^{n_e} \int_{\partial B_e} t_N \, \delta g_N \, dA \tag{5.28}$$

Differentiation with respect to the unknown displacement gives the contributions to the tangent stiffness matrix $\mathbf{K_T}$.

$$\frac{\partial G_c}{\partial \mathbf{u}} = \bigcup_{e=1}^{n_e} \int_{\partial B_c} \left[\frac{\partial t_N}{\partial \mathbf{u}} \, \delta g_N + t_N \frac{\partial (\delta g_N)}{\partial \mathbf{u}} \right] dA. \tag{5.29}$$

On the element level, the contributions can be written as

$$P_c = t_N \, \delta g_N \tag{5.30}$$

$$\frac{\partial P_c}{\partial \mathbf{u}} = \frac{\partial t_N}{\partial \mathbf{u}} \delta g_N + t_N \frac{\partial (\delta g_N)}{\partial \mathbf{u}}. \tag{5.31}$$

Doing the FEM approximation of the integrals by sums over the elements, equations (5.32) and (5.33) are obtained. The sum runs over all the slave nodes n_e.

$$G_c = \bigcup_{e=1}^{n_e} P_{ce} \tag{5.32}$$

$$\frac{\partial G_c}{\partial \mathbf{u}} = \bigcup_{i=1}^{n_e} \frac{\partial P_{ce}}{\partial \mathbf{u}} \tag{5.33}$$

Besides the gap function g_N itself, the variation δg_N is needed. With δg_N in terms of $\delta \mathbf{x}$ this is

$$\delta g_N = \left[\delta \mathbf{x}^S - \delta \overline{\mathbf{x}}^M \right] \cdot \overline{\mathbf{n}} + \underbrace{\left[\mathbf{x}^S - \overline{\mathbf{x}}^M \right]}_{= \overline{\mathbf{n}} \, const} \cdot \delta \overline{\mathbf{n}} \tag{5.34}$$

The second term in (5.34) is a multiple of the product $\delta \overline{\mathbf{n}} \cdot \overline{\mathbf{n}}$ and vanishes, because the variation $\delta \overline{\mathbf{n}}$ is perpendicular to the normal vector $\overline{\mathbf{n}}$. As defined in chapter 2 the current nodal coordinates are related to the reference coordinates by $\mathbf{x} = \mathbf{X} + \mathbf{u}$, which means that the variation of $\mathbf{x}$ is simply $\delta \mathbf{x} = \delta \mathbf{u}$. For the master node $\overline{\mathbf{x}}^M$ the variation is more complicated, see equation (5.36).

$$\delta \mathbf{x}^S \cdot \overline{\mathbf{n}} = \delta \mathbf{u}^S \cdot \overline{\mathbf{n}} \tag{5.35}$$

$$\delta \overline{\mathbf{x}}^M \cdot \overline{\mathbf{n}} = \underbrace{\frac{\partial \overline{\mathbf{x}}^M}{\partial \xi_\alpha} \delta \xi_\alpha \cdot \overline{\mathbf{n}}} + \frac{\partial \overline{\mathbf{x}}^M}{\partial \mathbf{u}} \delta \mathbf{u} \cdot \overline{\mathbf{n}} = \delta \overline{\mathbf{u}}^M \cdot \overline{\mathbf{n}} \tag{5.36}$$

$$= \mathbf{a}_\alpha \, \delta \xi_\alpha \cdot \overline{\mathbf{n}} = 0 \tag{5.37}$$

The first term in (5.36) can be omitted due to the perpendicularity of the normal $\overline{\mathbf{n}}$ to the tangent vectors $\mathbf{a}_\alpha$. The remaining second term is similar to the form of (5.35). Together with (5.34) this leads to equation (5.38) for the variation δg_N.

$$\delta g_N = \left[\delta \mathbf{u}^S - \delta \overline{\mathbf{u}}^M \right] \cdot \overline{\mathbf{n}} \tag{5.38}$$

And finally the last derivative missing is

$$\frac{\partial(\delta g_N)}{\partial \mathbf{u}} = \frac{\partial(\delta \mathbf{u}^M)}{\partial \mathbf{u}} \cdot \overline{\mathbf{n}} - \delta \mathbf{u}^M \cdot \frac{\partial \overline{\mathbf{n}}}{\partial \mathbf{u}}. \tag{5.39}$$

A general formulation of the contact linearization can be found in [Laursen and Simo, 1993].

5.6 Contact discretization

The master and slave contact boundaries have to parameterized. For this purpose the surfaces are interpolated with nodes and interpolation functions. In this section the generalized 3D contact formulation given in the previous sections will be specialized for 2D.

5.6.1 Contact elements

Different types of contact elements exist to implement the master–slave algorithm in the framework of the Finite Element Method. The easiest way is to use a node–to–node element. Prior to the computation a fixed nodal ordering scheme is constructed, where each slave node is bound to a master node. This element can only be used for geometrically linear problems, because a relative tangential movement and large deformations are not allowed in the contact zone.

A slightly better type is the iso-parametric discretization of the contact contribution (beam–to–beam element). Both boundaries are interpolated isoparametrically, using the same shape functions as for the elements in section 4.3. Here also a fixed relation between master and slave nodes is established, so that the same restrictions as for the node–to–node element hold.

Node–to–segment contact

The node–to–segment contact element does not suffer from the restrictions as the other two element types. Large deformations and relative tangential movement are permitted. This element type is used in this thesis and will thus be studied in more detail.
To introduce the geometrical variables figure 5.5 shows one master segment and the adjacent slave node. The interpolation is defined in equation (5.40) by the two nodes $\mathbf{x}_1^M, \mathbf{x}_1^M$ and the linear shape function

$$\mathbf{x}^M(\xi) = \mathbf{x}_1 + (\mathbf{x}_2 - \mathbf{x}_1)\,\xi \qquad \text{with} \quad \xi \in [0,1]. \tag{5.40}$$

In the 2D case only one surface parameter ξ is needed for the discretization. The derivative of the parameterization with respect to this parameter defines the tangent vector $\mathbf{a}$.

$$\overline{\mathbf{a}} = \frac{d\mathbf{x}^M}{d\xi} = \mathbf{x}_2 - \mathbf{x}_1 \tag{5.41}$$

$\overline{\mathbf{a}}$ can be normalized to $\overline{\mathbf{a}}^0 = \frac{\overline{\mathbf{a}}}{l}$ with l being the length of the element $l = \|\mathbf{x}_2 - \mathbf{x}_1\|$. Then the normal vector is obtained by $\overline{\mathbf{n}} = \mathbf{e}_3 \times \overline{\mathbf{a}}^0$. The formula for $\overline{\xi}$ can be deduced from figure 5.5:

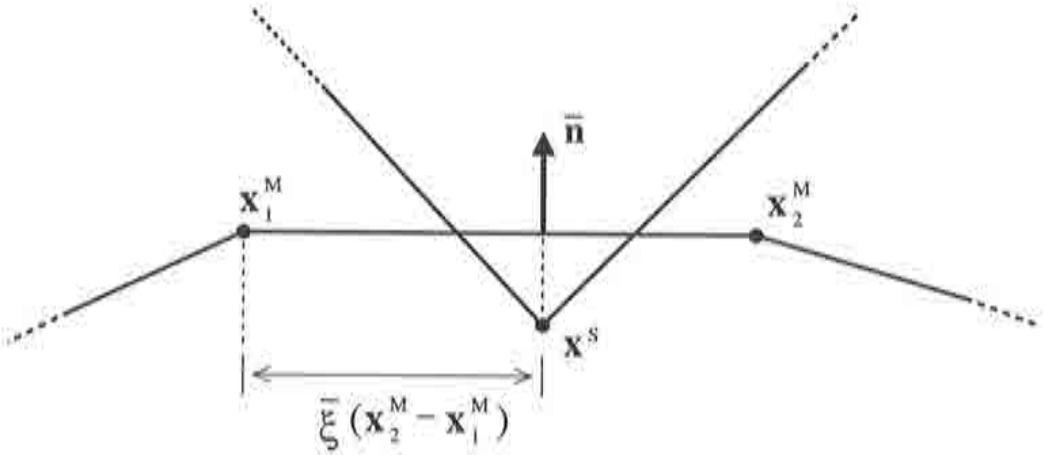

Figure 5.5: Node to segment element

$$\bar{\xi} = \frac{1}{l}(\mathbf{x}_2 - \mathbf{x}_1) \cdot \bar{\mathbf{a}}^0 \tag{5.42}$$

Inserting (5.40) in equation (5.5) together with $\bar{\xi}$ and $\bar{\mathbf{a}}$ from above lead to the gap function (5.43) for the node–to–segment contact and its variation (5.44). The tangent stiffness and residual contributions for this element will be calculated in the next section using the penalty method to regularize the constraints.

$$g_N = \left[\mathbf{x}^S - (1-\bar{\xi})\,\mathbf{x}_1 - \bar{\xi}\,\mathbf{x}_2\right] \cdot \bar{\mathbf{n}} \tag{5.43}$$

$$\delta g_N = \left[\delta\mathbf{v}^S - (1-\bar{\xi})\,\delta\mathbf{v}_1 - \bar{\xi}\,\delta\mathbf{v}_2\right] \cdot \bar{\mathbf{n}} \tag{5.44}$$

The key idea that enables a relative movement of the contact boundaries in this type is, that no mapping is specified a priori to the computation. In each iteration step it has to be checked, if the projection of a slave node $\mathbf{x}^S$ onto a master segment is still appropriate or if it has to be shifted to a different one. However, this comes with a big computational effort , so that a specification of possible contact surfaces $\partial\mathcal{B}_c^M$ and $\partial\mathcal{B}_c^S$ prior to the computation makes sense.

Another way of contact representation is to construct elements connecting both surfaces, which transmit the pressure from one body into the other. See e.g. [Tschöpe, 1996] and [Haraldsson et al., 1997], where the pressure of a fluid is transmitted into a solid this way. Here again a fixed mapping between the adjacent boundaries is a prerequisite.

More sophisticated elements have been developed using polynomial interpolation of the boundaries. See e.g. [Wriggers et al., 1999] for an interpolation with Hermite or Bezier splines. The advantage of those methods is the smoother surface, that can be obtained.

5.6.2 Node–to–segment contact and the penalty method

The contributions to the tangent stiffness matrix $\mathbf{K_T}$ and the residuum $\mathbf{R}$ will be derived in this section for the node–to–segment contact element. The penalty formulation (5.22) is used to add these constraints to the variational form. The g_N are replaced by g_N^+ as

is needed for the active set strategy of the penalty method. As stated in equation (5.23) the pressure in the penalty formulation is $t_N = p_N = \epsilon_N g_n$, so that equations (5.30) and (5.31) evolve to

$$P_c = \epsilon_N g_N^+ \, \delta g_N^+ \tag{5.45}$$

$$\frac{\partial P_c}{\partial \mathbf{v}} = \epsilon_N \left[\frac{\partial g_N^+}{\partial \mathbf{v}} \delta g_N^+ + g_N^+ \frac{\partial (\delta g_N^+)}{\partial \mathbf{v}} \right]. \tag{5.46}$$

Whereas the residual contributions are (5.45), (5.43) and (5.44), the tangent stiffness matrix terms require further discussion. Equation (5.46) contains two derivatives with respect to $\mathbf{v}$ that have to be split up into the nodal displacements $\mathbf{v}^S, \mathbf{v}_1, \mathbf{v}_2$. The individual derivatives then look like:

$$\frac{\partial g_N^+}{\partial \mathbf{v}^S} = \begin{pmatrix} \frac{\partial g_N^+}{\partial v^S{}_1} \\ \frac{\partial g_N^+}{\partial v^S{}_2} \end{pmatrix} = \overline{\mathbf{n}} \quad , \quad \frac{\partial g_N^+}{\partial \mathbf{v}_1} = (\overline{\xi} - 1)\, \overline{\mathbf{n}} \quad , \quad \frac{\partial g_N^+}{\partial \mathbf{v}_2} = -\,\overline{\xi}\, \overline{\mathbf{n}} \tag{5.47}$$

$$\begin{aligned}
\frac{\partial (\delta g_N^+)}{\partial \mathbf{v}^S} &= \mathbf{0} \\
\frac{\partial (\delta g_N^+)}{\partial \mathbf{v}_1} &= \left[\delta \mathbf{v}^S - (1 - \overline{\xi})\, \delta \mathbf{v}_1 - \overline{\xi}\, \delta \mathbf{v}_2 \right] \cdot \frac{\partial \overline{\mathbf{n}}}{\partial \mathbf{v}_1} - \left[\frac{\partial \overline{\xi}}{\partial \mathbf{v}_1} (\delta \mathbf{v}_1 + \delta \mathbf{v}_2) \right] \cdot \overline{\mathbf{n}} \\
\frac{\partial (\delta g_N^+)}{\partial \mathbf{v}_2} &= \left[\delta \mathbf{v}^S - (1 - \overline{\xi})\, \delta \mathbf{v}_1 - \overline{\xi}\, \delta \mathbf{v}_2 \right] \cdot \frac{\partial \overline{\mathbf{n}}}{\partial \mathbf{v}_2} - \left[\frac{\partial \overline{\xi}}{\partial \mathbf{v}_2} (\delta \mathbf{v}_1 + \delta \mathbf{v}_2) \right] \cdot \overline{\mathbf{n}}
\end{aligned}$$

The derivatives of the normal vector $\frac{\partial \overline{\mathbf{n}}}{\partial \mathbf{u}}$ and the surface parameter $\frac{\partial \overline{\xi}}{\partial \mathbf{u}}$ are:

$$\begin{aligned}
\frac{\partial \overline{\mathbf{n}}}{\partial \mathbf{v}_2} &= -\frac{\partial \overline{\mathbf{n}}}{\partial \mathbf{v}_1} = -\frac{1}{l} (\overline{\mathbf{a}} \otimes \overline{\mathbf{n}}) \quad , \quad \frac{\partial \overline{\mathbf{n}}}{\partial \mathbf{v}^S} = \mathbf{0} \\
\frac{\partial \overline{\xi}}{\partial \mathbf{v}_1} &= \frac{1}{l} \left[-(1 - \overline{\xi}) \cdot \overline{\mathbf{a}} - \frac{g_N^+}{l} \overline{\mathbf{n}} \right] \\
\frac{\partial \overline{\xi}}{\partial \mathbf{v}_2} &= \frac{1}{l} \left[-\overline{\xi} \cdot \overline{\mathbf{a}} + \frac{g_N^+}{l} \overline{\mathbf{n}} \right] \\
\frac{\partial \overline{\xi}}{\partial \mathbf{v}^S} &= \frac{1}{l} \overline{\mathbf{a}}
\end{aligned}$$

Putting all these parts together the quite lengthy form of $\frac{\partial P_c}{\partial \mathbf{u}}$ can be assembled. Defining the following vectors the contributions obtain a comparably simple form:

$$\mathbf{N}_0 = \begin{pmatrix} 0 \\ -\overline{\mathbf{n}} \\ \overline{\mathbf{n}} \end{pmatrix}, \qquad \mathbf{N} = \begin{pmatrix} \overline{\mathbf{n}} \\ -(1-\xi)\,\overline{\mathbf{n}} \\ -\xi\,\overline{\mathbf{n}} \end{pmatrix}, \qquad \mathbf{T}_0 = \begin{pmatrix} 0 \\ -\overline{\mathbf{a}} \\ \overline{\mathbf{a}} \end{pmatrix},$$

$$\mathbf{T} = \begin{pmatrix} \overline{\mathbf{a}} \\ -(1-\xi)\,\overline{\mathbf{a}} \\ -\xi\,\overline{\mathbf{a}} \end{pmatrix}, \qquad \delta\mathbf{v}_e = \begin{pmatrix} \delta\mathbf{v}^S \\ \delta\mathbf{v}_1 \\ \delta\mathbf{v}_2 \end{pmatrix}, \qquad {}_{\Delta}\mathbf{v}_e = \begin{pmatrix} {}_{\Delta}\mathbf{v}^S \\ {}_{\Delta}\mathbf{v}_1 \\ {}_{\Delta}\mathbf{v}_2 \end{pmatrix}$$

Then the residual terms are

$$\mathbf{P}_e = \delta\mathbf{v}_e^T \cdot \epsilon_N \, g_N^+ \mathbf{N}, \tag{5.48}$$

and finally the contributions to the tangent stiffness matrix, given already as a product with the displacement increments, have the following form:

$$\frac{\partial \mathbf{P}_e}{\partial \mathbf{v}_e} {}_{\Delta}\mathbf{v}_e = \epsilon_N \delta\mathbf{v}_e^T \cdot \left[\mathbf{N}\mathbf{N}^T - \frac{g_N^+}{l}\left(\mathbf{N}_0\mathbf{T}^T + \mathbf{T}\mathbf{N}_0\right) - \left(\frac{g_N^+}{l}\right)^2 \mathbf{N}_0\mathbf{N}_0^T \right] {}_{\Delta}\mathbf{v}_e \tag{5.49}$$

Chapter 6

Computation of critical points

The subject of this chapter is the computation of critical points on the equilibrium path. These points often described as well as geometrical instability points are associated with radical form changes of the underlying structure in mechanical engineering. Mathematically those points can be identified by certain criteria that can be derived performing a stability analysis of the equilibrium path, which will be done in the first section. In the next section these criteria are exploited further in order to be able to distinguish the different types of instability points. A more thorough examination of the main classification of limit and bifurcation points is made in the third section of this chapter.

Having defined mathematical equations characterizing critical points, methods for their detection can be developed. Generally two types of which exist: Indirect and direct methods. Indirect methods are computed accompanyingly to path following procedures. While the equilibrium path is traced with e.g. arclength at each converged equilibrium point of this computation test functions are evaluated. The results of those test functions give evidence of whether a critical point has been passed or hit in the last load step. For a determination of the critical point with high accuracy a coupling between path tracing and test function has to be established. Direct methods are more or less independent of the path following methods. These try to iterate directly to the critical point during the solution process which is done by including a mathematical condition for critical points as a constraint.

Several methods of both types are treated in this chapter. Special emphasis is put on the *critical displacement method* (CDM) and the *extended system*, which proved to give good results in various publications, see e.g. [Oñate and Matias, 1996] and [Wriggers et al., 1988] respectively.

An additional section is dedicated to branch switching procedures which are necessary in bifurcation points, when a tracing of secondary paths is desired. A reference for this chapter is [Wagner, 1991b] where the whole subject of this chapter is covered. The theory of critical points can be found as well in [Crisfield, 1991b].

6.1 Stability theory

Taking a closer look at the equilibrium path of an arbitrary mechanical structure in figure 6.1, certain points can be observed, where the path has a maximum L_1, minimum L_2 or bifurcates B. Before the mathematical criteria of those critical points can be defined,

a short excursion into stability theory will be made, following the theory presented in [Crisfield, 1991b].

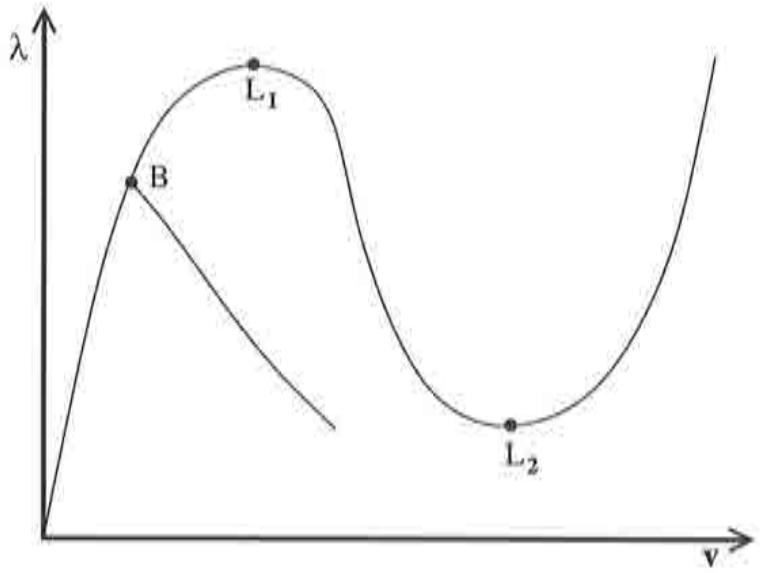

Figure 6.1: Equilibrium path with critical points

The stability analysis bases on the energy potential or functional defined in section 4.2. Starting with the variation of the potential (4.10), a Taylor series expansion for an arbitrary point on the equilibrium path of this variation with a fixed λ yields

$$\delta\,\Pi(\mathbf{u},\lambda) \;=\; \frac{\partial\,\Pi}{\partial\mathbf{u}}\;\delta\mathbf{u} \;+\; \frac{1}{2}\;\delta\mathbf{u}^T\;\frac{\partial^2\,\Pi}{\partial\mathbf{u}^2}\;\delta\mathbf{u} \;+\; O(\delta\mathbf{u}^3). \tag{6.1}$$

Third and higher order terms again are summarized in the term $O(\delta\mathbf{u}^3)$. Replacing the displacement function $\mathbf{u}$ by the FE approximation with the nodal displacement vectors $\mathbf{v}$ equation (6.1) is transfered to the form

$$G(\mathbf{v},\lambda) \;=\; \mathbf{G}^T\cdot\delta\mathbf{v} \;+\; \frac{1}{2}\;\delta\mathbf{v}^T\;\mathbf{K}_T\;\delta\mathbf{v} \;+\; O(\delta\mathbf{v}^3), \tag{6.2}$$

where the relations for the derivatives of $\delta\Pi$ established in chapter 4 have been used. For an equilibrium point the minimization of the energy potential Π is required. The energy change in (6.2) should be stationary which means that

$$\mathbf{G}(\mathbf{v},\lambda) \;=\; 0. \tag{6.3}$$

For a stable equilibrium the change in energy should be positive for any small perturbations $\delta\mathbf{v}$. This is equivalent to the requirement that the second term in (6.2) is greater than zero.

$$\delta\mathbf{v}^T\;\mathbf{K}_T\;\delta\mathbf{v} \;>\; 0 \qquad \forall \quad \delta\mathbf{v} \tag{6.4}$$

Equation (6.4) states that the tangent stiffness matrix $\mathbf{K}_T$ has to be positive definite and has only positive eigenvalues for a stable equilibrium point. In contrast to this an unstable equilibrium point is characterized by the following relationship:

$$\delta \mathbf{v}^T \, \mathbf{K}_T \, \delta \mathbf{v} \; < \; 0 \qquad \text{(unstable)} \tag{6.5}$$

The matrix $\mathbf{K}_T$ is not positive definite and has at least one negative eigenvalue. The neutral state, where the second term in equation (6.2) is equal to zero, is the conditions for critical points $\mathbf{v}_c$.

$$\delta \mathbf{v}^T \, \mathbf{K}_T \, \delta \mathbf{v} \; = \; 0 \qquad \text{for} \quad \delta \mathbf{v}_c \tag{6.6}$$

In this case the tangent stiffness matrix $\mathbf{K}_T$ becomes singular and has a rank deficiency. Formulating this in terms of the eigenvalue problem

$$[\mathbf{K}_T(\mathbf{v}_c) \; - \; \omega \mathbf{I}] \; \boldsymbol{\phi} \; = \; \mathbf{0} \tag{6.7}$$

the smallest eigenvalue becomes zero ($\omega_1 = 0$). Equation (6.7) simplifies to

$$\mathbf{K}_T(\mathbf{v}_c) \; \boldsymbol{\phi} \; = \; \mathbf{0}. \tag{6.8}$$

Another consequence of $\mathbf{K}_T$ becoming singular is that the determinant at a critical point vanishes:

$$\det \mathbf{K}_T(\mathbf{v}_c) \; = \; 0 \tag{6.9}$$

Applying these criteria to the equilibrium path in figure 6.1 means that in B, L_1 and L_2 the tangent stiffness matrix is singular. The paths from the origin to L_1 and to the right of L_2 are stable. The second path branching of in B and the part lying in between L_1 and L_2 are unstable.

In table 6.1 the criteria for the stability analysis of the equilibrium path are summarized.

Equilibrium point	$\mathbf{K}_T$	Eigenvalues	Determinant
Stable	positive definite	all $\omega_i > 0$	$\det \mathbf{K}_T > 0$
Unstable	not positive definite	at least one $\omega_k < 0$	$\det \mathbf{K}_T < 0$
Critical	singular	$\omega_1 = 0$	$\det \mathbf{K}_T = 0$

Table 6.1: Criteria for the stability analysis of the equilibrium path

6.2 Definition of singular points

For a classification of critical points the parameter s indicating the length of the curve is introduced and the quantities displacements $\mathbf{v}$ and load factor λ are expressed in terms of s:

$$\mathbf{v} \; = \; \mathbf{v}(s) \quad , \qquad \lambda \; = \; \lambda(s) \tag{6.10}$$

For the nonlinear equation system $\mathbf{G}$ this parameterization means that

$$\mathbf{G} = \mathbf{G}(\mathbf{v}(s), \lambda(s)) = \mathbf{0}. \tag{6.11}$$

According to the main theorem on implicit functions a solution point of (6.11) is a *regular point* if the inverse $\mathbf{G}_{,\mathbf{v}}(\overline{\mathbf{v}}, \overline{\lambda})^{-1}$ exists. The theorem guarantees furthermore the existence of a local solution path through $(\overline{\mathbf{v}}, \overline{\lambda})$ and the existence of the derivative $\frac{\partial \mathbf{v}}{\partial s}$ that fulfills

$$\frac{\partial \mathbf{G}}{\partial s} = \mathbf{G}_{,\mathbf{v}} \frac{\partial \mathbf{v}}{\partial s} + \mathbf{G}_{,\lambda} \frac{\partial \lambda}{\partial s} \tag{6.12}$$

Points where the main theorem on implicit functions does not hold are called *singular points*. In those points the inverse of $\mathbf{G}_{,\mathbf{v}}(\mathbf{v}_c, \lambda_c)$ does not exist or is singular.

A formulation of the eigenvalue problem for critical points reveals further details. With the left- and right eigenvectors Ψ and ϕ the eigenvalue equations are

$$(\mathbf{G}_{,\mathbf{v}} - \omega_k \mathbf{I})\, \boldsymbol{\phi}_k = \mathbf{0} \quad , \quad (\mathbf{G}_{,\mathbf{v}}^T - \omega_k \mathbf{I})\, \boldsymbol{\Psi}_k = \mathbf{0}. \tag{6.13}$$

The eigenvectors have the orthogonality properties $\boldsymbol{\Psi}_i \cdot \boldsymbol{\phi}_j = \delta_{ij}$. In the most general case of a critical point an m-fold zero eigenvalue has to be expected and for $k = 1, \ldots, m$ the eigenvalue equations are

$$\mathbf{G}_{,\mathbf{v}}\, \boldsymbol{\phi}_k = \mathbf{0} \quad , \quad \boldsymbol{\Psi}_k^T\, \mathbf{G}_{,\mathbf{v}} = \mathbf{0}. \tag{6.14}$$

Multiplying now the tangent $\frac{\partial \mathbf{G}}{\partial s}$ of equation (6.12) with the left eigenvectors $\boldsymbol{\Psi}_k$ yields

$$\boldsymbol{\Psi}_k^T\, [\mathbf{G}_{,\mathbf{v}}\, \mathbf{v}_{,s} + \mathbf{G}_{,\lambda}\, \lambda_{,s}] = \mathbf{0},$$

which simplifies when relation (6.14) is used:

$$\boldsymbol{\Psi}_k^T\, \mathbf{G}_{,\lambda}\, \lambda_{,s} = \mathbf{0} \tag{6.15}$$

Equation (6.15) has to hold in a critical point and gives the main criteria for a distinction of *bifurcation points* and *limit points*. A case study for the eigenvectors belonging to the smallest eigenvalue identifies the two possibilities:

$$\begin{array}{lll} \lambda_{,s} \neq 0 \quad , \quad \boldsymbol{\Psi}_1^T \mathbf{G}_{,\lambda} = 0 & \text{bifurcation point} \\ \lambda_{,s} = 0 \quad , \quad \boldsymbol{\Psi}_1^T \mathbf{G}_{,\lambda} \neq 0 & \text{limit point} \end{array}$$

For an even more exact classification of critical points the second derivative of $\mathbf{G}$ with respect to s is necessary.

$$\frac{\partial^2 \mathbf{G}}{\partial s^2} = \mathbf{G}_{,\mathbf{vv}} \left(\frac{\partial \mathbf{v}}{\partial s}\right)^2 + 2\mathbf{G}_{,\mathbf{v}\lambda} \frac{\partial \mathbf{v}}{\partial s} \frac{\partial \lambda}{\partial s} + \mathbf{G}_{,\mathbf{v}} \frac{\partial^2 \mathbf{v}}{\partial s^2} + \mathbf{G}_{,\lambda\lambda} \left(\frac{\partial \lambda}{\partial s}\right)^2 + \mathbf{G}_{,\lambda} \frac{\partial^2 \lambda}{\partial s^2} \tag{6.16}$$

According to [Wagner, 1991b] the general solution of (6.12) has the form (6.17) with m being the multiplicity of the zero eigenvector of (6.13).

$$\frac{\partial \mathbf{v}}{\partial s} = \frac{\partial \lambda}{\partial s} \mathbf{v}_0 + \sum_{k=1}^{m} \alpha_k \mathbf{v}_k \tag{6.17}$$

Bifurcation and limit points are differentiated further in the next sections, a graphical illustration of all the types of critical points is then shown in figure 6.2.

Remark: The fact that $\mathbf{G}_{,\mathbf{v}}(\mathbf{v}_c, \lambda_c) = \mathbf{K}_T(\mathbf{v}_c, \lambda_c)$ becomes singular in the critical point has consequences for the Newton–Raphson algorithm. It is not possible to solve (4.31) in the critical point. With the by one equation augmented system of the arclength method (4.34) the condition that $\Psi_1^T \mathbf{G}_{,\lambda} \neq 0$ at limit points guarantees a regularity of the augmented stiffness matrix on the left hand side of (4.34). A solution of (4.34) in limit points is possible, whereas at bifurcation points the stiffness matrix remains singular. Using the partitioning algorithm of table 4.2 however, destroys the regularity that arises from the augmentation of the equation system. Nevertheless practical experience showed that in numerical computations the critical point was almost never encountered exactly due to inevitable numerical inexactitudes.

6.2.1 Bifurcation points

The fundamental relations that hold in bifurcation points are $\lambda_{,s} \neq 0$ and $\Psi_1^T \mathbf{G}_{,\lambda} = 0$. With the general solution (6.17) equation (6.12) can be separated in two equations.

$$\begin{aligned} \mathbf{G}_{,\mathbf{v}}\ \mathbf{v}_0 &= -\mathbf{G}_{,\lambda} \quad &\Longrightarrow \quad \mathbf{v}_0 &= -\mathbf{G}_{,\mathbf{v}}^{-1}\mathbf{G}_{,\lambda} \\ \mathbf{G}_{,\mathbf{v}}\ \mathbf{v}_k &= -\mathbf{0} \quad &\Longrightarrow \quad \mathbf{v}_k &= -\boldsymbol{\phi}_k \end{aligned}$$

From the second equation it follows, that the general solution for bifurcation points is

$$\frac{\partial \mathbf{v}}{\partial s} = \frac{\partial \lambda}{\partial s}\mathbf{v}_0 + \sum_{k=1}^{m} \alpha_k \boldsymbol{\phi}_k \qquad \text{with} \quad \alpha_k \in \mathbb{R}. \tag{6.18}$$

Focusing now on a single instead of a multiple bifurcation point the sum vanishes and only the first term remains. ($\alpha = \alpha_1$)

$$\frac{\partial \mathbf{v}}{\partial s} = \frac{\partial \lambda}{\partial s}\mathbf{v}_0 + \alpha\boldsymbol{\phi} \tag{6.19}$$

For the classification of the types of single bifurcation points the second derivative of $\mathbf{G}$ (6.16) is multiplied by the left eigenvector Ψ. Together with $\Psi^T \mathbf{G}_{,\mathbf{v}} = \mathbf{0}$ and $\Psi^T \mathbf{G}_{,\lambda} = \mathbf{0}$ this results in

$$\Psi^T\ \mathbf{G}_{,\mathbf{v}\mathbf{v}} \left(\frac{\partial \mathbf{v}}{\partial s}\right)^2 + 2\Psi^T\ \mathbf{G}_{,\mathbf{v}\lambda} \frac{\partial \mathbf{v}}{\partial s}\frac{\partial \lambda}{\partial s} + \Psi^T\ \mathbf{G}_{,\lambda\lambda} \left(\frac{\partial \lambda}{\partial s}\right)^2 = 0. \tag{6.20}$$

Using equation (6.19) a quadratic equation for $\frac{\partial \lambda}{\partial s}$ is obtained. Introducing the following variables

$$\begin{aligned} a &= \Psi^T \left[(\mathbf{G}_{,\mathbf{v}\mathbf{v}}\boldsymbol{\phi})\,\boldsymbol{\phi}\right], \\ b &= \Psi^T \left[(\mathbf{G}_{,\mathbf{v}\mathbf{v}}\mathbf{v}_0 + \mathbf{G}_{,\mathbf{v}\lambda})\,\boldsymbol{\phi}\right], \\ c &= \Psi^T \left[(\mathbf{G}_{,\mathbf{v}\mathbf{v}}\mathbf{v}_0)\,\mathbf{v}_0 + 2\,\mathbf{G}_{,\mathbf{v}\lambda}\mathbf{v}_0 + \mathbf{G}_{,\lambda\lambda}\right], \\ D &= b^2 - ac, \end{aligned}$$

the solution formula for quadratic equations can be applied:

$$\left(\frac{\partial\lambda}{\partial s}\right)_{1,2} = -\frac{b\,\alpha}{c} \pm \frac{\alpha}{c}\sqrt{b^2 - ac} = -\frac{b\,\alpha}{c} \pm \frac{\alpha}{c}\sqrt{D} \tag{6.21}$$

Depending on the sign of the discriminant D a classification of single bifurcation points can be performed now. For the case of $D > 0$ under the additional assumptions that $b \neq 0$ and $c \neq 0$ it can be distinguished between *symmetric bifurcation points* ($a = 0$) and *asymmetric bifurcation points* ($a \neq 0$). If $D = 0$ the square root has only one solution and a *cusp point* is obtained. For $D < 0$ the solution of the square root is complex, which is the characteristic of an *isolated point*. In the following table 6.2 these cases are summarized in an overview:

$\Psi^T \mathbf{G}_{,\lambda} = 0,\ D > 0$	symmetric bifurcation point	$a = 0, b \neq 0, c \neq 0$
	asymmetric bifurcation point	$a \neq 0, b \neq 0, c \neq 0$
$\Psi^T \mathbf{G}_{,\lambda} = 0,\ D = 0$	cusp point	
$\Psi^T \mathbf{G}_{,\lambda} = 0,\ D < 0$	isolated point	

Table 6.2: Types of single bifurcation points

In literature those critical points sometimes have been named differently. Points with $D > 0$ are named simple transcritical bifurcation points in [Jepson and Spence, 1985]. The name simple pitchfork bifurcation point for a symmetric bifurcation point is rather common, too. A distinction into stable and unstable symmetric bifurcation points can be made as well, see figure 6.2. The name simple isola formation point can be found in [Jepson and Spence, 1985] for an isolated point. A more thorough discussion of all the cases can be found in [Wagner, 1991b], serving as well as references to additional literature covering this subject.

6.2.2 Limit points

Limit points are extremal points of the equilibrium path characterized by the relations $\lambda_{,s} = 0$ and $\Psi_1^T \mathbf{G}_{,\lambda} \neq 0$. The general solution (6.17) simply reduces to

$$\frac{\partial \mathbf{v}}{\partial s} = \alpha \boldsymbol{\phi}_1 \tag{6.22}$$

with only the first term of the sum remaining ($\alpha = \alpha_1$). The multiplication of (6.16) with the left eigenvector Ψ together with (6.22) yields

$$\Psi^T\ \mathbf{G}_{,\mathbf{v}\mathbf{v}} \left(\frac{\partial \mathbf{v}}{\partial s}\right)^2 + \Psi^T\ \mathbf{G}_{,\lambda} \frac{\partial^2 \lambda}{\partial s^2} = 0. \tag{6.23}$$

With simple arithmetic this equation can be solved for $\frac{\partial^2\lambda}{\partial s^2}$.

$$\frac{\partial^2 \lambda}{\partial s^2} = -\alpha\, \frac{\Psi^T \mathbf{G}_{,\mathbf{v}\mathbf{v}} \boldsymbol{\phi}\, \boldsymbol{\phi}}{\boldsymbol{\phi}^T \mathbf{G}_{,\lambda}} = -\alpha\, e \tag{6.24}$$

Here too, a case study for the sign of e has to be performed. A *maximum point* is obtained for $e < 0$. If $e > 0$ the path goes through a *minimum point*. For the nominator in (6.24) to become zero giving $e = 0$ the third derivative of λ with respect to s is needed. If $\frac{\partial^3 \lambda}{\partial s^3} \neq 0$ the critical point is a *saddle point*. The following table 6.3 shows the different possibilities for limit points in an overview.

$\Psi^T \mathbf{G}_{,\lambda} \neq 0,\ e < 0$	maximum point
$\Psi^T \mathbf{G}_{,\lambda} \neq 0,\ e < 0$	minimum point
$\Psi^T \mathbf{G}_{,\lambda} \neq 0,\ e = 0$	saddle point ($\frac{\partial^3 \lambda}{\partial s^3} \neq 0$)

Table 6.3: Types of limit points

6.3 General methods

Several methods have been proposed in literature to detect instability points. They are mostly indirect methods.

Limit load analysis

The classical *limit load analysis* aims at solving the eigenvalue problem in an equilibrium point. Using equation (6.7) yields

$$[\mathbf{K}_T(\mathbf{v}) - \varpi \mathbf{I}]\ \boldsymbol{\phi} = \mathbf{0} \tag{6.25}$$

which can be solved for the unknown eigenvalue ϖ and the eigenvector $\boldsymbol{\phi}$. (6.7) is a special eigenvalue problem with the second matrix being the unit matrix $\mathbf{I}$ needing lesser computational effort as a general eigenvalue problem.

A second eigenvalue problem for critical points known as classical non–linear buckling analysis is derived by exploiting the split of the tangent stiffness matrix $\mathbf{K}_T$ described in (4.25).

$$\mathbf{K}_T = \mathbf{K}_L + \mathbf{K}_U + \mathbf{K}_\sigma$$

Without mathematical reason a load factor $\overline{\lambda}$ is introduced and the following eigenvalue problem is formulated:

$$\left[\mathbf{K}_L + \mathbf{K}_U + \overline{\lambda}\mathbf{K}_\sigma\right]\ \boldsymbol{\phi} = \mathbf{0} \tag{6.26}$$

Besides (6.26) another form using the split of the tangent stiffness matrix can be constructed with

$$\left[\mathbf{K}_L + \overline{\lambda}(\mathbf{K}_U + \mathbf{K}_\sigma)\right]\ \boldsymbol{\phi} = \mathbf{0}. \tag{6.27}$$

Since both (6.26) and (6.27) are general eigenvalue problems they are more difficult to solve than (6.7). Moreover they require a special solver since the matrices $\mathbf{K}_U$ and $\mathbf{K}_\sigma$

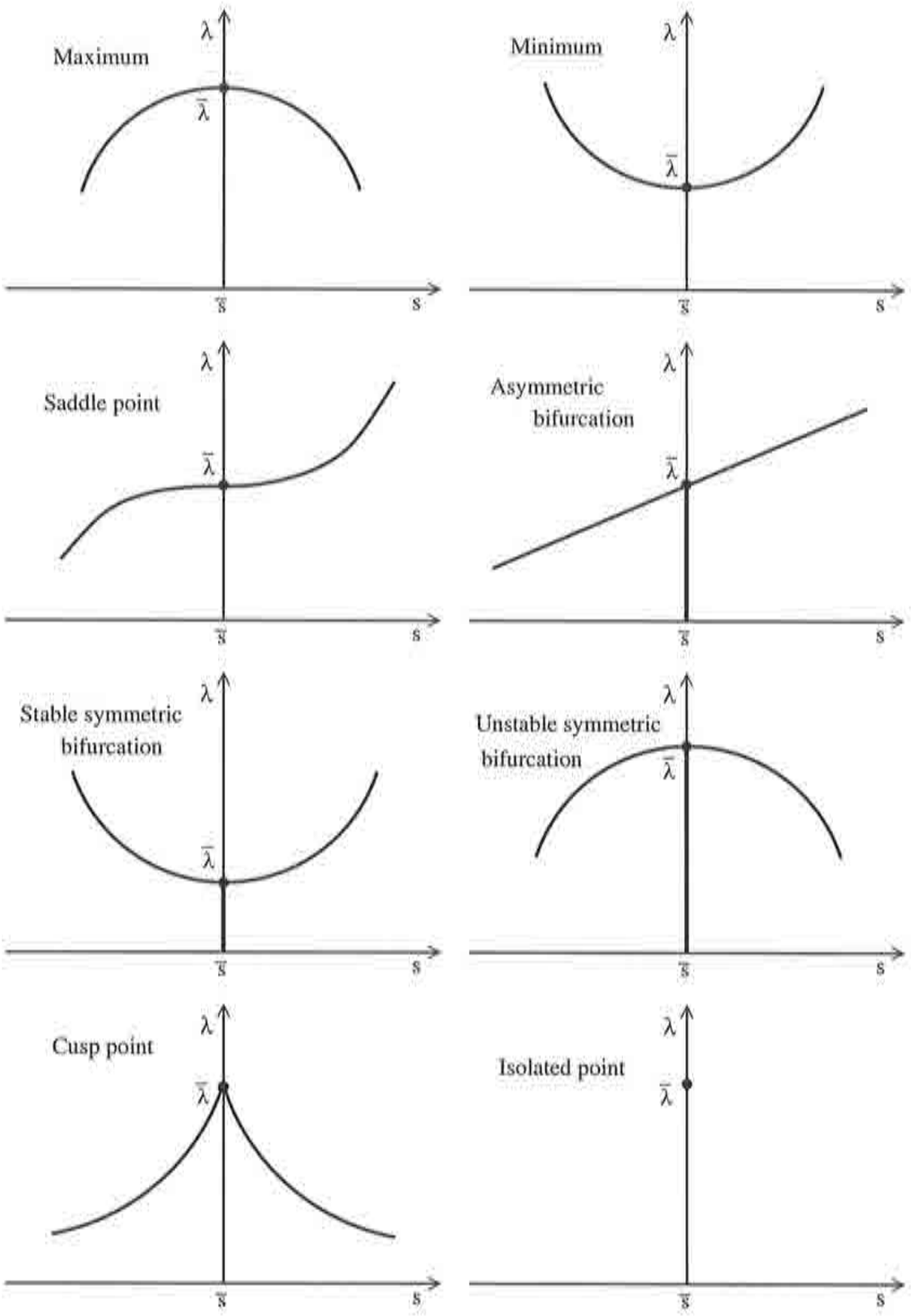

Figure 6.2: Types of critical points

are not necessarily positive definite. From the practical point of view the implementation of this algorithm is aggravated by the fact that the split (4.25) is usually not made when the tangent stiffness matrix is assembled. A solution procedure for eigenvalue problems is given in appendix B.

Linearizing the matrices $\mathbf{K}_U$ and $\mathbf{K}_\sigma$ and neglecting second order terms in (6.26) and (6.27) leads to the classical linear limit load analysis.

Comparing (6.26) and (6.27) with the standard eigenvalue problem for critical points (6.7) the behavior for the limit case is obtained.

$$\lim_{\mathbf{v}\to\mathbf{v}_c} \overline{\lambda}(\mathbf{v}) = \overline{\lambda}_c = 1 \qquad \lim_{\mathbf{v}\to\mathbf{v}_c} \overline{\omega}(\mathbf{v}) = \overline{\omega}_c = 1$$

This is obvious because in the critical point all eigenvalue problems have to be identical and fulfill (6.7) and (6.8). For $\overline{\lambda} = 1$ the matrix sum on the left side of (6.26) and (6.27) is the tangent stiffness matrix $\mathbf{K}_T$.

Test functions

The detection of critical points with test functions is as well an indirect method. A common choice for the test function is $\det \mathbf{K}_T$. In the solution process of the Newton–Raphson algorithm (4.31) often a diagonal triangularization $\mathbf{K}_T = \mathbf{L}^T\mathbf{D}\mathbf{L}$ is performed. The determinant can then be obtained easily as the product of the diagonal elements of $\mathbf{D}$

$$\det \mathbf{K}_T = \prod_{j=1}^{N} D_{jj}. \tag{6.28}$$

Due to the high values the determinant of larger matrices can assume, it can be scaled calculating the quotient with the value of the first load step:

$$\det \overline{\mathbf{K}}_T = \frac{\det \mathbf{K}_T(\mathbf{v}_t)}{\det \mathbf{K}_T(\mathbf{v}_1)} \tag{6.29}$$

For larger equation systems $\mathbf{G}$ with several thousands of unknowns the value of $\det \mathbf{K}_T$ can exceed the range of the computer. Using the logarithm function this problem is remedied.

$$\det_l \mathbf{K}_T = (-1)^{neg} \log \prod_{j=1}^{N} \|D_{jj}\| = (-1)^{neg} \sum_{j=1}^{N} \log \|D_{jj}\| \tag{6.30}$$

Plotting the value of the determinant during path computation provides additional information on the type of equilibrium point, see table 6.1. Examining the relation of $\det \mathbf{K}_T$ with the diagonal elements D_{jj}

$$\det \mathbf{K}_T \begin{cases} > 0 & \Longrightarrow \quad \forall\, D_{jj} : \; D_{jj} > 0 \\ = 0 & \Longrightarrow \quad \exists\, D_{jj} : \; D_{jj} = 0 \\ < 0 & \Longrightarrow \quad \exists\, D_{jj} : \; D_{jj} < 0 \end{cases}, \tag{6.31}$$

other test functions can be observed. The number of negative diagonal elements can be used for that purpose. Passing a critical point e.g. causes a change of this number. Other possibilities for test functions are the minimal diagonal element $Min(D_{jj})$ and the smallest eigenvalue ω_1 of (6.7) which both become zero at critical points.

Extrapolation methods

Extrapolation methods have to be seen in combination with test functions. With two or more values of test functions e.g. the determinant $\det \mathbf{K}_T$, ideally at least one on each side of the critical point a curve can be constructed. Performing a linear or quadratic interpolation with these points leads to an easy solvable equation that provides a coarse estimation for the critical point and a starting point for the next extrapolation step.

Instead of interpolating or extrapolating a simple bisection algorithm can be used, too. Starting with two points the interval is split into two by computing the middle point. Recursive splitting of the interval where the critical point is located (indicated by the test function) reduces the range and converges against the critical point in the limit case.

6.4 The Critical Displacement Method

The Critical Displacement Method (CDM) was developed recently and evaluated for truss and solid elements, see [Oñate and Matias, 1995] and [Oñate and Matias, 1996]. The method bases on the secant stiffness matrix, which is used to predict first the critical displacements and then the critical load. The first section is thus dedicated to the basics of the secant matrix following [Oñate, 1995] and shows how the approach is embedded in the general field of continuum mechanics and FEM. In the second section then it is described how the secant matrix can be exploited for predictions of critical values according to [Matias, 1996], which is the most detailed work on the subject of the CDM.

6.4.1 Derivation of the secant stiffness matrix

In order to derive the full incremental form of the principle of virtual work an updated configuration of the body $\mathcal{B}$ of chapter 2 is defined. Starting from the current configuration, see figure 6.3, the updated configuration $\mathcal{B}^{t+\Delta t}$ is constructed by setting the displacements $\mathbf{u}^{t+\Delta t}$ equal to

$$\mathbf{u}^{t+\Delta t} = \mathbf{u}^t + {}_{\Delta}\mathbf{u}. \tag{6.32}$$

According to equation (2.13) the Green–Lagrange strain tensor for the updated displacements in componential form is then

$$\mathbf{E}^{t+\Delta t} = \frac{1}{2}\left(Grad\,\mathbf{u}^{t+\Delta t} + Grad^T\mathbf{u}^{t+\Delta t} + Grad^T\mathbf{u}^{t+\Delta t}\,Grad\,\mathbf{u}^{t+\Delta t}\right). \tag{6.33}$$

Substituting the displacements of (6.32) in the Green strain tensor (6.33) the increment ${}_{\Delta}\mathbf{E}$ can be written as the difference of the Green–Lagrange strain tensors of updated and current configuration.

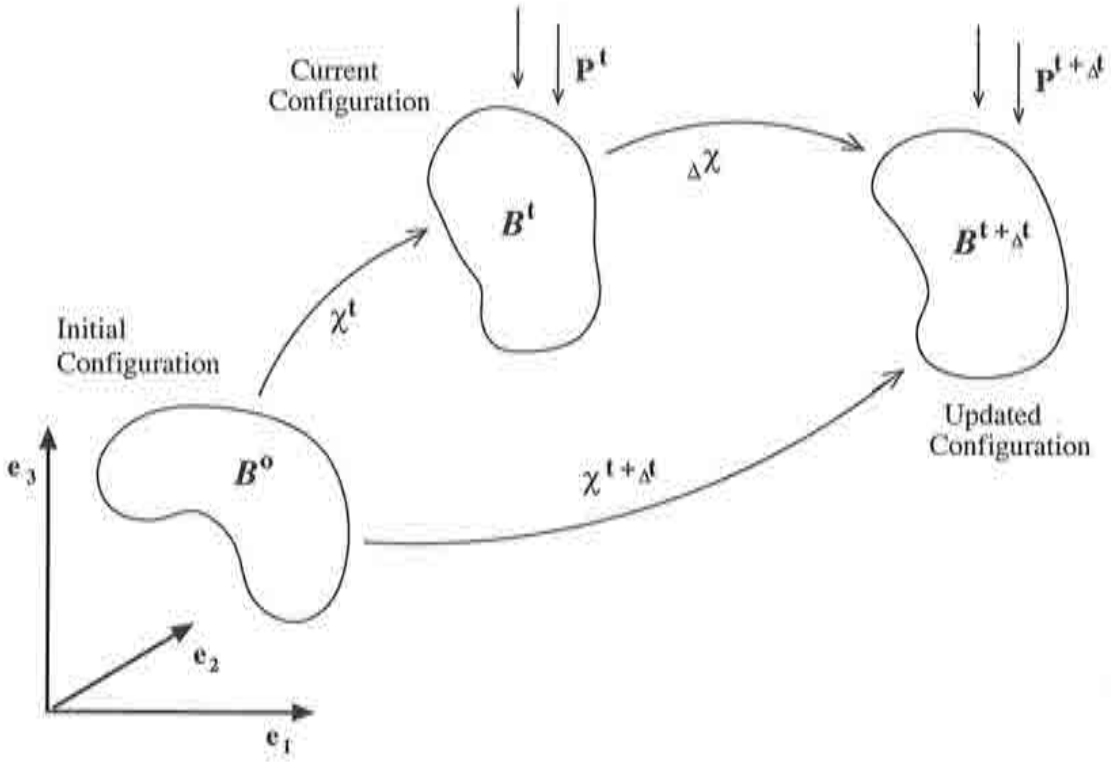

Figure 6.3: Updated configuration

$$ {}_{\Delta}\mathbf{E} = \mathbf{E}^{t+\Delta t} - \mathbf{E}^t = \boldsymbol{\xi} + \boldsymbol{\eta} \tag{6.34} $$

Exploiting the fact that $Grad\ \mathbf{u}^{t+\Delta t} = Grad\ \mathbf{u}^t + Grad_{\Delta}\mathbf{u}$ and sorting the terms in ${}_{\Delta}\mathbf{E}$ according to their dependence on the incremental displacements, the tensors $\boldsymbol{\xi}$ and $\boldsymbol{\eta}$ are obtained. $\boldsymbol{\xi}$ contains the linear terms and $\boldsymbol{\eta}$ the quadratic.

$$ \boldsymbol{\xi} = \frac{1}{2}\left(Grad_{\Delta}\mathbf{u} + Grad^T{}_{\Delta}\mathbf{u} + Grad^T\mathbf{u}^t\ Grad_{\Delta}\mathbf{u} + Grad^T{}_{\Delta}\mathbf{u}\ Grad\ \mathbf{u}^t\right) \tag{6.35} $$

$$ \boldsymbol{\eta} = \frac{1}{2}\ Grad^T{}_{\Delta}\mathbf{u}\ Grad_{\Delta}\mathbf{u} \tag{6.36} $$

Performing similar operations for the virtual displacements, the variation of the Green strain tensor $\delta\mathbf{E}^{t+\Delta t}$ and the increment $\delta_{\Delta}\mathbf{E}$ yield:

$$ \delta\mathbf{E}^{t+\Delta t} = \delta_{\Delta}\mathbf{E} = \delta\boldsymbol{\xi} + \delta\boldsymbol{\eta} \tag{6.37} $$

The displacements u_i^t can be considered as fixed during the deformation increment to the updated configuration and so $\delta\mathbf{u}^t = 0$. The corresponding expressions to (6.35) for $\delta\boldsymbol{\xi}$ and $\delta\boldsymbol{\eta}$ are then

$$\delta\boldsymbol{\xi} = \frac{1}{2}\left(Grad\,\delta_\Delta\mathbf{u} + Grad^T\delta_\Delta\mathbf{u} + Grad^T\mathbf{u}^t\;Grad\,\delta_\Delta\mathbf{u} + Grad^T\delta_\Delta\mathbf{u}\;Grad\,\mathbf{u}^t\right) \tag{6.38}$$

$$\delta\boldsymbol{\eta} = \frac{1}{2}\left(Grad^T\,\delta_\Delta\mathbf{u}\;Grad\,{}_\Delta\mathbf{u} + Grad^T{}_\Delta\mathbf{u}\;Grad\,\delta_\Delta\mathbf{u}\right) \tag{6.39}$$

For the 2. Piola–Kirchhoff stress tensor S_{ij} in the updated configuration the same incremental split as for the displacements can be made.

$$\mathbf{S}^{t+\Delta t} = \mathbf{S}^t + {}_\Delta\mathbf{S} \tag{6.40}$$

An incremental relation between the strain increment and the increment of the 2. Piola–Kirchhoff tensor is then defined as follows. Assuming the St.Venant material law of section 3.2.1 and dropping the subscript, so that $\mathbf{D}\hat{=}\mathbf{D}_{SV}$, results in

$${}_\Delta\mathbf{S} = \mathbf{D}\,{}_\Delta\mathbf{E} = \mathbf{D}\,(\boldsymbol{\xi} + \boldsymbol{\eta}) \tag{6.41}$$

With equations (6.34), (6.37), (6.40) and (6.41) the variational form (4.12) can be rewritten in an incremental form as

$$\begin{aligned}\int_{B_0}[\delta\boldsymbol{\xi}^T\,\mathbf{D}\,\boldsymbol{\xi} + \delta\boldsymbol{\xi}^T\,\mathbf{D}\,\boldsymbol{\eta} + \delta\boldsymbol{\eta}^T\,\mathbf{D}\,\boldsymbol{\xi} + \delta\boldsymbol{\eta}^T\,\mathbf{D}\,\boldsymbol{\eta} + \delta\boldsymbol{\eta}^T\,\mathbf{S}^t]\,dV &= \\ = \int_{B_0}\delta_\Delta\mathbf{u}^T\hat{\mathbf{b}}^{t+\Delta t}\rho_0\,dV + \int_{\partial B_{0\sigma}}\delta_\Delta\mathbf{u}^T\hat{\mathbf{T}}^{t+\Delta t}\,dA - \int_{B_0}\delta\boldsymbol{\xi}^T\,\mathbf{S}^t\,dV.&\end{aligned} \tag{6.42}$$

The integrals on the right hand side of equation (6.42) (second line) do not depend on ${}_\Delta\mathbf{u}$ and do therefore not contribute to the secant stiffness matrix. Only the integral on the left hand side of (6.42) form the secant matrix as the integrands depend at least linearly on the displacement increments ${}_\Delta\mathbf{u}$.

Besides the FEM interpolation for the displacements, displacement gradients and test functions as shown in section 4.3, further interpolations for the displacement increments have to be made:

$${}_\Delta\mathbf{u}^h = \sum_{i=1}^{n_n} N_i\,{}_\Delta\mathbf{v}_i \quad , \quad \delta_\Delta\mathbf{u}^h = \sum_{i=1}^{n_n} N_i\,\delta_\Delta\mathbf{v}_i \tag{6.43}$$

With the shape functions and nodal displacement vectors, the tensors $\boldsymbol{\xi}$ and $\boldsymbol{\eta}$ are rewritten using the $\mathbf{B}$–matrices, which contain the derivatives of the shape functions ∇N_i and nodal displacements $\mathbf{v}^t$ in an order depending on the element theory applied.

$$\boldsymbol{\xi} = \mathbf{B}(\mathbf{v}^t)_\Delta\mathbf{v} = \mathbf{B}^t{}_\Delta\mathbf{v} \quad , \qquad \boldsymbol{\eta} = \frac{1}{2}\mathbf{B}_{1\Delta}\mathbf{v} \tag{6.44}$$

The tensors $\delta\boldsymbol{\xi}$ and $\delta\boldsymbol{\eta}$ in terms of the $\mathbf{B}$–matrices are equal to

$$\delta\boldsymbol{\xi} = \mathbf{B}(\mathbf{v}^t)\delta_\Delta\mathbf{v} = \mathbf{B}^t{}_\Delta\mathbf{v} \quad , \qquad \delta\boldsymbol{\eta} = \mathbf{B}_1\delta_\Delta\mathbf{v}. \tag{6.45}$$

Equations (6.44) and (6.45) can now be inserted in the integrals involving displacement increments on the left hand side of (6.42). According to [Oñate, 1995] these integrands can be transformed after some algebra to

$$\begin{aligned}
\delta\boldsymbol{\xi}^T\mathbf{D}\boldsymbol{\xi} &= \delta_\Delta\mathbf{v}^T[\mathbf{B}^{t^T}\mathbf{D}\mathbf{B}^t]_\Delta\mathbf{v} \\
\delta\boldsymbol{\eta}^T\mathbf{D}\boldsymbol{\xi} + \delta\boldsymbol{\xi}^T\mathbf{D}\boldsymbol{\eta} &= \delta_\Delta\mathbf{v}^T\left[\frac{1}{2}\mathbf{B}^{t^T}\mathbf{D}\mathbf{B}_1 + \alpha\mathbf{B}_1^T\mathbf{D}\mathbf{B}^{t^T} + (1-\alpha)\hat{\mathbf{G}}^T\widetilde{\mathbf{D}}\hat{\mathbf{G}}\right]_\Delta\mathbf{v} \\
\delta\boldsymbol{\eta}^T\mathbf{D}\boldsymbol{\eta} &= \delta_\Delta\mathbf{v}^T\left[\frac{1}{4}(2-\beta)\mathbf{B}_1^T\mathbf{D}\mathbf{B}_1 + \frac{\beta}{4}\hat{\mathbf{G}}^T\widetilde{\mathbf{H}}\hat{\mathbf{G}}\right]_\Delta\mathbf{v} \\
\delta\boldsymbol{\eta}^T\boldsymbol{\sigma}^t &= \delta_\Delta\mathbf{v}^T[\overline{\mathbf{G}}^T\hat{\mathbf{S}}^t\overline{\mathbf{G}}]_\Delta\mathbf{v}.
\end{aligned}$$

The components of the matrix $\hat{\mathbf{G}}$ are derivatives of the shape functions in a special order; in $\widetilde{\mathbf{D}}$ the components of $\mathbf{D}$ are rearranged in a different order. Matrix $\widetilde{\mathbf{H}}$ contains terms quadratic in the displacement increments ${}_\Delta\mathbf{v}$. The detailed form of those matrices can be found in [Oñate, 1995] or [Matias, 1996]. The notation in both works differs slightly from the one here, but it should be no difficulty to relate the corresponding matrices.

Using the equations above and splitting the integral on the left hand side of (6.42), the following four matrices can be assembled from the elemental contributions:

$$\mathbf{K}_{LU} = \bigcup_{e=1}^{n_e}\int_{\Omega^e}\mathbf{B}_L^{t^T}\mathbf{D}\mathbf{B}_L^t\,dV \tag{6.46}$$

$$\mathbf{K}_M({}_\Delta\mathbf{v}) = \bigcup_{e=1}^{n_e}\int_{\Omega^e}\left[\frac{1}{2}\mathbf{B}_L^{t^T}\mathbf{D}\mathbf{B}_1 + \alpha\mathbf{B}_1^T\mathbf{D}\mathbf{B}_L^{t^T} + (1-\alpha)\mathbf{G}^T\widetilde{\mathbf{D}}\mathbf{G}\right]dV \tag{6.47}$$

$$\mathbf{K}_N({}_\Delta\mathbf{v}^2) = \bigcup_{e=1}^{n_e}\int_{\Omega^e}\left[\frac{1}{4}(2-\beta)\mathbf{B}_1^T\mathbf{D}\mathbf{B}_1 + \frac{\beta}{4}\mathbf{G}^T\widetilde{\mathbf{H}}\mathbf{G}\right]dV \tag{6.48}$$

$$\mathbf{K}_\sigma = \bigcup_{e=1}^{n_e}\int_{\Omega^e}\overline{\mathbf{G}}^T\hat{\mathbf{S}}^t\overline{\mathbf{G}}\,dV \tag{6.49}$$

Note, that two arbitrary parameters α and β were introduced in these matrices. A similar form of the secant stiffness matrix involving those parameters was deduced by [Felippa and Crivelli, 1991]. For values of $\alpha \neq \frac{1}{2}$ the incremental secant matrix will be non symmetric. For $\alpha = \frac{1}{2}$ an infinite set of symmetric forms is obtained depending on the values of β. The symmetric expression with $\alpha = \frac{1}{2}$ and $\beta = 0$ was derived by [Oñate, 1991].

The secant stiffness matrix $\mathbf{K}_S$ can now be obtained as the sum of those four matrices (6.46), (6.47), (6.48) and (6.49).

$$\mathbf{K}_S = \mathbf{K}_{LU} + \mathbf{K}_M + \mathbf{K}_N + \mathbf{K}_\sigma \tag{6.50}$$

Neglecting the matrices $\mathbf{K}_M$ and $\mathbf{K}_N$ in (6.50) yields the tangent stiffness matrix $\mathbf{K}_T$. An alternative way is to study the limit case, where the values of ${}_\Delta\mathbf{v}$ tend to zero, so that

$$\mathbf{K}_T = \lim_{\Delta \mathbf{v} \to 0} \mathbf{K}_S = \mathbf{K}_{LU} + \mathbf{K}_\sigma. \tag{6.51}$$

A comparison with the equations of section 4.3, where the tangent stiffness matrix $\mathbf{K}_T$ was derived, confirms that with $\mathbf{K}_{\mathrm{LU}} = \mathbf{K}_l + \mathbf{K}_{nl}$ both ways lead to the same result.

6.4.2 Prediction of the critical values

For the prediction of the critical values the configuration at a known equilibrium state $\mathcal{B}^t$ is considered as a basis. The intention is to compute the updated configuration $\mathcal{B}^{t+\Delta t}$ with the secant approach in such a way that this updated configuration approximates the critical configuration $\mathcal{B}_c$.

Similar to the derivation in the previous section the unknown displacements $\mathbf{v}^{t+\Delta t} = \mathbf{v}_c$ are supposed to be

$$\mathbf{v}_c = \mathbf{v}^t + {}_\Delta\mathbf{v} \qquad \text{with} \quad {}_\Delta\mathbf{v} = \rho\,\Phi. \tag{6.52}$$

The displacement increment ${}_\Delta\mathbf{v}$ is assumed to be the product of an estimate of the buckling pattern Φ and a scalar multiplier ρ. A common choice for Φ is the current displacement pattern $\mathbf{v}^t$.

The incremental constitutive relation (6.40) can be rewritten with (6.52), splitting the expression by dependence on ρ:

$$\mathbf{S}_c = \mathbf{S}^t + \mathbf{D}\left[\rho\mathbf{B}(\mathbf{v}^t)\Phi + \frac{\rho^2}{2}\mathbf{B}_1(\Phi)\Phi\right] = \mathbf{S}^t + \rho\mathbf{S}_1 + \rho^2\mathbf{S}_2 \tag{6.53}$$

The stresses $\mathbf{S}_1$ and $\mathbf{S}_2$ are equal to

$$\mathbf{S}_1 = \mathbf{D}\mathbf{B}(\mathbf{v}^t)\Phi \tag{6.54}$$

$$\mathbf{S}_2 = \frac{1}{2}\mathbf{D}\mathbf{B}_1(\Phi)\Phi. \tag{6.55}$$

It can be demonstrated that for the choice $\Phi = \mathbf{v}^t$ follows $\mathbf{B}_1(\phi) = \mathbf{B}_1(\mathbf{v}^t)$. The definition for the matrix $\mathbf{B}$ can be extracted as well from equation (6.53).

$$\mathbf{B}^t = \mathbf{B}(\mathbf{v}^t) + \rho\mathbf{B}_1(\Phi) \tag{6.56}$$

Substituting (6.53) and (6.56) into (6.51) the tangent stiffness matrix at the critical point is

$$\mathbf{K}_T(\mathbf{v}_c) \approx \mathbf{K}_T(\mathbf{v}^t) + \rho[\mathbf{K}_{L2} + \mathbf{K}_{\sigma 1}] + \rho^2[\mathbf{K}_{L3} + \mathbf{K}_{\sigma 2}], \tag{6.57}$$

with the matrices in this equation composed as follows:

$$\mathbf{K}_{L2} = \bigcup_{e=1}^{n_e} \int_{\Omega^e} \left[\mathbf{B}^{t^T} \mathbf{D} \mathbf{B}_1 + \mathbf{B}_1^T \mathbf{D} \mathbf{B}^{t^T} \right] dV \tag{6.58}$$

$$\mathbf{K}_{L3} = \bigcup_{e=1}^{n_e} \int_{\Omega^e} \mathbf{B}_1^T \mathbf{D} \mathbf{B}_1 \, dV \tag{6.59}$$

$$\mathbf{K}_{\sigma 1} = \bigcup_{e=1}^{n_e} \int_{\Omega^e} \overline{\mathbf{G}}^T \hat{\mathbf{S}}_1^t \overline{\mathbf{G}} \, dV \tag{6.60}$$

$$\mathbf{K}_{\sigma 2} = \bigcup_{e=1}^{n_e} \int_{\Omega^e} \overline{\mathbf{G}}^T \hat{\mathbf{S}}_2^t \overline{\mathbf{G}} \, dV \tag{6.61}$$

Neglecting the terms of second order in ρ a general eigenvalue problem yields that can be solved with an *inverse iteration* procedure, see appendix B for an outline of the algorithm.

$$[\mathbf{K}_T(\mathbf{v}^t) + \rho(\mathbf{K}_{L2} + \mathbf{K}_{\sigma 1})]\Psi = \mathbf{0} \tag{6.62}$$

Once the multiplier ρ is computed the estimation for the critical displacements results from equation (6.52). Using the increment ${}_\Delta\mathbf{v} = \rho\Phi$ the load increment can be computed by the following secant relationship with the secant matrix $\mathbf{K}_S$ of the previous section.

$${}_\Delta\mathbf{f}_c = \mathbf{K}_S(\rho\Phi)\rho\Phi = \left[\mathbf{K}_T(\mathbf{v}^t) + \mathbf{K}_M(\rho\Phi) + \mathbf{K}_N(\rho^2\Phi^2)\right] \rho\Phi \tag{6.63}$$

The estimation for the critical load is finally

$$\mathbf{f}_c = \mathbf{f}^t + {}_\Delta\mathbf{f}_c. \tag{6.64}$$

In each computed equilibrium point on the path a prediction of the critical displacements and critical loads can be performed this way with the CDM.

6.5 The extended system

A direct method for the computation of critical points is the *extended system*. In mathematical literature extended systems have been introduced years ago, see e.g. [Abbott, 1978] or [Seydel, 1979]. In the framework of Finite Elements extended systems appeared with the article of [Wriggers et al., 1988]. Some improvements on the methods were described later in [Wriggers and Simo, 1990].

The idea of the extended systems is to solve the equation system $\mathbf{G}$ simultaneously with a constraint characterizing critical points. Therefore the equation system $\mathbf{G}$ has to be extended and the number of unknowns increased. The fact that a condition for critical points is included in the solution procedure of the equation system permits the direct computation. Solving the extended system the computation is "aiming" at or heading for instability points. However the use of the extended system without a previous computation of an equilibrium point or a path tracing is difficult as the choice of the

starting values is crucial for the convergence properties. A consistent linearization of the constraint permits the use of the Newton–Raphson algorithm, which means quadratic convergence in the vicinity of the solution. Due to the large load steps that might occur in the direct computation of critical points convergence cannot always be assured.

In practical Finite Element engineering several steps of a path computations with arclength are performed before the extended system is used. The converged displacement vector then provides a good starting vector for the unknown critical displacements $\mathbf{v}_c$.

The method of the extended system describes actually a whole class of procedures, that differ mainly by the type of constraint used, but the underlying concept is the same. In [Wagner, 1991b] a very good overview on this subject can be found. Here three types of constraints will be presented in the next sections, among which especially the first with the eigenvalue problem (6.8) as constraint is of importance and was applied to the instability problems of this thesis. The other two implementing the determinant (6.9) or the scalarly formulated eigenvalue are mentioned for completition only.

6.5.1 Eigenvalue problem as constraint

By far the most attention in literature was drawn to this type of extended system, see [Wriggers et al., 1988], [Wriggers and Wagner, 1989] and [Wriggers and Simo, 1990] . With the eigenvector equation (6.8) as constraint the extended equation system that has to be solved looks like

$$\hat{\mathbf{G}}(\mathbf{v}, \lambda, \boldsymbol{\phi}) = \begin{pmatrix} \mathbf{G}(\mathbf{v}, \lambda) \\ \mathbf{K}_T(\mathbf{v}, \lambda)\ \boldsymbol{\phi} \\ l(\boldsymbol{\phi}) \end{pmatrix} = \mathbf{0} \tag{6.65}$$

$$\text{with} \quad l(\boldsymbol{\phi}) = \|\boldsymbol{\phi}\| - 1. \tag{6.66}$$

The vector of unknowns now consists of the displacements $\mathbf{v}$, the load factor λ and the eigenvector $\boldsymbol{\phi}$. A second constraint $l(\boldsymbol{\phi})$ has been added to provide a number of equations sufficient for the solution. $l(\boldsymbol{\phi})$ basically scales the norm of the eigenvector to one. A major advantage of the extended system with this type of constraint is, that the converged solution of (6.65) contains the eigenvector at the critical point belonging to the zero eigenvalue without additional calculations. With the critical load factor λ_c the critical displacements $\mathbf{v}_c$ and the eigenvector $\boldsymbol{\phi}_1$ all information needed for a classification of the critical point are provided.

Computing the necessary derivatives of (6.65) with respect to all the unknowns the extended tangent stiffness matrix is obtained. The Newton–Raphson (4.31) algorithm then has the form

$$\begin{bmatrix} \mathbf{K}_T & \mathbf{0} & -\mathbf{P} \\ (\mathbf{K}_T\boldsymbol{\phi})_{,\mathbf{v}} & \mathbf{K}_T & (\mathbf{K}_T\boldsymbol{\phi})_{,\lambda} \\ \mathbf{0}^T & \frac{\boldsymbol{\phi}^T}{\|\boldsymbol{\phi}\|} & 0 \end{bmatrix} \begin{pmatrix} \triangle\mathbf{v} \\ \triangle\boldsymbol{\phi} \\ \triangle\lambda \end{pmatrix} = -\begin{pmatrix} \mathbf{G}(\mathbf{v}, \lambda) \\ \mathbf{K}_T(\mathbf{v}, \lambda)\ \boldsymbol{\phi} \\ \|\boldsymbol{\phi}\| - 1 \end{pmatrix}. \tag{6.67}$$

Since the additional terms destroy the typical band structure of $\mathbf{K}_T$ completely the computational effort for a solution of (6.67) increases over-proportionally. Moreover the size of the equation system doubles with $2N+1$. To overcome this disadvantage the following partitioning algorithm has been developed:

Solve for $_\Delta\mathbf{v}$:	$\mathbf{K}_T\ {}_\Delta\mathbf{v}_P = \mathbf{P}$,	$\mathbf{K}_T\ {}_\Delta\mathbf{v}_G = -\mathbf{G}$
Compute:	$\mathbf{h}_1 = (\mathbf{K}_T\ \boldsymbol{\phi})_{,\mathbf{v}}\ {}_\Delta\mathbf{v}_P + (\mathbf{K}_T\ \boldsymbol{\phi})_{,\lambda}$	
	$\mathbf{h}_2 = (\mathbf{K}_T\ \boldsymbol{\phi})_{,\mathbf{v}}\ {}_\Delta\mathbf{v}_G$	
Solve for $_\Delta\boldsymbol{\phi}$:	$\mathbf{K}_T\ {}_\Delta\boldsymbol{\phi}_1 = -\mathbf{h}_1$,	$\mathbf{K}_T\ {}_\Delta\boldsymbol{\phi}_2 = -\mathbf{h}_2$
Compute increments:	$_\Delta\lambda = \dfrac{-\boldsymbol{\phi}^T\ {}_\Delta\boldsymbol{\phi}_2 + \|\boldsymbol{\phi}\|}{\boldsymbol{\phi}^T\ {}_\Delta\boldsymbol{\phi}_1}$	
	$_\Delta\mathbf{v} = {}_\Delta\lambda\ {}_\Delta\mathbf{v}_P + {}_\Delta\mathbf{v}_G$	
Update:	$\lambda = \lambda + {}_\Delta\lambda$,	$\mathbf{v} = \mathbf{v} + {}_\Delta\mathbf{v}$, $\boldsymbol{\phi} = {}_\Delta\lambda\ {}_\Delta\boldsymbol{\phi}_1 + {}_\Delta\boldsymbol{\phi}_2$

Table 6.4: Outline of the partitioning algorithm for the extended system

The first line of the partitioning algorithm is identical to the arclength method. The additional effort necessary for the solution of a second equation system remains moderate, as the tangent stiffness matrix is the same in both equations. The most time consuming step in the solution procedure is the diagonal triangularization of $\mathbf{K}_T$ which has to be performed only once. The second term in the calculation of h_1 vanishes for displacement independent loads ($(\mathbf{K}_T\boldsymbol{\phi})_{,\lambda} = \mathbf{0}$). The following two equation systems that have to be solved for the eigenvectors $\boldsymbol{\phi}_1$ and $\boldsymbol{\phi}_2$ are again moderate concerning the effort for the same reason that $\mathbf{K}_T$ does not have to be triangularized. The derivatives of the eigenvalue problem (6.8) with respect to the displacements requires special attention. Standard elements do not provide the second derivative of the tangent stiffness matrix $\mathbf{K}_T$, so that the element subroutines have to be modified for this purpose. It would be desirable to have a procedure that can be implemented independently of the elemental subroutines. The numerical approximation of the derivative assures this independence. The directional derivative of the eigenvalue problem with respect to the displacements can be written as

$$(\mathbf{K}_T\boldsymbol{\phi})_{,\mathbf{v}}\ {}_\Delta\mathbf{v} = \frac{d}{d\epsilon}\left[\mathbf{K}_T(\mathbf{v}+\epsilon\boldsymbol{\phi})\right]\ {}_\Delta\mathbf{v}\,\Big|_{\epsilon=0} . \tag{6.68}$$

According to the definition of differentiation this equation can be stated as the limit process of

$$(\mathbf{K}_T\boldsymbol{\phi})_{,\mathbf{v}\ \Delta}\mathbf{v} = \lim_{\epsilon\to 0}\frac{1}{\epsilon}\left[\mathbf{K}_T(\mathbf{v}+\epsilon\boldsymbol{\phi})\ {}_\Delta\mathbf{v} - \mathbf{K}_T(\mathbf{v})\ {}_\Delta\mathbf{v}\right]. \tag{6.69}$$

Equation (6.69) is suitable for the construction of a numerical approximation:

$$(\mathbf{K}_T\boldsymbol{\phi})_{,\mathbf{v}\ \Delta}\mathbf{v} \approx \frac{1}{\epsilon}\left[\mathbf{K}_T(\mathbf{v}+\epsilon\boldsymbol{\phi})\ {}_\Delta\mathbf{v} - \mathbf{K}_T(\mathbf{v})\ {}_\Delta\mathbf{v}\right] \tag{6.70}$$

With this, the two vectors h_1 and h_2 can be calculated as follows:

$$\mathbf{h}_1 \approx \frac{1}{\epsilon}\left[\mathbf{K}_T(\mathbf{v}+\epsilon\boldsymbol{\phi})\ {}_\Delta\mathbf{v}_P - \mathbf{P}\right] \tag{6.71}$$

$$\mathbf{h}_2 \approx \frac{1}{\epsilon}\left[\mathbf{K}_T(\mathbf{v}+\epsilon\boldsymbol{\phi})\ {}_\Delta\mathbf{v}_G + \mathbf{G}\right] \tag{6.72}$$

An important point in the algorithm of table 6.4 is the choice of the starting vector for the eigenvector $\boldsymbol{\phi}$. The most simple possibility is the vector $\mathbf{1}$, with all components equal to one. The normed vector of the converged displacements $\mathbf{v}_t$ and the first or higher step of an inverse iteration procedure, see appendix B, are other choices. Using an eigenvector out of the eigenvector equation (6.7) provides the by far best starting vector, but comes with a higher effort that has to be taken for the solution of the eigenvalue problem.

$$\boldsymbol{\phi}_0 = \begin{cases} \mathbf{1} & \text{unit vector} \\ \frac{\mathbf{v}_t}{\|\mathbf{v}_t\|} & \text{current displacement vector} \\ \frac{\mathbf{K_T}^{-1}\mathbf{1}}{\|\mathbf{K_T}^{-1}\mathbf{1}\|} & \text{1. step of an inverse iteration} \\ \boldsymbol{\phi}_0 & \text{from eigenvalue problem (6.7)} \end{cases} \tag{6.73}$$

Equation (6.73) summarizes the possible starting vectors for $\boldsymbol{\phi}$. The iterative loop of the whole algorithm with the derived simplifications is given in table 6.5.

6.5.2 Determinant as constraint

A second type of extended system can be constructed with the determinant from equation (6.9) as constraint. With the displacements $\mathbf{v}$ and the load factor λ the number of unknowns does not increase compared to the arclength method, which is a great advantage.

$$\hat{\mathbf{G}}(\mathbf{v},\lambda) = \begin{pmatrix} \mathbf{G}(\mathbf{v},\lambda) \\ \det(\mathbf{K}_T(\mathbf{v},\lambda)) \end{pmatrix} = \mathbf{0} \tag{6.74}$$

A major problem is encountered when the determinant has to be linearized and the derivative with respect to $\mathbf{v}$ has to be calculated. After some mathematical operations (see [Wagner, 1991b]) the numerical derivative is obtained from

$$\frac{d}{d\epsilon}\left[\det\mathbf{K}_T(\mathbf{v}+\epsilon\ {}_\Delta\mathbf{v})\right]\Big|_{\epsilon=0} = \det\mathbf{K}_T\ tr(\mathbf{K}_T^{-T}\mathbf{K}_{T,\mathbf{v}\ \Delta}\mathbf{v}). \tag{6.75}$$

The Newton–Raphson equation for this type of extended system has the two equations

Solve for $_{\Delta}\mathbf{v}^{i+1}$: $\quad \mathbf{K}_T(\mathbf{v}^i)\ {}_{\Delta}\mathbf{v}_P^{i+1} = \mathbf{P}\ ,\quad \mathbf{K}_T(\mathbf{v}^i)\ {}_{\Delta}\mathbf{v}_G^{i+1} = -\mathbf{G}$

Compute: $\quad \mathbf{h}_1^i = \frac{1}{\epsilon}\left[\mathbf{K}_T(\mathbf{v}^i + \epsilon\boldsymbol{\phi}^i)\ {}_{\Delta}\mathbf{v}_P^{i+1} - \mathbf{P}\right]$

$\quad \mathbf{h}_2^i = \frac{1}{\epsilon}\left[\mathbf{K}_T(\mathbf{v}^i + \epsilon\boldsymbol{\phi}^i)\ {}_{\Delta}\mathbf{v}_G^{i+1} + \mathbf{G}^i\right]$

Solve for $_{\Delta}\boldsymbol{\phi}^{i+1}$: $\quad \mathbf{K}_T(\mathbf{v}^i)\ {}_{\Delta}\boldsymbol{\phi}_1^{i+1} = -\mathbf{h}_1^i\ ,\quad \mathbf{K}_T(\mathbf{v}^i)\ {}_{\Delta}\boldsymbol{\phi}_2^{i+1} = -\mathbf{h}_2^i$

Compute increments: $\quad {}_{\Delta}\lambda^{i+1} = \dfrac{-\boldsymbol{\phi}^{iT}\ {}_{\Delta}\boldsymbol{\phi}_2^{i+1} + \|\boldsymbol{\phi}^i\|}{\boldsymbol{\phi}^{iT}\ {}_{\Delta}\boldsymbol{\phi}_1^{i+1}}$

$\quad {}_{\Delta}\mathbf{v}^{i+1} = {}_{\Delta}\lambda^{i+1}\ {}_{\Delta}\mathbf{v}_P^{i+1} + {}_{\Delta}\mathbf{v}_G^{i+1}$

Update: $\quad \lambda^{i+1} = \lambda^i + {}_{\Delta}\lambda^{i+1}\ ,\quad \mathbf{v}^{i+1} = \mathbf{v}^i + {}_{\Delta}\mathbf{v}^{i+1}\ ,$

$\quad \boldsymbol{\phi}^{i+1} = {}_{\Delta}\lambda^i\,{}_{\Delta}\boldsymbol{\phi}_1^{i+1} + {}_{\Delta}\boldsymbol{\phi}_2^{i+1}$

Table 6.5: Improved partitioning algorithm for the extended system

$$\mathbf{K}_T\ {}_{\Delta}\mathbf{v} - \mathbf{P}\ {}_{\Delta}\lambda = -\mathbf{G}(\mathbf{v},\lambda) \tag{6.76}$$

$$tr(\mathbf{K}_T^{-T}\mathbf{K}_{T,\mathbf{v}}\ {}_{\Delta}\mathbf{v}) = -1. \tag{6.77}$$

The first is easily solvable by the partitioning algorithm similar to the arclength method doing the split $\mathbf{v} = \mathbf{v}_G + \lambda\mathbf{v}_P$. The load increment is then

$${}_{\Delta}\lambda = -\frac{1 + tr[\mathbf{K}_T^{-T}(\mathbf{K}_T{}_{\Delta}\mathbf{v}_G)_{,\mathbf{v}}]}{tr[\mathbf{K}_T^{-T}(\mathbf{K}_T{}_{\Delta}\mathbf{v}_P)_{,\mathbf{v}}]}. \tag{6.78}$$

It is obvious that the computation of the terms in this equation is tedious. The derivative of $\mathbf{K}_T$ has to be evaluated for two vectors and the argument of the trace operator involves the inverse of $\mathbf{K}_T$. The complicated realization of this extended system type is the reason why it was not widely used in Finite Elements.

6.5.3 Scalary formulated eigenvalue problem as constraint

The third type of extended system to be presented here has the scalarly formulated eigenvector equation as constraint. The displacements $\mathbf{v}$ and the load factor λ are the only unknowns here, which keeps the problem simple:

$$\tilde{\mathbf{G}}(\mathbf{v},\lambda,\boldsymbol{\phi}) = \begin{pmatrix} \mathbf{G}(\mathbf{v},\lambda) \\ \boldsymbol{\phi}^T\ \mathbf{K}_T(\mathbf{v},\lambda)\ \boldsymbol{\phi} \end{pmatrix} = \mathbf{0} \tag{6.79}$$

The Newton–Raphson algorithm scheme is obtained by consistent linearization:

$$\begin{bmatrix} \mathbf{K}_T & -\mathbf{P} \\ \boldsymbol{\phi}^T(\mathbf{K}_T\boldsymbol{\phi})_{,\mathbf{v}} & \boldsymbol{\phi}^T(\mathbf{K}_T\boldsymbol{\phi})_{,\lambda} \end{bmatrix} \begin{pmatrix} \triangle\mathbf{v} \\ \triangle\lambda \end{pmatrix} = -\begin{pmatrix} \mathbf{G}(\mathbf{v},\lambda) \\ \boldsymbol{\phi}^T\ \mathbf{K}_T(\mathbf{v},\lambda)\ \boldsymbol{\phi} \end{pmatrix} \tag{6.80}$$

Although this constraint seems rather simple to handle it should be noted, that the eigenvector $\boldsymbol{\phi}$ is needed and has to be supplied by an external procedure, as e.g. the inverse iteration (see appendix B).

6.6 Branch switching

To fully compute an equilibrium path of a structure, the knowledge of secondary branches is of importance. Path following algorithms as the arclength method work as well on secondary branches without restrictions, so that the only difficulty is the branch switching from the primary to secondary branches in bifurcation points.

A quite simple method, which is relatively easy to implement in existing Finite Element code is the perturbation of the displacement pattern. From an engineering point of view it is obvious that the displacement pattern of secondary branches is described by the eigenvectors. Especially the eigenvector corresponding to the zero eigenvalue is of importance. [Wagner and Wriggers, 1988] proposed a perturbation of the following form:

$$\mathbf{v}_j = \mathbf{v}_c + \epsilon_j \frac{\boldsymbol{\phi}_j}{\|\boldsymbol{\phi}_j\|} \tag{6.81}$$

The perturbed displacement pattern $\mathbf{v}_j$ is computed as the sum of the displacement vector in the critical point $\mathbf{v}_c$ and the eigenvector $\boldsymbol{\phi}_j$ normed to 1 multiplied by a scalar perturbation factor ϵ_j. Based on this perturbed solution the next load step is calculated . Since the load level in the secondary branch might be lesser than the critical load a path following algorithm should be used in order to enable a decrease of the load.

A proper choice of the perturbation factor is of importance since for too small values the solution might fall back to the primary path. On the other hand a too big perturbation factor might lead to divergence.

Chapter 7

Computation of critical points with constraints

In this chapter some extensions for the critical point detection methods of the previous chapter are described. The extended system as a well known reliable algorithm and the recently developed CDM are subjected to constraints. Inequality constraints originating from damage and contact as well as displacement boundary conditions as equality constraints are considered.

The first two section of this chapter are dedicated to the combination of the simple damage model of section 3.3.2 with the extended system and the CDM. In the third section the *one step prediction* based on the extended system algorithm is presented. The idea of an integration of the critical point condition in the problem solution and a mere prediction instead of a direct computation leads to this algorithm. With the help of the one step prediction the fundamentally different methods CDM and extended system can be compared and the question of a possible combination of both methods can be answered.

Although the main intention of this work is to study the effect of inequality constraints in the critical point computation, prescribed displacements on the boundary as equality constraints are used because this way it is rather simple to introduce displacement boundary conditions in extended system and arclength procedures. The implementation of the extended system for contact problems using the contact representation of chapter 5 is the subject of the last section.

7.1 Extended system combined with damage

A path computation including damage effects is feasible in a straightforward manner, if the algorithm of table 3.1 is used. A combination of arclength method and constitutive damage model does not lead to major difficulties provided that the step lengths in the arclength method remain moderate.

For the computation of critical points however this is not the case. Especially with the extended system as a direct method larger load steps might occur depending on the difference of current and critical load level. As the examples in chapter 8 will show a computation of critical points is possible only if the starting point lies in the vicinity of the critical point.

Besides this the implementation of damage effects in connection with the extended system is as straightforward as with the arclength method. The St.Venant constitutive model (3.11) is extended by the simple damage model (3.30). Since damage is represented in the variational equation (4.14), the tangent stiffness matrix $\mathbf{K}_T$ depends as well on the damage parameter d. The constraint equation in the extended system (see section 6.5) contains the tangent stiffness matrix $\mathbf{K}_T$ and damage is thus taken into account in the critical point computation.

7.2 The CDM including damage

For the prediction of the critical values with the CDM the fact, that first a prediction of the critical displacements is made, can be exploited as described in [Tschöpe et al., 1999].

Starting from a known point $(\mathbf{v}^t; \lambda^t)$ on the equilibrium path, with a well defined damage level d^t a prediction of the critical displacements according to section 6.4.2 is performed basing on the values $(\mathbf{v}^t; \lambda^t)$. When the secant stiffness matrix $\mathbf{K}_S$ as an approximation for the singular tangent stiffness matrix $\mathbf{K}_T(\mathbf{v}_c)$ is assembled (see equation (6.57)) the constitutive tensor in the current damage state $(1 - d^t)\mathbf{D}$ is assumed.

With the prediction of the critical displacements resulting from the solution of (6.62) and (6.52) the new damage state d_c can be computed. The stress norm $\overline{\sigma}$ is then

$$\overline{\sigma}(\mathbf{E}_c) = \sqrt{\mathbf{E}_c \cdot (\mathbf{D}\mathbf{E}_c)}, \tag{7.1}$$

with $\mathbf{E}_c = \mathbf{E}(\mathbf{v}_c)$ according to (2.13). The damage parameter is now chosen according to the scheme

$$d_c = \begin{cases} d^t & \text{for} \quad \overline{\sigma}(\mathbf{E}_c) \leq r^t \\ \frac{1}{1+H}\left(1 - \frac{r_0}{\overline{\sigma}(\mathbf{E}_c)}\right) & \text{for} \quad \overline{\sigma}(\mathbf{E}_c) > r^t \end{cases}. \tag{7.2}$$

The predicted critical damage parameter d_c is equal to the current one, only if the predicted critical displacements indicate no further damage. Otherwise a new critical damage parameter prediction d_c is computed with the stress norm $\overline{\sigma}(\mathbf{E}_c)$ of (7.1).

For the now following prediction of the critical load f_c this possibly additional damage can be taken into account. The secant stiffness matrix $\mathbf{K_S}(\mathbf{v_c})$ in (6.63) is therefore constructed basing on the damage state d_c.

Attention should be paid, that the damage parameter or threshold value of the path computation are not updated when the critical displacement prediction requires a change in both variables.

7.3 One step prediction with the extended system

A comparison of critical point computation with CDM and extended system is difficult because of the fundamental different nature of both approaches. The extended system is a direct method, whereas the CDM only makes a prediction of the critical values. For the computations of critical points the extended system as a direct method is more likely to be used than the CDM. A crucial point for the convergence of the extended system is the proper choice of the starting values. A combination of both methods in such a way, that

as starting values for the extended system the results of a precendental CDM prediction are taken, would be a conceivable solution.

To evaluate this possibility a comparison of the predicted values and the common starting values of the extended system as described in section 6.5 has to be made. A simple way is to compare the predicted critical load of the CDM with the result of the first iteration of an extended system computation. The result of this first iteration then serves as a one step extended system prediction of the critical load.

Taking a closer look at the equation system (6.67) for the extended system with the eigenvector equation as constraint some simplifications can be introduced. Extracting the first equation of (6.67) yields

$$\mathbf{K}_T(\mathbf{v}^i)\,{}_\Delta\mathbf{v}^{i+1} - \mathbf{P}\,{}_\Delta\lambda^{i+1} = -\mathbf{G}(\mathbf{v}^i) = -\mathbf{R}(\mathbf{v}^i) + \lambda^i\mathbf{P} = \mathbf{0}. \tag{7.3}$$

In the first iteration of an extended system computation the starting values $\mathbf{v}^0$ and λ^0 are the converged solution in a point of the equilibrium path. This means that the right–hand side of equation (7.3) $\mathbf{G}(\mathbf{v}^0)$ is equal to 0.

$$-\mathbf{R}(\mathbf{v}^0) + \lambda^0\mathbf{P} = \mathbf{0} \tag{7.4}$$

With this the equation system (6.67) for the first iteration step can be rewritten as three coupled equations:

$$\mathbf{K}_T(\mathbf{v}^0)\,{}_\Delta\mathbf{v}^1 = {}_\Delta\lambda^1\mathbf{P} \tag{7.5}$$

$$(\mathbf{K}_T(\mathbf{v}^0)\boldsymbol{\phi})_{,\mathbf{v}}\,{}_\Delta\mathbf{v}^1 + \mathbf{K}_T(\mathbf{v}^0)\,{}_\Delta\boldsymbol{\phi}^1 = -\mathbf{K}_T(\mathbf{v}^0)\boldsymbol{\phi} \tag{7.6}$$

$$\boldsymbol{\phi}^T\,{}_\Delta\boldsymbol{\phi}^1 = \|\boldsymbol{\phi}\| - \|\boldsymbol{\phi}\|^2 \tag{7.7}$$

For the eigenvector which is chosen according to the relations (6.73) the shorthand notation $\boldsymbol{\phi} = \boldsymbol{\phi}^0$ is used here. Solving (7.5) for the displacement increments ${}_\Delta\mathbf{v}^1$ yields

$${}_\Delta\mathbf{v}^1 = \mathbf{K}_T^{-1}\mathbf{P}\,{}_\Delta\lambda^1 = {}_\Delta\mathbf{v}_P^1\,{}_\Delta\lambda^1. \tag{7.8}$$

As in the partitioning algorithm of table 6.4 the product $\mathbf{K}_T^{-1}\mathbf{P}$ is denoted as $\mathbf{v}_P$. Inserting this result in (7.6) and multiplying the equation by $\mathbf{K}_T^{-1}$ gives

$$\mathbf{K}_T^{-1}(\mathbf{K}_T\boldsymbol{\phi})_{,\mathbf{v}}\,{}_\Delta\mathbf{v}_P^1\,{}_\Delta\lambda^1 + {}_\Delta\boldsymbol{\phi}^1 = -\boldsymbol{\phi}. \tag{7.9}$$

Equation (7.9) can be solved for the eigenvector increment ${}_\Delta\boldsymbol{\phi}$ and with this (7.7) can be rewritten as

$$-\boldsymbol{\phi}^T\boldsymbol{\phi} - \boldsymbol{\phi}^T\mathbf{K}_T^{-1}(\mathbf{K}_T\boldsymbol{\phi})_{,\mathbf{v}}\,{}_\Delta\mathbf{v}_P^1\,{}_\Delta\lambda^1 = \|\boldsymbol{\phi}\| - \|\boldsymbol{\phi}\|^2. \tag{7.10}$$

The increment of the load parameter ${}_\Delta\lambda$ can be obtained then from (7.10):

$${}_\Delta\lambda^1 = -\frac{\|\boldsymbol{\phi}\|}{\boldsymbol{\phi}^T\mathbf{K}_T^{-1}[(\mathbf{K}_T\boldsymbol{\phi})_{,\mathbf{v}}\,{}_\Delta\mathbf{v}_P^1]} \tag{7.11}$$

As the starting value for the eigenvector is commonly normed to one, probably a better formulation of (7.11) is

$$ {}_{\Delta}\lambda^1 = -\frac{1}{\frac{\phi^T}{\|\phi\|}\mathbf{K}_T^{-1}[(\mathbf{K}_T\phi)_{,\mathbf{v}}\,{}_{\Delta}\mathbf{v}_P^1]}. \tag{7.12} $$

The derivative of the eigenvector equation with respect to the displacements can again be computed numerically using a relation similar to (6.70):

$$ (\mathbf{K}_T\phi)_{,\mathbf{v}}\,{}_{\Delta}\mathbf{v}_P^1 \approx \frac{1}{\epsilon}[\mathbf{K}_T(\mathbf{v}^0+\epsilon\phi)\,{}_{\Delta}\mathbf{v}_P^1 - \mathbf{K}_T(\mathbf{v}^0)\,{}_{\Delta}\mathbf{v}_P^1] \tag{7.13} $$

The prediction of the critical load follows from the update equation

$$ \lambda^1 = \lambda^0 + {}_{\Delta}\lambda^1. \tag{7.14} $$

Calculation λ^1 with ${}_{\Delta}\lambda^1$ from (7.12) in each converged point of an equilibrium path computation, a curve of one step prediction values of λ^c is obtained.

7.4 Displacement boundary conditions as constraint

For problems where no force boundary conditions are supplied, the vector $\mathbf{P}$ which contains the load terms is equal to $\mathbf{0}$. In FE-programs displacement boundary conditions are introduced in the solution algorithm of the equation system (4.31). Applying the arclength method for path computation or the extended system for critical point computation this is no longer possible. A rather simple way of representing the displacement boundary conditions is seeing them as equality constraints of the form

$$ \mathbf{v} - \overline{\mathbf{v}} = 0. \tag{7.15} $$

Using the penalty method of chapter 5 the constraints can be represented in (4.20) as

$$ \mathbf{G}(\mathbf{v},\lambda) = \mathbf{R}(\mathbf{v}) + \epsilon_p\,\mathbf{I}_{\mathbf{v}}(\mathbf{v}-\overline{\mathbf{v}}) = \mathbf{0}. \tag{7.16} $$

ϵ_P is the penalty parameter, the vector $\overline{\mathbf{v}}$ has nonzero terms only at positions corresponding to the degrees of freedom that are prescribed by the boundary conditions. The matrix $\mathbf{I}_{\mathbf{v}}$ is a diagonal matrix with ones at positions corresponding to the prescribed displacement degrees of freedom.

$$ \mathbf{I}_{\mathbf{v}} = \begin{pmatrix} 0 & 0 & \dots & 0 \\ 0 & 1 & \dots & 0 \\ \vdots & \vdots & \ddots & \vdots \\ 0 & 0 & 0 & 1 \end{pmatrix} \qquad \overline{\mathbf{v}} = \begin{pmatrix} 0 \\ \overline{v}_1 \\ \vdots \\ \overline{v}_n \end{pmatrix} \tag{7.17} $$

The advantage of this method is the ease of implementation in existing FE programs. This will become apparent in the next two sections, where arclength method and extended system are combined with displacement boundary conditions. Since equation (7.15) is an equality constraint no check for active and non–active constraints has to be made.

Remark: Due to the choice of a reasonable value for the penalty parameter the constraint (7.15) is fulfilled only approximately. Further details of the penalty method can be found in section 5.4.2.

7.4.1 Arclength with displacement boundary conditions

For the equilibrium path computation the introduction of the scalable load parameter λ is necessary. Equation (7.15) then can be rewritten as

$$\mathbf{v} - \lambda\overline{\mathbf{v}} = 0. \tag{7.18}$$

With the definitions 7.17 for $\mathbf{I_v}$ and $\overline{\mathbf{v}}$ the equation system (4.32) obtains the following form

$$\mathbf{G}(\mathbf{v},\lambda) = \mathbf{R}(\mathbf{v}) + \epsilon_p\, \mathbf{I_v}(\mathbf{v} - \lambda\overline{\mathbf{v}}) = \mathbf{0}. \tag{7.19}$$

The Newton–Raphson algorithm (4.34) has to be modified as well for this type of boundary conditions:

$$\begin{bmatrix} \mathbf{K}_T^i + \epsilon_P\mathbf{I_v} & -\epsilon_P\mathbf{I_v}\overline{\mathbf{v}} \\ \mathbf{f}_{,u}^{i\,T} & f_{,\lambda}^i \end{bmatrix} \begin{pmatrix} {}_\Delta\mathbf{v}^{i+1} \\ {}_\Delta\lambda^{i+1} \end{pmatrix} = - \begin{pmatrix} \mathbf{R}(\mathbf{v}^i) + \epsilon_P\mathbf{I_v}(\mathbf{v}^i - \lambda\overline{\mathbf{v}}) \\ f^i(\mathbf{v}^i,\lambda^i) \end{pmatrix} \tag{7.20}$$

The partitioning algorithm for the arclength method (see table 4.2) has to be rewritten as depicted in table 7.1. Note that the changes in table 7.1 compared to table 4.2 effect $\mathbf{K}_T$, $\mathbf{P}$ and $\mathbf{G}$ only.

Predictor:
$$[\mathbf{K}_T(\mathbf{v}^0) + \epsilon_p\, \mathbf{I_v}]\; {}_\Delta\mathbf{v}_P^0 = \epsilon_p\, \mathbf{I_v}\overline{\mathbf{v}}$$
$${}_\Delta\lambda^0 = \pm \frac{\Delta s}{\sqrt{({}_\Delta\mathbf{v}_P^0)^T\, {}_\Delta\mathbf{v}_P^0}}$$

Iteration loop: $i = 0, 1, \ldots$ until convergence

$$[\mathbf{K}_T(\mathbf{v}^i) + \epsilon_p\, \mathbf{I_v}]\; {}_\Delta\mathbf{v}_G^{i+1} = - \mathbf{R}(\mathbf{v}^i) - \epsilon_P\mathbf{I_v}(\mathbf{v}^i - \lambda^i\overline{\mathbf{v}})$$
$$[\mathbf{K}_T(\mathbf{v}^i) + \epsilon_p\, \mathbf{I_v}]\; {}_\Delta\mathbf{v}_P^{i+1} = \epsilon_p\, \mathbf{I_v}\overline{\mathbf{v}}$$

$${}_\Delta\lambda^{i+1} = -\frac{f^i + \mathbf{f}_{,\mathbf{v}}^{i\,T}\, {}_\Delta\mathbf{v}_G^{i+1}}{f_{,\lambda}^i + \mathbf{f}_{,\mathbf{v}}^{i\,T}\, {}_\Delta\mathbf{v}_P^{i+1}}$$

$${}_\Delta\mathbf{v}^{i+1} = {}_\Delta\mathbf{v}_G^{i+1} + {}_\Delta\lambda^{i+1}\, {}_\Delta\mathbf{v}_P^{i+1}$$
$$\mathbf{v}^{i+1} = \mathbf{v}^i + {}_\Delta\mathbf{v}^{i+1}\quad,\quad \lambda^{i+1} = \lambda^i + {}_\Delta\lambda^{i+1}$$

Convergence:
$$\|\mathbf{G}_S(\mathbf{v}^{i+1},\lambda^{i+1})\| \le TOL$$

Table 7.1: Algorithm for arclength with displacement boundary conditions

7.4.2 Extended system with displacement boundary conditions

Similar to the arclength method the displacement boundary constraints are introduced into the extended system. With the definitions $\mathbf{I}_\mathbf{v}$, $\overline{\mathbf{v}}$ and the abbreviation $\hat{\mathbf{K}}_T = \mathbf{K}_T + \epsilon_P \mathbf{I}_\mathbf{v}$ the Newton–Raphson form of the extended system with the eigenvalue problem as constraint of section 6.5.1 is:

$$\begin{bmatrix} \hat{\mathbf{K}}_T & 0 & -\epsilon_P \mathbf{I}_\mathbf{v} \\ (\hat{\mathbf{K}}_T \boldsymbol{\phi})_{,\mathbf{v}} & \hat{\mathbf{K}}_T & (\hat{\mathbf{K}}_T \boldsymbol{\phi})_{,\lambda} \\ 0^T & \frac{\boldsymbol{\phi}^T}{\|\boldsymbol{\phi}\|} & 0 \end{bmatrix} \begin{pmatrix} {}_\Delta\mathbf{v} \\ {}_\Delta\boldsymbol{\phi} \\ {}_\Delta\lambda \end{pmatrix} = - \begin{pmatrix} \mathbf{R}(\mathbf{v}) + \epsilon_P \mathbf{I}_\mathbf{v}(\mathbf{v} - \lambda\overline{\mathbf{v}}) \\ \hat{\mathbf{K}}_T(\mathbf{v})\ \boldsymbol{\phi} \\ \|\boldsymbol{\phi}\| - 1 \end{pmatrix} \tag{7.21}$$

The partitioning algorithm can then be obtained in a straightforward manner and is given in table 7.2. Note that the addition of penalty terms in the tangent stiffness matrix affects as well the eigenvector equation.

Solve for ${}_\Delta\mathbf{v}^{i+1}$:

$$[\mathbf{K}_T(\mathbf{v}^i) + \epsilon_P \mathbf{I}_\mathbf{v}]\ {}_\Delta\mathbf{v}_P^{i+1} = \epsilon_P \mathbf{I}_\mathbf{v}\overline{\mathbf{v}}$$

$$[\mathbf{K}_T(\mathbf{v}^i) + \epsilon_P \mathbf{I}_\mathbf{v}]\ {}_\Delta\mathbf{v}_G^{i+1} = -\mathbf{R}(\mathbf{v}^i) - \epsilon_P \mathbf{I}_\mathbf{v}(\mathbf{v}^i - \lambda\overline{\mathbf{v}})$$

Compute:

$$\mathbf{h}_1^i = \frac{1}{\epsilon}\left[(\mathbf{K}_T(\mathbf{v}^i + \epsilon\boldsymbol{\phi}^i) + \epsilon_P \mathbf{I}_\mathbf{v})\ {}_\Delta\mathbf{v}_P^{i+1} - \epsilon_P \mathbf{I}_\mathbf{v}\overline{\mathbf{v}}\right]$$

$$\mathbf{h}_2^i = \frac{1}{\epsilon}\left[(\mathbf{K}_T(\mathbf{v}^i + \epsilon\boldsymbol{\phi}^i) + \epsilon_P \mathbf{I}_\mathbf{v})\ {}_\Delta\mathbf{v}_G^{i+1} + \mathbf{R}(\mathbf{v}^i) + \epsilon_P \mathbf{I}_\mathbf{v}(\mathbf{v}^i - \lambda\overline{\mathbf{v}})\right]$$

Solve for ${}_\Delta\boldsymbol{\phi}^{i+1}$:

$$[\mathbf{K}_T(\mathbf{v}^i) + \epsilon_P \mathbf{I}_\mathbf{v}]\ {}_\Delta\boldsymbol{\phi}_1^{i+1} = -\mathbf{h}_1^i$$

$$[\mathbf{K}_T(\mathbf{v}^i) + \epsilon_P \mathbf{I}_\mathbf{v}]\ {}_\Delta\boldsymbol{\phi}_2^{i+1} = -\mathbf{h}_2^i$$

Compute increments:

$${}_\Delta\lambda^{i+1} = \frac{-\boldsymbol{\phi}^{iT}\ {}_\Delta\boldsymbol{\phi}_2^{i+1} + \|\boldsymbol{\phi}^i\|}{\boldsymbol{\phi}^{iT}\ {}_\Delta\boldsymbol{\phi}_1^{i+1}}$$

$${}_\Delta\mathbf{v}^{i+1} = {}_\Delta\lambda^{i+1}\ {}_\Delta\mathbf{v}_P^{i+1} + {}_\Delta\mathbf{v}_G^{i+1}$$

Update:

$$\lambda^{i+1} = \lambda^i + {}_\Delta\lambda^{i+1}\ ,\quad \mathbf{v}^{i+1} = \mathbf{v}^i + {}_\Delta\mathbf{v}^{i+1}\ ,$$

$$\boldsymbol{\phi}^{i+1} = {}_\Delta\lambda^i\,{}_\Delta\boldsymbol{\phi}_1^{i+1} + {}_\Delta\boldsymbol{\phi}_2^{i+1}$$

Table 7.2: Partitioning algorithm for the extended system with displacement boundary conditions

Remark: For many problems limit load points associated with snap through cannot be encountered when the corresponding dual problem with displacement boundary conditions

is computed. The prescribing of displacement degrees of freedom prevents the singularity of the tangent stiffness matrix in those cases.

7.5 Extended system with contact

An interesting aspect in the extension of the applicability of the extended system is the critical point computation in combination with contact. In [Simo et al., 1986] results of a buckling analysis with unilateral contact using arclength procedures are published. Due to the emerging inequality constraints the underlying mathematics is rather complex. Related literature is restricted mainly to unilateral contact problems with rigid obstacles, see [Klarbring, 1988], [Björkman, 1992], [Rohde and Stavroulakis, 1997b] or [Rohde and Stavroulakis, 1997a]. In those papers the mathematics of path following and critical points with inequality constraints originating from unilateral contact problems is studied. [Björkman, 1992] describes the occurrence of end points in these cases, where the equilibrium path ends. Those points are no real critical points in the sense, that the stiffness matrix is not singular and the usual conditions (6.8) and (6.9) do not hold. It is apparent that the extended system with the constraints of section 6.5 is not able to encounter these points.
Applying the extended system procedure to the equation system (5.15) yields:

$$\begin{bmatrix} \mathbf{K}_T + \mathbf{K}_c & 0 & -\mathbf{P} \\ [(\mathbf{K}_T + \mathbf{K}_c)\boldsymbol{\phi}]_{,\mathbf{v}} & \mathbf{K}_T + \mathbf{K}_c & [(\mathbf{K}_T + \mathbf{K}_c)\boldsymbol{\phi}]_{,\lambda} \\ 0^T & \frac{\boldsymbol{\phi}^T}{\|\boldsymbol{\phi}\|} & 0 \end{bmatrix} \begin{pmatrix} \Delta\mathbf{v} \\ \Delta\boldsymbol{\phi} \\ \Delta\lambda \end{pmatrix} = - \begin{pmatrix} \mathbf{G}_S(\mathbf{v}) + \mathbf{G}_C(\mathbf{v}) \\ [\mathbf{K}_T(\mathbf{v}) + \mathbf{K}_c(\mathbf{v})]\boldsymbol{\phi} \\ \|\boldsymbol{\phi}\| - 1 \end{pmatrix} \tag{7.22}$$

Here $\mathbf{K}_c$ is the matrix notation for the derivatives of the contact terms $\mathbf{G}_c$ with respect to the displacements.($\mathbf{K}_c = \frac{\partial \mathbf{G}_c}{\partial \mathbf{v}}$) The penalty method was chosen to incorporate the contact inequality constraints in the equation system $\mathbf{G}$. The vector $\mathbf{G}_c$ consists of penalty terms that are subjected to the changes in the active set as described in section 5.4.2. It can be thought of two strategies for the choice of the active set. The first is a constant verification and reorganization of the active set after each iteration step. The second possibility is a change of the active set only after convergence has been achieved. The first time a constraint becomes active the active set is formed and held fixed until the iteration converges. Then the active set is verified and changes are made accordingly. The whole process is repeated until the final convergence, where no changes in the active set are necessary. Compared to the first strategy this means a higher computational effort caused by the additional iteration loop. On the other hand the iteration process might become more stable by this second approach as changes in the active set occur less frequently.

The partitioning algorithm can be used without major difficulties for the solution of equation system (7.22), see table 7.3. The numerical derivative that is used to compute the vectors $\mathbf{h_1}$ and $\mathbf{h_2}$ deserves special attention:

$$\begin{aligned}
\mathbf{h}_1 &\approx \frac{1}{\epsilon}\left[\mathbf{K}_T(\mathbf{v}+\epsilon\boldsymbol{\phi})\ {}_{\Delta}\mathbf{v}_P + \mathbf{K}_c(\mathbf{v}+\epsilon\boldsymbol{\phi})\ {}_{\Delta}\mathbf{v}_P - \mathbf{P}\right] \\
\mathbf{h}_2 &\approx \frac{1}{\epsilon}\left[\mathbf{K}_T(\mathbf{v}+\epsilon\boldsymbol{\phi})\ {}_{\Delta}\mathbf{v}_G + \mathbf{K}_c(\mathbf{v}+\epsilon\boldsymbol{\phi})\ {}_{\Delta}\mathbf{v}_G + \mathbf{G}_S(\mathbf{v}) + \mathbf{G}_c(\mathbf{v})\right] \qquad (7.23)
\end{aligned}$$

$\mathbf{K}_c(\mathbf{v})$ and $\mathbf{K}_c(\mathbf{v}+\epsilon\boldsymbol{\phi})$ in (7.23) can differ substantially, if the displacement values $\mathbf{v}$ and $\mathbf{v}+\epsilon\boldsymbol{\phi}$ cause a change in the active set. The result is that the structures of the matrix $\mathbf{K}_c$ is no longer the same. To prevent this, the assemblation of $\mathbf{K}_c(\mathbf{v}+\epsilon\boldsymbol{\phi})$ is made basing on the active set used for $\mathbf{K}_c(\mathbf{v})$. In other words, when the numerical derivative is computed no new search for the closest master segment of each slave node is performed. The active set is not changed either. The disadvantage is that penetration can occur or that adhesive forces are applied for a degree of freedom in the active set whose gap was closed but becomes open now. But taking into account the order of magnitude of $\epsilon\boldsymbol{\phi}$ with $\epsilon = 10^{-7}$ these effects are negligible.

Concerning the strategy for the active set, the examples showed that the converged active set strategy did not provide any advantages compared to the active set strategy. In the contrary, in some computations the converged active set strategy lead to divergence.

Solve for ${}_{\Delta}\mathbf{v}^{i+1}$:

$$\begin{aligned}
\left[\mathbf{K}_T(\mathbf{v}^i) + \mathbf{K}_c(\mathbf{v}^i)\right]\ {}_{\Delta}\mathbf{v}_P^{i+1} &= \mathbf{P} \\
\left[\mathbf{K}_T(\mathbf{v}^i) + \mathbf{K}_c(\mathbf{v}^i)\right]\ {}_{\Delta}\mathbf{v}_G^{i+1} &= -\mathbf{G}_S(\mathbf{v}^i) - \mathbf{G}_c(\mathbf{v}^i)
\end{aligned}$$

Compute:

$$\begin{aligned}
\mathbf{h}_1^i &= \frac{1}{\epsilon}\left[\mathbf{K}_T(\mathbf{v}^i+\epsilon\boldsymbol{\phi}^i)\ {}_{\Delta}\mathbf{v}_P^{i+1} + \mathbf{K}_c(\mathbf{v}^i+\epsilon\boldsymbol{\phi}^i)\ {}_{\Delta}\mathbf{v}_P^{i+1} - \mathbf{P}\right] \\
\mathbf{h}_2^i &= \frac{1}{\epsilon}\left[\mathbf{K}_T(\mathbf{v}^i+\epsilon\boldsymbol{\phi}^i)\ {}_{\Delta}\mathbf{v}_G^{i+1} + \mathbf{K}_c(\mathbf{v}^i+\epsilon\boldsymbol{\phi}^i)\ {}_{\Delta}\mathbf{v}_G^{i+1} + \mathbf{G}_S(\mathbf{v}^i) + \mathbf{G}_c(\mathbf{v}^i)\right]
\end{aligned}$$

Solve for ${}_{\Delta}\boldsymbol{\phi}^{i+1}$:

$$\begin{aligned}
\left[\mathbf{K}_T(\mathbf{v}^i) + \mathbf{K}_c(\mathbf{v}^i)\right]\ {}_{\Delta}\boldsymbol{\phi}_1^{i+1} &= -\mathbf{h}_1^i \\
\left[\mathbf{K}_T(\mathbf{v}^i) + \mathbf{K}_c(\mathbf{v}^i)\right]\ {}_{\Delta}\boldsymbol{\phi}_2^{i+1} &= -\mathbf{h}_2^i
\end{aligned}$$

Compute increments:

$$\begin{aligned}
{}_{\Delta}\lambda^{i+1} &= \frac{-\boldsymbol{\phi}^{iT}\ {}_{\Delta}\boldsymbol{\phi}_2^{i+1} + \|\boldsymbol{\phi}^i\|}{\boldsymbol{\phi}^{iT}\ {}_{\Delta}\boldsymbol{\phi}_1^{i+1}} \\
{}_{\Delta}\mathbf{v}^{i+1} &= {}_{\Delta}\lambda^{i+1}\ {}_{\Delta}\mathbf{v}_P^{i+1} + {}_{\Delta}\mathbf{v}_G^{i+1}
\end{aligned}$$

Update:

$$\lambda^{i+1} = \lambda^i + {}_{\Delta}\lambda^{i+1}\ , \quad \mathbf{v}^{i+1} = \mathbf{v}^i + {}_{\Delta}\mathbf{v}^{i+1}\ ,$$
$$\boldsymbol{\phi}^{i+1} = {}_{\Delta}\lambda^i\ {}_{\Delta}\boldsymbol{\phi}_1^{i+1} + {}_{\Delta}\boldsymbol{\phi}_2^{i+1}$$

Table 7.3: Partitioning algorithm for the extended system with contact

Chapter 8

Examples

The algorithms described in chapter 7 were tested in several examples. For the detection of critical points the CDM, the extended system with the eigenvalue problem as constraint and the one step prediction with the extended system were applied. Inequality constrains were introduced in the examples by the occurrence of damage or contact.

The algorithms have been implemented in various finite element programs. The simple damage model was combined with the CDM in the programs *truss-test* with truss elements and in *solid-test* with two dimensional 8 node quadrilaterals. Both programs were written by W.T. Matias the author of [Matias, 1996] and included already the CDM as a method for the critical point prediction. All the algorithms involving the extended system were implemented in the 'Finite Element Analysis Program' (FEAP) written by R.L. Taylor, see [Zienkiewicz and Taylor, 1989] and [Zienkiewicz and Taylor, 1991] for further details of the code. This implementation comprises the simple damage model for truss and two dimensional quadrilaterals, the displacement boundary conditions with the penalty method (section 7.4), the one step prediction with the extended system (section 7.3), the contact algorithms of chapter 5 and the extended system with the eigenvalue problem constraint (section 6.5.1).

This chapter is divided in two parts. The first part is dedicated to the comparison between the CDM and the extended system. Among the linear elastic examples that will be shown, the simple damage model as a simple form of inequality constraint was tested. In the second part only the extended system will be studied for various continuum mechanical contact problems.

8.1 Comparison of CDM and extended system

The comparison of both methods in this section is made by means of standard examples that can be found in literature. They range from simple truss problems to two and three dimensional ones with solid elements. Almost all of them can be found in [Matias, 1996]. Except for the last example, where three dimensional solid elements were used, damage was introduced in all of them.

8.1.1 Simple truss structure

The first example is the simple truss structure from [Wriggers et al., 1988]. It consists of 7 nodes and 10 truss elements. An outline of the structure including the geometrical data can be seen in figure 8.1. The product of Young's modulus and cross section area is $EA = 5000$, a unit load is applied at the center node.

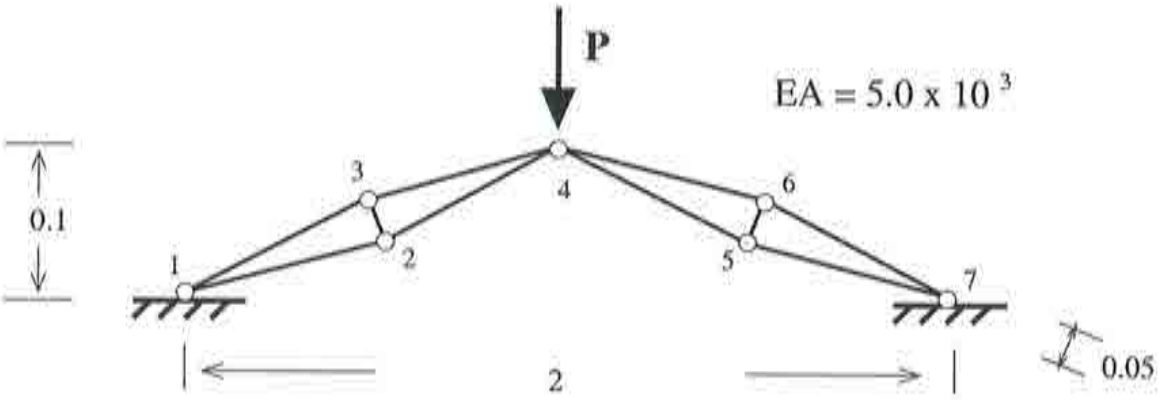

Figure 8.1: Simple truss structure

Although very simple this structure allows the demonstration of limit load points as well as bifurcation points. Plotting the negative y-displacement of the center node 4, the equilibrium path shown in figure 8.2 is obtained.

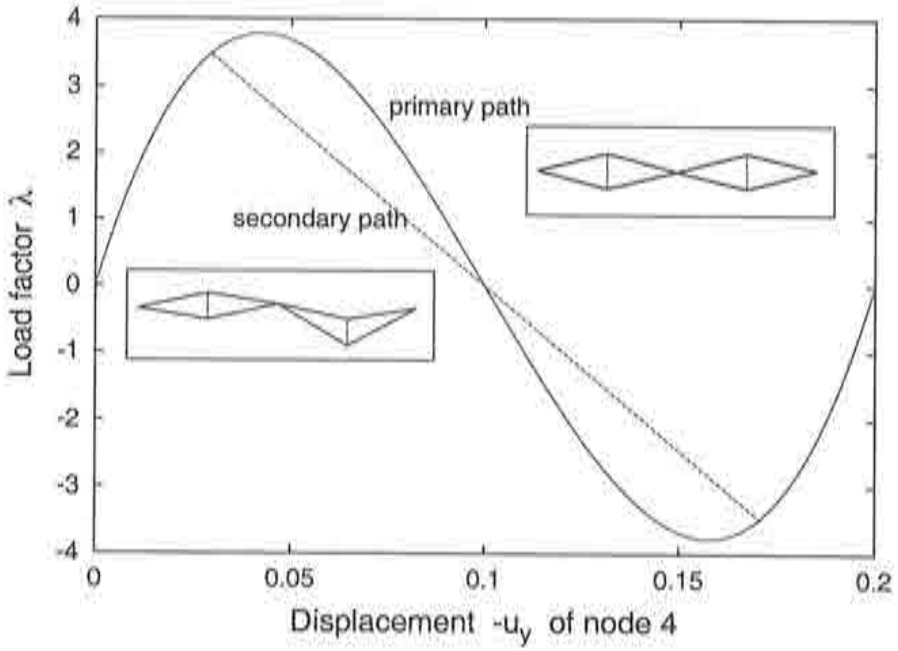

Figure 8.2: Equilibrium path of the simple truss structure

The path has a first bifurcation point B_1 at a load level of $\lambda = 3.474$ with $u_y = -0.0293$. Here the secondary path associated with the asymmetric buckling pattern indicated in

the left small picture in figure 8.2 branches off. Branch switching to the secondary path was performed by the method described in section 6.6. The primary path undergoes a symmetric buckling at the limit load point L_1 with $(u_y; \lambda) = (-0.042; 3.777)$. Further critical points are the second limit load point L_2 at $(u_y; \lambda) = (-0.157; -3.777)$ and the second bifurcation point B_2 at $(u_y; \lambda) = (-0.171; -3.474)$.

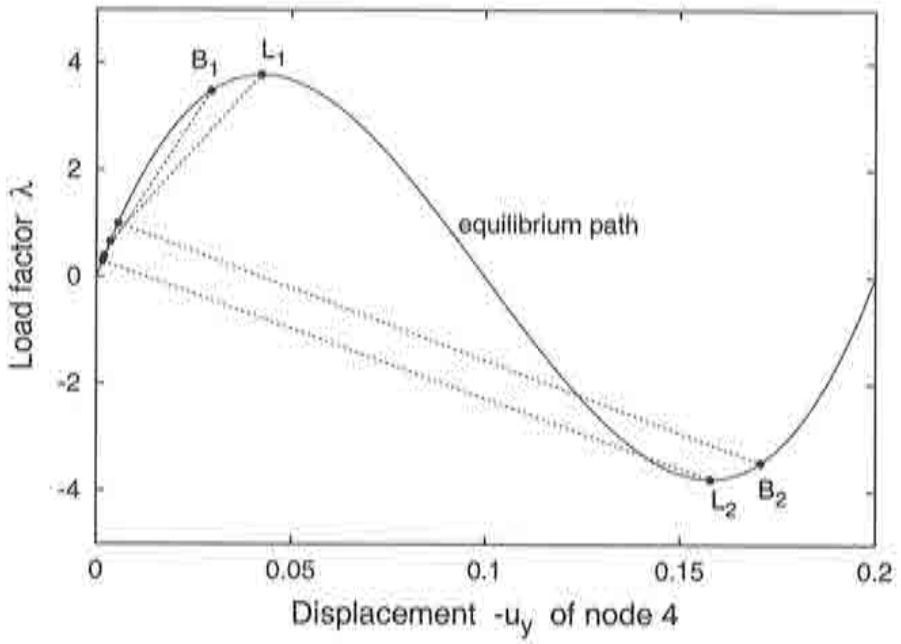

Figure 8.3: Computation of the critical points with the extended system

Figure 8.3 demonstrates the direct computation of the critical points with the extended system. The extended system computations are symbolized by the dashed lines in figure 8.3 with the starting points and the yielding critical points as dots. With different starting values for the eigenvector ϕ all the critical points can be obtained departing from points at the early state of path computation. The number of iterations necessary for the convergence of the extended system typically lies in the range of 5–10. The fact that even the remote critical points L_2 and B_2 can be computed directly starting from points located at the very beginning of the equilibrium path is not common. Conveniently it can be expected to obtain those points within closer distances. [Wriggers et al., 1988] demonstrated a detection of these critical points using the extended system with starting values of $u_y \approx -0.1$. Due to the good results this examples can serve as a primary example for the potential of the extended system.

The diagram 8.4 with the prediction made with the CDM needs some explication to be understood correctly. Starting from every equilibrium point (u^t, λ^t) of a path computation with an arclength procedure, a prediction according to the algorithm of section 6.4 was made giving the estimated values u^e and λ^e. The points in figure 8.4 denoted by 'critical load' have the coordinates $(u^t; \lambda^e)$ and are thus a plot of the estimated critical load against the current displacements. The points denoted by 'critical displacement' are a plot of the current load against the estimated critical displacements $(u^e; \lambda^t)$. As the diagram shows even the first predictions yield critical values quite close to the exact ones. After the

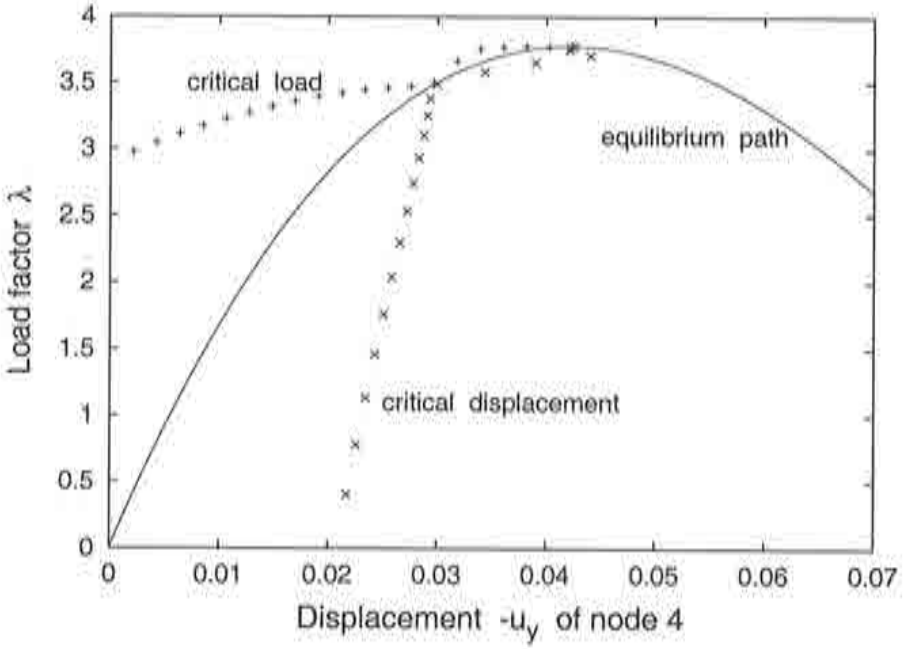

Figure 8.4: Critical point prediction with the CDM

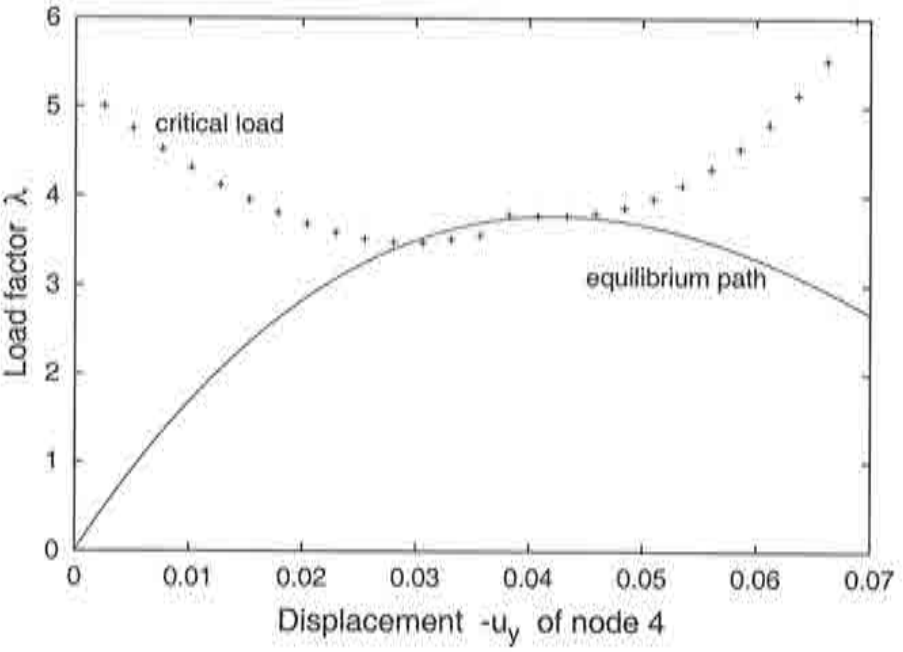

Figure 8.5: One step prediction with the extended system

bifurcation point B_1 is passed the predicted critical values head for the limit load point L_1.

Performing the one step prediction with the extended system in each point of the path computation the curve of figure 8.5 results. The points are a plot of the predicted critical load at the current displacement state (u^t, λ^c). To study the behavior of the

method even after the critical point is passed, the predictions were not stopped when the path computation had reached the critical point. The first predicted loads are quite good although they are not as close to the exact value as the CDM predictions. Closer to the critical point the predictions become more and more exact. The 'lasting effect' of a critical point can be seen when looking at the values after passing the critical point. A switch from the prediction of the bifurcation point B_1 to the limit load point L_1 occurs approximately in the middle between both points.

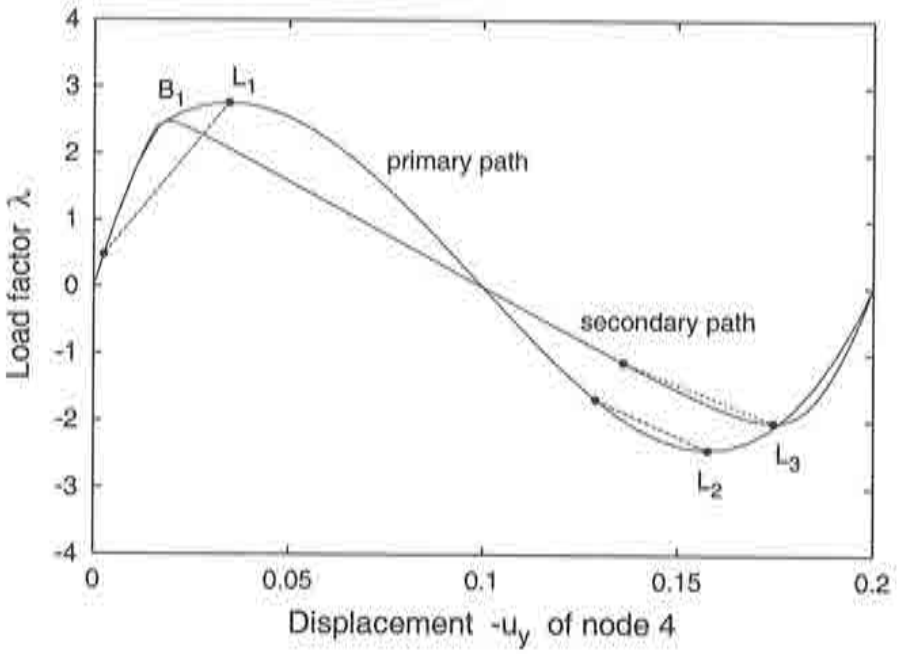

Figure 8.6: Equilibrium path with damage $\tau_0 = 0.1$, $H = 1$

With damage the structure suffers degradation which affects as well the equilibrium path. The damage parameters in all examples were chosen in such a way, that the occurrence of damage becomes noticeable in the equilibrium path before a critical point is reached. This way the influence of the damage inequality constraint on the critical point computation can be studied. On the other hand this means that the values of the damage parameters are not always realistic compared to real–life engineering applications.

Figure 8.6 shows the equilibrium path for damage with an initial threshold value of $\tau_0 = 0.1$ and a hardening parameter of $H = 1.0$. The limit load is lesser, L_1 has the coordinates $(u_y; \lambda) = (-0.035; 2.755)$. L_1 and the other limit points $L_2 : (u_y; \lambda) = (-0.157; -2.429)$, $L_3 : (u_y; \lambda) = (-0.174; -2.02)$ can be computed with the extended system as indicated by the dashed lines in figure 8.6. Bifurcation points $B_1 : (u_y; \lambda) \approx (-0.019; 2.473)$ and a second one $B_2 : (u_y; \lambda) \approx (-0.173; -2.123)$ could not be calculated directly. Although it looks like L_3 on the secondary branch is a bifurcation point, where path switching is possible, it is not. The reason is that each branch has a different loading history, which implies as well, that the individual damage parameters do not coincide and both structures are substantially different.

Note, that large load steps will always lead to inaccuracies when damage is involved, because of the numerical approximation that is made. This effect already noticeable

during a path computation with rather large load steps, is especially true for the extended system, where the step size is not limited as in arclength procedures. In this simple example however, the calculation of L_1 remains unaffected by this effect.

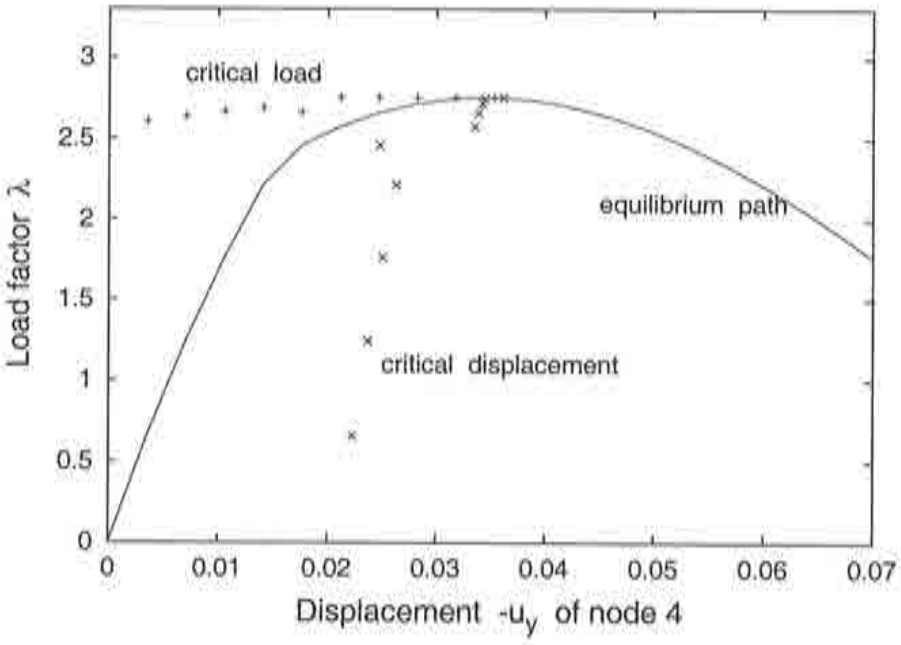

Figure 8.7: CDM predictions with damage $\tau_0 = 0.1$, $H = 1$

The results for the CDM predictions (see diagram 8.7) are more or less as expected. The predictions seem to head towards the bifurcation point B_1 but detect L_1 instead. Comparing the predicted critical loads in figure 8.7 and the undamaged case in 8.3 the effect of the algorithm described in section 7.2 is noticeable. Already at states where the equilibrium path is not degradated the critical load is lesser than for the undamaged structure.

The one step prediction with the extended system in figure 8.8 shows the influence of damage not prior to the degradation of the equilibrium path. Almost the same effect as with the CDM can be contemplated in the vicinity of the bifurcation point B_1. The method seems to predict B_1 but goes towards L_1 in the end.

The second damage case has the parameters $\tau_0 = 0.1$ and $H = 0.5$. Equilibrium path and the results of the extended system computations are plotted in diagram 8.9. The coordinates of the critical points are, $B_1 : (u_y; \lambda) \approx (-0.016; 2.39)$, $L_1 : (u_y; \lambda) = (-0.028; 2.48)$, $L_2 : (u_y; \lambda) = (-0.157; -1.98)$, $B_2 : (u_y; \lambda) = (-0.17; -1.82)$ and $B_3 : (u_y; \lambda) = (-0.175; -1.57)$.

For this example the CDM values are quite exact from the beginning, which is especially true for the critical loads (see diagram 8.10). The one step prediction in figure 8.11 shows diffuse results . In between the critical points B_1 and L_1 the points scatter around the equilibrium path but give the exact result in the limit load point L_1.

The damage parameters $\tau_0 = 0.05$ and $H = 1.0$ yield the curves depicted in figure 8.12. Bifurcation point $B_1 : (u_y; \lambda) = (-0.019; 1.97)$ and limit load point $L_1 : (u_y; \lambda) = (-0.038; 2.31)$ can be calculated with the extended system using different starting values.

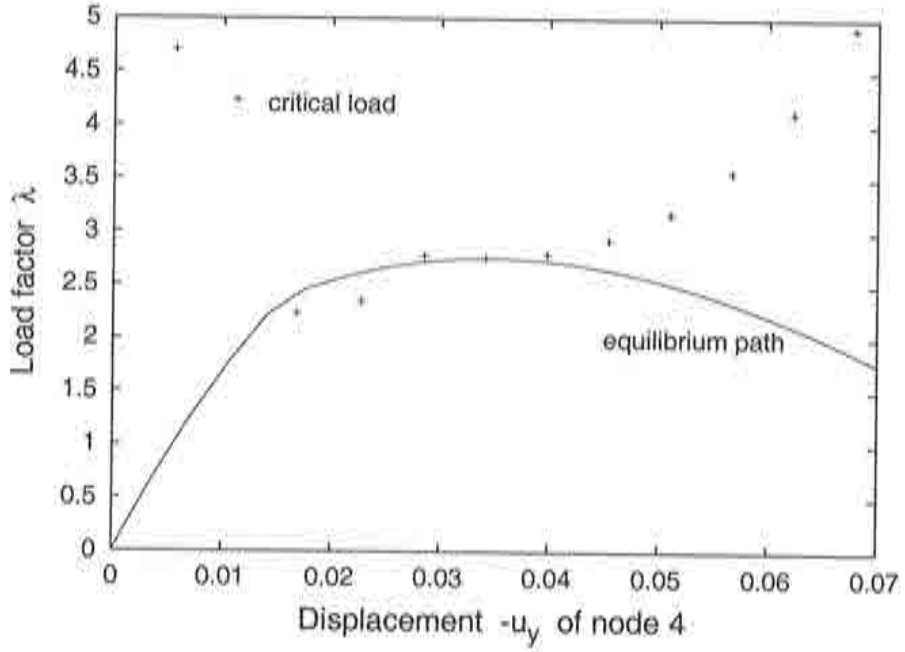

Figure 8.8: One step prediction with damage $\tau_0 = 0.1$, $H = 1$

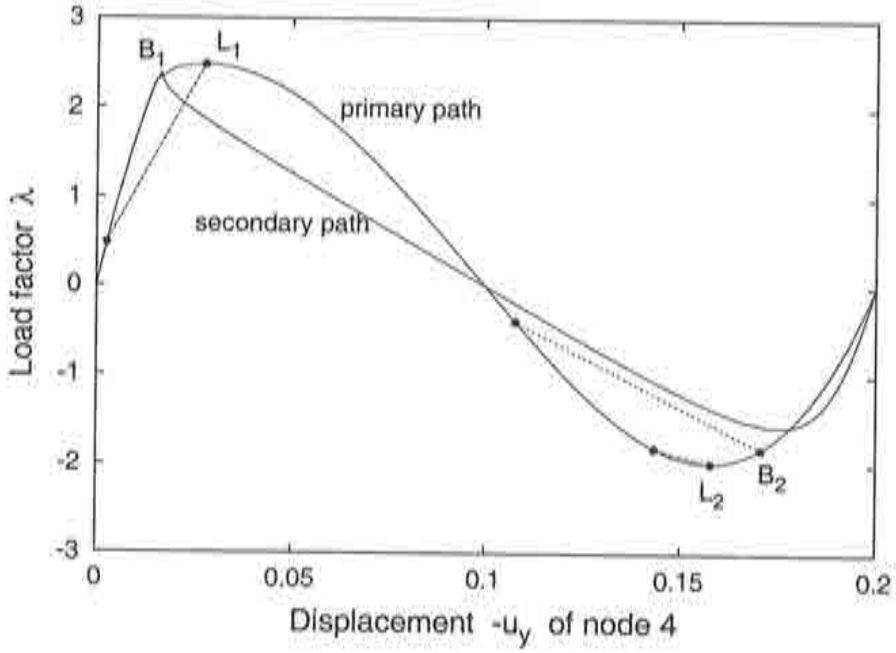

Figure 8.9: Equilibrium path with damage $\tau_0 = 0.1$, $H = 0.5$

This time the CDM detects both points B_1 and L_1 as can be seen in figure 8.13, whereas the one step prediction curve of figure 8.14 only goes through the bifurcation point B_1.

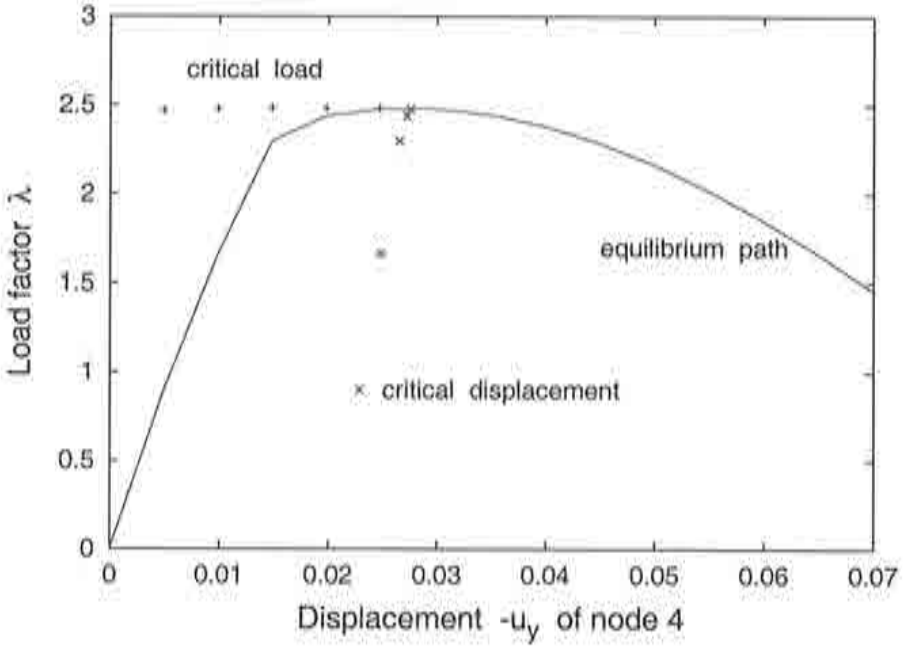

Figure 8.10: CDM prediction with damage $\tau_0 = 0.1$, $H = 0.5$

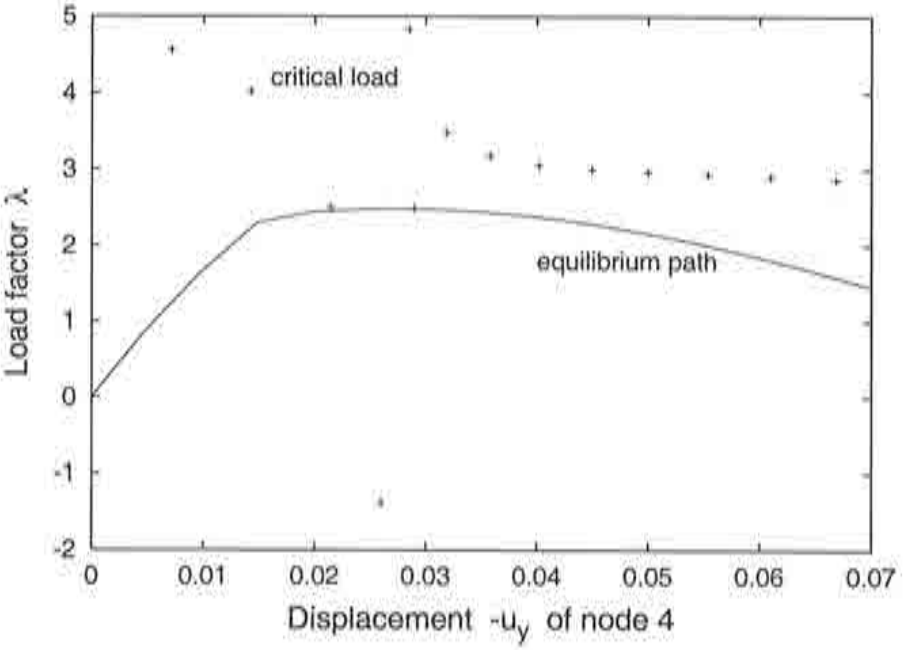

Figure 8.11: One step prediction with damage $\tau_0 = 0.1$, $H = 0.5$

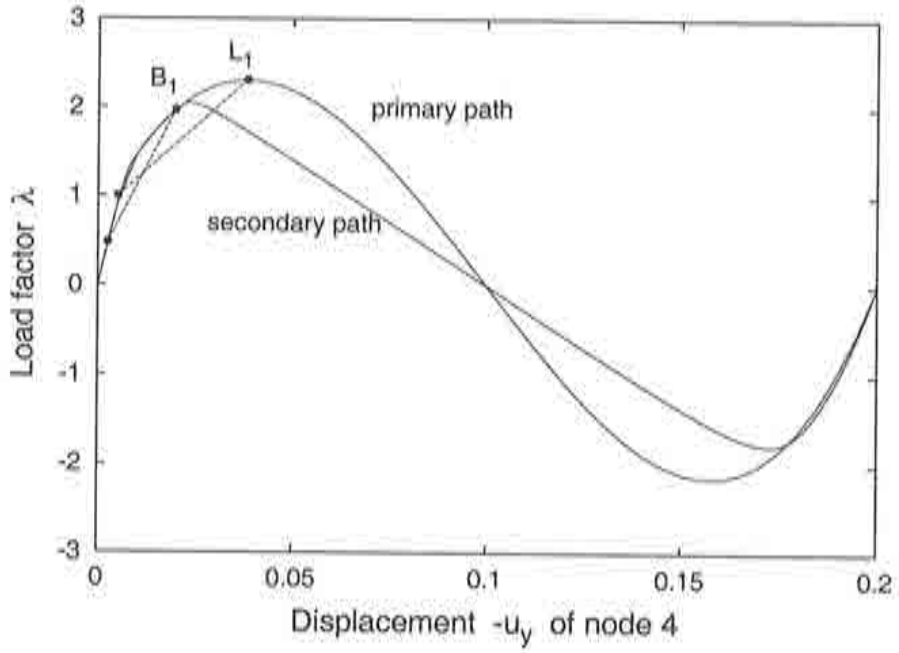

Figure 8.12: Equilibrium path with damage $\tau_0 = 0.05$, $H = 1$

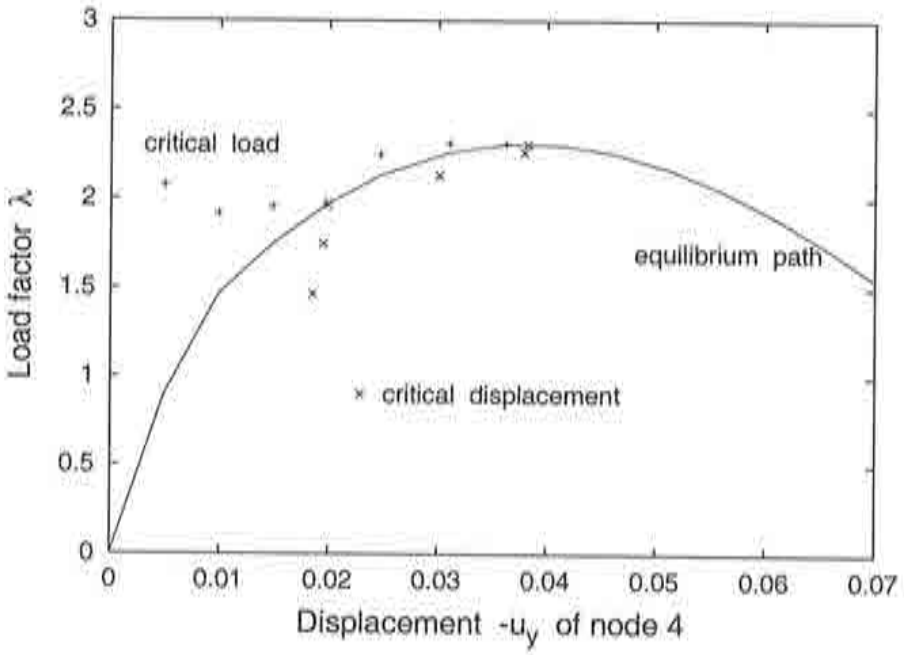

Figure 8.13: CDM prediction with damage $\tau_0 = 0.05$, $H = 1$

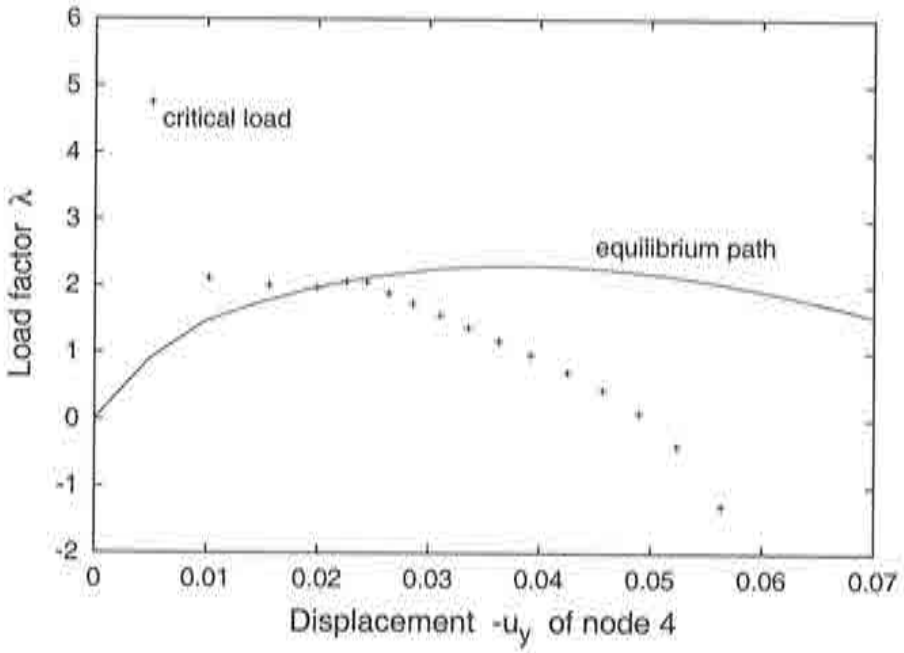

Figure 8.14: One step prediction with damage $\tau_0 = 0.05$, $H = 1$

8.1.2 Bridge–truss structure

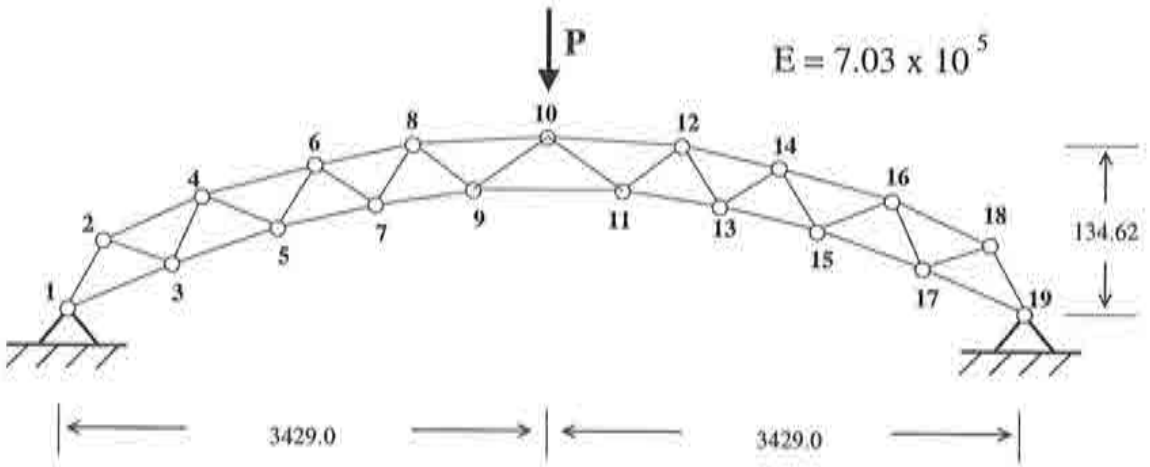

Figure 8.15: Bridge–truss structure modeled with truss elements

The second example is the bridge–truss structure of figure 8.15. It was analyzed before by [Kondoh and Atluri, 1985] or [Oñate and Matias, 1996]. The structure consists of 19 nodes and 35 truss elements connecting them. The geometric data are given in figure 8.15. A unit load is placed in the apex of the bridge, where node 10 is situated. All the truss elements have the same Young's modulus of $E = 7.03 \times 10^5$, but different cross section areas, which are given in table 8.1

Element connecting nodes N_1 – N_2	Area A
1–2, 2–4, 4–5, 6–7, 8–9, 9–11, 11–12, 13–14, 15–16, 16–18, 18–19	51.61
2–3, 17–18	64.52
3–4, 5–6, 14–15, 16–17	83.87
4–6, 14–16	96.77
7–8, 9–10, 10–11, 12–13	103.23
7–9, 11–13	161.29
6–8, 12–14	193.55
5–7, 13–15	258.06
1–3, 3–5, 15–17, 17–19	290.32
8–10, 10–12	309.68

Table 8.1: Cross section areas of the bridge–truss structure

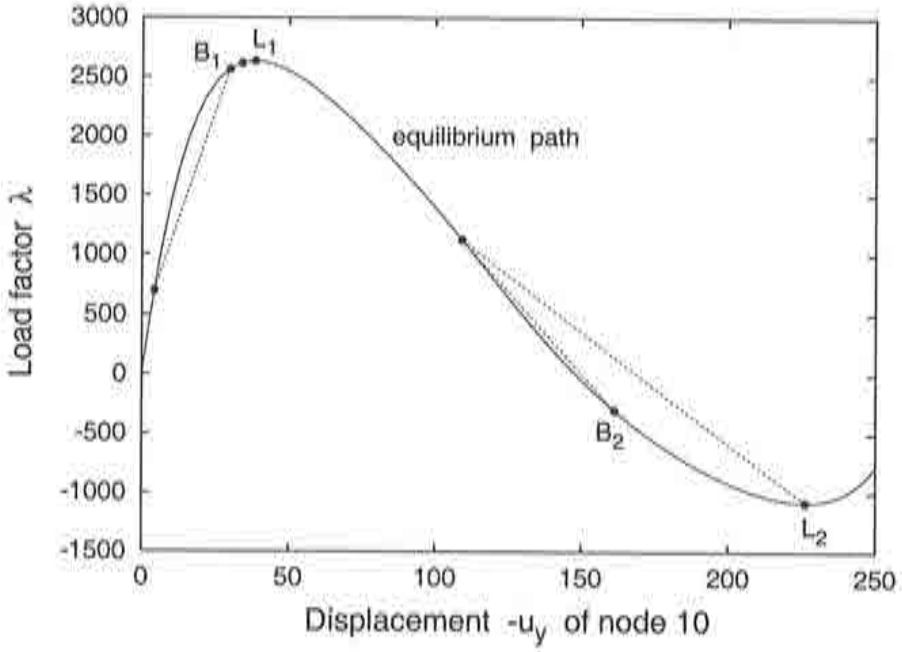

Figure 8.16: Equilibrium path with extended system results

In diagram 8.16 the equilibrium path can be seen for the negative y–displacements of node 10. All the critical points, bifurcation points $B_1 : (u_y; \lambda) = (-29.7; 2563)$ and $B_2 : (u_y; \lambda) = (-161.3; -301)$, as well as the limit load points $L_1 : (u_y; \lambda) = (-38.3; 2632)$ and $L_2 : (u_y; \lambda) = (-226; -1078)$ can be obtained by the extended system as the dashed lines indicate. The results are in good accordance with the literature. Except for the first limit load point L_1, the extended system was started a larger distance away from the critical points. The starting approximation for the eigenvector ϕ in the extended system procedure was the unit vector for B_1 and L_2, one step of inverse iteration for L_1 and the current displacement vector for B_2.

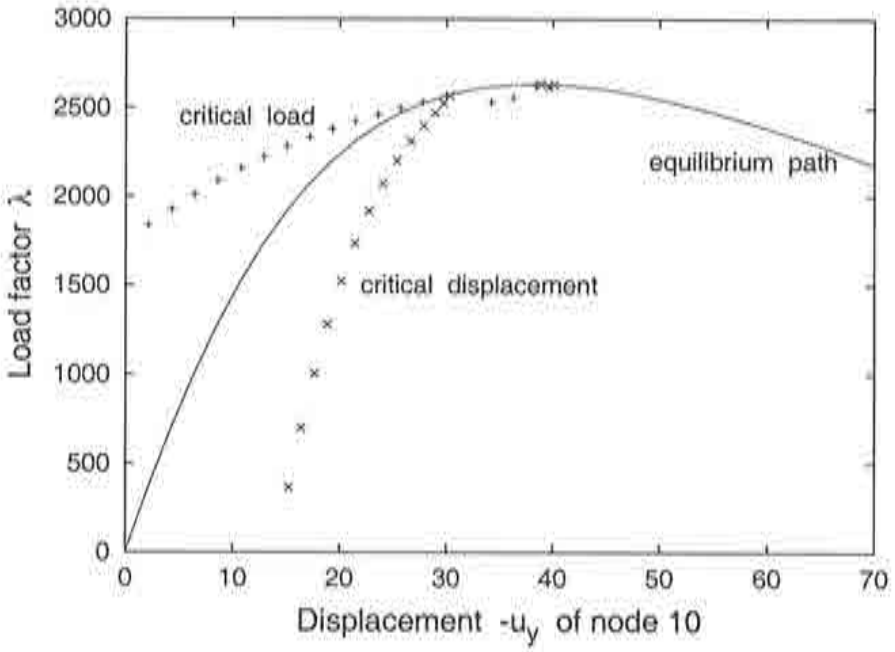

Figure 8.17: CDM prediction for the bridge–truss structure

The results with the CDM are quite good, too. As figure 8.17 demonstrates the predictions head towards the bifurcation point B_1. The limit load point is predicted as well, but not very good.

The one step prediction with the extended system in figure 8.18 goes smoothly toward B_1. The first load values are too high but comparing them with the too low values of the CDM, the absolute difference to the exact critical load is more or less equal. The curve hits also L_1, the jump in between both critical points marks the switching from one point to the other.

When damage with the parameters $\tau_0 = 2.5$ and $H = 1.0$ is involved the first bifurcation point vanishes and only the limit load point L_1 remains at $(u_y; \lambda) = (-29.7; 2273)$ (see figure 8.19). The first bifurcation point is located now on the declining path $B_1 : (u_y; \lambda) = (-190; -582.2)$ and the second limit load point at $L_2 : (u_y; \lambda) = (-231; -880.2)$. The extended system converges correctly against all three points.

The CDM prediction in figure 8.20 also gives the correct results in the end. The tilt in the critical load curve, which is the effect of the enhancement proposed in section 7.2, occurs later in the path history compared to the first example.

The one step prediction of figure 8.21 shows two discontinuities , the end result however is correct.

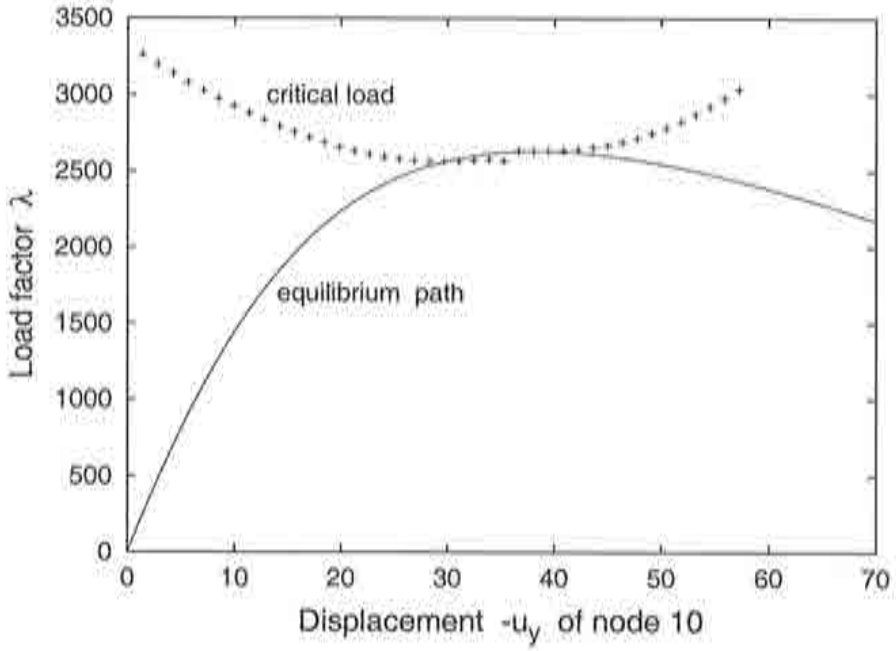

Figure 8.18: One step prediction for the bridge–truss structure

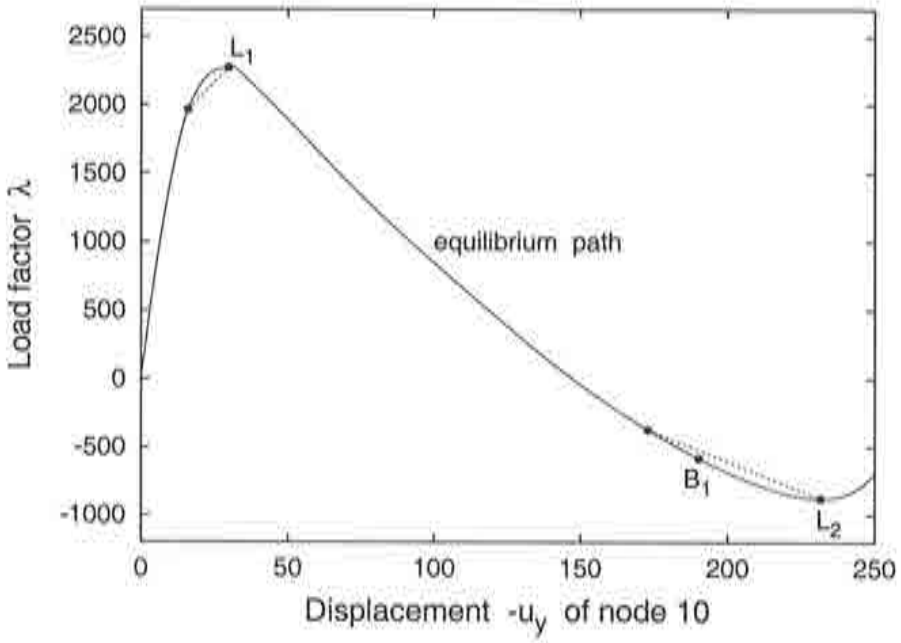

Figure 8.19: Equilibrium path with damage $\tau_0 = 2.5$, $H = 1.0$

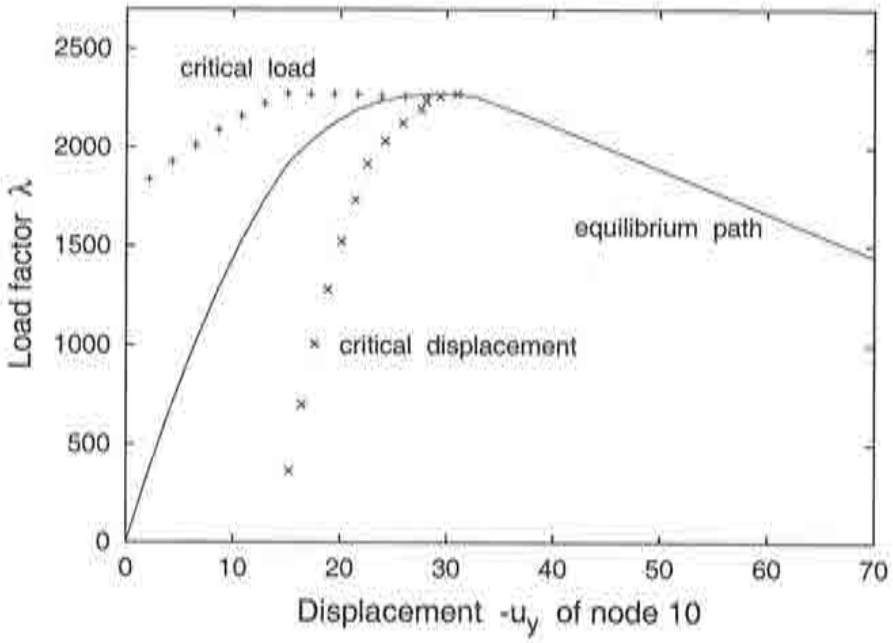

Figure 8.20: CDM prediction with damage $\tau_0 = 2.5$, $H = 1.0$

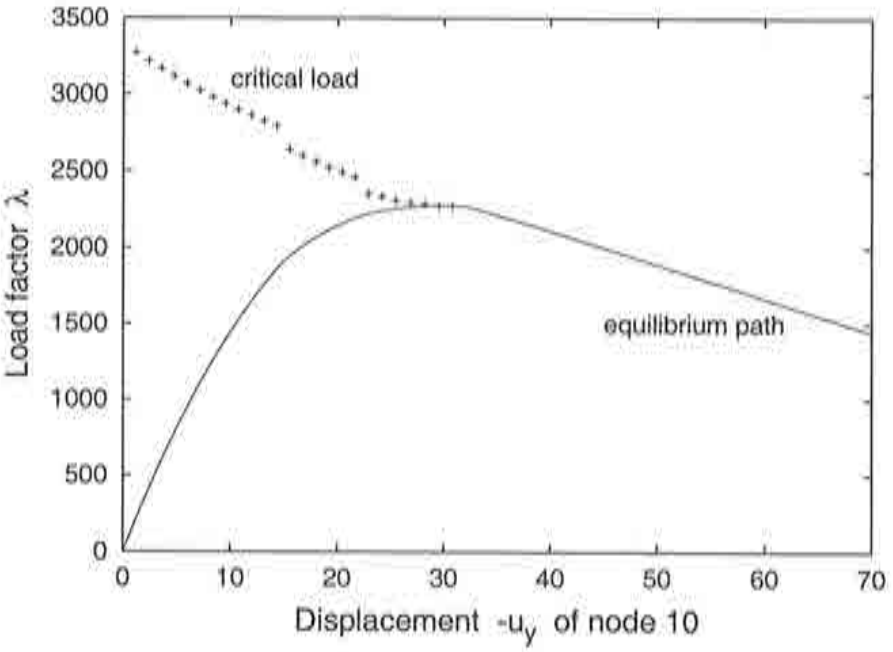

Figure 8.21: One step prediction with damage $\tau_0 = 2.5$, $H = 1.0$

8.1.3 3D star–shaped dome

The next example is the star–shaped dome of figure 8.22. It is geometrically identical to the one studied in [Papadrakakis, 1981] or [Wriggers et al., 1988], but has vertical loads applied in all free nodes as in [Oñate and Matias, 1996]. The structure is formed by 13 nodes and 24 truss elements, the product of Young's modulus and cross section area is $EA = 10^4$.

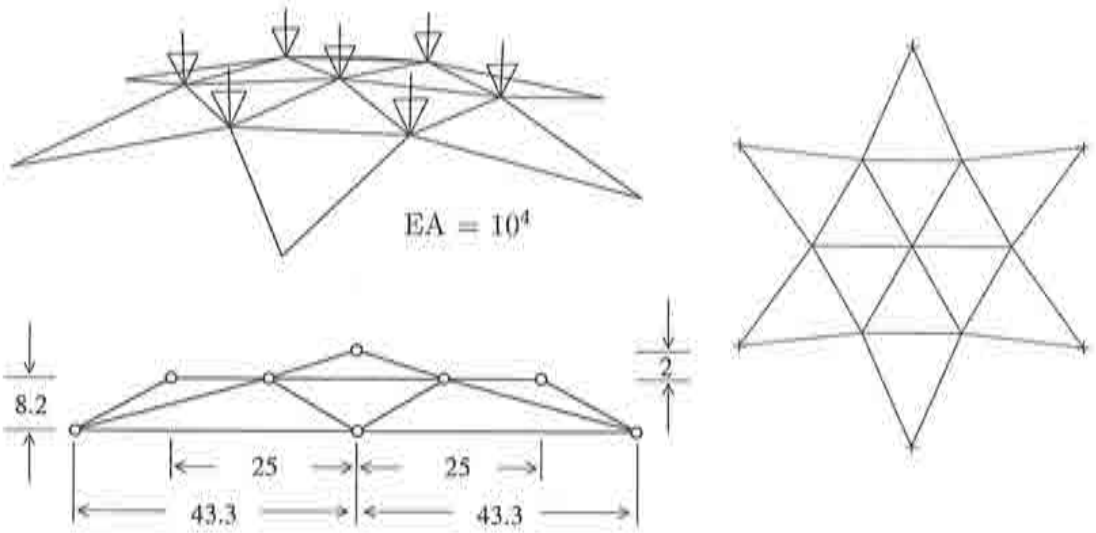

Figure 8.22: 3d star–shaped dome

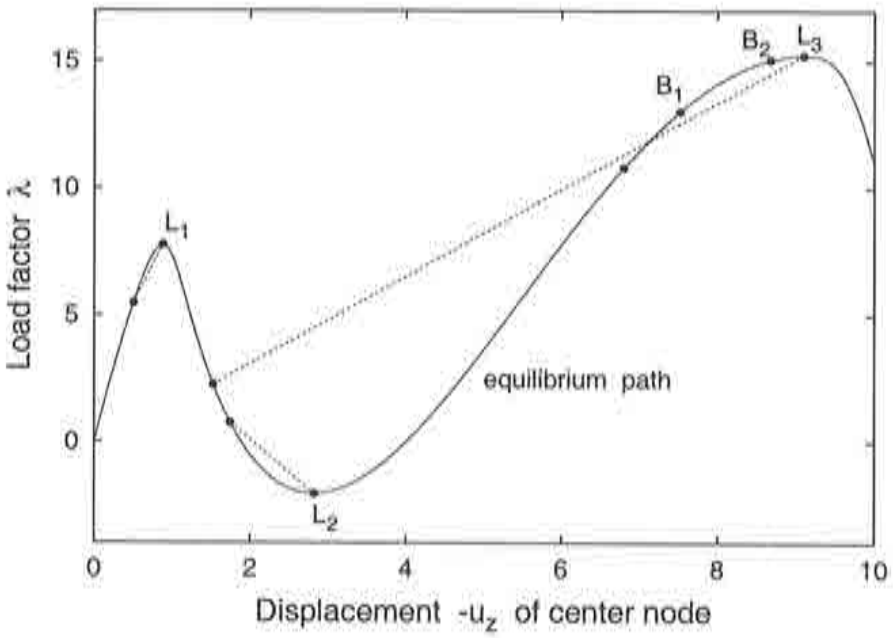

Figure 8.23: Equilibrium path with critical points of the star–shaped dome

The equilibrium path, plotted in figure 8.23 for negative vertical displacements of the center node, has various critical points. Except for the bifurcation point B_2, which could be computed only in the closer vicinity, all were obtained with the extended system without problems. The data of the points are: $L_1 : (u_z; \lambda = (-0.88; 7.76)$, $L_2 : (u_z; \lambda = (-2.81; -2.05)$, $B_1 : (u_z; \lambda = (-7.52; 13.02)$, $B_2 : (u_z; \lambda = (-8.67; 15.06)$, $L_3 : (u_z; \lambda = (-9.09; 15.2)$.

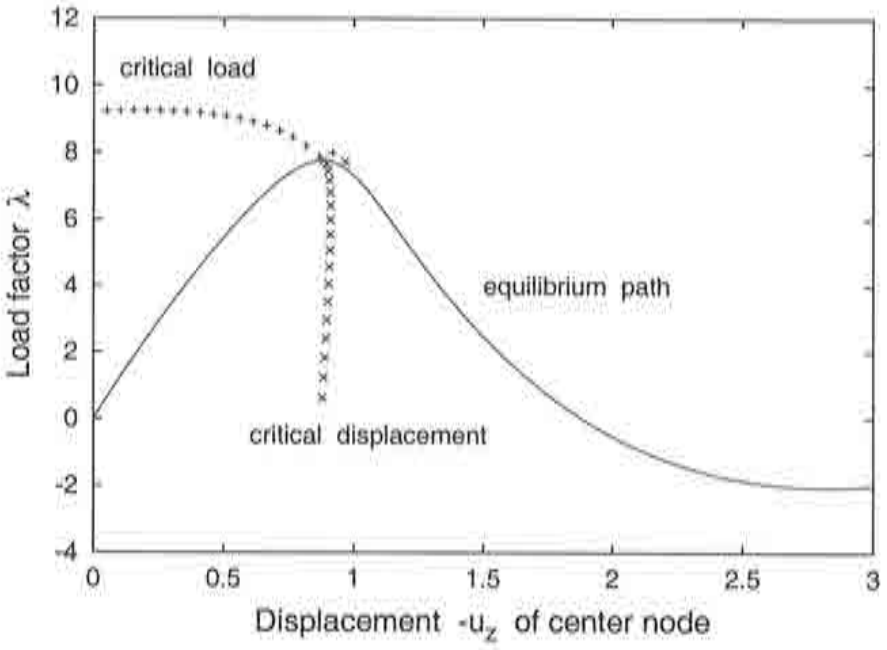

Figure 8.24: CDM predictions for the star–shaped dome

The first limit load point is predicted by the CDM rather good, as figure 8.24 shows. Compared to the one step prediction of figure 8.25 it is slightly better.
Internal degradation with the damage parameters $\tau_0 = 0.1$ and $H = 1.0$ alters the values of the limit load points $L_1 : (u_z; \lambda) = (-0.82; 5.19)$ and $L_2 : (u_z; \lambda) = (-2.82; -1.601)$. The extended system again has no difficulties in finding those points (see diagram 8.26).

Looking at the CDM (diagram 8.27) and the one step prediction (diagram 8.28) the CDM provides the better predictions, which is as well a consequence of the enhancements of section 7.2. The one step predictions become significantly better, when the critical point is approached.

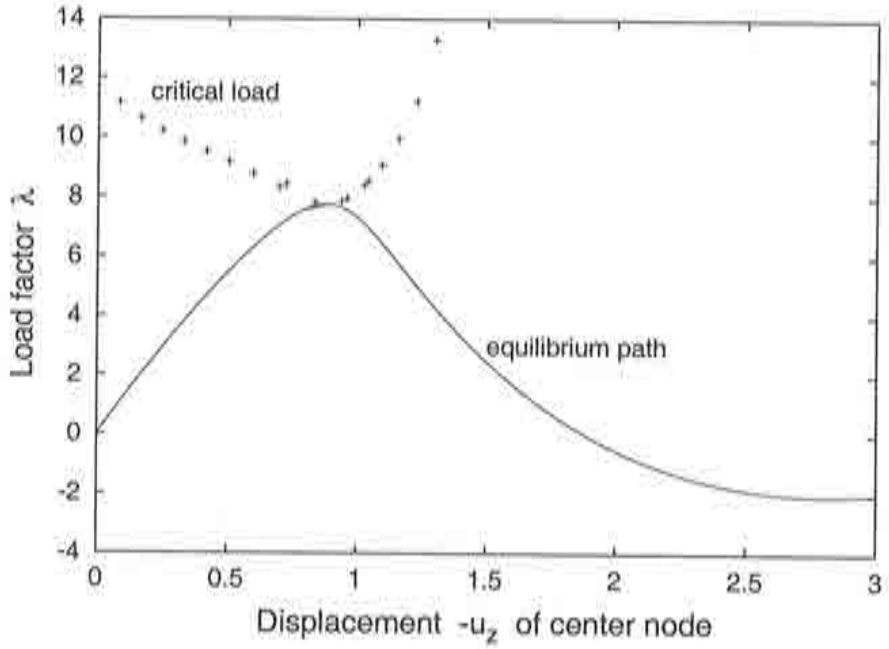

Figure 8.25: One step prediction for the star–shaped dome

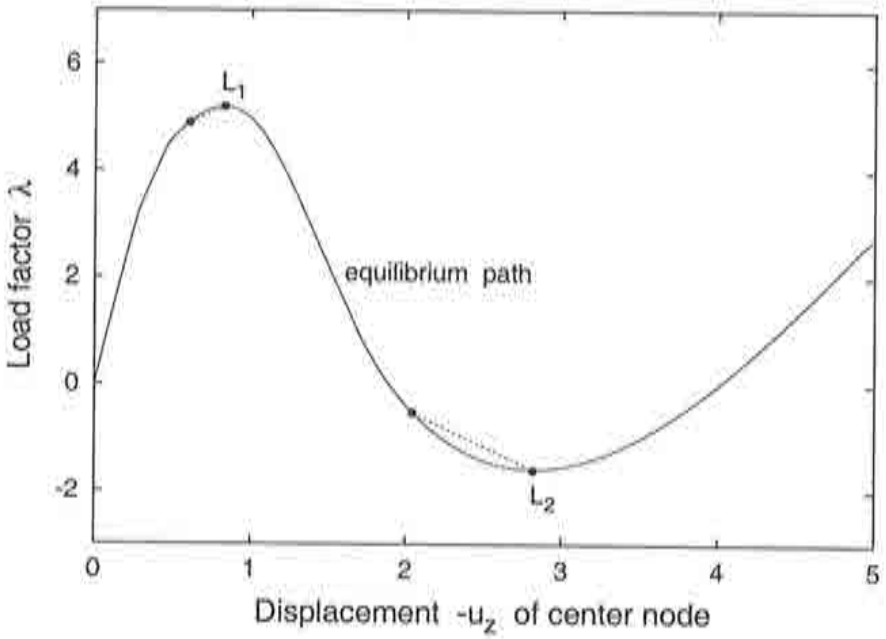

Figure 8.26: Equilibrium path with damage, $\tau_0 = 0.1, H = 1.0$

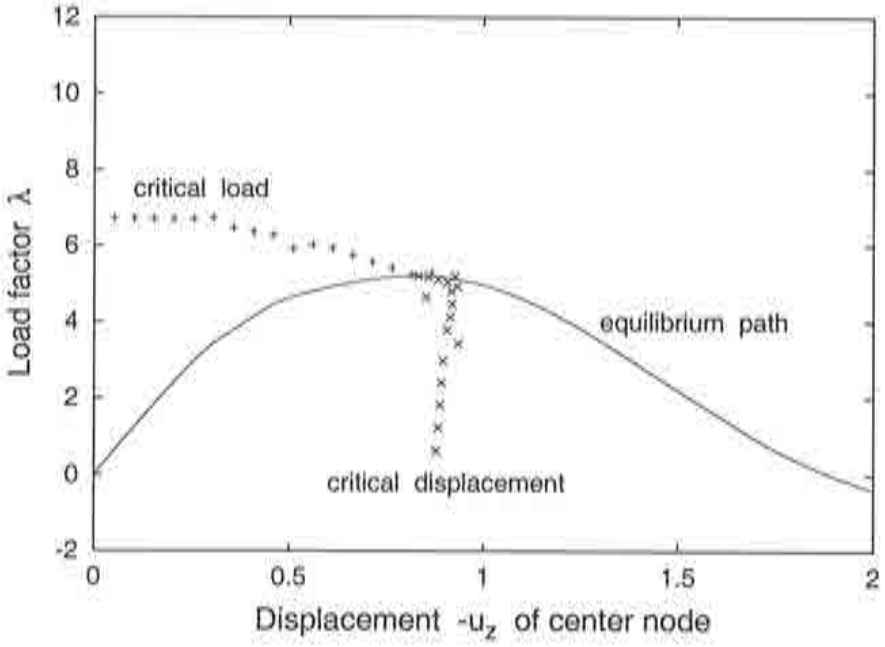

Figure 8.27: CDM prediction with damage $\tau_0 = 0.1, H = 1.0$

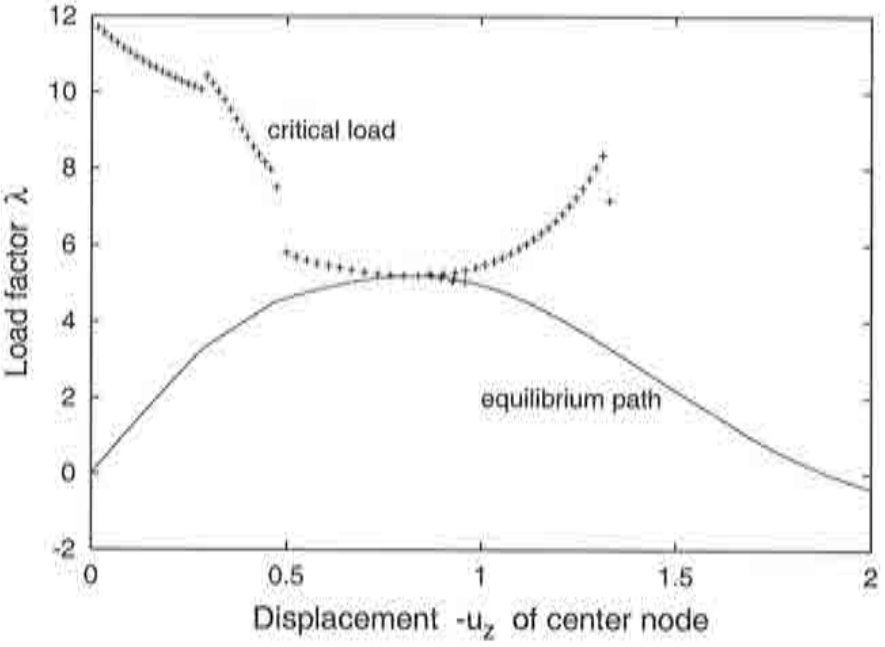

Figure 8.28: One step prediction with damage $\tau_0 = 0.1, H = 1.0$

8.1.4 3D pin–jointed truss dome

The last example with truss elements is the 3D pin–jointed truss dome that has been examined in [Choong and Hangai, 1993] and [Oñate and Matias, 1996]. Figure 8.29 shows an outline of the structure. 25 nodes are connected with 60 truss elements with Young's modulus times the cross section area $EA = 10^4$. 6 vertical loads are applied in the third level of the dome.

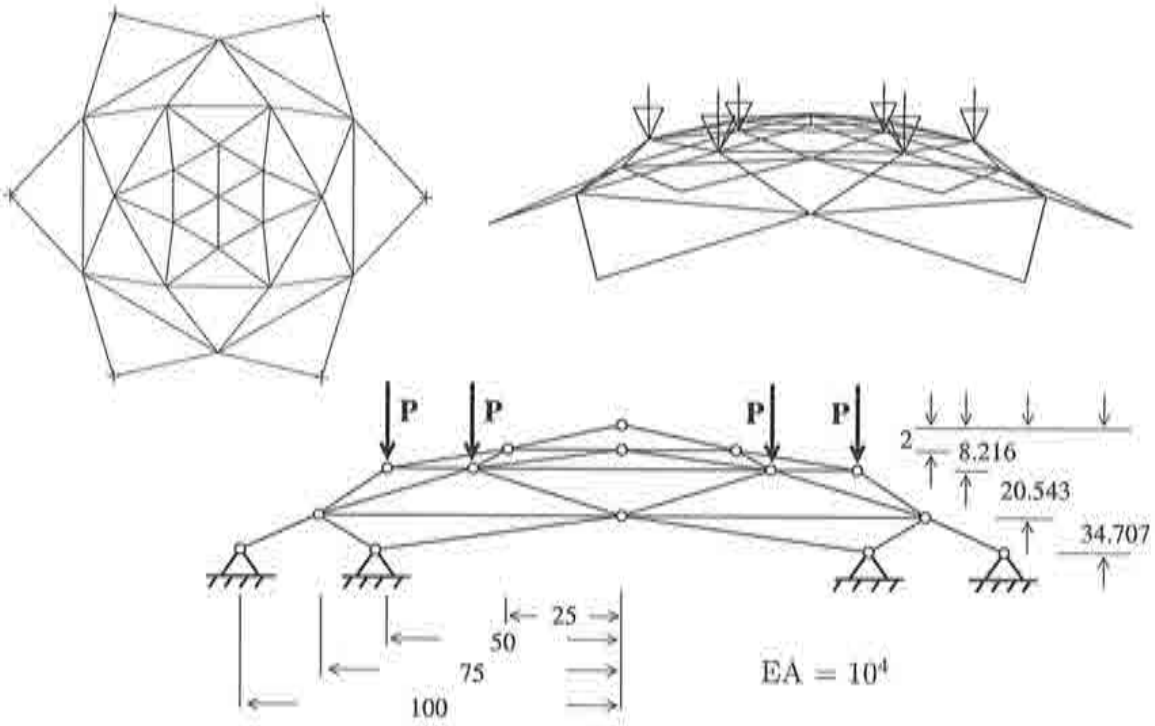

Figure 8.29: 3D pin–jointed truss dome

In figure 8.30 the load factor is plotted against the negative vertical displacement of the center node. The path has several critical points, which could all be obtained with the extended system procedure. The limit points have the coordinates $L_1 : (u_z; \lambda) = (-4.01; 31.4)$ and $L_2 : (u_z; \lambda) = (-16.7; -25.75)$, the bifurcation points $B_1 : (u_z; \lambda) = (-2.35; 25.89)$, $B_2 : (u_z; \lambda) = (-2.85; 28.7)$, $B_3 : (u_z; \lambda) = (-12.5; -17.93)$ and $B_4 : (u_z; \lambda) = (-13.78; -22.16)$.
CDM predictions in figure 8.31 and one step predictions in figure 8.32 show fundamentally different results. The critical values of the CDM head directly towards the first bifurcation point B_1, already the first values are rather exact. The other critical points are hit but not reliably predicted. The one step prediction starts with rather bad predictions and goes towards the limit point L_1, in the closer vicinity of the bifurcation points then the values change abruptly and predict the bifurcation loads.
The 3D pin jointed truss dome was studied with damage of initial threshold $\tau_0 = 0.5$ and hardening $H = 1.0$. The focus was laid on the first part of the equilibrium path, so that only a part of the critical points was computed. One bifurcation point $B_1 : (u_z; \lambda) =$

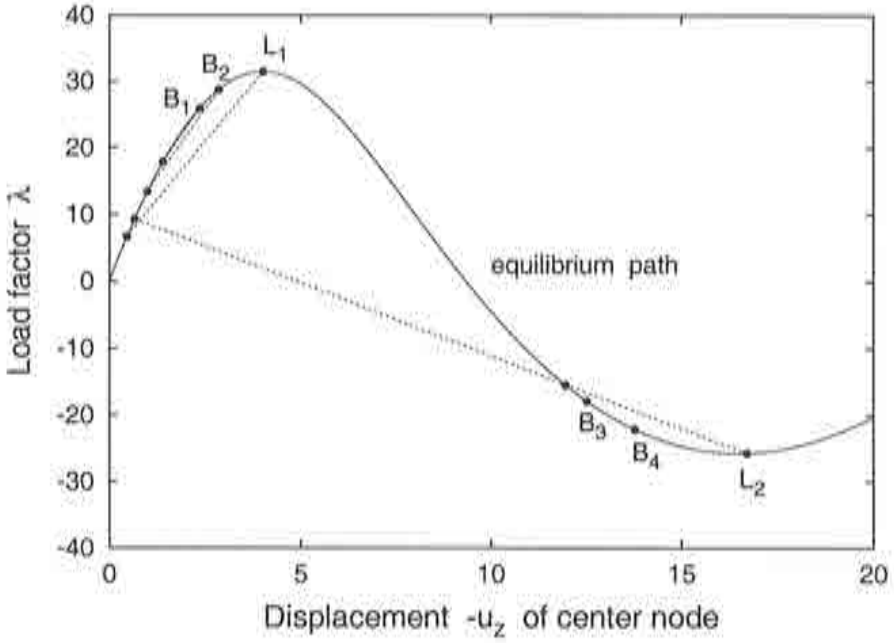

Figure 8.30: Equilibrium path of the 3D pin–jointed truss dome

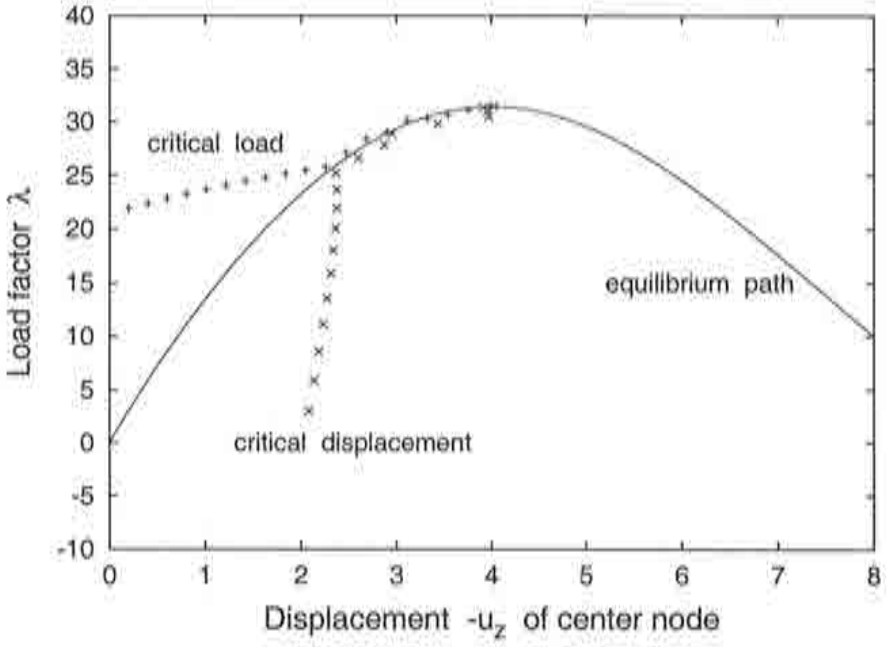

Figure 8.31: CDM prediction of the 3D pin–jointed truss dome

$(-2.19; 32.42)$ and one limit load point $L_1 : (u_z; \lambda) = (-3.16; 2.45)$ were calculated exactly with the extended system.
Looking at both predictions, the CDM prediction in figure 8.34 and the one step prediction in figure 8.35, there are no big differences to the undamaged case to be seen. The CDM converges against the bifurcation point and the one step prediction against the limit point.

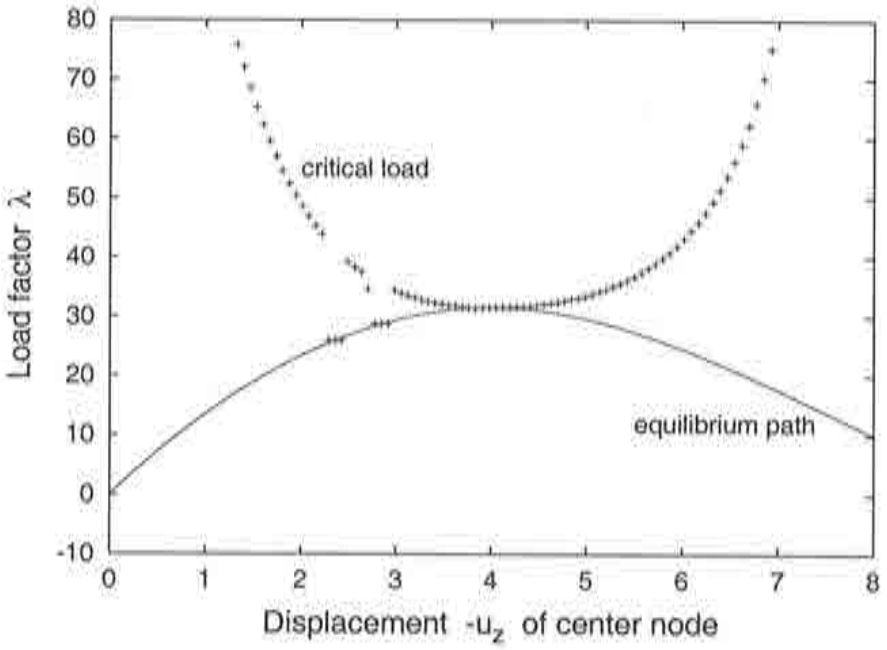

Figure 8.32: One step prediction for the 3D pin-jointed truss dome

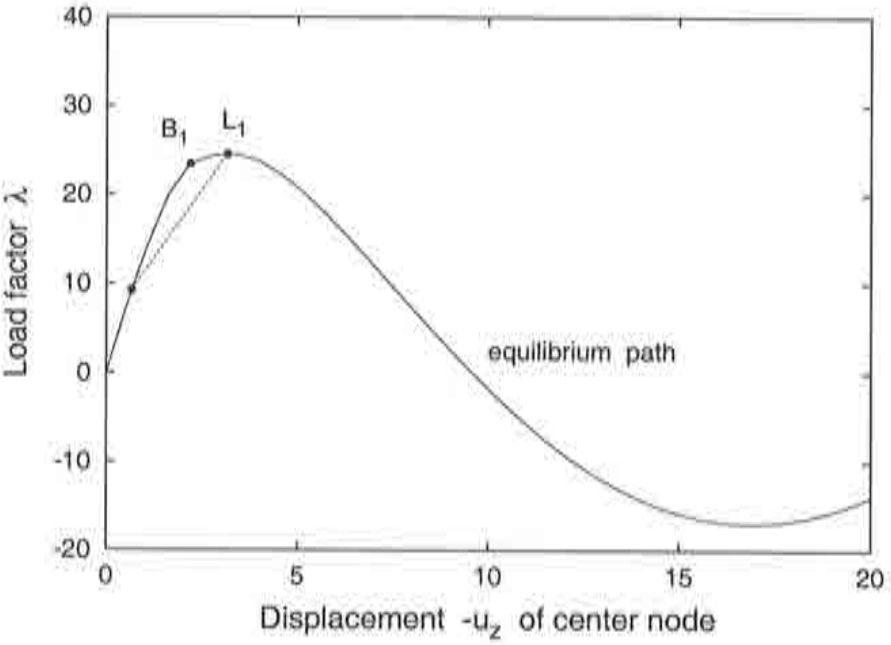

Figure 8.33: Equilibrium path of the truss dome with damage $r_0 = 0.5$, $H = 1.0$

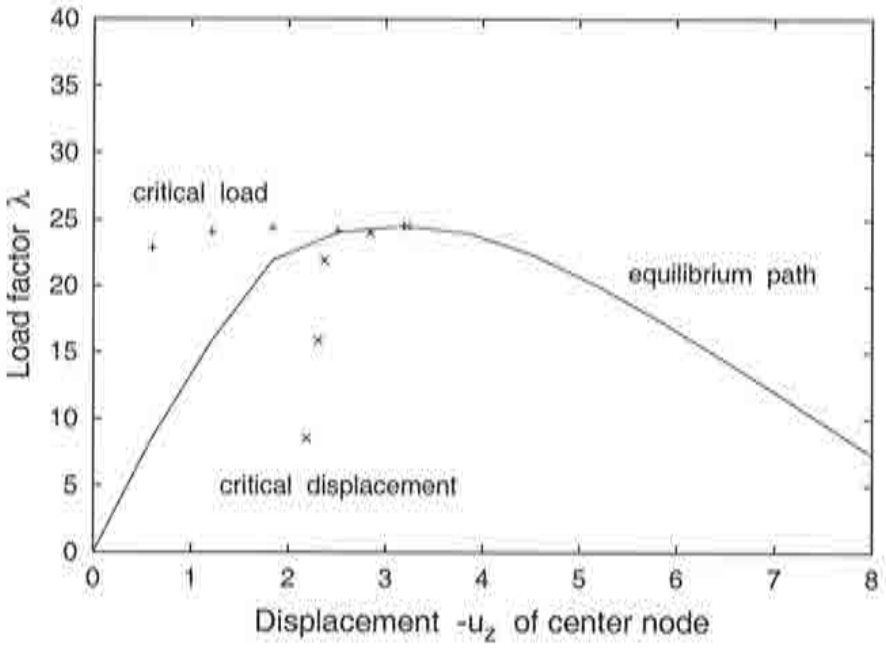

Figure 8.34: CDM prediction with damage $\tau_0 = 0.5$, $H = 1.0$

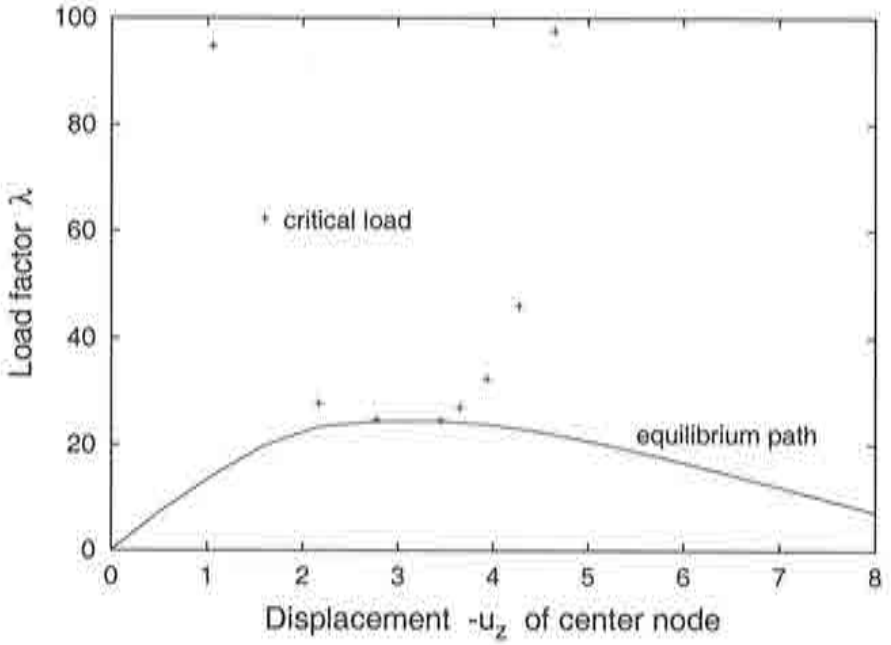

Figure 8.35: One step prediction with damage $\tau_0 = 0.5$, $H = 1.0$

8.1.5 Clamped shallow arch

The next example was discretized with quadrilateral solid elements. The clamped shallow arch of figure 8.36 was studied by [Oliver and Oñate, 1986] and previously by [Dawe, 1971]. As usual a vertical load is placed in the apex of the arch. Besides the geometrical data figure 8.36 shows one representative finite element and the material properties ($E = 72395$, $\nu = 0.0$). The arch was modeled with one layer of 20 solid elements. Two different types of quadrilateral elements were used. For the extended system a 9 node element and for the CDM an element consisting of 8 nodes as described in [Matias, 1996] were chosen.

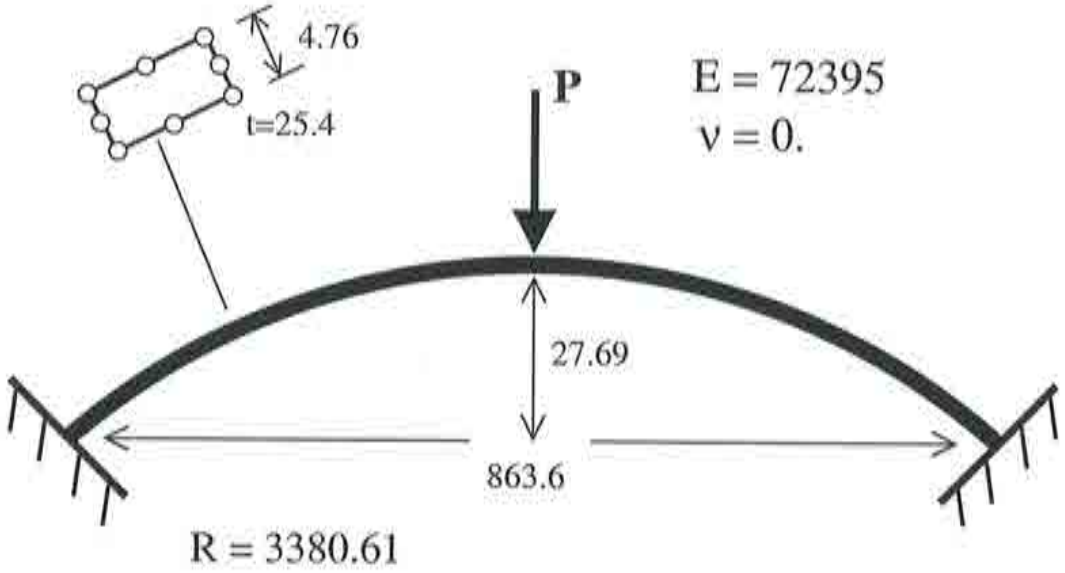

Figure 8.36: Clamped shallow arch with solid elements

A plot of the load factor λ and the vertical displacements of the center node yields the curve of figure 8.37. Since only the first part of the path until snap–through takes place is of interest, no detailed studied of the other critical points were made. The first limit load point L_1 is situated at $(u_y; \lambda) = (-9.7; 162.65)$. A computation with the extended system algorithm has no difficulties in locating the point.
Both, the CDM in figure 8.38 and the one step prediction in figure 8.39 detect the critical point. The quality of the predictions is rather similar, whereas the first predictions of the CDM are too low the one step predictions values are too high.
The effects of damage on this structure have been studied more thoroughly than in the last examples, because of the higher complexity of solid elements compared to simple truss elements. The first damage parameters chosen are $\tau_0 = 1.0$ and $H = 0.5$. The results of an extended system calculation are demonstrated in diagram 8.40. The limit point L_1 is shifted to a lower load level of $\lambda = 138.34$ with a displacement of $u_y = -6.79$.
For the predictions of the CDM the occurrence of damage has significant consequences as diagram 8.41 shows. The critical load curve is no longer straight and goes through a minimum, some points even scatter around the interpolated path. The one step predictions in diagram 8.42 scatter also, but this time the regression curve is a straight line that goes towards the limit load point.

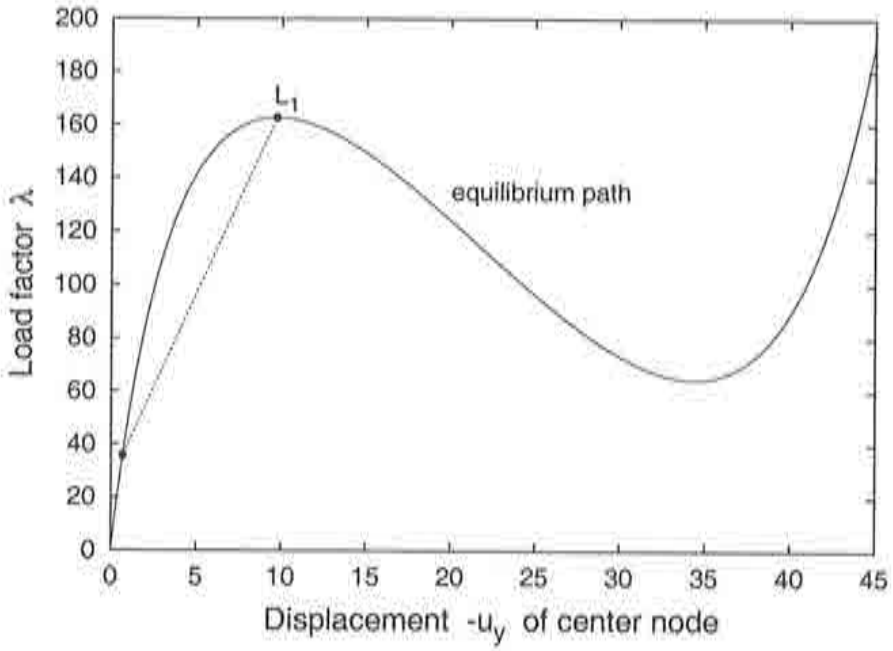

Figure 8.37: Equilibrium path of the clamped shallow arch

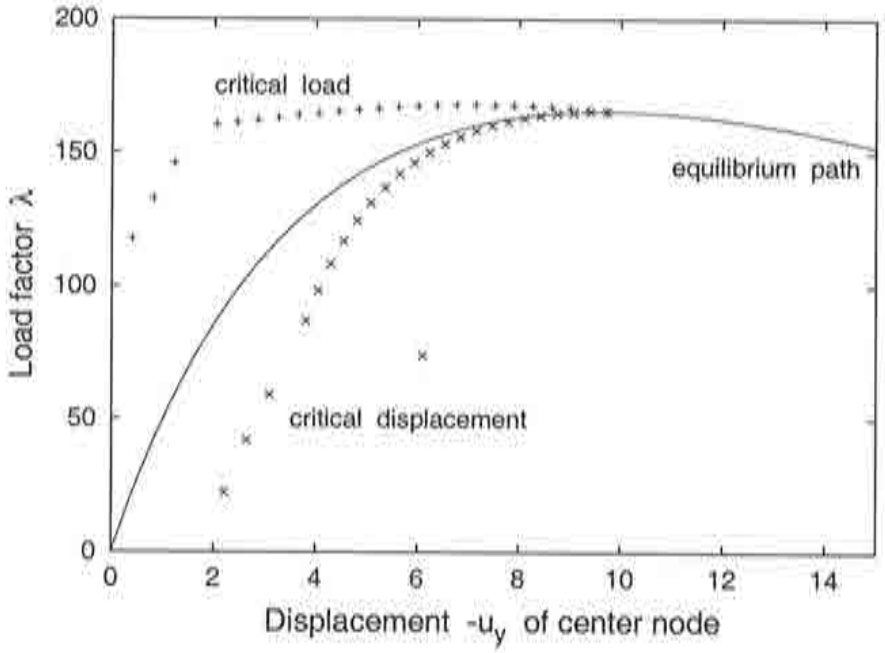

Figure 8.38: CDM prediction for the clamped shallow arch

A second set of damage values $\tau_0 = 0.6$, $H = 1.0$ provides similar results. The extended system in figure 8.43 yields the exact coordinates of the limit load point L_1 : $(u_y; \lambda) = (-7.21; 125.76)$. The critical loads predicted by the CDM look rather randomly distributed in the beginning, but form a curve in the end that converges against L_1. The predicted values however are not very good. The one step predictions provides rather

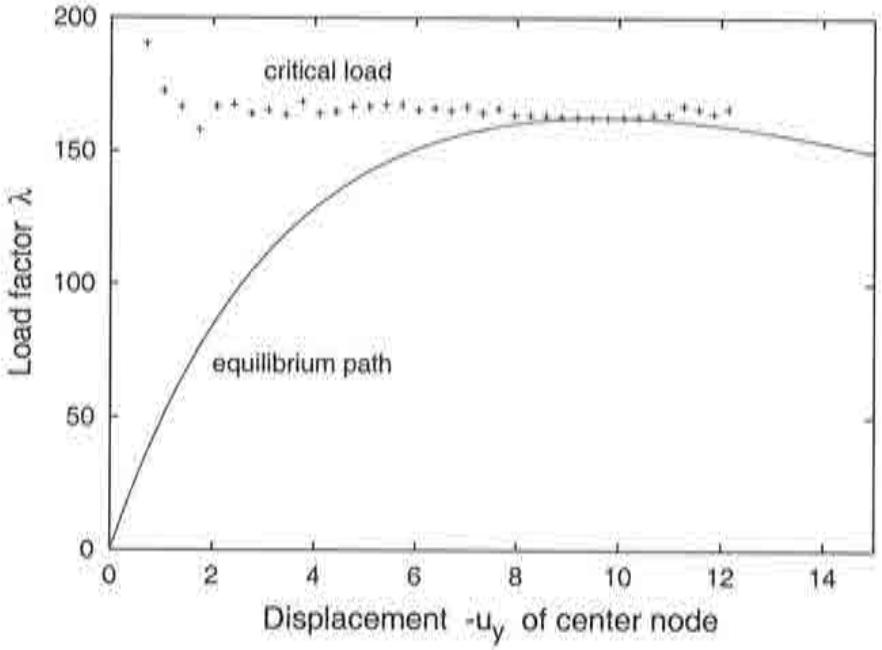

Figure 8.39: One step prediction for the clamped shallow arch

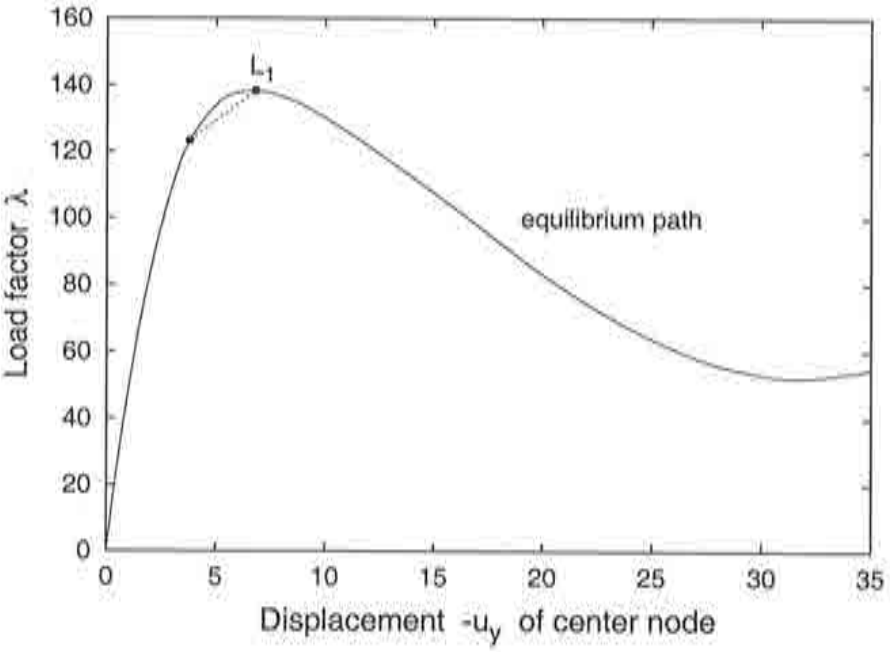

Figure 8.40: Clamped shallow arch with damage $\tau_0 = 1.0$, $H = 0.5$

good results, as figure 8.45 shows.

The last damage values for this structure are $\tau_0 = 0.2$ and $H = 1.5$. As usual the extended system values $L_1 : (u_y; \lambda) = (-8.56; 110.29)$ are obtained without major problems (see diagram 8.46). The predictions, CDM in diagram 8.47 and one step prediction in diagram 8.48, are as good as in the undamaged case. Although the initial threshold value τ_0 is

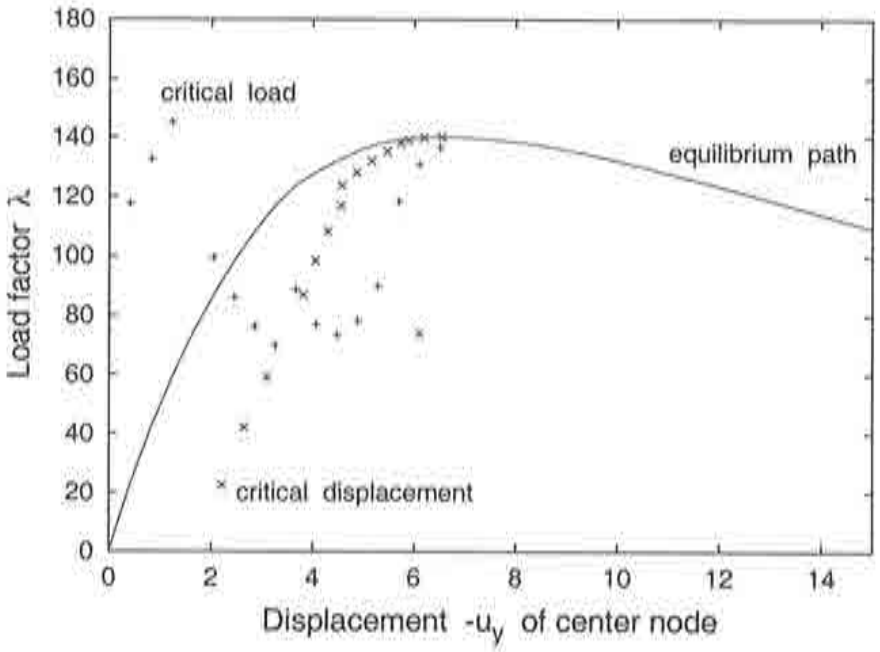

Figure 8.41: CDM prediction for the shallow arch with damage $\tau_0 = 1.0$, $H = 0.5$

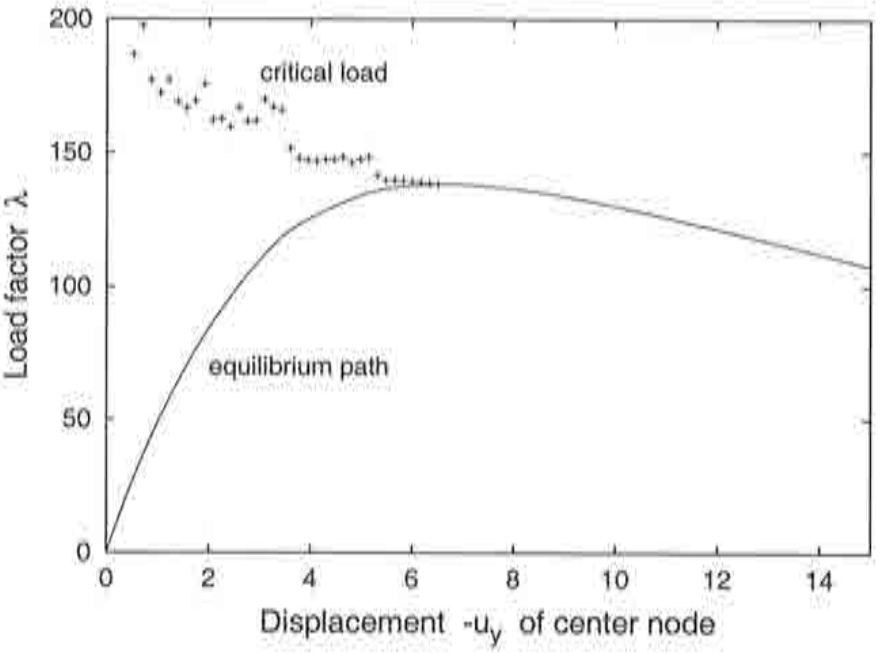

Figure 8.42: One step prediction with damage $\tau_0 = 1.0$, $H = 0.5$

more restrictive in this case the predictions are the best of all the damage cases. It seems that the hardening parameter H, which is the biggest of the three, has a considerable influence on the CDM prediction of the critical load.

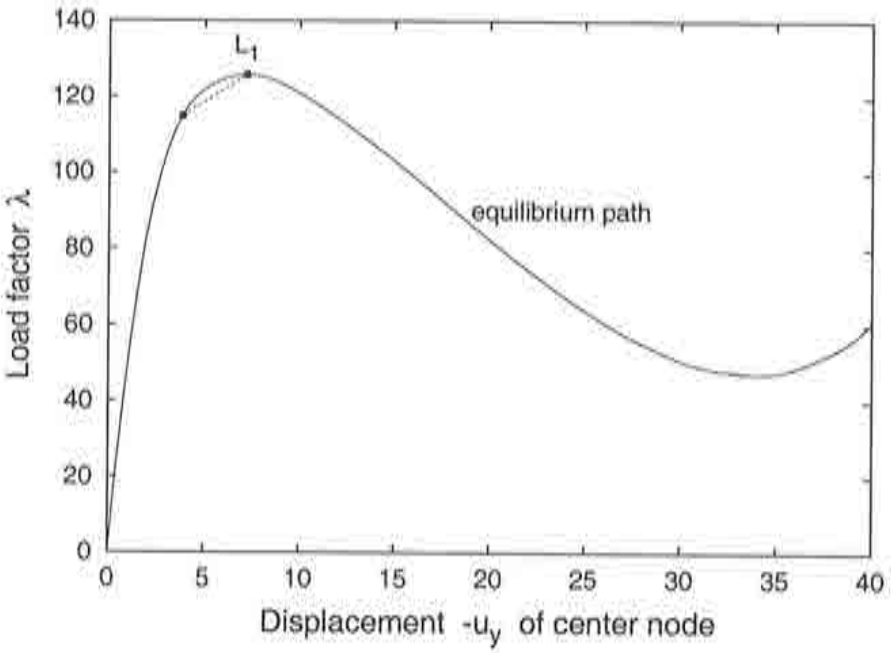

Figure 8.43: Clamped shallow arch with damage $\tau_0 = 0.6$, $H = 1.0$

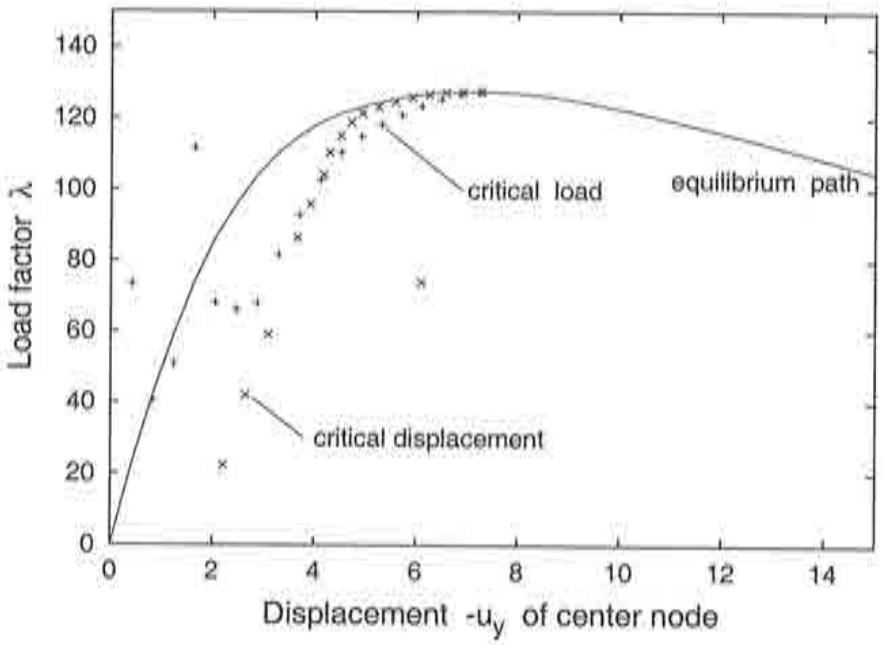

Figure 8.44: CDM prediction with damage $\tau_0 = 0.6$, $H = 1.0$

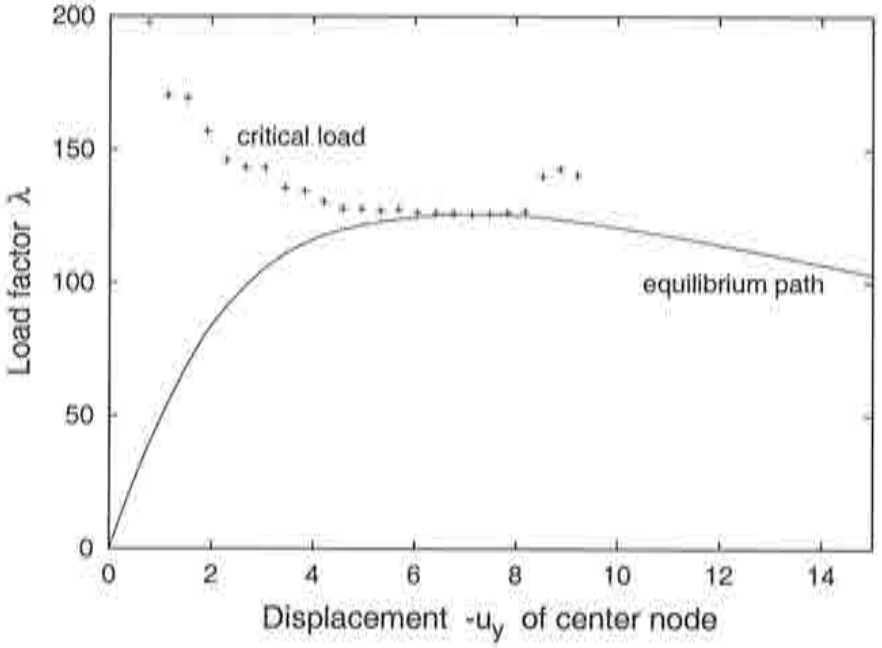

Figure 8.45: One step prediction for the arch with damage $\tau_0 = 0.6$, $H = 1.0$

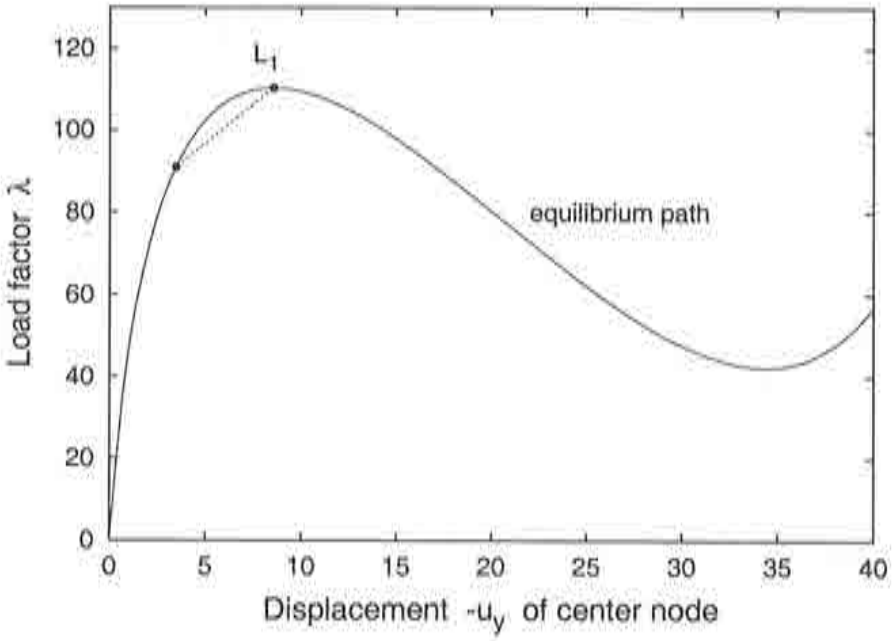

Figure 8.46: Equilibrium path of the shallow arch with damage $\tau_0 = 0.2$, $H = 1.5$

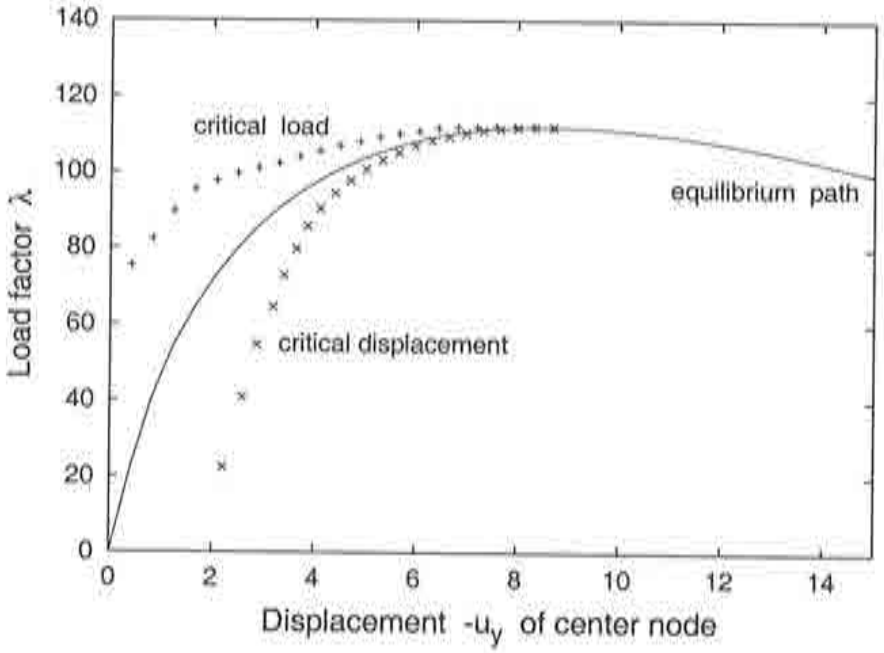

Figure 8.47: CDM predictions of the shallow arch with damage $\tau_0 = 0.2$, $H = 1.5$

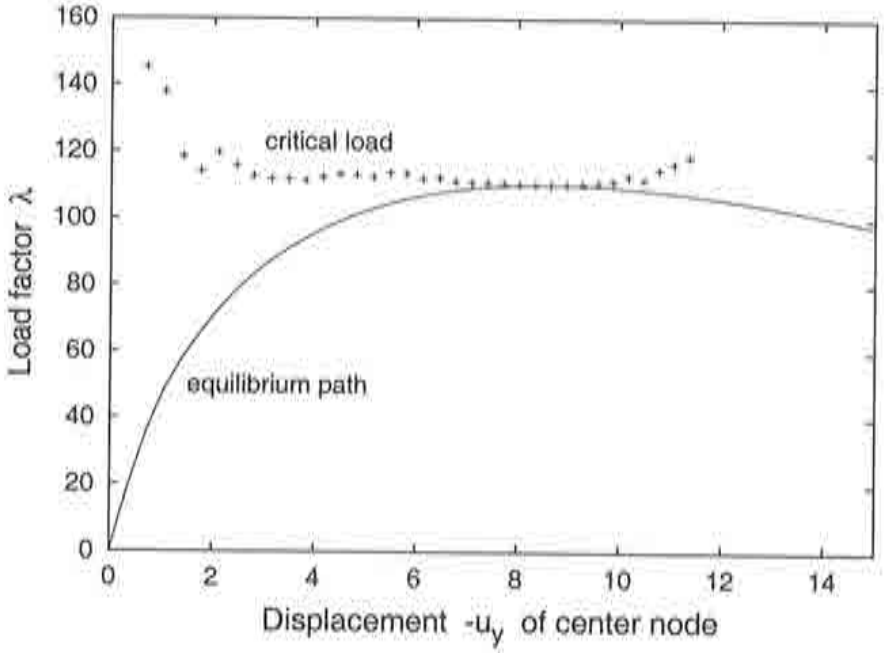

Figure 8.48: One step prediction with damage $\tau_0 = 0.2$, $H = 1.5$

8.1.6 Hinged circular arch

The hinged circular arch from [Wood and Zienkiewicz, 1977] is the second example with solid elements. The geometrical and material data of this high arch are given in figure 8.49. The original discretization was one layer of 10 elements as in [Matias, 1996], each having 8 nodes. The results were verified with FEAP and the extended system with a finer discretization of one layer with 50 elements, 9 nodes each.

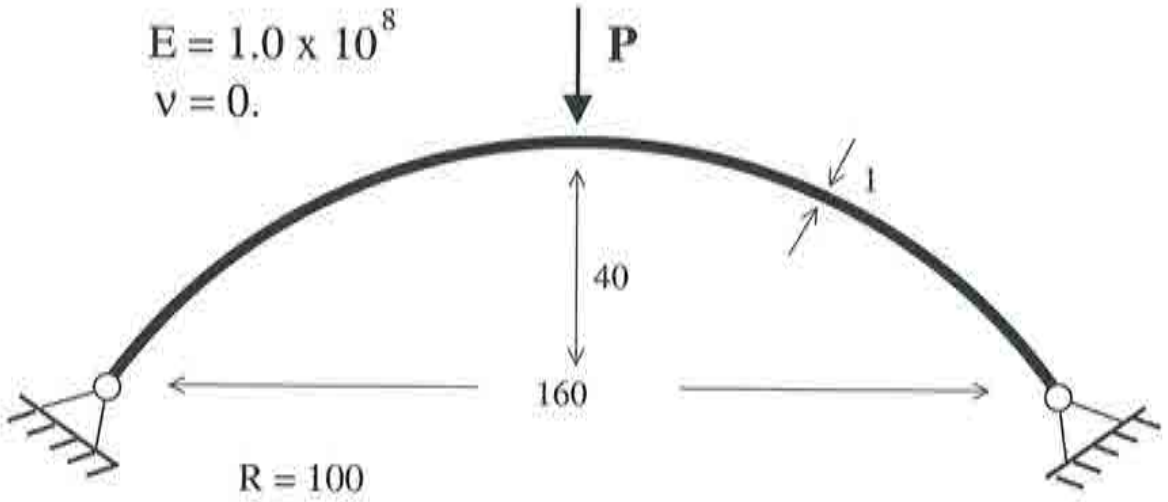

Figure 8.49: Hinged circular arch with solid elements

The equilibrium path with extended system computations (figure 8.50) demonstrates the potential of the method. A bifurcation point $B_1 : (u_y; \lambda) = (-10.76; 1073.2)$ and a limit load point $L_1 : (u_y; \lambda) = (-22.16; 1262)$ were found. The CDM confirms the bifurcation point (figure 8.51) and so does the one step prediction (figure 8.52), which predicts also the limit load point. A second computation with the finer discretization of 50 elements for the CDM (figure 8.53) leaves a completely different impression. The critical displacement curve is identical to figure 8.51, but here the predicted critical loads are more or less equal to the current load in each point. The only explanation for this phenomenon is, that the CDM seems to be dependent on the discretization.
Including damage effects in the computation of the hinged circular arch requires the finer discretization. Nevertheless some peculiarities remain. The equilibrium paths of CDM and extended system differ substantially for damage parameters $r_0 = 8.0$, $H = 0.5$ as the diagrams 8.53 and 8.52 demonstrate. For the CDM predictions applies the same as in the undamaged case, the predicted loads are approximately equal to the current loads. The one step prediction shows not very promising results.

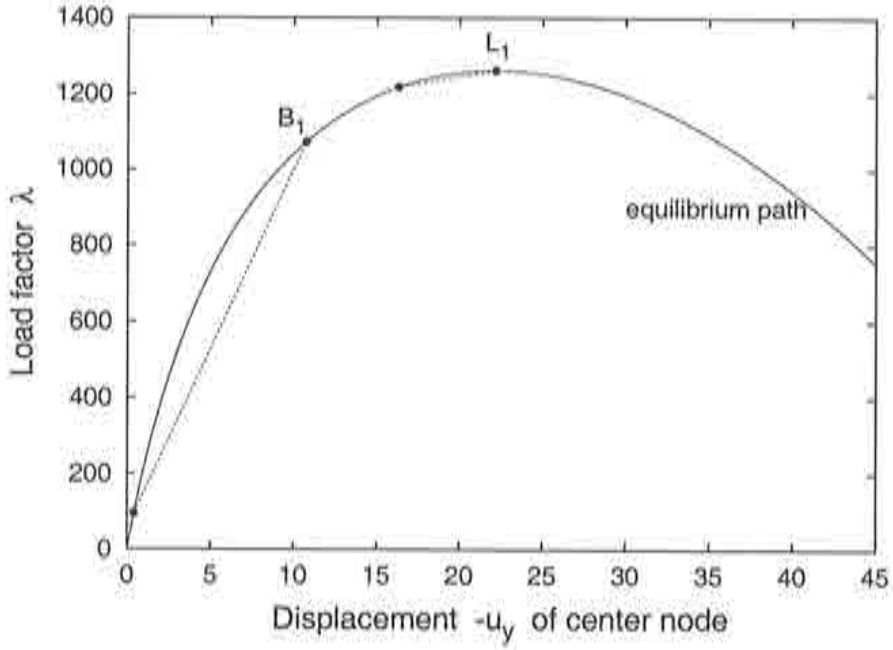

Figure 8.50: Equilibrium path for the hinged circular arch

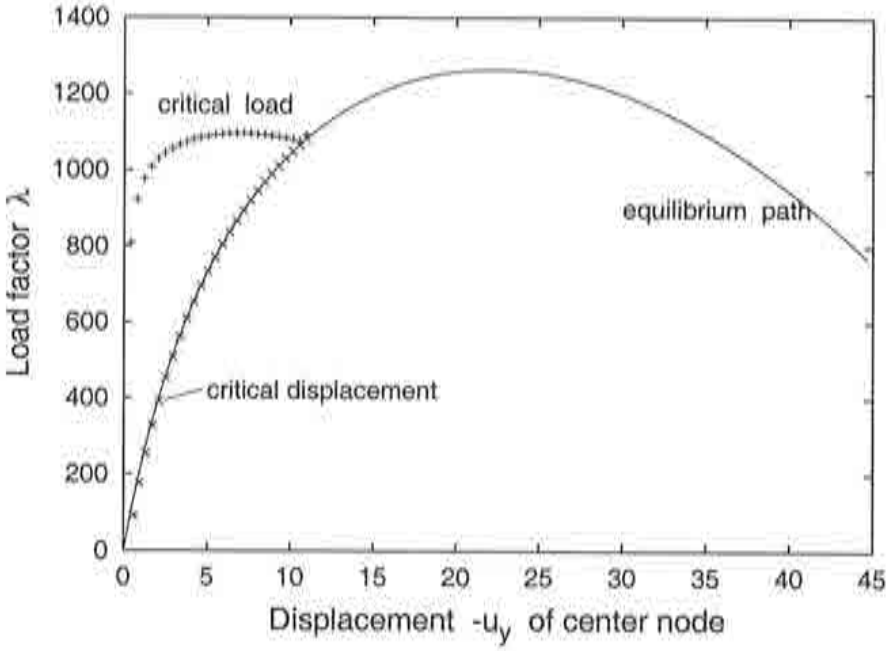

Figure 8.51: CDM prediction for the hinged circular arch

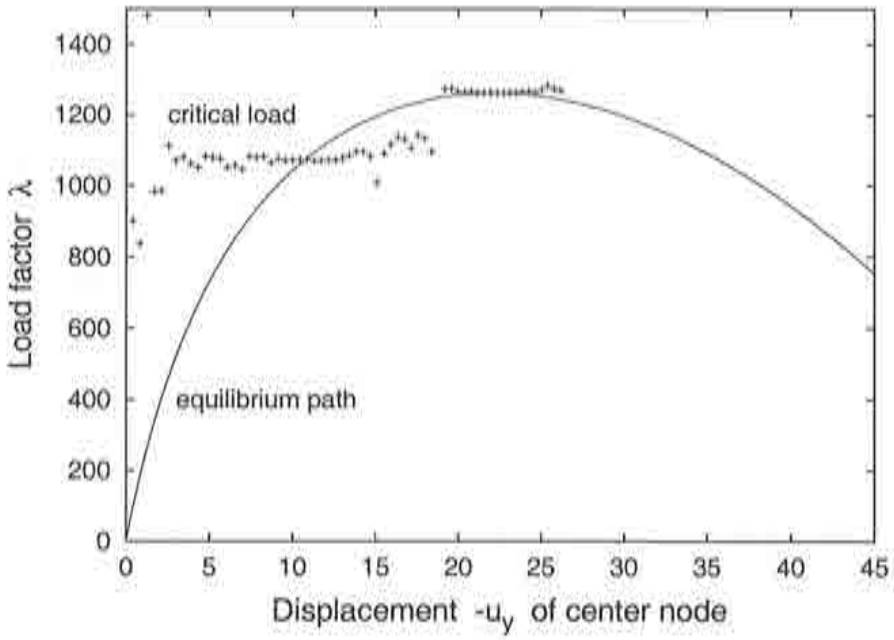

Figure 8.52: One step prediction for the hinged circular arch

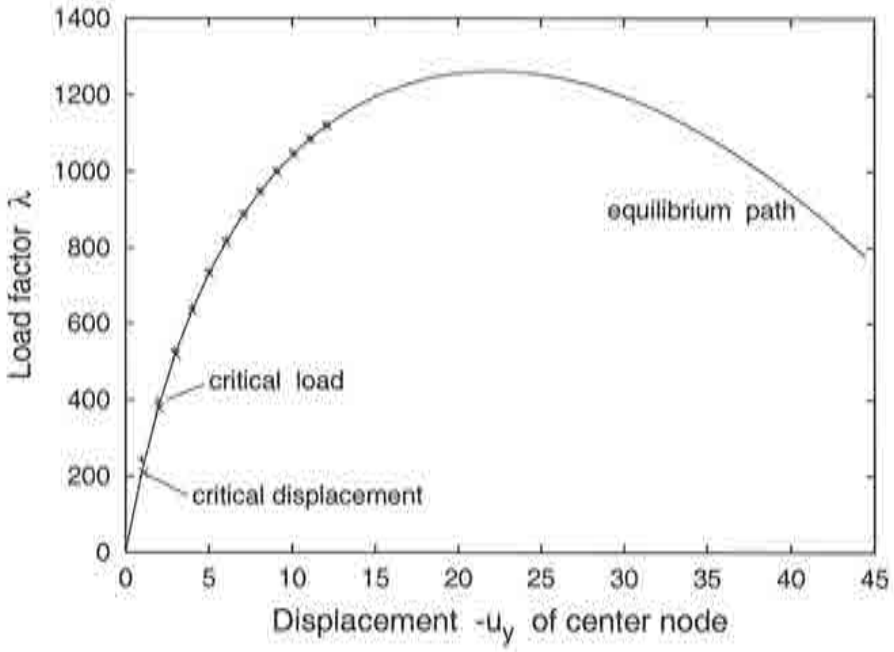

Figure 8.53: CDM prediction with finer discretization of the circular arch

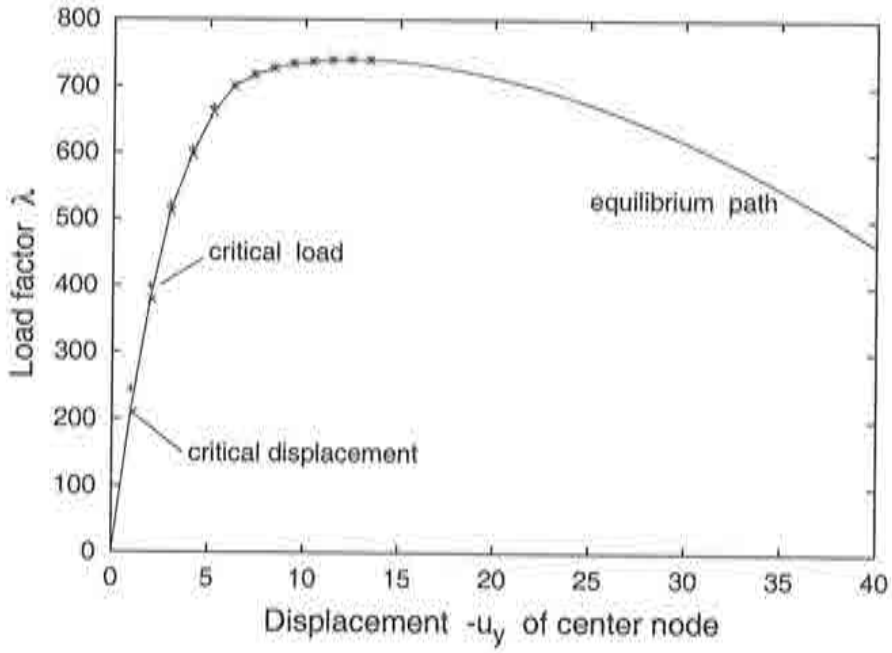

Figure 8.54: CDM prediction for the circular arch with damage $\tau_0 = 8.0$, $H = 0.5$

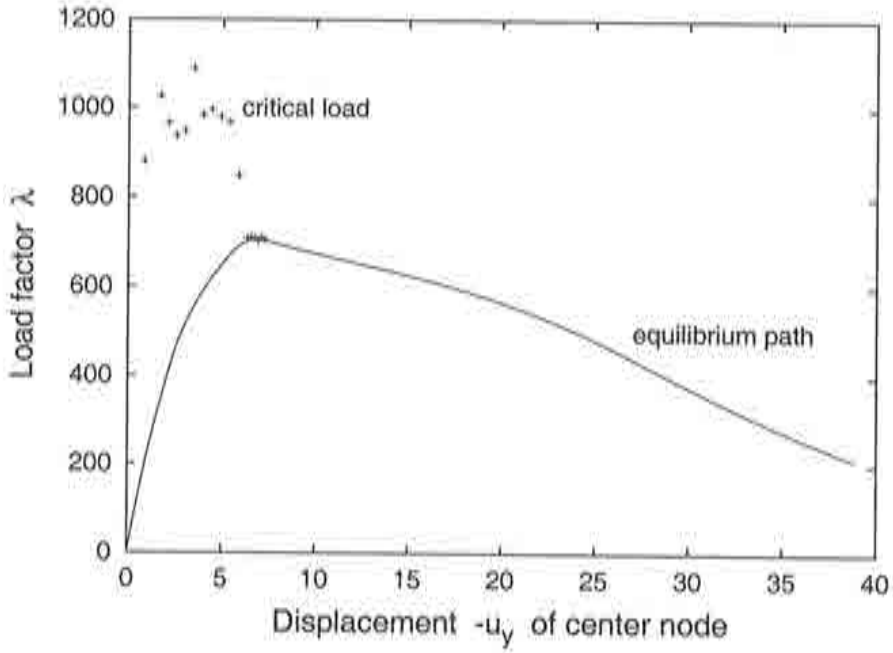

Figure 8.55: One step prediction with damage $\tau_0 = 8.0$, $H = 0.5$

8.1.7 Cylindrical shell

The last example for the comparison of both methods is the cylindrical shell taken from [Surana, 1983]. It was studied as well in [Simo et al., 1990] and [Matias, 1996]. Figure 8.56 shows an outline of the three dimensional problem with geometrical and material data. Two different versions of the shell one with thickness $h = 12.7$ the other with $h = 6.35$ are examined. The edges are hinged and a vertical load is placed in the center of the shell. The entire shell is discretized with 64 elements. As in [Oñate and Matias, 1995] and [Matias, 1996] only one quarter of the shell was calculated with 20 node brick elements for the CDM predictions. The FEAP modeling was made with nonlinear 4 node Mindlin-Reissner shell elements described in [Tessmer, 2000].

In contrary to the CDM a change of the element type with the extended system does not pose major difficulties, as standard elements can be used. The CDM requires the secant matrix assemblation, which is commonly not implemented in FE programs. A change of the element requires thus often an extension of already existing elements.

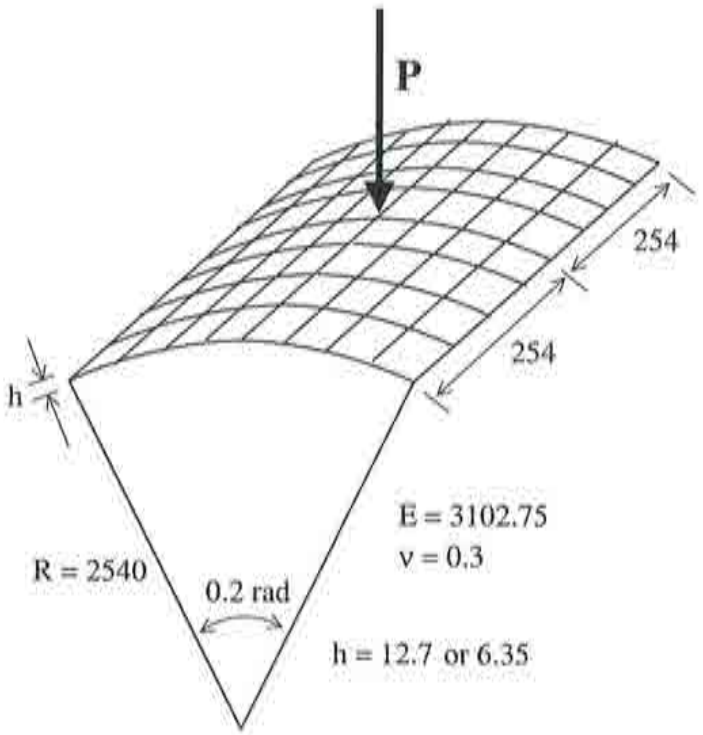

Figure 8.56: Cylindrical shell

The equilibrium path in figure 8.57 where the negative vertical displacements of the central node are plotted has four critical points. The limit points $L_1 : (u_z; \lambda) = (-10.69; 2221.2)$, $L_2 : (u_z; \lambda) = (-19.4; 564.9)$ and the bifurcation points $B_1 : (u_z; \lambda) = (-14.6; 1660.5)$ and $B_2 : (u_z; \lambda) = (-16.6; 946.3)$. The limit points can be computed with the extended system without problems as the size of the load step shows. For the bifurcation points this is only true in their vicinity.

The CDM prediction in figure 8.58 hits the first limit load points correctly. The critical displacements seem to pass the point, only the final prediction is exact. The critical load

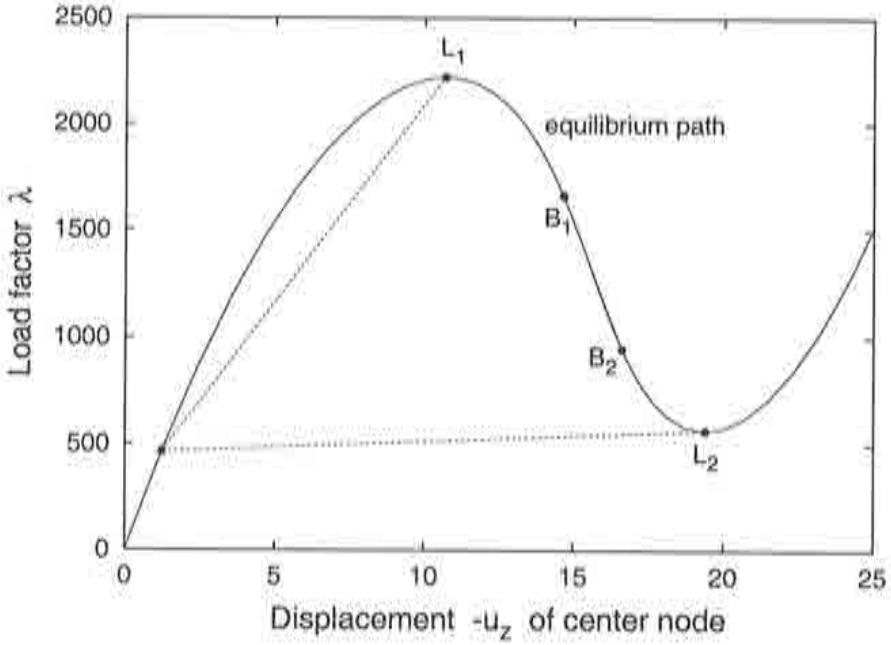

Figure 8.57: Equilibrium path for the shell with $h = 12.7$

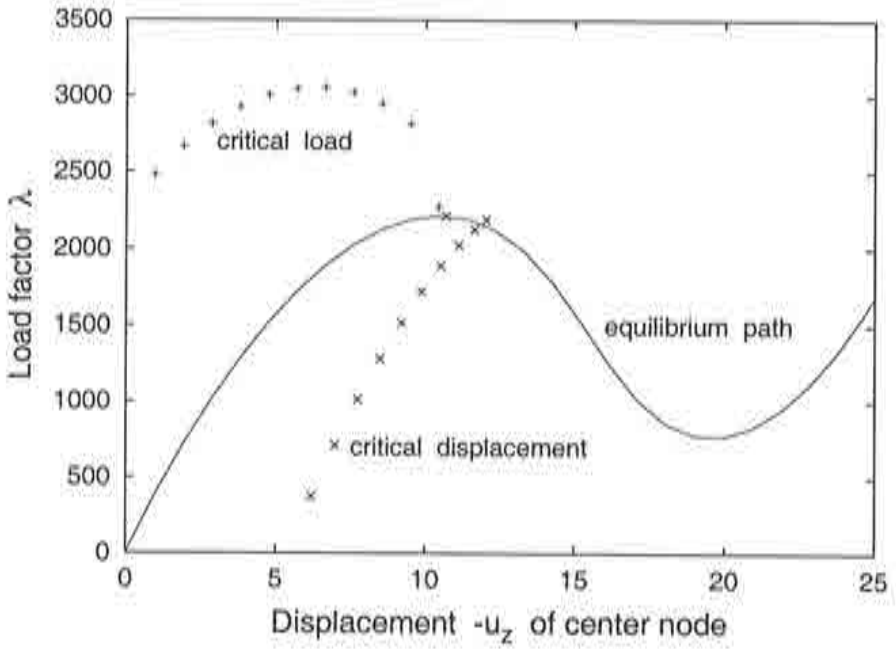

Figure 8.58: CDM prediction for the shell with $h = 12.7$

curve approaches the point in a convex circle, becoming less exact after a rather good first approximation.

The one step prediction in figure 8.59 detects all the critical points in the closer area around each point. The predictions become better the closer to the critical point they come.

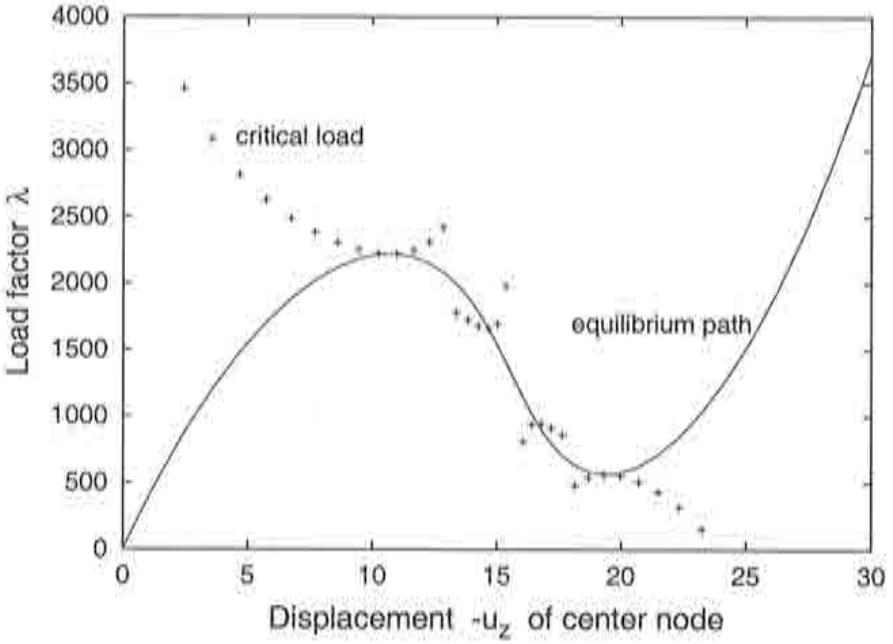

Figure 8.59: One step prediction for the shell with $h = 12.7$

Reducing the thickness of the shell by one half changes its behavior substantially. The equilibrium path in figure 8.60 reveals a snap–back. In total 8 critical points can be observed. Two limit load points $L_1 : (u_z; \lambda) = (-13.69; 617.35)$, $L_2 : (u_z; \lambda) = (-16.7; -371.6)$ and 6 bifurcation points $B_1 : (u_z; \lambda) = (-9.57; 546.6)$, $B_2 : (u_z; \lambda) = (-16.2; 537.2)$, $B_3 : (u_z; \lambda) = (-16.8; 219.4)$, $B_4 : (u_z; \lambda) = (-13.4; -185.4)$, $B_5 : (u_z; \lambda) = (-13.68; 617.35)$ and $B_6 : (u_z; \lambda) = (-21.37; -250.6)$. All were encountered with the extended system, some even starting the procedure from a greater distance, see figure 8.60 for details.
The fact that only one quarter of the shell is modeled, is the reason, why the first bifurcation point is not found by the CDM. The predictions in figure 8.61 head towards the limit load point and are quite exact after some time.

Looking at the one step prediction in figure 8.62 it can be seen, that all critical points are detected. The predictions form smooth curves, scattered values can be observed only in between critical points, when the switch from one to another takes place.

8.1.8 Conclusion of the comparison

Comparing CDM and one step prediction critical loads in all the examples, the CDM load predictions are better. This can be seen especially when looking at the examples with truss elements. Moreover in the damage examples the advantage of the enhanced predictions with the algorithm described in section 7.2 is noticeable. In the examples with solid elements the results are more or less equal. The CDM predictions are still better, but when damage occurs the predictions become worse. The discretization dependence of the CDM for the hinged circular arch of section 8.1.6 and the fact, that the CDM only predicts some (mostly the first) critical points of the path are negative points.

The examples of the comparison confirm, that the extended system as a direct method

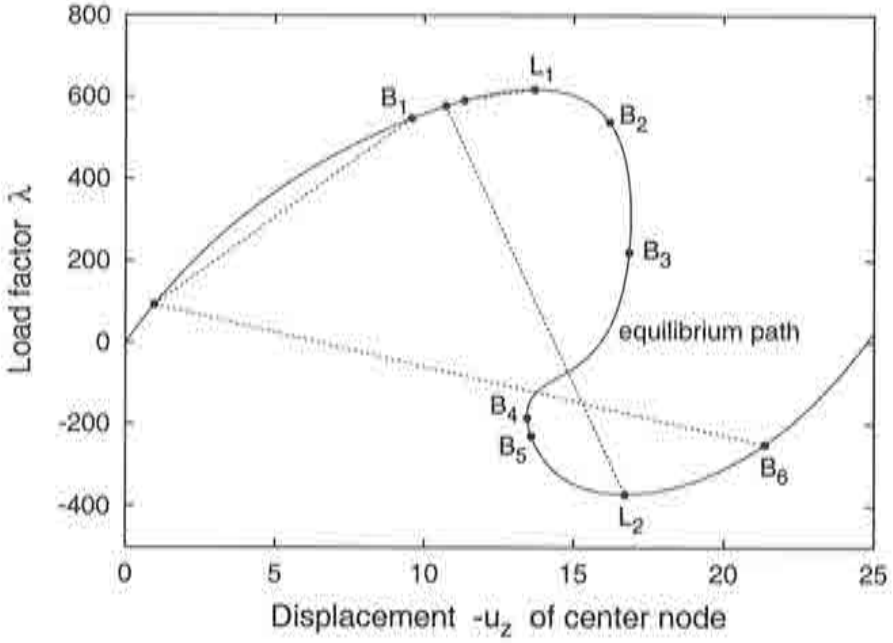

Figure 8.60: Equilibrium path for the shell with $h = 6.35$

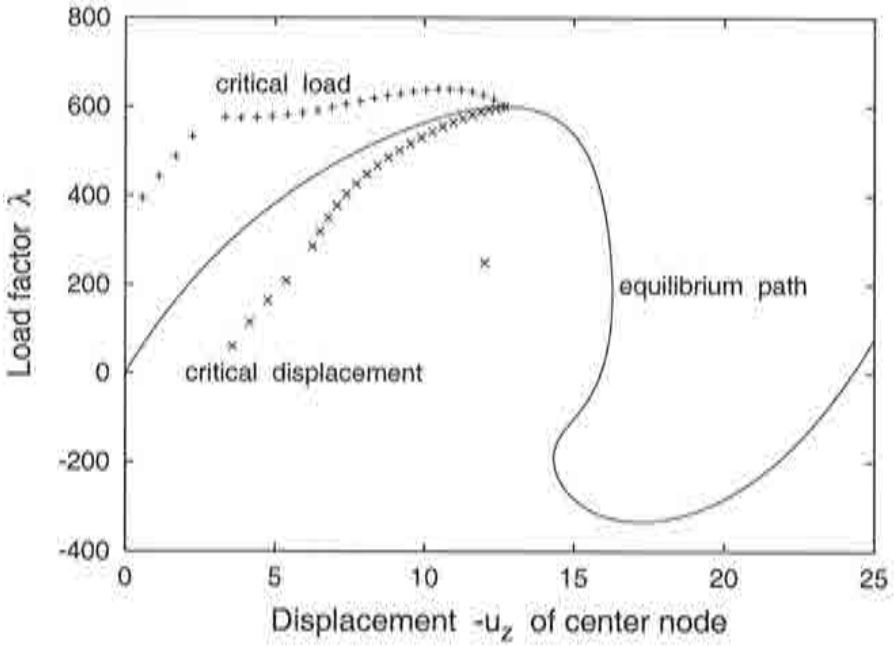

Figure 8.61: CDM prediction for the shell with $h = 6.35$

is the method of choice for the exact computation of critical points. Since the CDM only makes predictions of the critical values this was obvious from the beginning and thus not an issue of examination. It remains to be discussed, if the output of the CDM can serve as starting values for the extended system.

The critical displacement pattern that is computed by the CDM is not different from

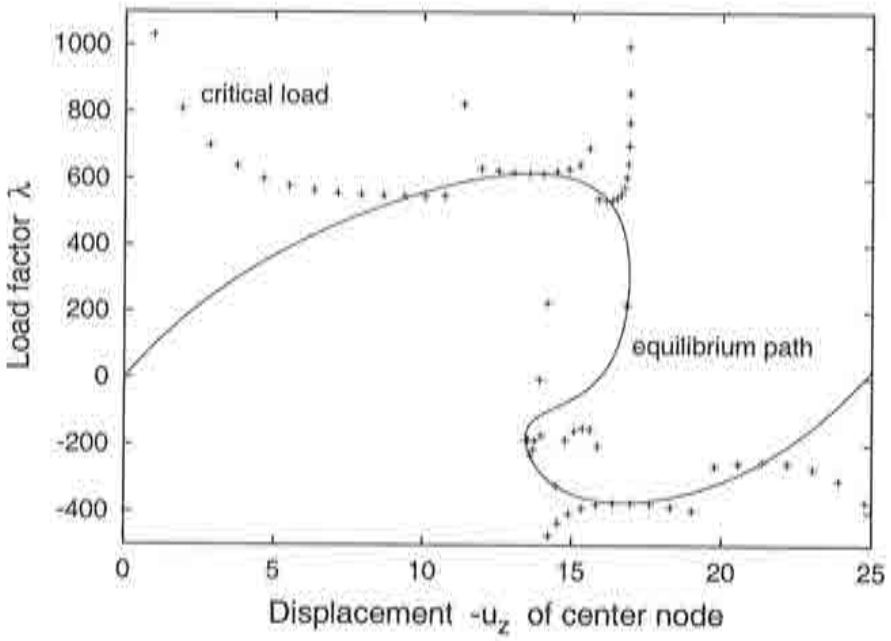

Figure 8.62: One step prediction for the shell with $h = 6.35$

the starting values for the extended system. As mentioned in section 6.4.2 the current displacement pattern is chosen as an estimation for the critical displacements. Together with equation (6.52) this means that after computing the only unknown, the factor ρ in (6.52) the predicted critical displacements are a multiple of the current ones. This is identical to the first possibility of the proposed starting values for the eigenvector in the extended system (see equation (6.73)). The fact that limits the use of the predicted critical displacements by the CDM is, that no reiteration of the displacement vector takes place and the initial pattern remains unchanged.

The only values that can provide meaningful starting value for the extended system are the predicted critical loads. Therefore the one step prediction with the extended system was made to evaluate this possibility. Despite the fact that the CDM load predictions were better than the one step predictions, the CDM predictions were not taken as starting values for the extended system. The reason is, that the effort to implement the CDM in already existing FE programs is considerably high, since the secant stiffness matrix has to be constructed. The extended system on the other side with the partitioning algorithm is quite easy to implement. This also holds for the one step prediction that is based on the same algorithm. Moreover with the extended system the corresponding eigenvector is computed automatically.

For this reason only the extended system will be used in the following examples, where the computation of critical points in combination with contact inequality constraints will be studied.

8.2 Extended system with contact

All the examples of this section were computed with the Finite Element program FEAP, where the contact algorithm of chapter 5, the displacement boundary conditions with the penalty method of section 7.4 and the extended system procedure of section 6.5.1 were implemented.

8.2.1 Arch with obstacles

The first example with contact is an arch with two obstacles placed above and below it at one side. Figure 8.63 shows an outline of the structure including geometrical and material data. A load is placed in the apex and the distance between obstacles and arch is 0.1. The arch is discretized with 20 layers of 300 Q1–elements each, the obstacles consist of 100 elements in 10 layers. In a first step basically two different versions of the arch were computed, with clamped ends and with hinged ends.

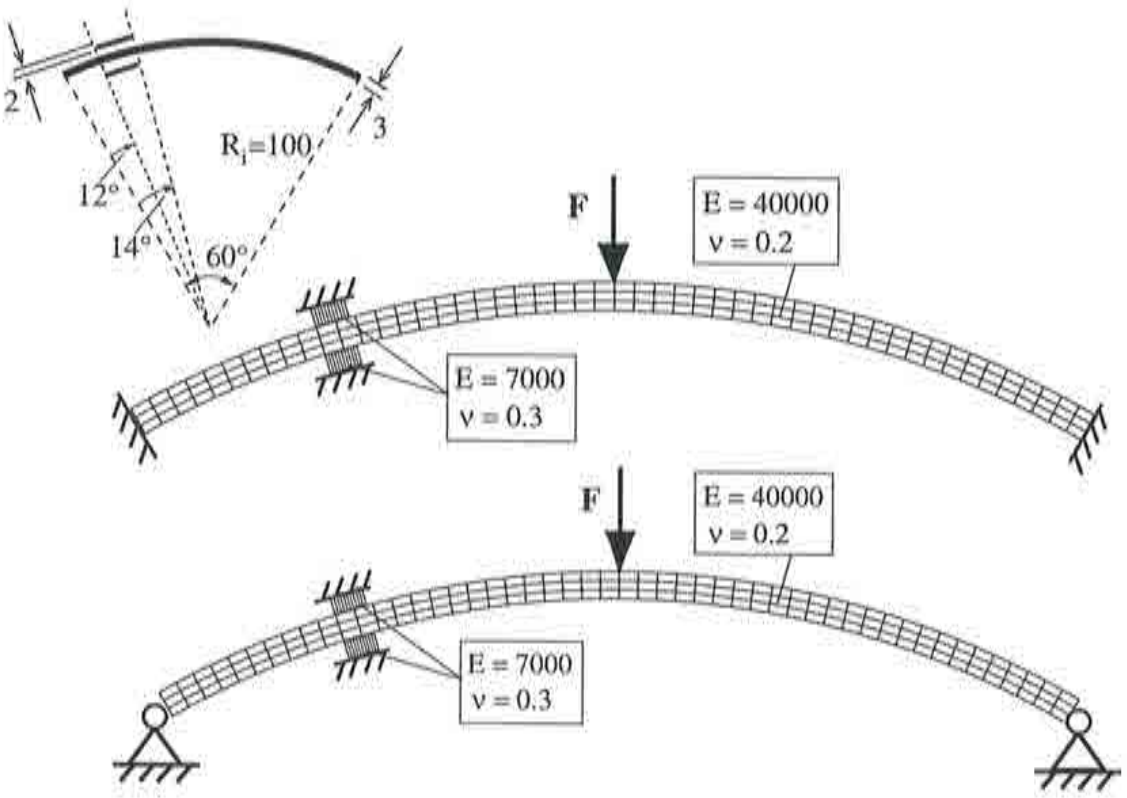

Figure 8.63: Arch with obstacles (clamped and hinged)

To study the influence of contact on the equilibrium path of the structure at first the normal path of the arch without obstacles is computed. Figure 8.64 shows the expected result. Since the arch is clamped the curve has two limit points L_1 with the values $(u_y; \lambda) = (-4.93; 233.7)$ and L_2 with $(u_y; \lambda) = (-16.38; 115.9)$. The deformed arch can be seen in the small images in figure 8.64. Both points are computable with the extended

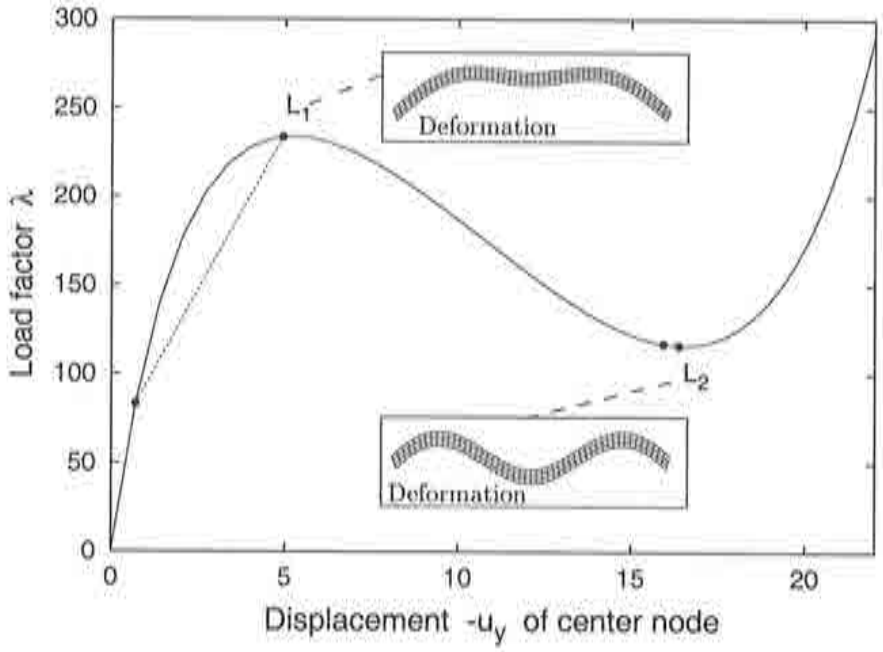

Figure 8.64: Equilibrium path for the clamped arch without obstacles

system, the limit point L_1 even starting from further apart as the dashed line indicates, L_2 only with starting points in the vicinity of the critical point.

In diagram 8.65 the equilibrium path of the clamped arch can be seen when the obstacles are present. The path still has two limit load points, but the values have changed: $(u_y; \lambda) = (-5.62; 242.2)$ and $(u_y; \lambda) = (-9.84; 214.4)$. The pictures of the deformed structure in figure 8.65 demonstrate the changes in the deformation process. The results of the extended system are good, both points are found, L_1 from a greater distance and L_2 only in the closer area.

The one step prediction for the clamped arch with obstacles is shown in figure 8.66. The curve hits both points exactly, in between the points it is noticeable, when the prediction switches from one point to the other. Comparison with the result of the extended system computations suggests that the one step prediction is a good indicator for an efficient application of the extended system. The one step prediction which is basically identical to the first iteration of the extended system procedure (see section 7.3) can indicate from which points on the equilibrium path an extended system algorithm converges to a critical point.

Looking at diagram 8.66 it seems obvious that for obtaining L_2 the extended system should not be started from points with $-u_y < 8$, as the procedure might fall back to L_1 otherwise. It might be even better not to take the first point with $-u_y > 8$ but the second or the third. For a successful computation of L_1 it seems as if a convergence is possible from the first points of the equilibrium path. A comparison of these indications with the results in diagram 8.65 confirms the assumption.

The next figure 8.67 contains the equilibrium path for the hinged arch without obstacles. A bifurcation point $B_1 : (-u_y; \lambda) = (-3.72; 196.8)$ and a limit load point $L_1 : (-u_y; \lambda) = (-6.86; 223.0)$ are detected by the extended system. For L_1 the deformed arch is plotted

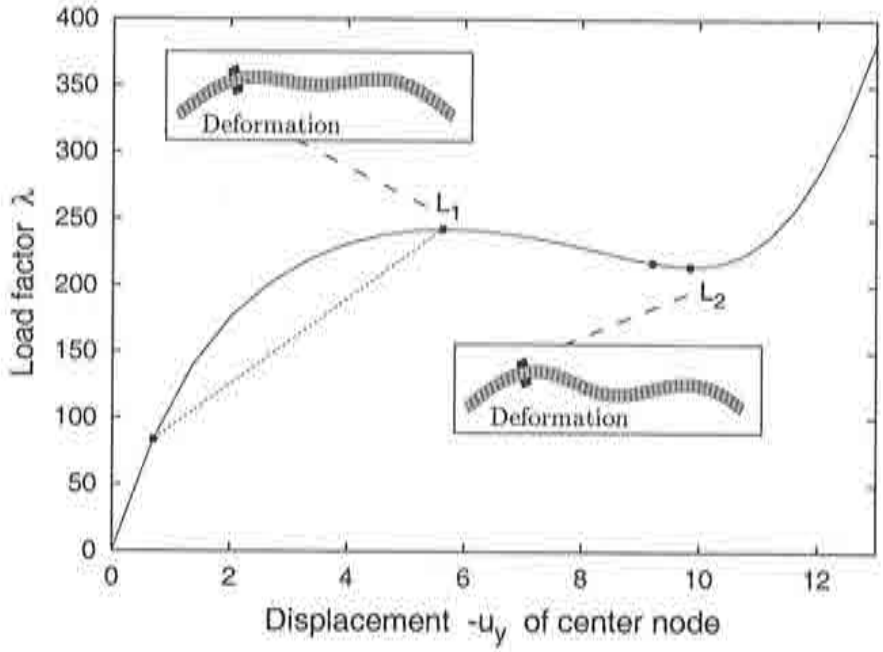

Figure 8.65: Equilibrium path for the clamped arch with contact

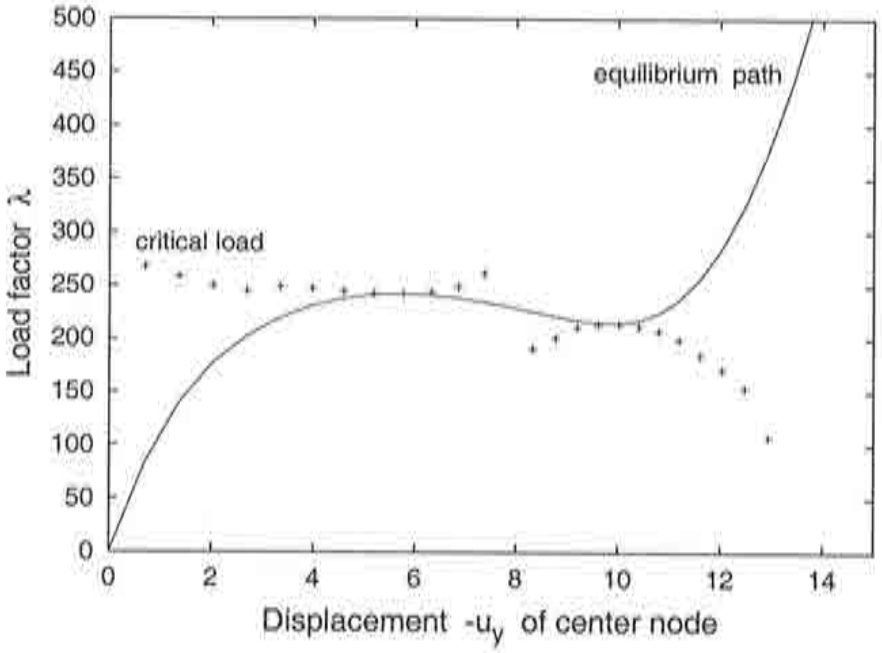

Figure 8.66: One step predictions for the clamped arch with contact

in the small picture, for B_1 the deformation of the secondary path branching off at this point is given. This secondary path deformation is actually the eigenvector corresponding to the zero eigenvalue in B_1. The displacements are multiplied by a factor to make the difference to the primary path deformation noticeable.
For the hinged arch with obstacles in diagram 8.68 the bifurcation point vanishes and

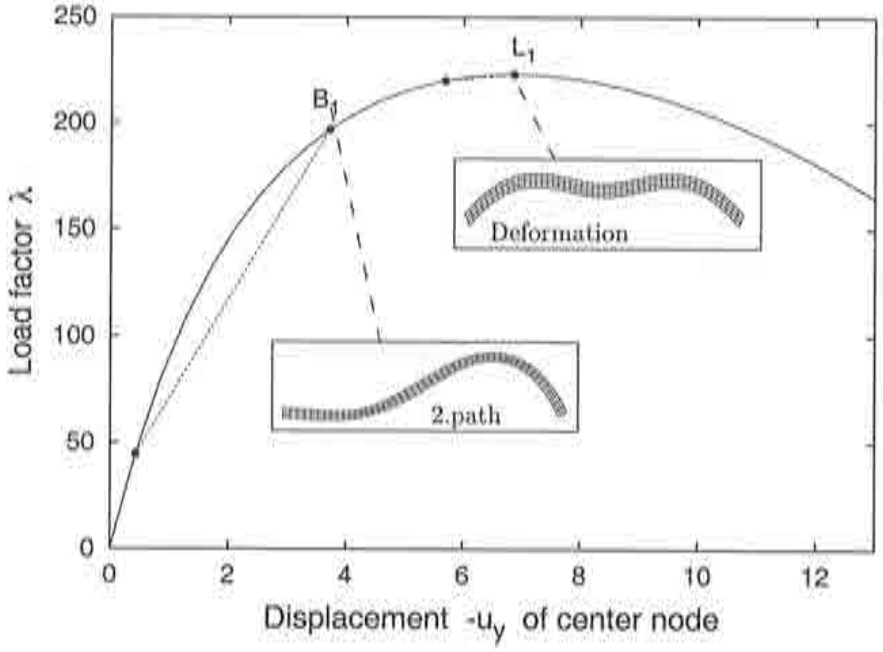

Figure 8.67: Equilibrium path for the hinged arch without obstacles

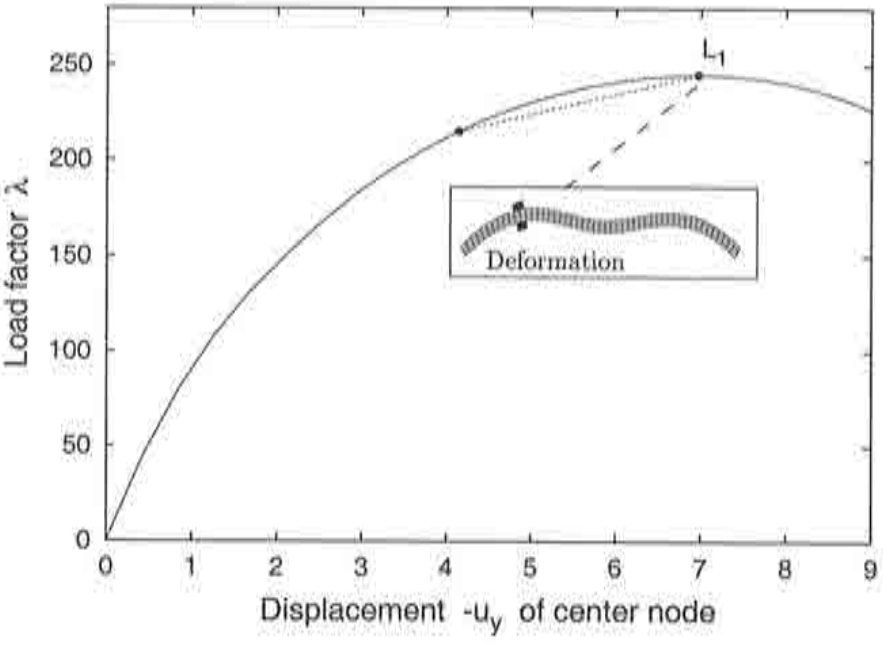

Figure 8.68: Equilibrium path for the hinged arch with contact

only a limit load point at $(-u_y; \lambda) = (-6.97; 245.0)$ remains. The extended system is able to hit this point directly from a distance. The one step prediction in figure 8.72 is quite good. After some initial up and down the curve stabilizes for points with $-u_y > 3.5$, which is in accordance with the results of the extended system in diagram 8.68.
Besides applying a force as boundary conditions, there can also be applied displacements.

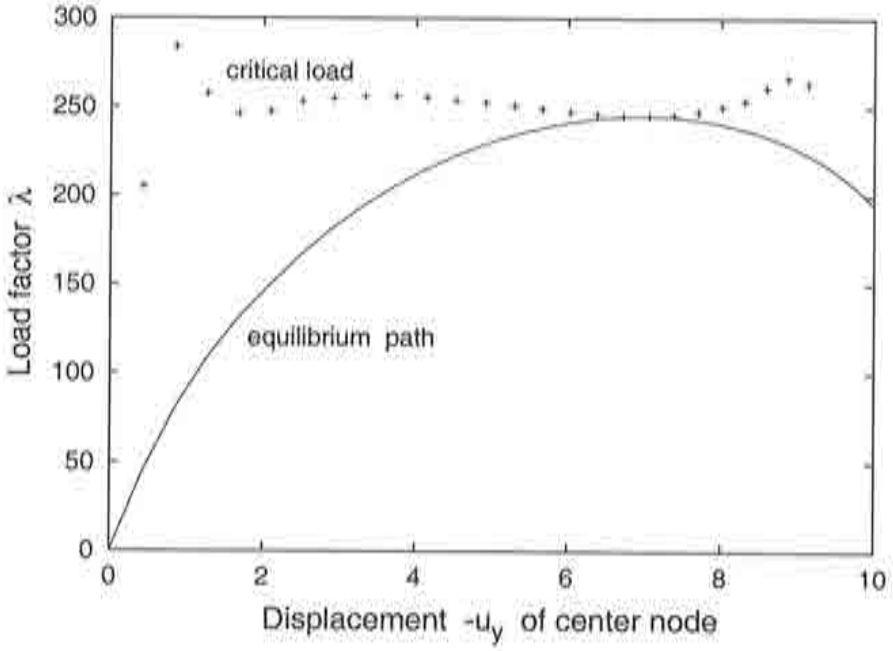

Figure 8.69: One step prediction for the hinged arch with contact

In the next examples the hinged arch is studied with a displacement of $u_y = -1$ in the apex node. Plotting then the load factor against the displacement does not make much sense any more, as both are linear dependent. Instead of the load factor the nodal reaction in the apex node are used for this type of boundary value problems.
The hinged arch without obstacles and displacement boundary conditions has the equilibrium path of figure 8.70. Using the extended system for this problem reveals two bifurcation points $B_1 : (u_y; F_y) = (-3.69; -196.3)$ and $B_2 : (u_y; F_y) = (-25.62; -345.9)$. The results are almost identical to the dual problem with force boundary conditions, see figure 8.67. The small pictures of the deformed arch confirm this result. As mentioned in section 7.4 the equilibrium path has no limit load point, due to the displacement boundary condition. This example shows, that the extended system works good as well with the dual boundary conditions.
Adding the obstacles to the problem the curve of diagram 8.71 is obtained. The limit load point of diagram 8.68 disappears and only one bifurcation point at $B_1 : (u_y; F_y) = (-10.48, 97.5)$ can be detected. Primary and secondary path deformations are shown in the small pictures in figure 8.71. The secondary path deformed structure is the up–scaled eigenvector in the bifurcation point.
The one step prediction for this problem is plotted in a different manner than the other results. Here again the representation of the load factor λ versus the displacements of the center node is used. Although the curve is a straight line, the one step predictions can be interpreted. It was plotted this way, because the predictions yield the load factor, that cannot be put directly in a reaction–displacement diagram. The predicted values can be seen in figure 8.72. In the beginning the curve seems to head towards a critical point but then turns away. This happens in the moment when contact occurs, because before this moment the problem does not differ form the unconstraint one of figure 8.70.

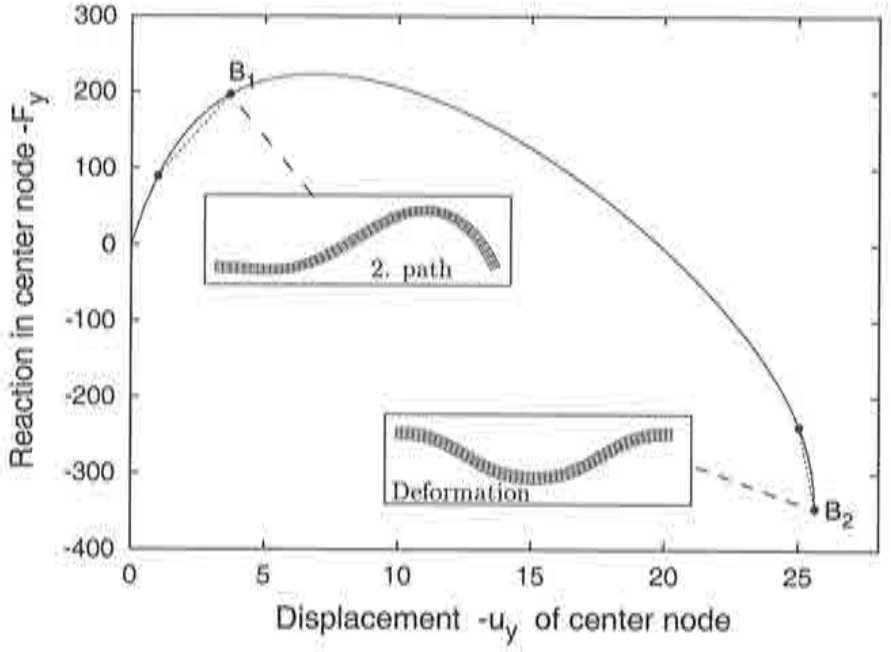

Figure 8.70: Equilibrium path for the hinged arch without obstacles with displacement boundary conditions

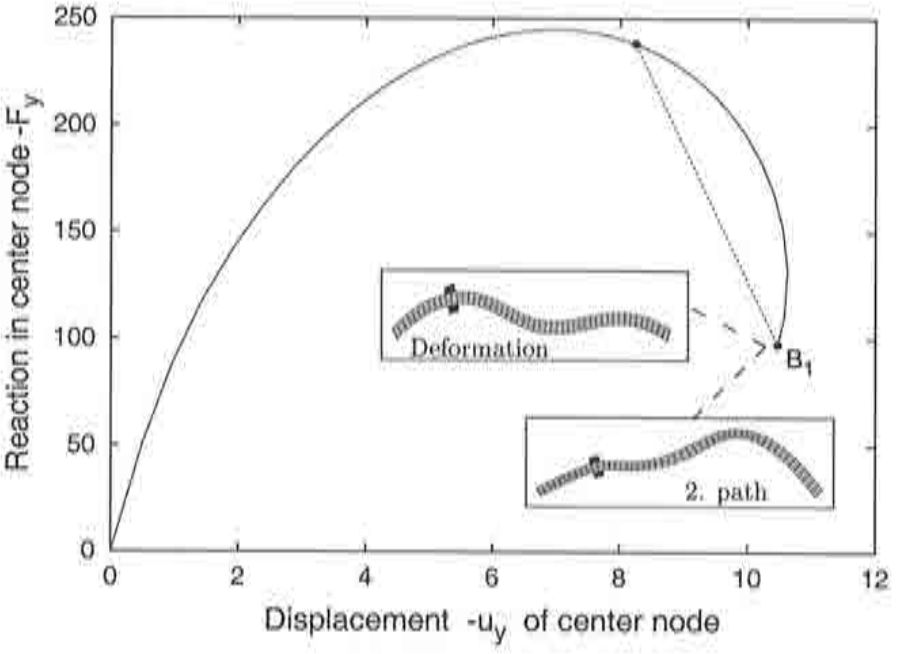

Figure 8.71: Equilibrium path for the hinged arch with contact and displacement boundary conditions

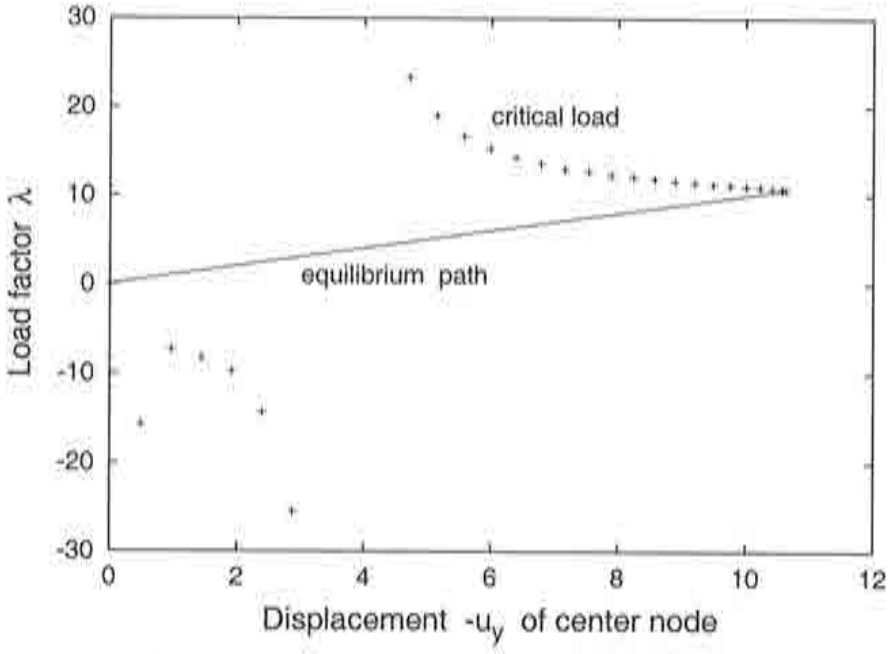

Figure 8.72: One step predictions for the hinged arch with contact and displacement boundary conditions

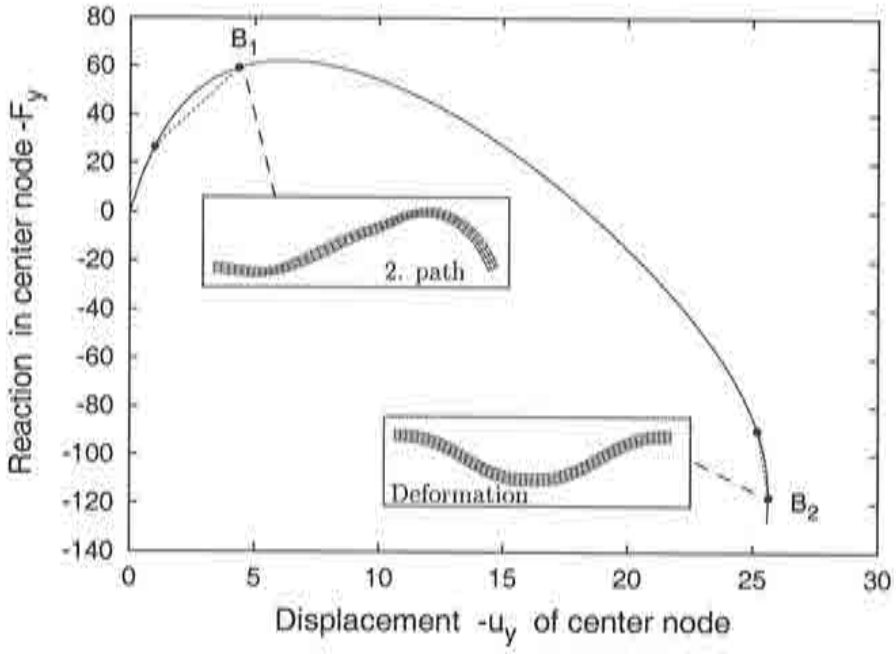

Figure 8.73: Equilibrium path for the hinged arch without obstacles with multiple displacement boundary conditions

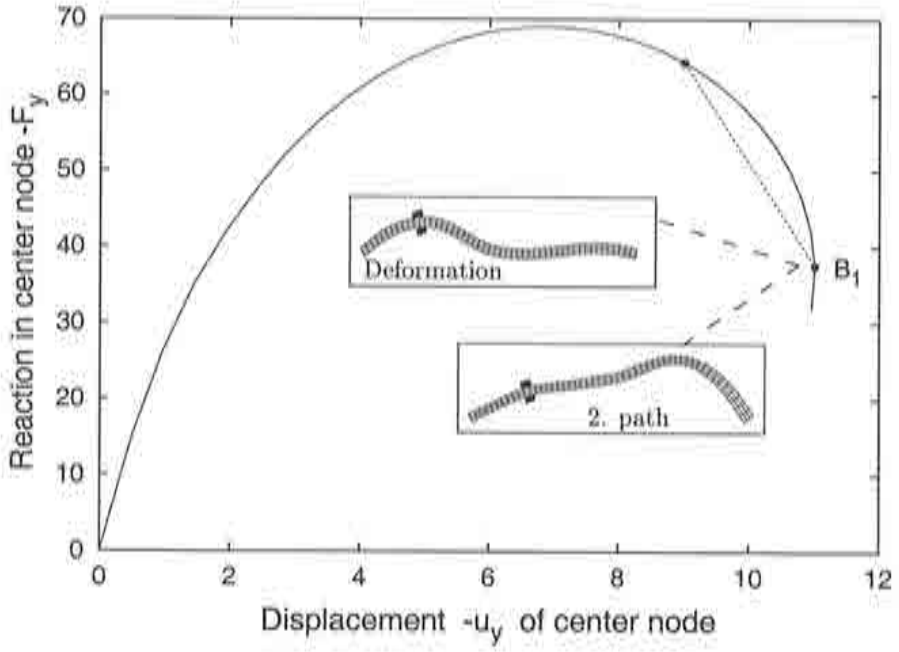

Figure 8.74: Equilibrium path for the hinged arch with contact and multiple displacement boundary conditions

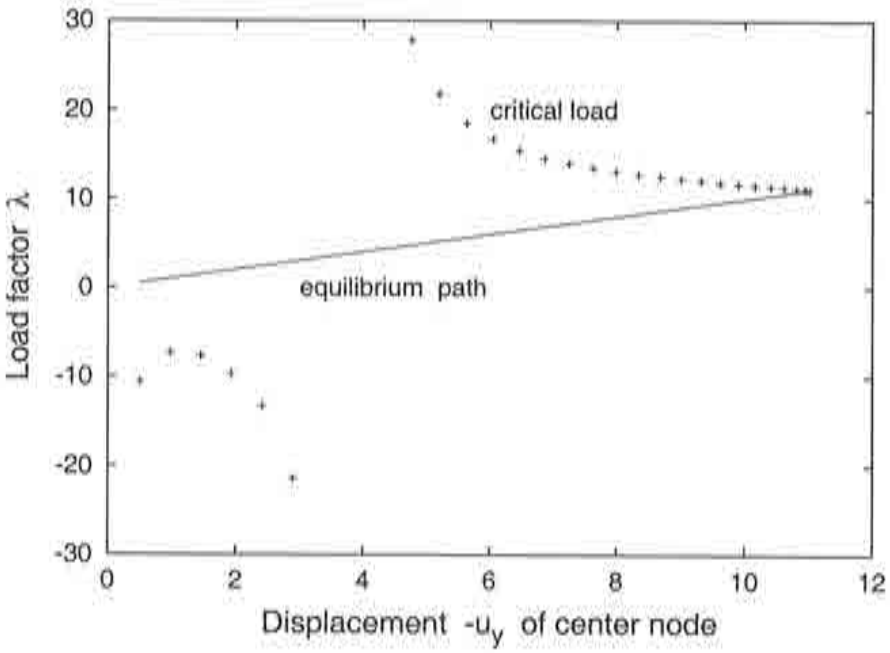

Figure 8.75: One step predictions for the hinged arch with contact and multiple displacement boundary conditions

As it is interesting to see, if the penalty method for displacement boundary conditions works also with prescribed values in multiple nodes, the displacement values of the three center nodes are constrained with $u_y = -1$. The equilibrium path for the structure without obstacles is shown in figure 8.73. Two bifurcation points similar to figure 8.70 are found: $B_1 : (u_y; F_y) = (-4.36; -59.2)$ and $B_2 : (u_y; F_y) = (-25.63; -117.3)$. Reactional forces and displacement still belong to the apex node of the arch.

When the obstacles are present, the behavior changes as the equilibrium path in diagram 8.74 demonstrates. Only one bifurcation point B_1 can be computed at $(u_y; F_y) = (-11.01; -37.6)$ with deformation similar to diagram 8.71.

The last figure 8.75 contains the one step prediction, which is also similar to figure 8.72. It indicates that good starting values for the critical point computation have displacements $-u_y > 8$.

8.2.2 Block pressing on arch

A block pressing on an arch is the next example with contact. The geometrical and material data are to be seen in figure 8.76. The block is loaded with a unit load in all the nodes, except for the corner nodes, where half of the load is specified. The block is located on top of the arch. The discretization of the arch is 20 layer with 400 elements each and the block has 11 layers with 300 elements each. Besides with the arch in figure 8.76 that is clamped, the example was also computed with a hinged arch. A sidewards movement of the block is prevented by fixating the x–displacements of the upper corner nodes of the block.

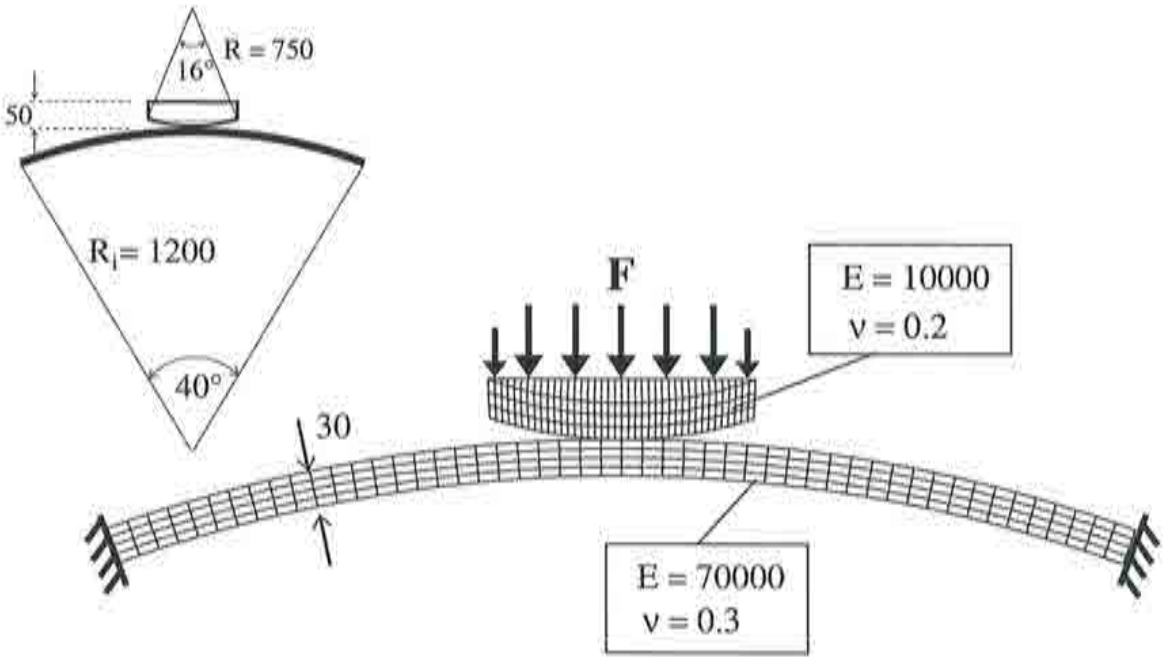

Figure 8.76: Block pressing on clamped arch

Figure 8.77 shows the equilibrium path and the typical behavior of a clamped arch with two limit points. The extended system yields the exact coordinates with $L_1 : (u_y; \lambda) = (-37.87; 12.88)$ and $L_2 : (u_y; \lambda) = (-81.97; 10.18)$. The symmetric deformation of the arch are given in the smaller pictures.

The one step predictions in figure 8.78 are quite good, the curve goes through both points. A comparison of one step prediction with figure 8.78 confirms the convergence radius of the extended system computations.

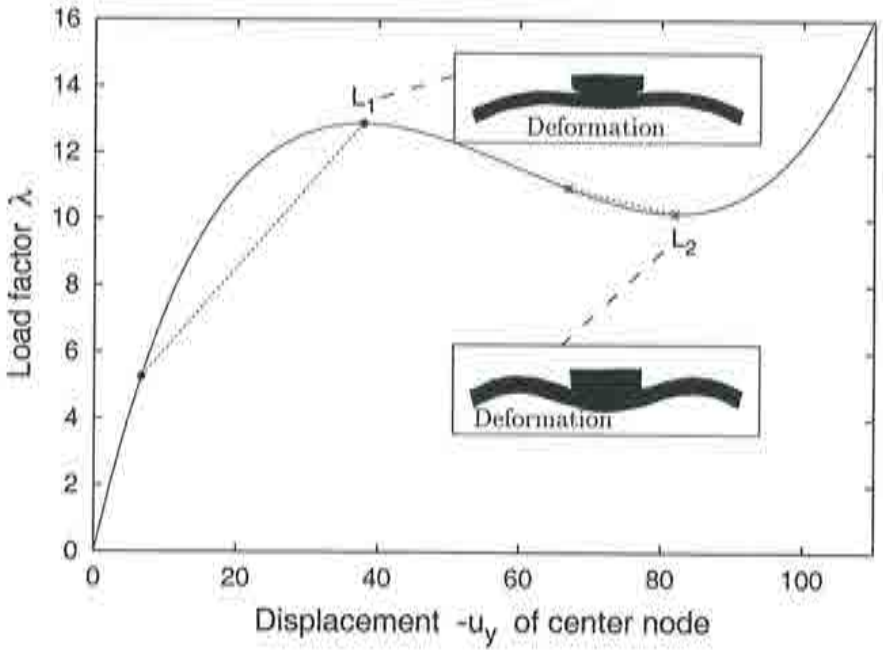

Figure 8.77: Equilibrium path for the block pressing on clamped arch

Changing the boundary conditions for the arch in such a way, that the ends are hinged, enables bifurcating of the equilibrium path, see diagram 8.79. The extended system has no problem in locating the bifurcation point $B_1 : (u_y; \lambda) = (-23.02; 11.03)$ and the limit point $L_1 : (u_y; \lambda) = (-40.75; 126.45)$. The up-scaled secondary path deformation associated with the eigenvector in B_1 can be seen in figure 8.79. The good results of the one step prediction (figure 8.80) are in accordance with the convergence radius of the extended system.

A further interesting load case of this example is the hinged arch with the block on top of it and a unit displacement prescribed in the upper center node of the block. The equilibrium path in diagram 8.81 has no limit point, only the bifurcation point $B_1 : (u_y; F_y) = (-26.89; -3440)$ is left. F_y is the reactional force in the upper center node of the block. In the diagram 8.82 the one step prediction for this load case is given.

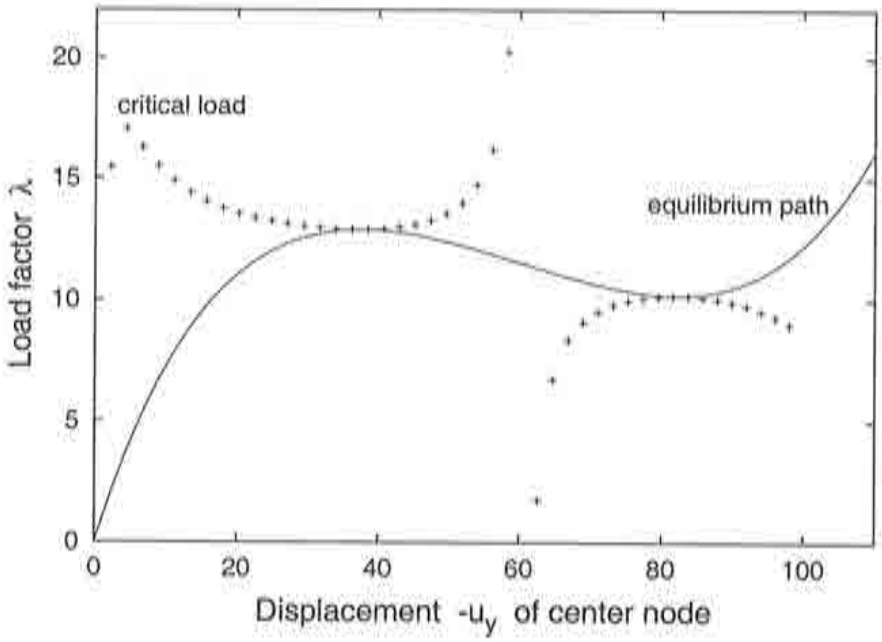

Figure 8.78: One step predictions for the block pressing on clamped arch

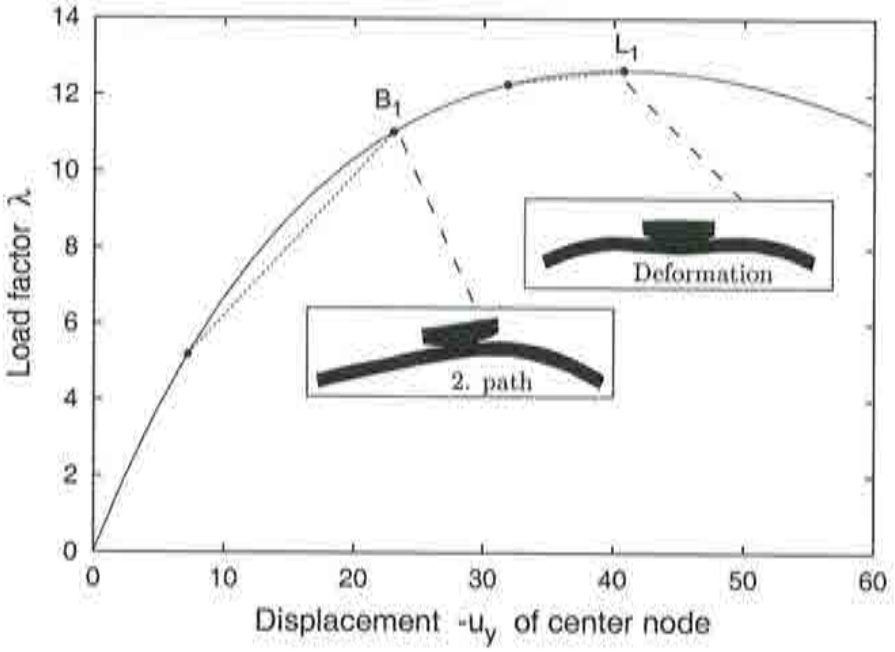

Figure 8.79: Equilibrium path for the block pressing on hinged arch

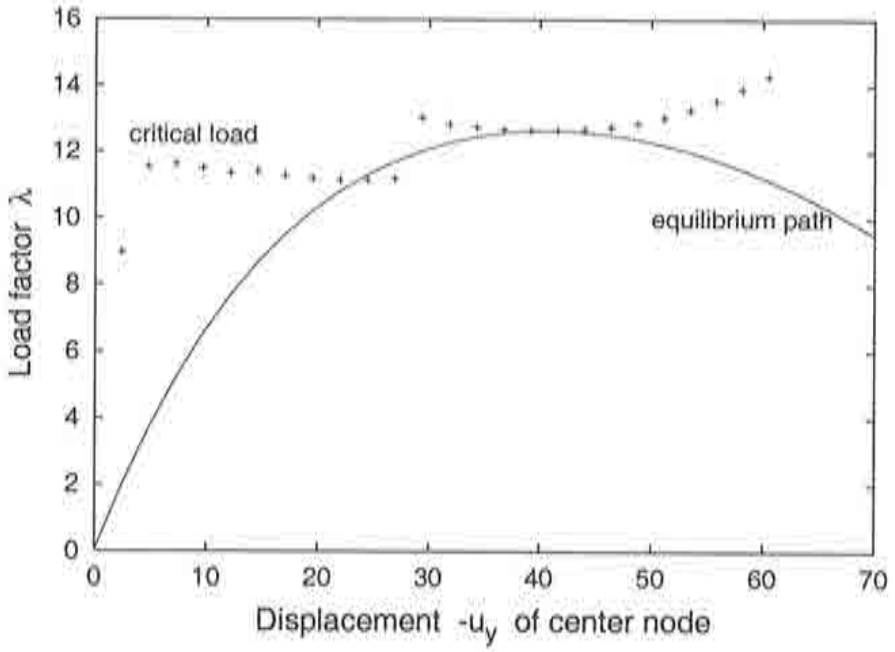

Figure 8.80: One step predictions for the block pressing on hinged arch

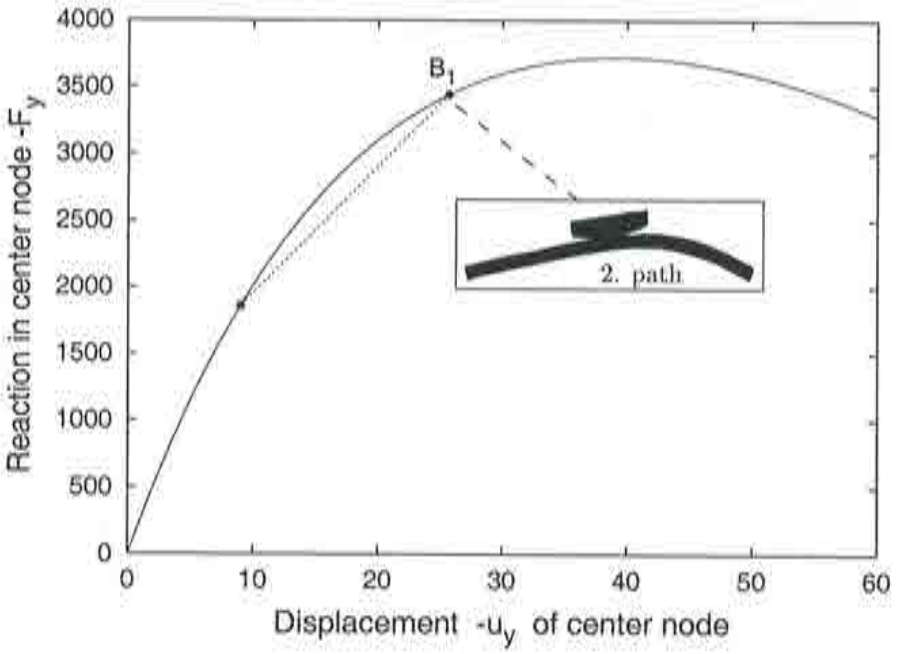

Figure 8.81: Equilibrium path for the hinged arch with displacement boundary conditions

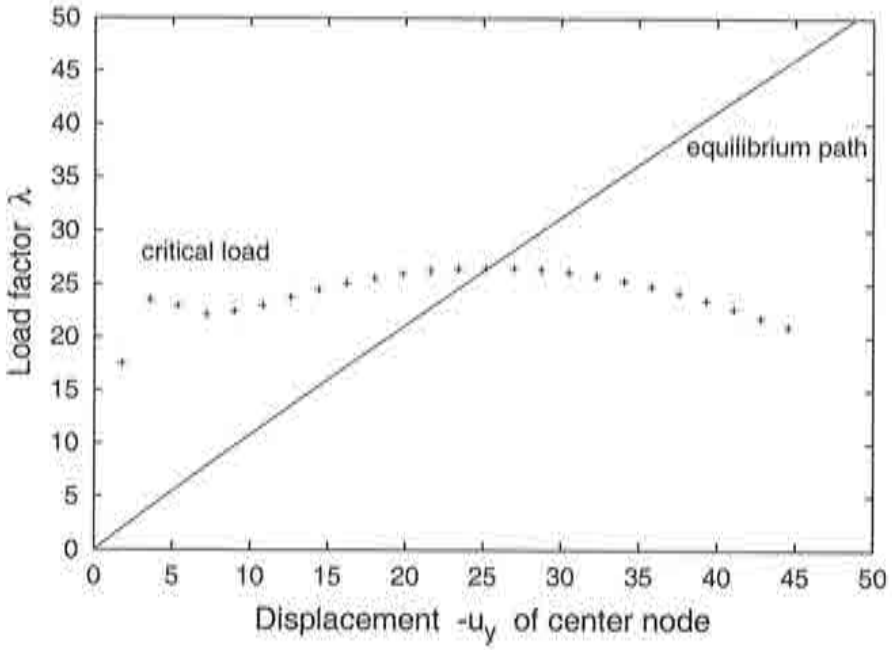

Figure 8.82: One step predictions for the hinged arch with displacement boundary conditions

8.2.3 Two arches

The next example is the structure of figure 8.83 with two arches. The lower arch is clamped and the sidewards movement (x–direction) of the upper arch is prevented by the boundary conditions in the corner nodes, where the unit loads are applied.

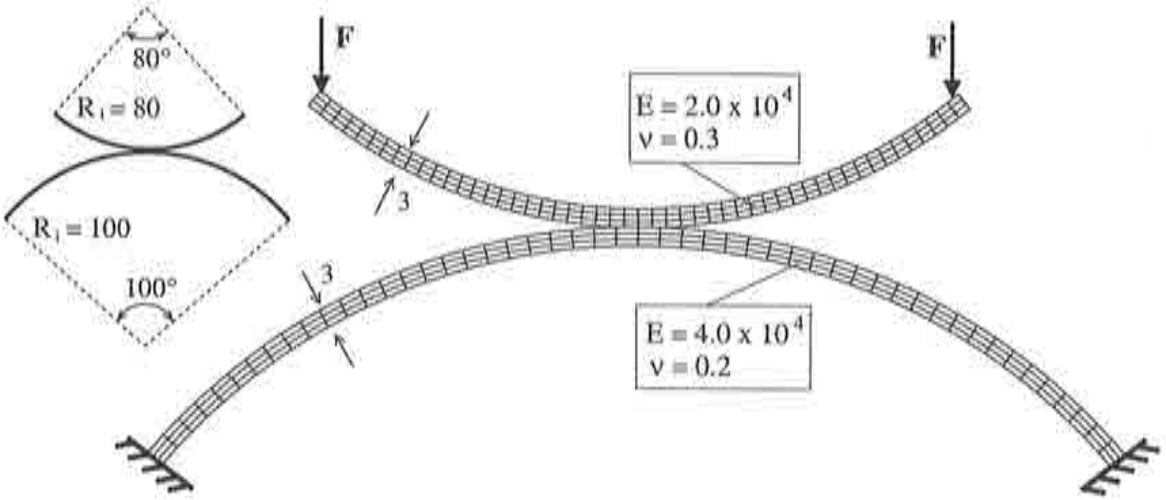

Figure 8.83: Outline of the two arches

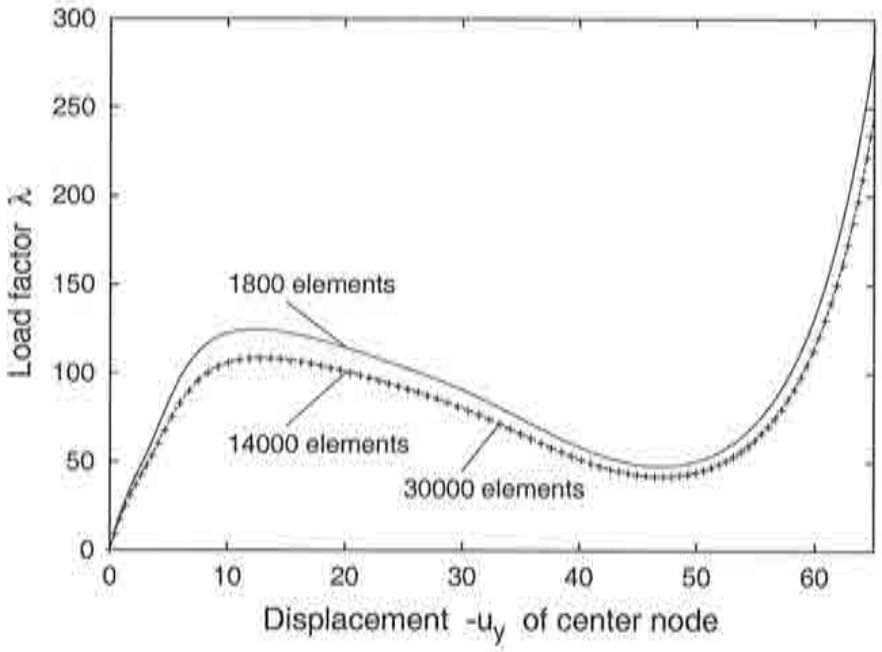

Figure 8.84: Equilibrium path of the two arches structure for different discretizations

Since only four node elements with linear shape functions are used, the question arises, if the elementation chosen is sufficient for a proper computation of the structure. Therefore a convergence test with different discretizations is made to see, how many elements are necessary. Figure 8.84 shows the results for the three discretizations with 1800, 14000 and 30000 elements. The curves demonstrate, that there is practically no difference anymore between the 14000 and the 30000 element curve, so that 14000 elements can be considered as sufficient for this example.

Looking in detail at the equilibrium path of diagram 8.85 reveals four critical points. Two bifurcation points with $B_1 : (u_y; \lambda) = (-0.85; 17.21)$ and $B_2 : (u_y; \lambda) = (-4.77; 75.94)$ and two limit load points with $L_1 : (u_y; \lambda) = (-12.94; 108.83)$ and $L_2 : (u_y; \lambda) = (-47.73; 42.14)$ are found. The deformed arches and the secondary path deformation respectively are depicted in the small pictures next to each critical point.

A comparison of these results with the one step prediction in diagram 8.86 demonstrates clearly the switching of the prediction from one critical point to another. Again the similarity of convergence radius of the extended system and the one step prediction curve is apparent.

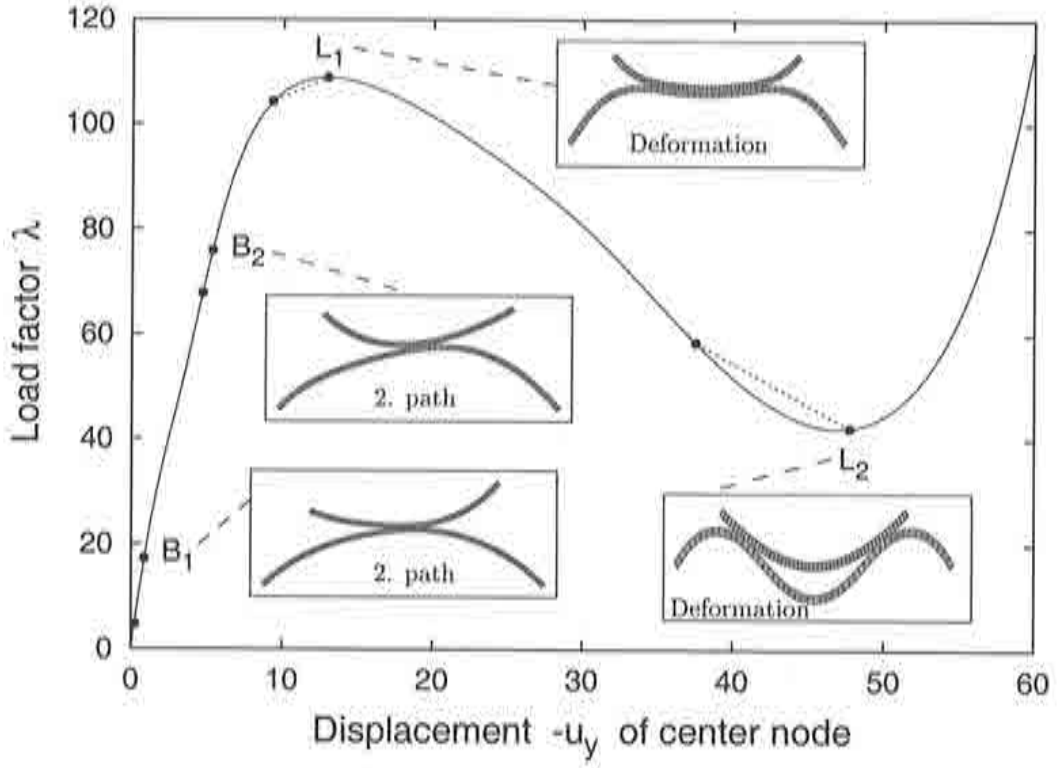

Figure 8.85: Equilibrium path with critical points

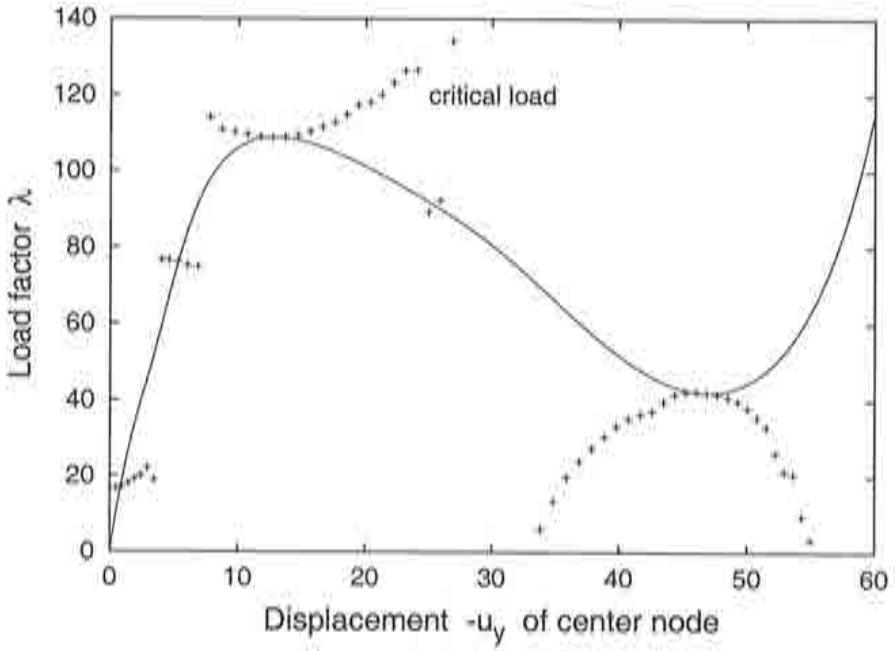

Figure 8.86: One step prediction for the two arches structure

8.2.4 Embedded deep arch

A further example is the hinged deep arch with two rectangular blocks at the bottom as depicted in figure 8.87. The blocks are clamped on one side. The deep arch has an inner radius of $R_i = 98$ and spans an angle of $\alpha = 289°$. Unit loads are applied in the 41 center nodes of the arch. The discretization chosen was 12 layers of 600 elements each for the deep arch and 8 layers of 300 elements each for the blocks.

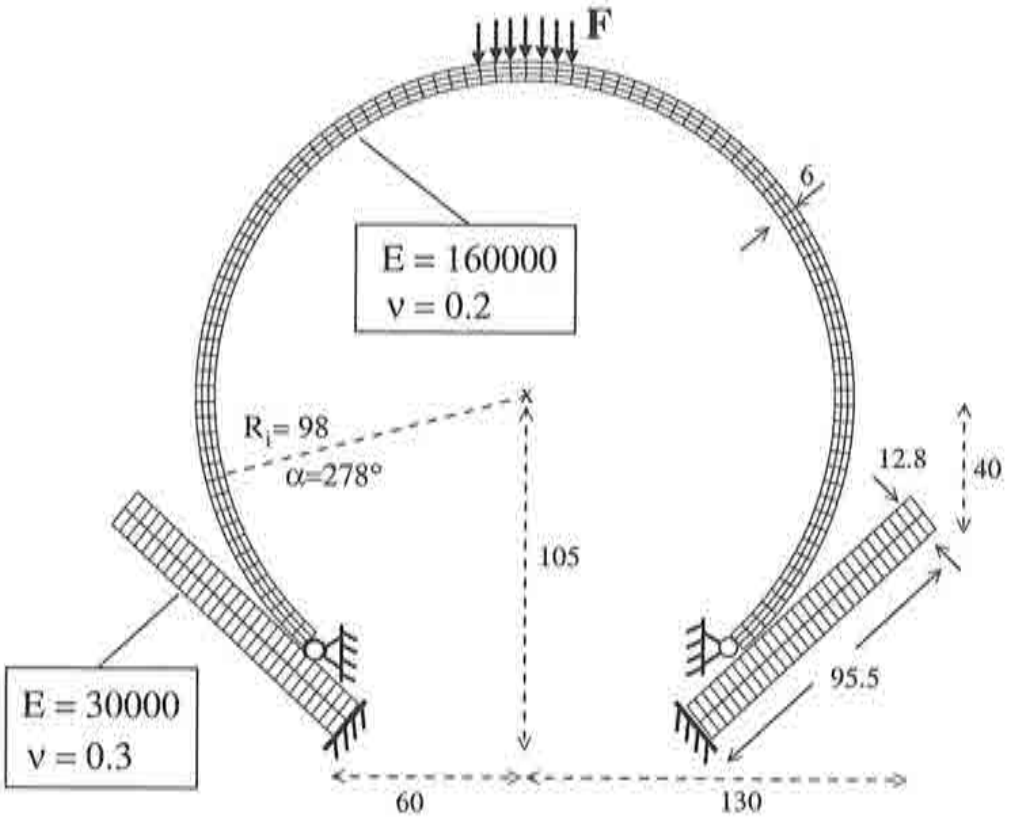

Figure 8.87: Outline of the embedded deep arch

The equilibrium path in figure 8.88 shows a bifurcation point $B_1 : (u_y; \lambda) = (-7.90; 5.31)$ and a limit load point $L_1 : (u_y; \lambda) = (-170.29; 61.55)$. Both points can be computed with the extended system, as is also indicated by the one step prediction in figure 8.89.
Replacing the force boundary conditions with displacement boundary conditions (unit displacements in the 41 center nodes) changes the behavior (see figure 8.90). Two bifurcation points can be computed with the extended system: $B_1 : (u_y; F_y) = (-72.37; 377.9)$ and $B_2 : (u_y; F_y) = (-143.64; 720.0)$. The one step prediction in figure 8.91 confirms the starting points for the extended system procedure.

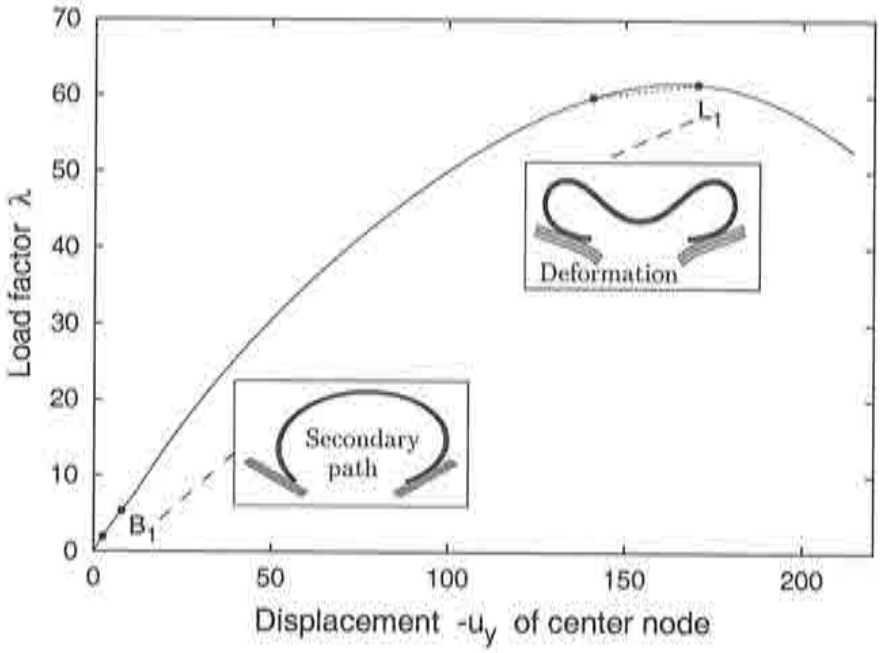

Figure 8.88: Equilibrium path for the embedded deep arch

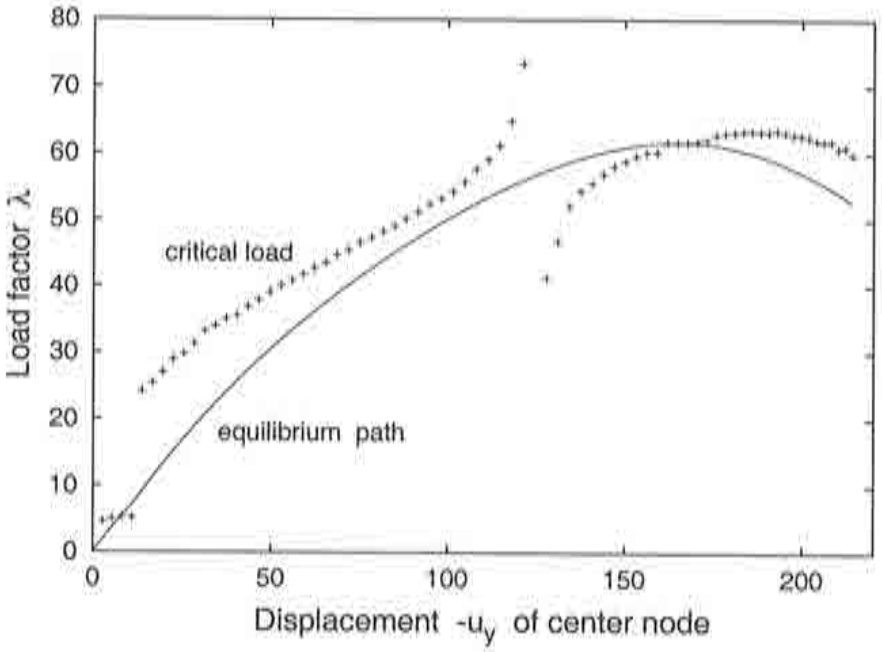

Figure 8.89: One step predictions for the embedded deep arch

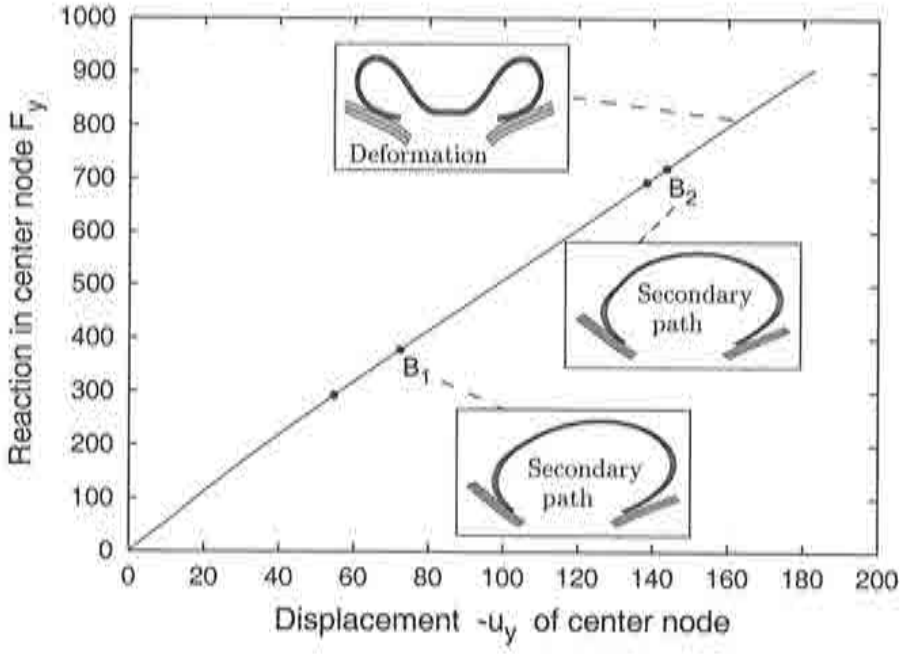

Figure 8.90: Equilibrium path for the embedded deep arch with displacement boundary conditions

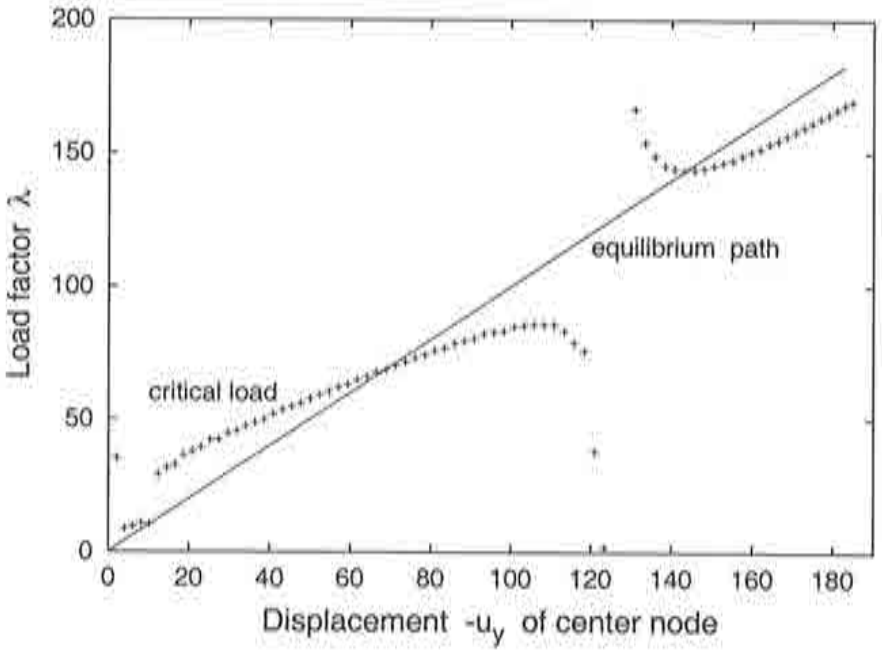

Figure 8.91: One step predictions for the embedded deep arch with displacement boundary conditions

8.2.5 Deep arch with obstacles

The geometrical data of the hinged deep arch with two arches as obstacles is outlined in figure 8.92. The obstacles are clamped on one side. The elementation of the deep arch is 12 layers with 600 elements each, the obstacles have 300 elements times 8 layers. Here also unit loads are placed in the 41 center nodes of the deep arch.

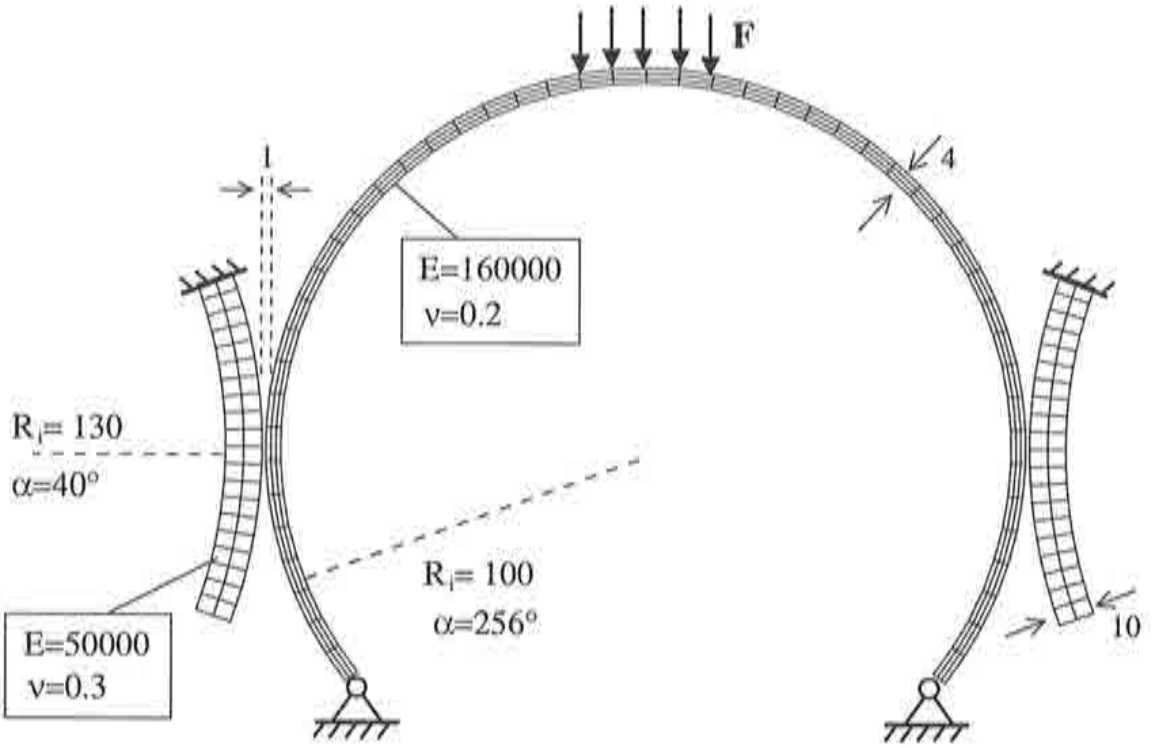

Figure 8.92: Outline of the deep arch with obstacles

The two limit load points $L_1 : (u_y; \lambda) = (-50.44; 20.94)$ and $L_2 : (u_y; \lambda) = (-144.4; 8.74)$ can be calculated with the extended system, as demonstrated in figure 8.93. The extended system computations for the points are started from a not to far distance as indicated by the one step predictions of figure 8.94.

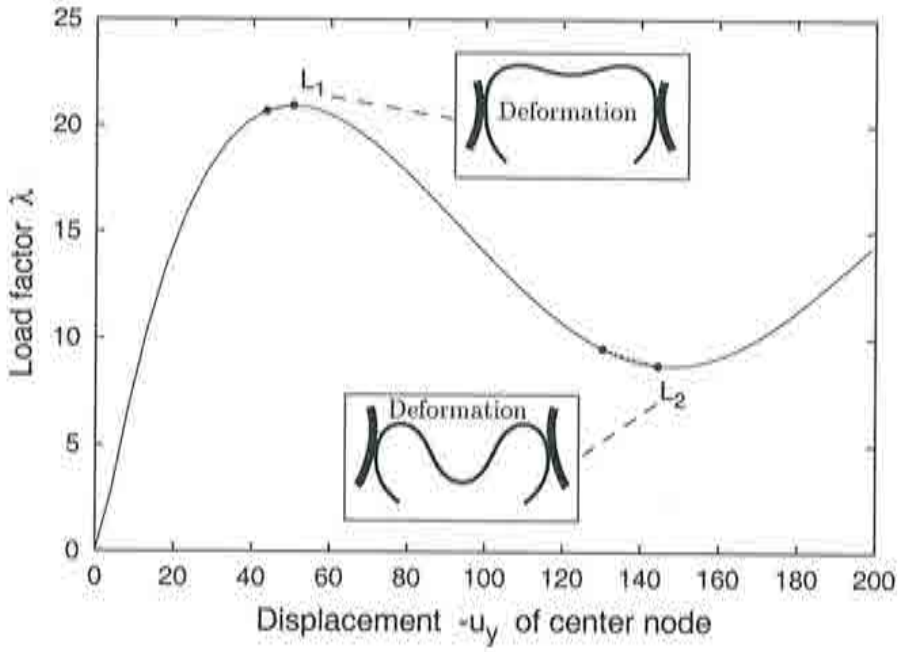

Figure 8.93: Equilibrium path for the deep arch with obstacles

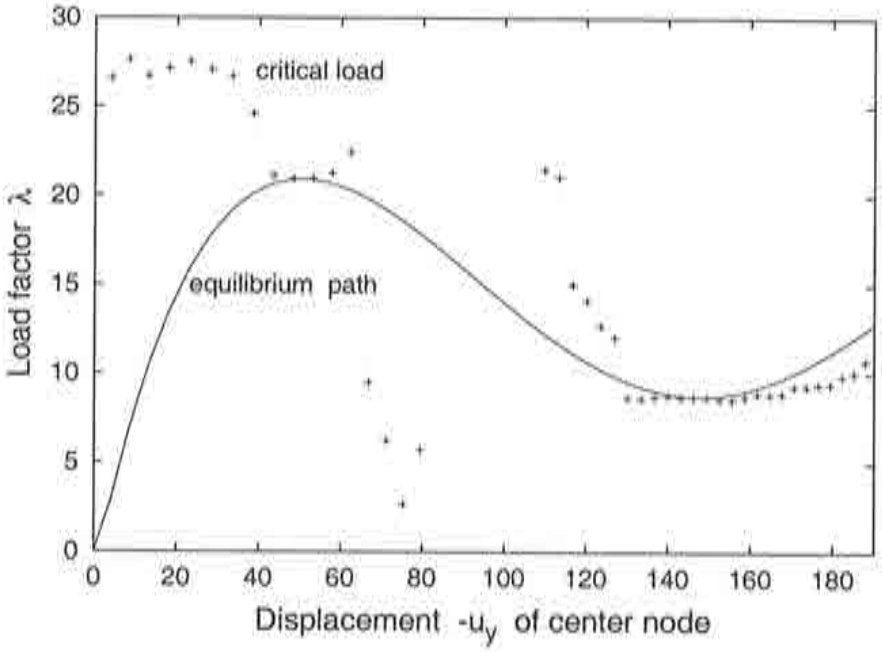

Figure 8.94: One step predictions for the deep arch with obstacles

8.2.6 Large deformation of a ring

The last example is a ring which undergoes large deformations. An outline of the cross section of this 3D problem is depicted in figure 8.95. Due to the symmetry only one quarter of the ring is computed with a discretization of 5 layers for the height with an array of 30 times 20 elements each. 8 node nonlinear brick elements are used. The contact interface of chapter 5 was derived for two dimensional problems and cannot be applied here. Since this is a unilateral contact problems, where the constraints coincide with a global degree of freedom, a simple penalty formulation for the z-degree of freedom of the nodes on the upper and lower side of the ring is used. Denoting an representative degree of freedom by an subscript k, the contact terms are:

$$P_c = \epsilon_N \, (v_k - v_{max}) \, \delta v_k \tag{8.1}$$

$$\frac{\partial P}{\partial v_k} \Delta v_k = \epsilon_N \delta v_k \, \Delta v_k \tag{8.2}$$

v_{max} is the maximal allowed z-displacement for the node. In other words equations (8.1) imply that if the constraint for a degree of freedom k is active ϵ_N has to be added to the diagonal of the tangent stiffness matrix $\mathbf{K}_T$ at the corresponding position.

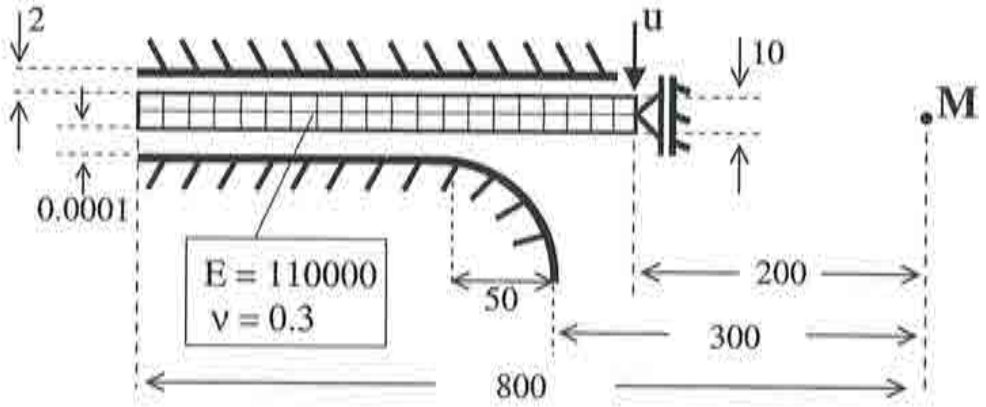

Figure 8.95: Outline of the cross section of the ring

As boundary conditions the in–plane movement of the inner nodes of the ring were fixed and a unit displacement was applied on all upper nodes of the inner ring. Symmetry boundary conditions were used to enable the modeling of the entire ring by computing only one quarter.

The equilibrium path of this problem is given in figure 8.96. The deformations of the structure are plotted on the left side of figure 8.97. The two bifurcation points $B_1 : (-u_z; \lambda) = (-43.9; 69.8)$ and $B_2 : (-u_z; \lambda) = (-68.6; 135.2)$ that are indicated by the one step prediction in diagram 8.96 are conformed by the count of negative diagonal elements during the arclength path computation. The one step prediction indicates, that the computation of B_1 is feasible in the nearer area, whereas B_2 seems problematic. The first iterations in the extended system computation of B_1 indicated convergence against the correct point, but then the iteration process diverged. A check of the eigenvector

that is computed by the extended system in the iteration before divergence takes place, demonstrates the expected buckling of the ring. (see right side of figure 8.97).

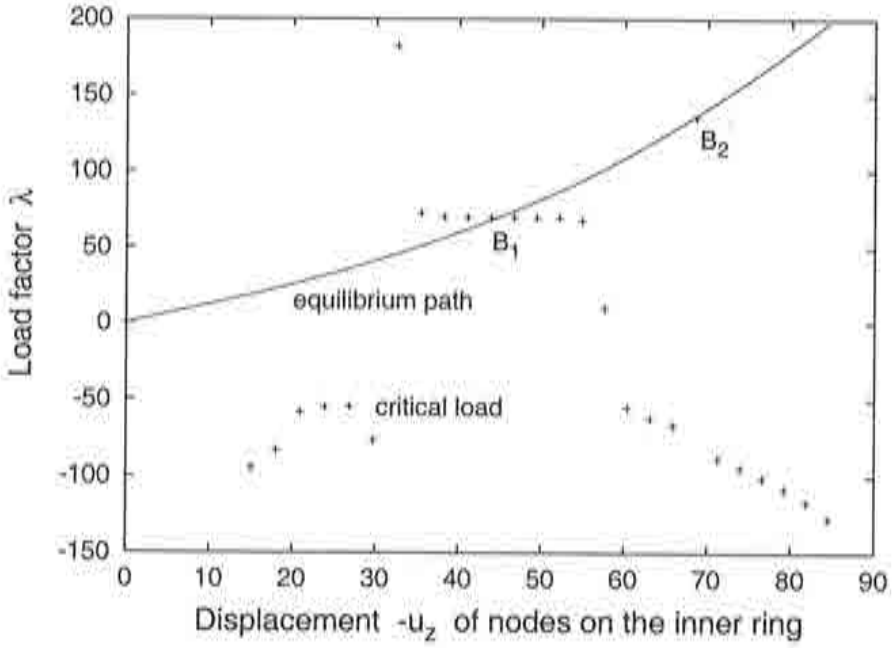

Figure 8.96: One step predictions for the ring

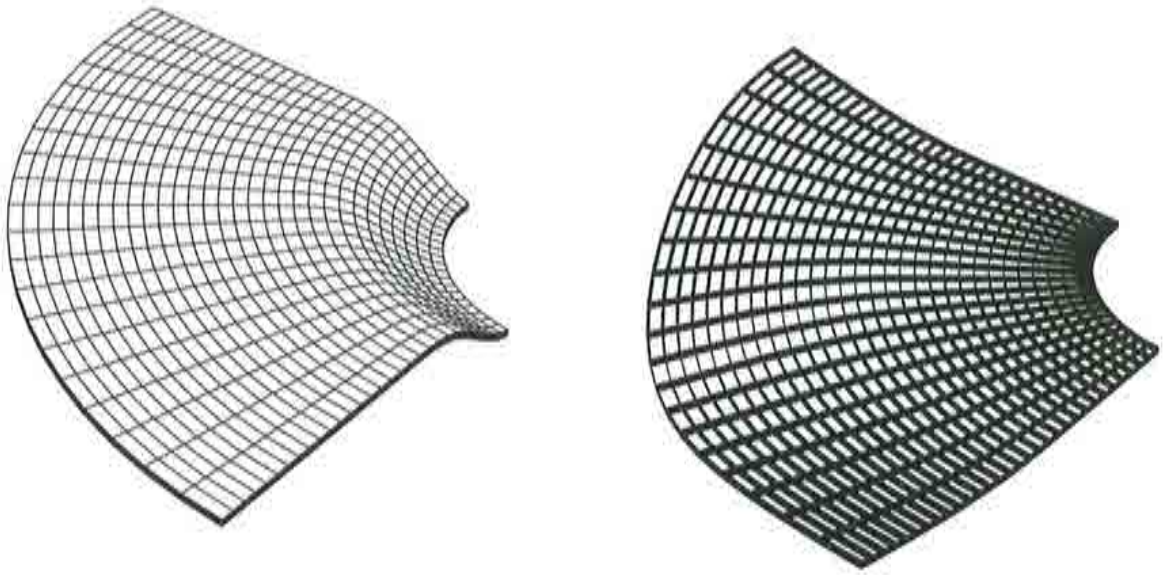

Figure 8.97: Ring: Deformation (left) and eigenvector at point B_1 (right)

Chapter 9

Conclusion

This thesis is concerned with instability points in structural mechanics. The objective was to directly compute critical points in combination with inequality constraints. Only isothermal, static or quasi–static mechanical problems were considered for this purpose. Inequality constraints were chosen which originate from internal damage or contact. All problems were solved numerically with the Finite Element Method.

A simple damage model without plasticity effects was used as constitutive law for the problems with damage inequality constraints. The model is bilinear and bases on the hyperelelastic St.Venant material law. It was chosen because of its simplicity and ease of implementation. The way this model is represented in the global set of equations facilitates a combination with the critical point detection methods.

Contact constraints were the second type of inequality constraints that were considered. A general formulation for bilateral contact was used, following the master–slave concept. A node–to–segment contact element for two–dimensional problems allowed a tangential movement of the bodies. The incorporation of the inequality constraints in the set of equations is more difficult than in the damage case. Among the common methods that were presented the penalty method was chosen. It is used frequently for contact problems of this formulation type and is easy to implement in existing FE programs. Moreover it does not lead to an augmentation of the number of equations and unknowns.

The governing equations of the isothermal quasi–static problems in this thesis were derived from the weak form of the balance of linear momentum. These equations were solved with the FEM in combination with the Newton–Raphson method. Prior to a critical point computation the equilibrium path of all problems was calculated. Due to the complexity of the load–deflection paths arclength methods were used. A variety of control equations was presented among which the iteration on a normal plane was implemented. The efficiency of this control equation type was confirmed in the examples..

In stability theory the energy potential was used to define the criteria for stable and unstable parts of the equilibrium path. The conditions for singular points were also derived in this context and a distinction of limit load points and bifurcation points was made. Among the methods for a critical point detection, generally indirect and direct methods can be distinguished. For the objective of a calculation of critical points, the direct methods were preferred as these provide a faster, direct and more exact way. The extended system proved to be reliable in this field. A factor that could be improved in this method is the dependence on the starting values. Therefore, a possible combination

of the extended system with a second method was studied. The CDM showed to give rather good predictions of the critical values with the help of secant stiffness relations.

A conceivable combination of both methods, to use the results of the CDM as input values for the extended system was evaluated. The critical displacements predicted by the CDM were not suitable, as the critical displacements are merely a multiple of the current displacement pattern of the starting value. Without a reiteration of the displacement vector this does not make any difference to using the current displacement pattern, as it is already done in the extended system. A use of this critical displacement prediction for the eigenvector starting value does not make much sense either then. The critical load predicted by the CDM was evaluated as input for the extended system. Therefore the one step prediction methods based on the ideas of the extended system was developed. The out–coming critical load was then compared to the CDM prediction. The first part of the examples was dedicated to this comparison. Additionally to the normal constraint free cases, damage was introduced. For the CDM in combination with damage the fact that first a prediction of the critical displacements was made was exploited to enhance the critical load prediction. The prediction was then based on the damage state corresponding to the predicted critical displacements.

The comparison of the critical load predicted by CDM and one step prediction demonstrated that the CDM values generally were better than the one step prediction values. In the damage problems the CDM enhanced predictions mentioned above showed the expected improvements. In some problems with solid elements and with damage however, the one step prediction values were better. Despite these results, the critical load remains the only meaningful starting value for the extended system that can be taken from CDM predictions. Taking further into account that the effort for the implementation of the CDM is rather high due to the use of the secant stiffness matrix, the conclusion of this comparison was that a combination does not offer any substantial advantages.

In the second part the extended system was evaluated for problems with contact constraints. A rather straightforward way of combining extended system and contact was presented. The idea of a critical point computation with the extended system for problems with displacement boundary conditions lead to the development of a representation of these with a penalty method. Prescribed displacements were treated as equality constraints. Using this, several contact examples with force and displacement boundary conditions were computed. It turned out that the one step predictions provides a good indicator for meaningful starting points of the extended system. Common test functions for critical points such as the determinant or the smallest eigenvalue of the tangent stiffness matrix can be used to detect critical points when they are calculated accompaningly to a path computations, but do not provide any information about a successful application of the extended system. Here the one step prediction can at least give hints. In regions where the one step prediction values form a smooth curve the use of the extended system seems appropriate. One step prediction values lying scattered around indicate unfavorable starting values. The fact that the one step predictions in between two critical points clearly reflects the jump from one point to the other, confirms the use as an indicator.

The results of the extended system with contact problems were good. Most of the critical points were correctly detected, although some of them only with starting values in the closer vicinity of the critical point. This holds especially for critical points situated in between others or close to others, so that the extended system showed problems in

resolving each point. In the last example the extended system did not work, but the critical point was found by the one step prediction. Although the extended system diverged, the eigenvector in the critical point was correct.

The combination of extended system and one step prediction proved to be useful also in the computation of critical points for more complex contact problems. Besides its ease of implementation in existing FE programs, another advantage of the extended system is that the eigenvector belonging to the critical point is computed automatically within this process. In bifurcation points this eigenvector provides information about the secondary path and can be used in branch switching procedures.

Appendix A

Constrained optimization problems

The most general form of constrained optimization problems is the constrained nonlinear optimization problem. The mathematical form of which looks like:

$$\begin{array}{lll} \text{minimize} & f(\mathbf{x}) & \mathbf{x} \in \Gamma \subset E^n \\ \text{subject to} & \mathbf{h}(\mathbf{x}) = 0 & \mathbf{g}(\mathbf{x}) \leq 0 \end{array} \tag{A.1}$$

The function $\mathbf{f}$ has to be minimized subject to equality constraints $\mathbf{h}$ and inequality constraints $\mathbf{g}$. Both are vector functions, of the dimensions m and p respectively, with $m, p \leq n$.

$$\mathbf{h}(\mathbf{x}) = \begin{pmatrix} h_1(\mathbf{x}) \\ h_2(\mathbf{x}) \\ \vdots \\ h_m(\mathbf{x}) \end{pmatrix} = 0 \qquad \mathbf{g}(\mathbf{x}) = \begin{pmatrix} g_1(\mathbf{x}) \\ g_2(\mathbf{x}) \\ \vdots \\ g_p(\mathbf{x}) \end{pmatrix} \leq 0$$

A point $\hat{\mathbf{x}}$ that satisfies (A.1) is called *feasible*. An inequality constraint $g_i(\mathbf{x}) \leq 0$ is said to be *active* at a feasible point $\hat{\mathbf{x}}$, if $g_i(\hat{\mathbf{x}}) = 0$ and *inactive*, if $g_i(\hat{\mathbf{x}}) < 0$. Transferring this back to the problem of contact, this can be connected to the terms of the active $\partial\mathcal{B}_c^*$ and the inactive contact surface $\partial\mathcal{B}_c \backslash \partial\mathcal{B}_c^*$.

If it were known a priori which constraints were active at the solution to (A.1) the inactive constraints could be ignored and the active ones treated as equality constraints. Generally this is not the case, but nevertheless using this as a simplification leads to the definition of the *active set*. The underlying idea is to partition the inequality constraints in two groups: those that are to be treated as active and those that are to be treated as inactive. Forming now a set of the active ones and ignoring the inactive gives the active set. It is evident that the active set in not constant during the computation. In the same manner as constraints become active or inactive the active set has to be changed.

According to [Luenberger, 1992], where the following definitions are taken from, for a regular point $\mathbf{x}^*$ to be solution point of (A.1), the following first-order necessary conditions (A.2), called the *Kuhn-Tucker Conditions*, have to be fulfilled:

$$\nabla f(\mathbf{x}^*) + \boldsymbol{\mu}^T \nabla \mathbf{h}(\mathbf{x}^*) + \boldsymbol{\lambda}^T \nabla \mathbf{g}(\mathbf{x}^* = 0 \quad \text{(A.2)}$$

$$\boldsymbol{\lambda}^T \mathbf{g}(\mathbf{x}^*) = 0 \quad \text{(A.3)}$$

$$\text{with} \quad \boldsymbol{\mu} \in E^m, \quad \boldsymbol{\lambda} \in E^p, \quad \boldsymbol{\lambda} \geq \mathbf{0}$$

The vectors $\boldsymbol{\mu}$ and $\boldsymbol{\lambda}$ are called the vectors of the *Lagrangian Multipliers*. The last two terms of the first equation assure, that the gradient vectors $\nabla \mathbf{g}$ and $\nabla \mathbf{h}$ are linearly independent. Differentiating equation A.2 one more time the Hessian matrix $\mathbf{L}$ is obtained.

$$\mathbf{L}(\mathbf{x}) = \frac{\partial^2}{\partial x^2} \left[f(\mathbf{x}) + \boldsymbol{\mu}^T \mathbf{h}(\mathbf{x}) + \boldsymbol{\lambda}^T \mathbf{g}(\mathbf{x}) \right] \quad \text{(A.4)}$$

The second-order necessary condition for a regular point $\mathbf{x}^*$ satisfying the constraints $\mathbf{f}, \mathbf{g}$ to be a minimum point of (A.1) is, that the Hessian matrix $\mathbf{L}$ is positive semidefinite.

$$\mathbf{L}(\mathbf{x}^*) = \mathbf{F}(\mathbf{x}^*) + \boldsymbol{\mu}^T \mathbf{H}(\mathbf{x}^*) + \boldsymbol{\lambda}^T \mathbf{G}(\mathbf{x}^*) \quad \text{(A.5)}$$

Here $f, \mathbf{h}, \mathbf{g} \in C^2$ is required, whereas for the Kuhn-Tucker Conditions $f, \mathbf{h}, \mathbf{g} \in C^1$ is sufficient.

Appendix B

Inverse Iteration

Among the solution procedures for eigenvalue problems two main groups can be distinguished: Iterative and direct procedures. Especially for large matrices iterative methods are superior in computation time, but suffer from the disadvantage that they only compute few eigenvalues and -vectors. The *inverse iteration*, the *Jacobi method* and the *subspace iteration* are common mathematical procedures for solving eigenvalue problems. Details about those methods can be found in [Bathe, 1996] and [Wagner, 1991b]. Here only the inverse iteration will be described briefly as it is used in the CDM.

With the inverse iteration the smallest eigenvalue and the accompanying eigenvector of an eigenvalue problem can be computed. A similar procedure called the *forward iteration* exists for the calculation of the largest eigenvalue. As stability problems in mechanics always are connected with the smallest eigenvector only the inverse iteration is of interest in this thesis.

The eigenvalue problem to be solved can be formulated as

$$(\mathbf{K} - \omega \mathbf{M})\ \boldsymbol{\phi} \ = \ \mathbf{0}, \tag{B.1}$$

where $\mathbf{K}$ is a positive definite matrix, $\mathbf{M}$ a banded matrix typically, ω the eigenvalue and $\boldsymbol{\phi}$ the associated eigenvector. The inverse iteration algorithm is shown in table B.1.
As a starting vector for $\mathbf{x}$ the vector $\mathbf{1}$ with all components equal to one is a good choice, because it still "contains all information". The Rayleigh quotient $\rho(\bar{\mathbf{x}})$ is used as an approximation of the first eigenvalue.

If $\mathbf{M}$ is equal to the unit matrix $\mathbf{I}$ the problem simplifies considerably. To solve the problem

$$(\mathbf{K} - \omega \mathbf{I})\ \boldsymbol{\Phi} \ = \ \mathbf{0}, \tag{B.2}$$

the inverse iteration algorithm from B.1 can be altered as presented in table B.2
The convergence proof for both procedures can be found in [Bathe, 1996]. [Wagner, 1991b] contains a short discussion of the practical aspects, which are important for the application of the inverse iteration. The method can be extended to the computation of higher eigenvalues with a *Gram–Schmidt–orthogonalization*, see e.g. [Wagner, 1991b].

Starting value: $\mathbf{x}^1 = \mathbf{1}, \quad \mathbf{y}^1 = -\mathbf{M}\mathbf{x}^1$

Iteration loop: $i = 0, 1, \ldots$ until convergence

$$\begin{aligned}
\overline{\mathbf{x}}^{i+1} &= \mathbf{K}^{-1}\mathbf{y}^i \\
\overline{\mathbf{y}}^{i+1} &= -\mathbf{M}\,\overline{\mathbf{x}}^{i+1} \\
\rho(\overline{\mathbf{x}}^{i+1}) &= \frac{\overline{\mathbf{x}}^{i+1^T}\,\mathbf{y}^i}{\overline{\mathbf{x}}^{i+1^T}\,\overline{\mathbf{y}}^{i+1}} \\
\mathbf{y}^{i+1} &= \frac{\overline{\mathbf{y}}^{i+1}}{(\overline{\mathbf{x}}^{i+1^T}\,\overline{\mathbf{y}}^{i+1})^{\frac{1}{2}}} \\
\omega^{i+1} &= \rho(\overline{\mathbf{x}}^{i+1})
\end{aligned}$$

Convergence: $\dfrac{\|\omega^{i+1} - \omega^i\|}{\omega^{i+1}} \leq TOL$

Solution: $\omega_1 = \omega^{i+1}, \quad \phi_1 = \dfrac{\overline{\mathbf{x}}^{i+1}}{(\overline{\mathbf{x}}^{i+1^T}\,\overline{\mathbf{y}}^{i+1})^{\frac{1}{2}}}$

Table B.1: Inverse iteration algorithm for the general eigenvalue problem

Starting value: $\mathbf{x}^1 = \mathbf{1}$

Iteration loop: $i = 0, 1, \ldots$ until convergence

$$\begin{aligned}
\overline{\mathbf{x}}^{i+1} &= \mathbf{K}^{-1}\mathbf{x}^i \\
\rho(\overline{\mathbf{x}}^{i+1}) &= \frac{\overline{\mathbf{x}}^{i+1^T}\,\mathbf{x}^i}{\overline{\mathbf{x}}^{i+1^T}\,\overline{\mathbf{x}}^{i+1}} \\
\mathbf{x}^{i+1} &= \frac{\overline{\mathbf{x}}^{i+1}}{\|\overline{\mathbf{x}}^{i+1^T}\|} \\
\omega^{i+1} &= \rho(\overline{\mathbf{x}}^{i+1})
\end{aligned}$$

Convergence: $\dfrac{\|\omega^{i+1} - \omega^i\|}{\omega^{i+1}} \leq TOL$

Solution: $\omega_1 = \omega^{i+1}, \quad \phi_1 = \mathbf{x}^{i+1}$

Table B.2: Inverse iteration algorithm for the special eigenvalue problem

Bibliography

Abbott, J. (1978). An efficient algorithm for the determination of certain bifurcation points. *Journal of Computational and Applied Mathematics*, 4(1):19–27.

Bathe, K. (1996). *Finite element procedures*. Prentice Hall, Englewood Cliffs, New Jersey.

Becker, E. and Bürger, W. (1975). *Kontinuumsmechanik*. B.G. Teubner, Stuttgart, Germany.

Bergan, P., Horrigmoe, G., Krakeland, B., and Soreide, T. (1978). Solution techniques for non–linear finite element problems. *International Journal for Numerical Methods in Engineering*, 12:1677–1696.

Bertsekas, D. (1982). *Constrained optimization and Lagrange multiplier methods*. Academic Press, New York.

Björkman, G. (1992). Path following and critical points for contact problems. *Computational Mechanics*, 10:231–246.

Chaboche, J. (1974). Une loi différentielle d'endommagement de fatigue avec cumulation non linéaire. *Rev. Fr. Méc.*, 50–51.

Chaboche, J. (1984). Anisotropic creep damage in the framework of continuum damage mechanics. *Nuclear Engineering Design*, 79:309–319.

Choong, K. and Hangai, Y. (1993). Review on methods of bifurcation anaylsis for geometrically non linear structures. *Bolletin of IASS*, 34(112):133–149.

Christensen, C., Klarbring, A., Pang, J., and Strömberg, N. (1998). Formulation and comparison of algorithms for frictional contact problems. *International Journal for Numerical Methods in Engineering*, 42:145–173.

Crisfield, M. (1981). A fast incremental/iterative solution procedure that handles snap through. *Computers and Structures*, 13:55–62.

Crisfield, M. (1991a). *Non–linear finite element analysis of solids and structures*, volume 1. John Wiley & Sons, Chichester.

Crisfield, M. (1991b). *Non–linear finite element analysis of solids and structures*, volume 2. John Wiley & Sons, Chichester.

Curnier, A. (1984). A theory of friction. *International Journal of Solids and Structures*, 20:637–647.

Curnier, A., He, Q., and Klarbring, A. (1994). Continuum mechanics modeling of large deformation contact with friction. In J.J. Moreau, M.Raous, M. J., editor, *Contact Mechanics, Proceedings of the 2nd Contact Mechanics International Symposium 1994*, London. Plenum Publishing.

Dawe, D. (1971). Finite deflection analysis of shallow arches by discrete element method. *International Journal for Numerical Methods in Engineering*, 3(4).

de Boer, R. (1982). *Vektor- und Tensorrechnung für Ingenieure*. Springer Verlag, Berlin, Heidelberg.

de Souza Neto, E., Perić, D., and Owen, D. (1998). Continuum modeling and numerical simulation of material damage at finite strains. *Archives of Computational Methods in Engineering*, 5(4):311–384.

Decker, D. and Keller, H. (1980). Solution branching – a constructive technique. In Holmes, P., editor, *New Approaches to Nonlinear Problems in Dynamics*, pages 53–69. SIAM, Philadelphia, PA.

Euler, L. (1774). *Methodus inveniendi lineas curvas maximi minimive propietate gaudentes, (Appendix, De curvis elasticis)*. Lausanne and Geneva.

Felippa, C. and Crivelli, L. (1991). A congruential formulation of nonlinear finite elements. In Wriggers, P. and Wagner, W., editors, *Non linear computational mechanics, The state of the art*, pages 283–302, Berlin. Springer–Verlag.

Gurson, A. (1977). Continuum theory of ductile rupture by void nucleation and growth - part 1: Yield criteria and flow rule for porous media. *Journal of Engineering and Mathematical Techniques*, 99:2–15.

Hallquist, J. (1979). Nike2d: An implicit finite deformation, finite element code for analyzing the static and dynamic response on two– dimensional solids. Report UCRL-52678, UC-Lawrence Livermore National Laboratory.

Haraldsson, A., Han, C., Tschöpe, H., and Wriggers, P. (1997). Shape optimization of a lubricated journal bearing with regard to the distribution of pressure in the fluid. *Engineering Optimization*, 29:259–275.

Jepson, A. and Spence, A. (1985). Folds in solutions of two parameter systems and their calculation. *SIAM Journal of Numerical Analysis*, 22:347–369.

Kachanov, L. (1958). Time of the rupture process under creep conditions. *IVZ Akad. Nauk., S.S.R., Otd. Tekhn. Nauk.*, 8:26–31.

Keller, H. (1977). Numerical solution of bifurcation and nonlinear eigenvalue problems. In Rabinowitz, P., editor, *Application of Bifurcation Theory*, pages 359–384. Academic Press, New York.

Klarbring, A. (1988). On discrete and discretized non-linear elastic structures in unilateral contact (stability, uniqueness and variational principles). *International Journal of Solids and Structures*, 24(5):459–479.

Klingbeil, E. (1989). *Tensorrechnung für Ingenieure*. BI-Wissenschaftsverlag, Mannheim.

Koiter, W. (1945). Over de stabiliteit von het elastisch evenwicht. H.J. Paris, Amsterdam.

Kondoh, K. and Atluri, S. (1985). Influence of local buckling on global instability: simplified, large deformation, post–buckling analysis of plane trusses. *Computers and Structures*, 21(4):613–627.

Kragelski, I., Dobychin, M., and Kombalov, V. (1982). *Friction and wear – Calculation methods*. Pergamon Press, Oxford.

Laursen, T. and Simo, J. (1993). A continuum-based finite element formulation for the implicit solution of multibody large deformation fricitional contact problems. *International Journal for Numerical Methods in Engineering*, 36:3451–3485.

Lemaitre, J. (1971). Evaluation of dissipation and damage in metals. In *Proceedings of I.C.M. Kyoto, Japan*, volume 1, Kyoto.

Lemaitre, J. (1984). How to use damage mechanics. *Nuclear Engineering and Design*, 80:233–245.

Lemaitre, J. (1996). *A course on damage mechanics*. Springer, Berlin, Heidelberg.

Lemaitre, J. and Chaboche, J.-L. (1990). *Mechanics of solid materials*. Cambridge University press, Cambridge, New York.

Lorenz, R. (1908). Achsensymmetrische verzerrungen in dünnwandigen hohlzylindern. *Zeitschrift Verein deutscher Ingenieure*, 52:1706–1713.

Lubliner, J. (1990). *Plasticity theory*. Macmillan Publishing company, New York.

Luenberger, D. (1992). *Linear and nonlinear programming*. Addison–Wesley, Massachusetts.

Marsden, J. and Hughes, T. (1983). *Mathematical Foundations of Elasticity*. Prentice–Hall, Englewood Cliffs.

Matias, W. (1996). *El método de desplazamiento crítico en el análisis de inestabilidad estrucural*. PhD thesis, Universitat Pollitècnica de Catalunya, departament de resistència de materials i estructures a l'enginyeria, Barcelona, Spain.

Menzel, R. and Schwetlick, H. (1978). Zur Lösung parameterabhängiger nichtlinearer Gleichungen mit singulären Jacobi-Matrizen. *Numerische Mathematik*, 30:65–79.

Moore, G. and Spence, A. (1980). The calculation of turning points of nonlinear equations. *SIAM Journal of Numerical Analysis*, 17:567–576.

Murakami, S. and Ohno, N. (1981). A continuum theory of creep and creep damage. In *Proceedings of the IUTAM symposium on creep in structures*, Leicester. Springer.

Oden, J. and Martins, J. (1985). Models and computational methods for dynamic friction phenomena. *Computer Methods in Applied Mechanics and Engineering*, 52:527–634.

Ogden, R. (1984). *Non-linear elastic deformations*. Ellis Harwood Ltd.; Halsted Press/John Wiley & sons, Chichester, England; New York.

Oliver, J. (1995). Continuum modeling of strong discontinuities in solid mechanics using damage models. *Computational Mechanics*, 17:49–61.

Oliver, J., Cervera, M., Oller, S., and Lubliner, J. (1990). Isotropic damage models and smeared crack analysis of concrete. In et. al., N. B., editor, *Proceedings SCI-C Computer Aided Analysis and Design of Concrete Structures*, pages 945–958, Swansea. Pineridge Press.

Oliver, J. and Oñate, E. (1986). A total lagrangian formulation for the the geometrically non linear analysis of structures using finite elements. part 2: Arches, frames and axisymmetric shells. *International Journal for Numerical Methods in Engineering*, 23:253–274.

Oliver, J. and Pulido, M. (1999). Dearrollos recientes sobre la simulación de discontinuidades fuertes utilizando modelos de daño continuo. In *IV Congreso Métodos Numéricos en Ingeniería*, Sevilla, Spain.

Oñate, E. (1991). Possibilities of the secant stiffness matrix for non linear finite elements analysis. *Non-linear Engineering Computations*.

Oñate, E. (1994). Reliability analysis of concrete structures and numerical experimental studies. In *Seminar on "Evoluzione nella sperimentazione per le costuzioni", Merano*, Merano, Italy.

Oñate, E. (1995). On the derivation and possibilities of the secant stiffness matrix for non linear finite element analysis. *Computational Mechanics*, 15:572–593.

Oñate, E. and Matias, W. (1995). Enhanced prediction of structural instability points using a critical displacement method. In Wiberg, N.-E., editor, *Advances in Finite Element Technology*, pages 62–89. CIMNE, Barcelona.

Oñate, E. and Matias, W. (1996). A critical displacement approach for predicting structural instability. *Computer Methods in Applied Mechanics and Engineering*, 134:135–161.

Papadrakakis, M. (1981). Post-buckling analysis of spatial structures by vector iteration methods. *Computers and Structures*, 14(5-6):393–402.

Ramm, E. (1981). Strategies for tracing the nonlinear response near limit points. In Wunderlich, W., Stein, E., and Bathe, K.-J., editors, *Nonlinear Finite Element Analysis in Structural Mechanics*, pages 63–89. Springer Verlag, Berlin, Heidelberg, New York.

Reitinger, R. (1994). *Stabilität und Optimierung imperfektionsempfindlicher Tragwerke.* PhD thesis, Universität Stuttgart, Institut für Baustatik.

Rheinboldt, W. (1981). Numerical analysis of continuation methods for nonlinear structural problems. *Computers and Structures*, 13:103–113.

Ricks, E. (1979). An incremental approach to the solution of snapping and buckling problems. *International Journal of Solids and Structures*, 15:529–551.

Riks, E. (1972). The application of newtons method to the problem of elastic stability. *Journal of Applied Mechanics*, 39:1060–1066.

Rohde, A. and Stavroulakis, G. (1997a). Genericity analysis for path-following methods. application in unilateral contact elastostatics. *ZAMM*, 77(10):777–790.

Rohde, A. and Stavroulakis, G. (1997b). Genericity results for path-following in discretized unilateral contact mechanics. In Guddat, J., editor, *Parametric optimization and related topics IV, Proceedings of the International Conference*, pages 315–328, Frankfurt. Lang.

Scherf, O. (1997). *Kontinuumsmechanische Modellierung nichtlinearer Kontaktprobleme und ihre numerische Aanalyse mit adaptiven Finite-Element-Methoden.* PhD thesis, Technische Hochschule Darmstadt, Institut für Mechanik.

Schweizerhof, K. and P.Wriggers (1986). Consistent linearization for path following methods in nonlinear FE analysis. *Computational Method in Applied Mechanical Engineering*, 59:261–279.

Seydel, R. (1979). Numerical computation of branch points in nonlinear equations. *Numerische Mathematik*, 33:339–352.

Simo, J., Fox, D., and Rifai, M. (1990). Formulation and computational aspects of a stress resultant geometrically exact shell model. In Krätzig, W. and Oñate, E., editors, *Computational Mechanics of nonlinear Response of Shells*, pages 62–89. Springer Verlag, Berlin.

Simo, J., Wriggers, P., Schweizerhof, K., and Taylor, R. (1986). Finite deformation postbuckling analysis involving inelasticity and contact constraints. *International Journal for Numerical Methods in Engineering*, 23:779–800.

Song, S. and Yovanovich, M. (1987). Explicit relative contact pressure expression: Dependence upon surface roughness parameters and vickers microhardness coefficients. Technical Report 87-0152, AIAA-paper.

Surana, K. (1983). Geometrically nonlinear formulation for the curved shell elements. *International Journal for Numerical Methods in Engineering*, 19(1):581–615.

Tessmer, J. (2000). *Theoretische und algorithmische Beiträge zur Berechnung von Faserverbundschalen.* PhD thesis, Universität Hannover, Institut für Baumechanik und numerische Mechanik.

Timoshenko, S. (1910). Einige stabilitätsprobleme der elastizitätstheorie. *Zeitschrift für Mathematik und Physik*, 58:337–385.

Truesdell, C. and Noll, W. (1965). *The nonlinear field theories of mechanics, Handbuch der Physik*, volume III/3. Springer Verlag, Berlin.

Tschöpe, H. (1996). Theoretische und numerische Untersuchung der Schmierspaltströmung elastischer wassergeschmierter Lager. Technical report, TU Darmstadt, Institute for Mechanics IV.

Tschöpe, H., Oñate, E., and Wriggers, P. (1999). The critical displacement method with a constitutive damage model. In *IV Congreso Métodos Numéricos en Ingeniería*, Sevilla, Spain.

Wagner, W. (1991a). A path–following algorithm with quadratic predictor. *Computers and Structures*, 39:339–348.

Wagner, W. (1991b). Zur Behandlung von Stabilitätsproblemen der Elastostatik mit der Methode der Finiten Elemente. Forschungs- und Seminarberichte aus dem Bereich der Mechanik der Universität Hannover F 91/1, IBNM, Universität Hannover.

Wagner, W. and Wriggers, P. (1988). A simple method for the calculation of postcritical branches. *Engineering Computations*, 5:103–109.

Wemper, G. (1971). Discrete approximation related to nonlinear theories of solids. *International Journal of Solids and Structures*, 7:1581–1599.

Werner, B. and Spence, A. (1984). The computation of symmetry–breaking bifurcation points. *SIAM Journal of Numerical Anaylsis*, 21:388–399.

Wood, R. and Zienkiewicz, O. (1977). Geometrically nonlinear finite element analysis of beams, frames, arches and axisymmetric shells. *Computers and Structures*, 7:725–735.

Wriggers, P. (1988). Konsistente Liearisierungen in der Kontinuumsmechanik und ihre Anwendungen auf die Finite–Element–Methode. Forschungs- und Seminarberichte aus dem Bereich der Mechanik der Universität Hannover F 90/2, IBNM, Universität Hannover.

Wriggers, P. (1995). *Finite Element algorithms for contact problems*, volume 2, pages 1–49. CIMNE, Barcelona.

Wriggers, P., Krstulovic, L., and Korelc, J. (1999). Development of 2d smooth polynomial frictional contact element based on a symbolic approach. In Wunderlich, W., editor, *Proceedings of the European Conference on Computational Mechanics*.

Wriggers, P. and Miehe, C. (1992). Recent advances in the simulation of thermomechanical contact processes. In D.R.J. Owen, E. Hinton, E. O., editor, *Proceedings of COMPLAS III*, Swansea. Pineridge Press.

Wriggers, P. and Miehe, C. (1994). Contact constraints within coupled thermomechanical analysis – a finite element model. *Computer Methods in Applied Mechanics and Engineering*, 113:301–319.

Wriggers, P. and Simo, J. (1990). A general procedure for the direct computation of turning and bifurcation points. *International Journal for Numerical Methods in Engineering*, 30:155–176.

Wriggers, P., Simo, J., and Taylor, R. (1985). Penalty and augmented lagrangian formulations for contact problems. In J. Middelton, G. P., editor, *Proceedings of NUMETA 85 Conference*, Rotterdam. Balkema.

Wriggers, P. and Wagner, W. (1989). Ein quadratisch konvergentes Verfahren zur Berechnung von Stabilitätspunkten. *ZAMM, Zeitschrift für angewandte Mathematik und Mechanik*, 69(4):T 219– T 222.

Wriggers, P., Wagner, W., and Miehe, C. (1988). A quadratically convergent procedure for the calculation of stability points in finite element analysis. *Computer Methods in Applied Mechanics and Engineering*, 70:329–347.

Zavarise, G., Schrefler, B., and Wriggers, P. (1992). Consistent formulation for thermomechanical contact based on microscopic interface laws. In D.R.J Owen, E. Hinton, E. O., editor, *Proceedings of COMPLAS III*, Swansea. Pineridge Press.

Zavarise, G., Wriggers, P., and Schrefler, B. (1998). A method for solving contact problems. *International Journal for Numerical Methods in Engineering*, 42:473–498.

Zienkiewicz, O. and Taylor, R. (1989). *The Finite Element Method*, volume 1. McGraw–Hill.

Zienkiewicz, O. and Taylor, R. (1991). *The Finite Element Method*, volume 2. McGraw–Hill.

Zoelly, R. (1915). *Über ein Knickungsproblem an der Kugelschale*. PhD thesis, Technische Hochschule Zürich, Zürich, Switzerland.